Plasmon Supported Defect Absorption in Amorphous Silicon Thin Film Solar Cells and Devices

Dissertation

for awarding the degree of
Doktor der Naturwissenschaften
(Dr. rer. nat.)

Faculty of Physics
University of Bielefeld

submitted by
Florian Lükermann

Bielefeld, 17th April 2013

This dissertation was carried out in the Molecular and Surface Physics group at the University of Bielefeld in collaboration with the Malibu GmbH & Co. KG (subsidiary of Schüco International KG).

I declare that this dissertation is original and no unauthorized source material or aids other then specified in the bibliography are used. All passages are indicated where references to the work of others are made.

Bielefeld, 17th April 2013

Florian Lükermann

Date of oral examination 5th June 2013

Examination Panel:

Prof. Dr. DrSc. h.c. Ulrich Heinzmann (Reviewer)
Prof. Dr. Helmut Stiebig (Reviewer)
Prof. Dr. Dietrich Bödeker (Examiner)
Prof. Dr. Thomas Huser (Examiner, Chairman)

Abstract

In this thesis the influence of metallic nanoparticles on the absorption of hydrogenated amorphous silicon (a-Si:H) thin film solar cell devices is investigated. Small metal nanostructures with lateral dimensions well below $100\,\mathrm{nm}$ accompany strong absorption and large electric field amplitudes in their vicinity. This is caused by the localized surface plasmon (LSP) resonances that are excited upon interaction of light with the nanostructures. By combining silver nanoparticles (Ag NPs) with amorphous silicon photovoltaic devices the influence of the enhanced fields on the amorphous silicon absorption is investigated.

In the presence of Ag NPs an enhanced optical absorption is measured, assigned to the LSP resonances. The Ag NPs are incorporated in different configurations in direct contact to the active a-Si:H layer of thin film devices. Irrespective of the device configuration an external quantum efficiency (EQE) signal is observed for photon energies below the bandgap of a-Si:H. States must be present that allow transitions for sub-bandgap energies. By a variation of the Ag NP position within the applied devices the role of interface states is evaluated. It turns out that defects in the a-Si:H material are responsible, that are created by the presence of the NPs and the internal surfaces. The according defect levels energetically lie within the a-Si:H bandgap. The exposure of defects to the strong fields in direct vicinity of the resonant absorbing NPs enable high transition rates from the defect levels to the conduction band. According to this mechanism, a model is proposed that in addition incorporates a charge compensation and transport process. Thermal escape provides the completion of transitions from the inner gap states to the nearest band edge (Fig. 5.11). No direct contact to the TCO (transparent conductive oxide) is necessary to provide carriers for charge compensation. The applied devices are a demonstration of the impurity photovoltaic (IPV) effect in a-Si:H.

The defect states contributing to the observed transitions are broadly distributed in the band gap. Most dominant transitions belong to states at a typical distance of $0.15\,\mathrm{eV}$ from the valence band edge, while also states deeper in the gap with a distance of up to $0.5\,\mathrm{eV}$ contribute.

Since these transitions are related to the enhanced fields caused by the LSP resonances, transitions are most dominantly observed when they overlap with the LSP resonance energy. Influencing the LSP resonance position by using different NP sizes also

Abstract

influences the position of dominant transitions. The observed signal in EQE measurements is shifted to longer wavelengths in agreement with a shifted LSP absorption.

The energetic position of the Fermi level (E_F) determines the occupation of inner gap defect states. When E_F is shifted downwards by a variation of the doping concentration in the NP environment, the sub-bandgap response decreases. This is related to inner gap defect states that become unoccupied. Occupied defect levels near the valence band are necessary for the generation process. The decreasing tendency could also be caused by recombination processes related to the introduced doping impurities or due to limitations of the charge transport.

For microcrystalline silicon (µc-Si:H) devices a similar EQE enhancement is found in the presence of Ag NPs for near or sub-bandgap light. With increasing Raman crystallinity of the host material, i.e. with decreasing bandgap, the IPV induced signal is shifted towards lower energies. The IPV effect is therefore not limited to the a-Si:H phase.

The exposure of Ag NPs to the atmosphere decreases the measured EQE enhancement. This could be related to the formation of an oxide shell that changes the field strength at the defect location.

The approach will likely not be feasible for the enhancement of solar cell performance. Parasitic absorption in the NPs decreases the EQE in the high absorption regime of a-Si:H. These losses are not compensated by the advantages in the sub-bandgap regime. However, the effect can be of interest for near infrared detector applications. Especially due to the enormous enhancement factors that are possible with these systems. Depending on the used photosensitive device structure, enhancement factors between 40 and 200-500 are achieved.

The investigations show the feasibility of a controlled large area deposition of metallic nanostructures. This is definitely of interest for a variety of future applications that utilize plasmonic effects, either in photovoltaic or other thin film electronic devices.

Keywords

localized surface plasmon resonance, silver nanoparticles, hydrogenated amorphous silicon, sub-bandgap photocurrent, impurity photovoltaic effect, resonant defect absorption

Kurzzusammenfassung

In dieser Arbeit wird der Einfluss von Metall-Nanopartikeln auf die Absorption von Dünnschicht Solarzell-Bauteilen aus hydrogenisiertem amorphem Silizium (a-Si:H) untersucht. Kleine Metall-Nanostrukturen mit einer lateralen Ausdehnung unterhalb von 100 nm besitzen eine starke Absorption und sind von großen Amplituden des elektrischen Feldes in ihrer direkten Umgebung begleitet. Dies ist auf die lokalisierten Oberflächenplasmonen-Resonanzen (englisch: localized surface plasmon (LSP) resonances) zurückzuführen, die durch die Interaktion von Licht mit den Nanostrukturen angeregt werden. Durch die Kombination von Silber Nanopartikeln (Ag NP) mit amorphen Silizium Photovoltaik-Bauteilen kann der Einfluss der Feldüberhöhung auf die Absorption des amorphen Siliziums untersucht werden.

Bei Anwesenheit der Ag NP ist eine erhöhte optische Absorption messbar, hervorgerufen durch die LSP Resonanzen. Die Ag NP werden dabei in verschiedenen Konfigurationen, in direktem Kontakt zur aktiven a-Si:H Schicht der Dünnschicht-Bauteile integriert. Unabhängig von der Bauteil Konfiguration kann ein externes Quanteneffizienz (EQE) Signal für Photonenenergien unterhalb der a-Si:H Bandlückenenergie gemessen werden. Es müssen daher Zustände existieren, die elektronische Übergänge für diese Photonenenergien ermöglichen. Durch die Variation der Ag NP Position innerhalb der Bauteile, kann der Einfluss von Grenzflächenzuständen evaluiert werden. Dabei zeigt sich, dass elektronische Defekte im a-Si:H Material für den Effekt verantwortlich sind. Diese werden durch die Anwesenheit der Ag NP an den internen a-Si:H Oberflächen erzeugt. Die dazugehörigen Defektzustände liegen energetisch innerhalb der a-Si:H Bandlücke. Die Tatsache, dass die Defekte den starken Feldern in der direkten Umgebung der resonant absorbierenden NP ausgesetzt sind, ermöglicht große Übergangsraten von den Defekt-Niveaus zum Leitungsband. Bezüglich dieses Mechanismus wird in der vorliegenden Arbeit ein Modell vorgeschlagen, das zusätzlich die Prozesse des Ladungsausgleichs und -transports erklärt. Thermische Anregung erlaubt Übergänge von Ladungsträgern aus den Defektzuständen zur nächstgelegenen Bandkante und komplettiert damit die Anregung der Ladungsträger vom Valenz- ins Leitungsband. In diesem Modell ist kein direkter Kontakt zum TCO (transparent conductive oxide) für den Ladungsausgleich notwendig. Mit den vorgestellten Bauteilen konnte der *impurity photovoltaic effect* (IPV) (Photovoltaischer Effekt aus Defektzuständen) für a-Si:H demonstriert werden.

Kurzzusammenfassung

Die Defektzustände, die zu den elektronischen Übergängen beitragen zeigen eine breite Verteilung in der Bandlücke. Die dominanten Übergänge gehören zu Zuständen mit einer typischen Lage von 0,15 eV oberhalb des Valenzbandes. Darüber hinaus tragen auch Zustände von bis zu 0,5 eV oberhalb E_V bei.

Da die elektronischen Übergänge mit den, durch die LSP Resonanzen hervorgerufenen, Feldüberhöhungen verbunden sind, finden Übergänge am wahrscheinlichsten für Defektzustände statt, deren energetischer Abstand zum Leitungsband gerade der LSP Resonanzenergie entspricht. Verändert man die LSP Resonanzenergie durch eine Variation der Ag NP Größe, so verschiebt sich auch die Position der dominanten Übergänge. In EQE Messungen ist eine Verschiebung des Signals in Übereinstimmung mit einer Verschiebung der LSP Resonanzposition zu beobachten.

Die energetische Lage des Fermi-Niveaus (E_F) bestimmt die Besetzung der Defektzustände innerhalb der Bandlücke. Wenn E_F durch eine Veränderung der Dotierkonzentration in der NP Umgebung nach unten verschoben wird, führt dies zu einer Verringerung des EQE Signals für Photonenenergien unterhalb der a-Si:H Bandlücke. Dies ist auf die Entleerung der beteiligten Zustände zurückzuführen. Besetzte Zustände in der Nähe des Valenzbandes sind notwendig für den Anregungsprozess. Die Verringerung des EQE Signals kann aber auch durch eine Erhöhte Rekombination, aufgrund der eingebauten Dotieratome oder Einschränkungen im Ladungsträgertransport hervorgerufen sein.

Für photosensitive Bauteile aus mikrokristallinem Silizium (µc-Si:H) wird der Effekt ebenfalls unter Anwesenheit von Ag NP beobachtet. Mit zunehmender Raman-Kristallinität des µc-Si:H Materials und somit kleiner werdender Bandlücke, wird das IPV induzierte Signal zu kleineren Energien verschoben. Der IPV Effekt ist daher nicht auf die a-Si:H Phase beschränkt.

Der Kontakt der Ag NP mit Atmosphäre verringert das gemessene EQE Signal. Dies könnte mit der Bildung einer Oxid-Hülle verbunden sein, die die Feldstärke am Ort der Defekte im a-Si:H verringert.

Die Eignung des gezeigten Effekts für die Verbesserung der Leistung von Solarzellen is fraglich. Die parasitäre Absorption der NP verringert das EQE Signal im Bereich, in dem die a-Si:H Absorption groß ist. Die hierdurch hervorgerufenen Verluste werden nicht durch die Gewinne im Bereich der schwachen Absorption (für Photonenenergien unterhalb der Bandlücke) kompensiert. Der Effekt könnte allerdings für die Anwendung in Detektoren für das nahe Infrarot von Interesse sein. Besonders durch die großen Verstärkungsfaktoren die in diesem Bereich möglich sind. Abhängig von der verwendeten Konfiguration der photosensitiven Bauteile sind Verstärkungen zwischen 40 und im Bereich von 200-500 fach möglich.

Die Untersuchungen demonstrieren die Eignung einer kontrollierten, großflächigen Abscheidung von Metall-Nanostrukturen. Dies is definitiv von Interesse für eine Viel-

zahl von zukünftigen Anwendungen, die plasmonische Effekte, entweder in photovoltaischen oder anderen elektronischen Dünnschicht Bauteilen integrieren sollen.

Schlagworte

Lokalisierte Oberflächen Plasmonen Resonanz, Silber Nanopartikel, Hydrogenisiertes Amorphes Silizium, Sub-Bandlücken Photostrom, Photovolatischer Effekt aus Defektzuständen, Resonante Defektabsorption

Contents

Contents

List of Figures

1. Introduction

The need for a sustainable development of the global economy and society is based on environmental friendly and resource conserving technology. Beneath the energy-efficient use, the regenerative generation of energy is a key issue. Amongst the other renewable energy sources as wind, water and bio-fuel the use of solar energy is of great importance.

Solar energy can be converted to usable energy by solar hot water technology or production of electricity from solar radiation with photovoltaic (PV) cells. The most dominant share of photovoltaic cells is based on silicon and especially on crystalline silicon wafer technology [1]. The decreasing price of solar modules in the past years led to an increase of the installed photovoltaic power. The price reduction is related to an excess production capacity of solar cells as well as decreasing silicon prices. Worldwide solar cells with a power outcome of $50\,\mathrm{GW}$ are produced in 2012, while the demand was only $35\,\mathrm{GW}$. The prices for wafers reduced from 2008 to 2012 from $450\,\$/\mathrm{kg}$ to less than $27\,\$/\mathrm{kg}$. This is caused by a strong increase of silicon production capacity [2]. The increase in installed power is also owing to governmental subsidies for example in Spain and Germany. Due to increasing costs these subsidiaries are going to be reduced [3]. The production of solar electricity is at the moment not price competitive with generation from fossil fuels. It is believed when the price for a kWh solar electricity is equal to or drops below the price for a kWh available from the grid it should be economically reasonable to use photovoltaic power generation. A price reduction is on the one hand accessible by reducing the manufacturing costs and/or by increasing the performance i.e. the efficiency of available PV technology. Further research and development is necessary to improve the quality and function of PV cells [4, p. 69].

Due to the abundance of silicon dioxide (SiO_2), a comprehensive supply of silicon is guarantied. Crystalline silicon (c-Si) solar cell technology is the most common technology on the one hand because of the Si availability, as well as comparably high efficiencies. c-Si solar cells show efficiencies of $25\,\%$ on cell level and around $23\,\%$ on module level[1] [5]. The disadvantage of c-Si technology is the large amount of material required for the conversion of sunlight, due to the indirect bandgap of c-Si. The production of silicon is energy consuming, therefore the need for an economic material usage is evident. Thin film technology, that uses only a fraction of material compared

---

[1]these values represent record efficiencies and should not be mixed up with values for commercially available modules, that in fact have lower efficiencies

to c-Si technology, provides the possibility of reducing material consumption. Together with the ability of large area deposition gives the opportunity of cost reduction. In particular thin film silicon solar cell technology has profited from innovations in deposition technology used in LCD displays [6]. Therefore large area deposition equipment on $1.4\,m^2$ [7] and nowadays even on $5.7\,m^2$ [8] are available. Thin film silicon requires low deposition temperatures, in the $200\,°C$ range which gives the flexibility of choosing a variety of substrates. Commonly cheap glass substrates are applied, while also flexible substrates like metal or plastic foils are possible. This opens a way for new applications and integration. Thin film technology on the other hand has to cope with lower efficiencies. Especially amorphous silicon is at the moment limited to around $10\,\%$ cell efficiency [5], while modules suffer from an efficiency around $6\,\%$ [6].

The combination of thin film materials with semiconductors of different bandgap are applied to spectrally split the solar irradiation. Such multi junction cells are prepared from hydrogenated amorphous silicon (a-Si:H) and microcrystalline silicon (µc-Si:H) or using alloys with germanium (Ge) to form a-SiGe:H material. These systems reach efficiencies around $12\,\%$ on cell and about $10\,\%$ on module level [5], their preparation is though technologically sophisticated.

For reaching high efficiencies in thin film silicon solar cells it is essential to exploit the available solar radiation as effective as possible. Beneath high material quality, light trapping approaches are essential for an efficient use of near bandgap light. Rough interfaces are needed in order to scatter incident light and enlarge the optical path inside the relevant absorber layers. It is commonly applied by using rough transparent conducting oxide (TCO) layers. In the case of ZnO or SnO_2 that are deposited by *Chemical Vapor Deposition (CVD)* inhibit a rough, textured surface. This surface texture provides good scattering abilities [9, 10]. The TCO layers also function as conductor for generated charge carriers. Apart from the CVD grown TCOs, also initially smooth, sputter deposited ZnO layers are used [11–13]. These have to undergo a wet chemical etching process in order to form crater like structures on the surface, that also act as efficient light trapping substrate for the deposition of thin film solar cells.

In recent years the use of localized surface plasmon (LSP) resonances that are excited upon the interaction between electromagnetic radiation and metal nanostructures is of growing interest. LSP resonances promote scattering of light or absorption depending on the size of the nanostructure. Relatively large structures in the order of $100\,nm$ can be used for scattering of light, while small particles result in a near field scattering, i.e. strong enhancements of the electromagnetic field in the vicinity of the nanostructures.

Plasmonic light scattering was investigated for light in-coupling into solar cells [14–17] as well as out-coupling from light emitting diodes [15, 16]. The large silver nanoparticles used here have a large scattering cross section and are in analogy to rough interfaces able to scatter incident light under large angles [18]. Hereby the optical path

inside the cells is increased. In the case of light emitting devices, the NPs couple the emitted light more efficiently to the far field and reduce the reflections at the device surface. For thin film a-Si:H solar cells the light scattering approach is also demonstrated with large nanoparticles [19–23] or similar to that with structured metal back reflectors [24–26]. With respect to the far field scattering approach also the use of dielectric NPs is proposed to result in a beneficial effect. These materials have the advantage of lower losses because they avoid parasitic absorption going along with plasmonic response of metals [18]. Beside the approach focusing on light trapping by scattering, near field scattering can be applied to solar cells. Here the incident radiation is stored in a locally confined mode in direct vicinity of the plasmonic nanostructure [27]. The concept of using near field enhancements is similar to approaches in molecular spectroscopy, especially in Raman scattering. Here the interaction of intense near fields with molecules can increase the Raman signal of the molecules by orders of magnitude. The intense fields are excited at rough metal surfaces due to sharp asperities that give rise to localized surface plasmon resonances and accompany strong fields [28, p. 235-239][29, p. 168-173]. This method is known as *Surface Enhanced Raman Scattering (SERS)*. Concerning light harvesting structures, Hägglund et al. [30] propose the use of ultra-thin absorber layers, 100 times thinner than conventional thin film photovoltaic devices (so called *'two dimensional'* photovoltaics) in combination with plasmonic structures. This is investigated in order to profit from the near field enhancement around these structures. The necessity to avoid recombination channels for generated charge carriers as well as to minimize damping losses associated to the plasmonic excitations is claimed here. Plasmonic enhancement of electron hole pair generation is observed in various materials including photocatalytic water splitting [31], organic solar cells [32–36] and also for amorphous silicon based solar cells. It has been shown that embedding small silver (Ag) NPs ($\approx 20\,\mathrm{nm}$) in between the front TCO and the intrinsic absorber layer of a-Si:H photosensitive devices can yield a photocurrent for energies below the a-Si:H bandgap [37, 38]. The effect is attributed to charge carrier excitation at the TCO/AgNP/a-Si:H Schottky contact, that is enhanced due to the LSP induced increase of the electromagnetic field in the vicinity of the NPs.

In this thesis the influence of Ag NPs on a-Si:H is investigated. Especially a deeper understanding of the involved processes and the origin of the electronic states that contribute to the sub-bandgap generation of charge carriers should be acquired. The role of involved materials for the effect of sub-bandgap current generation is not yet understood. Since it is observed for NPs at the interface of TCO to a-Si:H, various excitation paths could exist. For instance, surface states at the TCO/a-Si:H interface, states in the ZnO, the metal NP or the a-Si:H itself can in principle be involved in the generation mechanism.

Further the question whether the effect depends on the used thin film silicon material, i.e. if a variation of the absorber material to µc-Si:H has an influence and if the effect can even be observed for such a device.

A more technical question is related to the scalability of the used processes for device manufacturing. Since the amorphous silicon devices are usually deposited on large area substrates with a lateral dimension of $1.4\,\mathrm{m}^2$, the relevant layers especially the metal nanoparticles should be prepared on the same substrate size. Thin layers with a thickness in the order of $10\,\mathrm{nm}$ have to be deposited. This is a challenge for large area deposition facilities, because they are usually operated for the deposition of much thicker layers.

2. Fundamentals

In this section the principles of solar energy conversion are introduced. The operation of solar cells are discussed, while the main focus is based on thin film solar cells. Here the properties of hydrogenated amorphous silicon (a-Si:H), an important absorber material for thin film silicon solar cell technology is presented in more detail. Further optical loss mechanisms for solar cells are discussed. An approach concerning the enhancement of the spectral sensitivity with the impurity photovoltaic effect is highlighted.

In the end basic principles for the interaction of light with metal nanostructures and the related phenomena like plasmons and enhanced electromagnetic fields are discussed. The ability of the NPs related to strong absorption and field enhancements in their environment are applied in this work to influence the spectral sensitivity of amorphous silicon solar cells.

2.1. Solar Cells - Fundamental Principles

The fundamental operation principle of a solar cell is the conversion of electromagnetic energy into electrical energy by the *Photovoltaic Effect*. Incident photons are absorbed by a semiconducting material to create electron hole pairs. These charge carriers have to be separated and collected at different electrodes to draw electrical energy from the solar cell [39, p. 3]. This is discussed in more detail in section 2.2. Since solar cells in general are used to convert the electromagnetic radiation provided by the sun into electrical energy, the solar spectral radiation and consequences of specific features for solar cells and the outcome have to be considered.

2.1.1. Solar Spectral Radiation

The (extraterrestrial) solar spectrum emitted by the sun has a maximum near 500 nm, as shown in Fig. 2.1. This is quite close to the black body radiation according to the suns surface temperature of 5777 K [40].

Before the light reaches the ground surface, it has to pass the earth's atmosphere. Here certain parts of the extraterrestrial spectrum are absorbed, resulting in the Air Mass (AM) 1.5 spectrum (blue curve). For the UV light below 300 nm the main absorption bands are caused by ozone O_3. The absorption bands for longer wavelengths
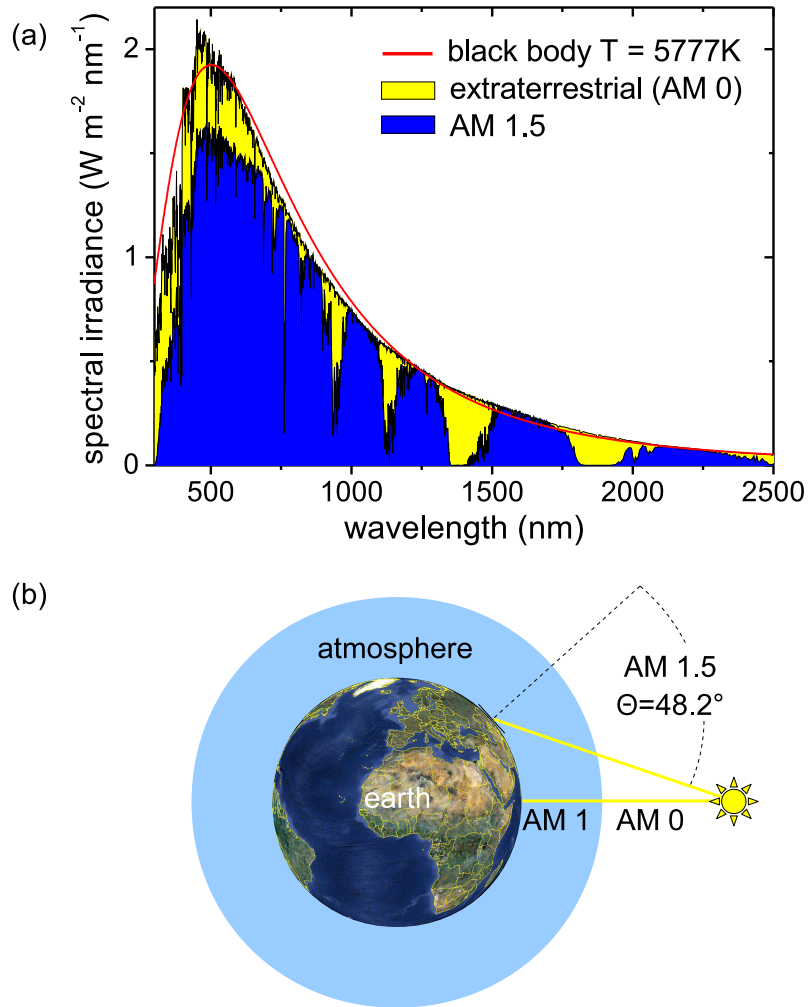
Figure 2.1.: (a) Black body radiation at $5777\,\mathrm{K}$, extraterrestrial solar spectrum and AM 1.5 spectrum [41, 42] and (b) schematic illustration of the Air Mass definition (not true to scale), the picture of the earth is taken from [43].

are due to O_2, H_2O and to a certain portion CO_2 [44, p. 16]. The denotation Air Mass (AM) is related to the elongated path length of the sunlight through the atmosphere with respect to normal incidence. The AM factor is determined by the angle of incidence θ with respect to the earth's surface normal. It depends on the suns elevation as well as the geographic latitude on earth. It is defined by the ratio of the path L and the thickness of the atmosphere L_0 by: $AM = \frac{L}{L_0} \approx \frac{1}{\cos(\theta)}$ [45, p. 26-27]. The extraterrestrial spectrum outside the atmosphere corresponds to AM 0. AM 1 corresponds to the perpendicular passage, while AM 1.5 refers to an angle of about $48.2°$ with respect to the surface normal. The path lengths of AM 1.5 is 1.5 times longer than for AM 1. The characterization of solar cells is executed by convention under AM 1.5 spectral

irradiation. It represents roughly the average value in the mid latitudes where most of the industrialized countries and installed solar cells are situated. For details on solar cell test conditions see section 3.2.10.

2.1.2. Electronic states in semiconductors

The occupation of electronic states in a semiconductor is described by a Fermi distribution f(E, T) [45, p. 45]:

$$f(E,T) = \frac{1}{\exp\left(\frac{E-E_F}{k_B T}\right) + 1} \tag{2.1}$$

where T is the temperature, k_B the Boltzmann constant and E_F is the Fermi energy. At T=0 the Fermi energy separates the occupied from the unoccupied states. The energetic states of a semiconductor are comprised of a filled valence band and an empty conduction band. These are separated by a forbidden energy gap, with the width E_g. At T=0 the Fermi level lies in the center of the gap. An electron from the valence band is excited by the absorption of a photon to the conduction band if the photon energy $h\nu$ is larger than the bandgap ($h\nu \geq E_g$). After excitation the electron quickly releases its access energy by emitting phonons until it relaxes to the conduction band edge E_C. The same applies to the hole left in the valence band (see Fig. 2.2 (b)). This process known as *thermalization* is fast (in the order of 10^{-12}s [45, p. 59]). The further release of energy is hindered due to the bandgap and lack of available states. Therefore transitions across the bandgap by radiative recombination is much slower (in the order of 10^{-3}s [45, p. 44]). Eq. 2.1 can be applied in thermal equilibrium. If charge carries are injected by an applied voltage or by illumination, the system deviates from thermal equilibrium. Due to the fast thermalization of excited electrons in the conduction band (and holes in the valence band), they are considered to be in thermal equilibrium with their band. This allows to describe the distribution of charge carriers in the conduction and valence band by two different Fermi distributions (*quasi Fermi distributions*). One Fermi distribution is defined for the electrons in the conduction band (f_{FC}) and one for the holes in the valence band (f_{FV}). The concept of quasi Fermi levels is valuable to describe solar cells in situations away from thermal equilibrium which is the case under normal operation, i.e. under illumination and applied voltages [45, p. 136-137] [46, p. 363].

2.1.3. Spectral Loss Mechanisms in Solar Cells

The solar energy that reaches the earth's surface has to be used as efficient as possible. Due to the light harvesting principle of a solar cell by a semiconducting material with a certain bandbap, this conversion has certain limits. Fig. 2.2 demonstrates the use of the AM 1.5 spectral radiation for the example of crystalline silicon with a bandgap of

1.12 eV (1100 nm). The two main loss mechanisms concerning the utilization of the solar spectrum are illustrated here.

(a) (b)
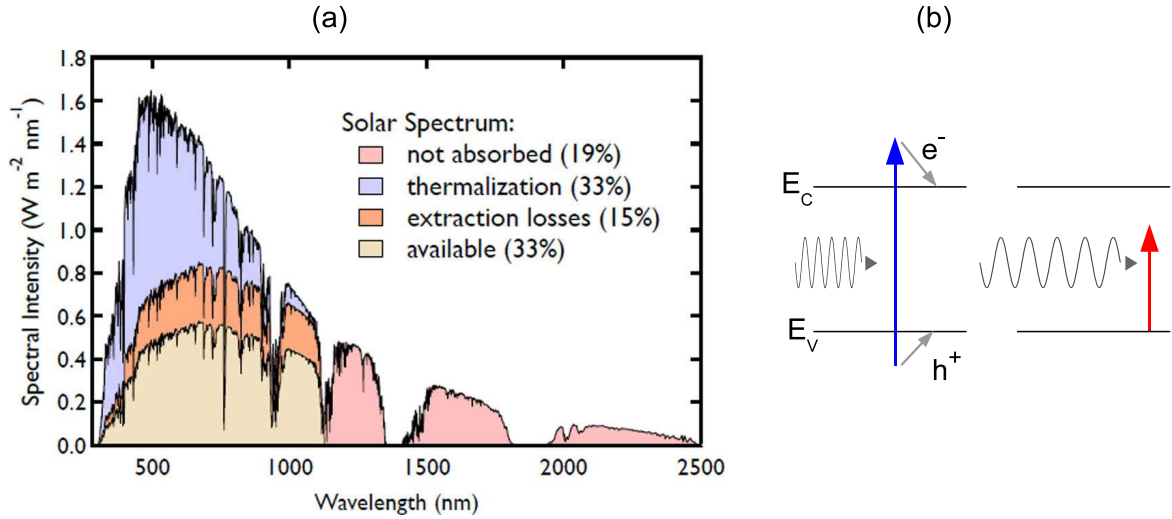
Figure 2.2.: (a) Exploitation of the AM 1.5 spectrum by a c-Si solar cell, from [47] and (b) according losses due to thermalization and sub-bandgap photons.

A photon with an energy larger than the semiconductor bandgap is consumed in the transition of an electron from the valence to the conduction band. The electron is excited to an energy level above E_C. The maximum energy that can be gained from this process is the bandgap energy E_g, because the electron quickly releases its excess energy with respect to E_C (and the hole with respect to E_V) to heat by emitting phonons (Fig. 2.2 (b)). The associated wavelength dependent losses are shown in (a). A way to use a larger amount of energy from these photons is the application of *photon down-conversion*. Here one photon with $h\nu > 2\ E_g$ is split in two photons with $h\nu \geq E_g$. The down-converter is either placed behind or simpler in front of the actual absorber. It utilizes a three level system, while high energy photons are absorbed by the large energy transition. The emission of lower energy photons is then accomplished by recombination via the intermediate level [45, p. 206-209]. Thermalization can also be reduced by dividing the solar spectrum in different parts and using for example stacked multi junction cells whose different bandgaps are designed for the absorption of different spectral regions [48, p. 59-62]. In principle thermalization losses occur for all photons with energies larger E_g, also for those very close to E_g. For these photons a further loss mechanism becomes more important. Since the absorption coefficient decreases near E_g, the efficiency for charge carrier generation becomes smaller in this regime. For amorphous silicon solar cells as will be discussed in detail later, above 650 nm the generation of charge carriers drastically decrease. Collection losses of generated charge

carriers due to recombination and parasitic resistances etc. further lower the outcome of the usable solar spectrum.

The second main loss mechanism occurs due to sub-bandbap photons whose energy is not sufficient to drive electronic transitions across the bandgap. For c-Si this applies to wavelengths above 1100 nm, for a-Si:H approximately above 800 nm. To utilize these photons for solar energy generation one either has to apply semiconductors with smaller bandgaps or two low energy photons have to be converted into one high energy photon that is able to drive transitions across the bandgap. This concept, known as *photon up-conversion* utilizes a material that is electrically isolated from the solar cell and interacts only optically with it [49, 50]. In the up-converter a three or four level system is used to absorb two photons, while a photon with the sum of both absorbed energy portions is emitted via radiative recombination to the ground state [45, p. 206-209]. This photon is then absorbed in the solar absorber to drive an electronic transition. A similar approach is the application of the *Impurity Photovoltaic Effect (IPV)* where impurities or defect levels of the solar cell semiconductor itself are used as intermediate step to drive electronic transitions from the valence to the conduction band. This will be discussed in more detail in section 2.1.8.
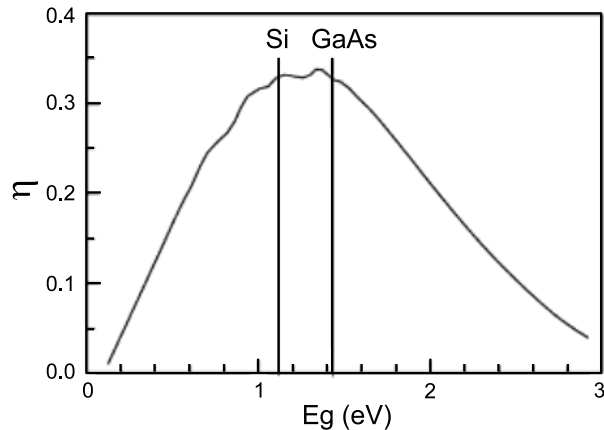
Figure 2.3.: Conversion efficiency η versus semiconductor bandgap of a single junction solar cell under AM 1.5 illumination, from [45, p. 171].

Apart from these sophisticated strategies, the losses caused by thermalization and sub-bandgap photons are influenced by the bandgap of the semiconductor. For a smaller bandgap a larger amount of photons is absorbed. Low energy photons also contribute to the photocurrent. On the other hand thermalization losses are much more crucial for low bandgap solar cells. A lot of energy is wasted for high energy photons. The opposite is true if a wide bandgap semiconductor is used. Here thermalization of high energy electrons is minimized but the long wavelength part of the spectrum is wasted. This results in a trade-off for optimum utilization of the solar

spectrum with respect to the semiconductor bandgap. It is illustrated in the calculated curve in Fig. 2.3 for the conversion efficiency η of a single junction solar cell with respect to its bandgap under AM 1.5 radiation. In this curve the *Shockley-Queisser limit* that only considers radiative recombination processes is taken into account [51]. η has a maximum for bandgaps between 1 and 1.5 eV and approaches zero for a $E_g = 0$ and large bandgaps $E_g >> 1$. Semiconductors like c-Si or GaAs are well suited for application in solar cells with respect to their bandgap. For these materials efficiencies around 30 % are possible [45, p. 170-171]. The application of the here discussed strategies of reducing thermalization and sub-bandgap losses is able to raise the efficiency to even higher values [45, p. 187-209].

2.1.4. Recombination of Charge Carriers

With the generation of charge carriers a deviation from thermal equilibrium goes along. The system aims to reach equilibrium by release of energy. This is accomplished by recombination of charge carriers. There are three types of recombination [45, p. 74-85]. The first one is *radiative recombination* of electrons and holes across the bandgap under the release of electromagnetic radiation. In addition there are two types of nonradiative processes, *Auger recombination* and *defect recombination*. Auger recombination is a process where the difference energy of a recombination process across the bandgap is transfered to a second charge carrier. For n-type material a conduction band electron is excited high into the band where it thermalizes by the release of phonons to E_C. Auger recombination dominantly takes place in highly doped regions, because the density of charge carriers must be large enough for an energy transfer to another carrier. The third recombination path via defects in the bandgap is also known as *Shockley-Read-Hall* recombination [52, 53]. The defect state captures electrons from the conduction band, while the energy is dissipated by the release of phonons. From that level the electron can recombine with a hole in the valence band. States near mid-gap are the most effective recombination centers. Their energetic position is close to the intrinsic Fermi energy and therefore parts of these states are occupied, while others are empty. Therefore a lot of states are available for capture of electrons from the conduction or holes from the valence band [45, p.84-85].

Recombination at interfaces is similar to recombination via defects, since at an interface a continuum of defects is available for nonradiative recombinations.

2.1.5. Solar Cell Dark Current Characteristics

In a solar cell generated electron hole pairs have to be separated and extracted at opposite electrodes in order to draw electrical energy from the device. The separation

of charge carriers is executed by a p-n junction, i.e. a junction between a p-doped and an n-doped region.

The doping of a semiconductor results in a shift of the Fermi level, for n-type doping towards the conduction and for p-type doping towards the valence band. In the case of a p-n junction both types of doped regions are in direct contact to each other. The different concentrations of electrons and holes in the adjacent materials leads to a redistribution of charge carriers. Electrons diffuse from the n- to the p-side while holes from p- to n-side giving rise to a space charge region. This process elapses until an equilibrium between diffusion and electrical potential due to the space charge is build-up. In thermal equilibrium the Fermi level is constant over the complete device (see Fig. 2.4 (a)). Since the Fermi levels far apart from the space charge region are different for both doping regions, the bands have to bend. This is an indication for the build-up of the potential difference caused by the charge carrier diffusion. The built-in potential is responsible for the separation of excited charge carriers, electrons in the conduction band are transported to the n-side while holes in the valence band are transported to the p-side [39, p. 2-6].

A p-n junction without illumination, i.e. in the dark, can be considered as an ideal diode. Without an applied voltage the total current density j(x) at a certain location x is the balance of recombination current density j_{rec}(x), caused by recombination of minority carriers and generation current density j_{gen}(x) caused by thermally generated carriers [39, p.13]:

$$j(x) = j_{rec}(x) - j_{gen}(x) = 0 \,. \tag{2.2}$$

If an external voltage is applied or the p-n junction is illuminated, minority carriers are injected and the junction is not in equilibrium any more. The concentration of charge carriers in the conduction and valence band cannot be described by a common Fermi distribution. Instead a *quasi Fermi energy* for the electrons in the conduction E_{FC} and holes in the valence band E_{FV} have to be applied (Fig. 2.4 (b)+(c)). Considering the dark state of a p-n junction and increasing the applied voltage U in forward direction, the potential barrier for diffusion is reduced. Thus more electrons from the n-side diffuse to the p-side, where they recombine. This can be expressed with a Boltzmann factor $\exp\left(\frac{qU}{nkT}\right)$ that appears in the recombination current [46, p- 362]:

$$j_{rec}(U) = j_{rec}(U = 0) \cdot \exp\left(\frac{qU}{nkT}\right) . \tag{2.3}$$

Here q is the elementary charge and n is the so called diode ideality factor. This factor incorporates the influence of thermal generation and recombination inside the depletion region of the p-n junction. In ideal case of a p-n junction $n = 1$ (when diffusion current dominates) or $n = 2$ for a p-i-n type diode when recombination and generation
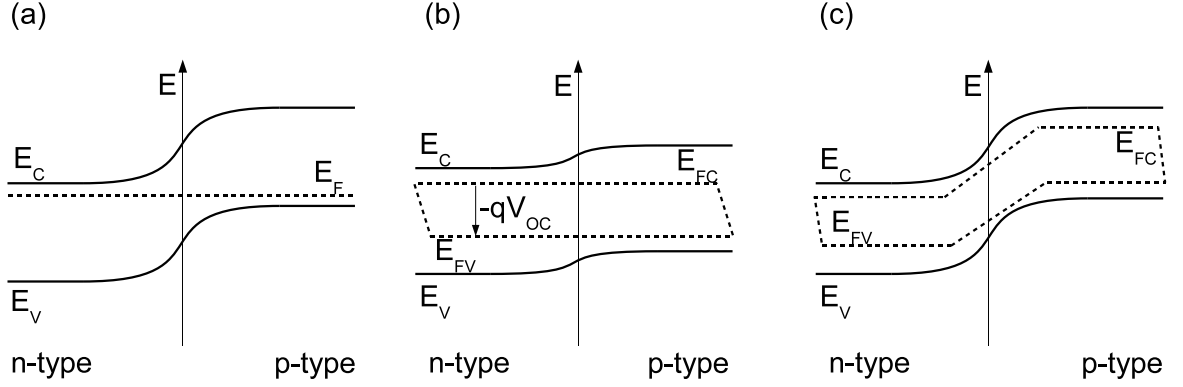
Figure 2.4.: p-n junction in thermal equilibrium and under illumination. (a) in thermal equilibrium without illumination or applied voltage a common Fermi level, constant across the whole junction, is used to describe the occupation of states in the semiconductor. (b)+(c) p-n junction under illumination in the (b) open circuit and (c) short circuit condition. Here due to illumination the quasi Fermi levels for electrons in the conduction and holes in the valence band have to be used to describe the occupation of states, after [39, p. 5-15].

dominate, like for a-Si:H solar cells (see Section 2.2.3) [54, p. 157-158]. The generation current j_{gen} does not depend on the applied voltage $j_{gen}(U = 0) \approx j_{gen}(U) \equiv j_0$ [46, p- 361-363], where j_0 is the saturation current density. The total current density can be expressed with these definitions as:

$$ j(U) = j_{rec}(U) - j_{gen}(U) = j_0 \cdot \left(\exp\left(\frac{qU}{nkT} \right) - 1 \right) . \tag{2.4} $$

The saturation current can be expressed as [45, p. 140]:

$$ j_0 = q \ G^0_{e,h}(L_e + L_h) , \tag{2.5} $$

where $G^0_{e,h}$ is the generation rate in the dark and $L_{e,h}$ are the diffusion lengths for electrons and holes. These are linked to the diffusion constants $D_{e,h}$ and lifetimes $\tau_{e,h}$ of electrons and holes via $L_{e,h} = \sqrt{D_{e,h} \cdot \tau_{e,h}}$. In equilibrium generation $G^0_{e,h}$ and recombination rates $R^0_{e,h}$ are equal. They are determined by the concentration of the minority carriers, i.e. electrons in the p-region n^p_e and holes in the n-region n^n_h and the according carrier life times by [45, p. 140-141]:

$$ G^0_{e,h} = R^0_{e,h} = \frac{n^p_e}{\tau_e} = \frac{n^n_h}{\tau_h} . \tag{2.6} $$

With the substitutions $n^p_e = \frac{n_i^2}{n_A}$ and $n^n_h = \frac{n_i^2}{n_D}$ (i.e. expressing the density of electrons and holes by the intrinsic carrier density n_i and the density of acceptors in the p- as

well as donors in the n-region) and $\tau_e = \frac{L_e^2}{D_e}$, $\tau_h = \frac{L_h^2}{D_h}$, j_0 can be written by using Eq. 2.5 and 2.6 as follows:

$$j_0 = q \ n_i^2 \left(\frac{D_e}{n_A L_e} + \frac{D_h}{n_D L_h} \right) . \tag{2.7}$$

2.1.6. Solar Cell Characteristics Under Illumination

When the solar cell is considered in the illuminated case, additional generation of charge carriers arises from absorption of photons. This photo current density j_{ph} is added under assumption of the superposition principle (recombination of the photogenerated carriers are neglected) to the generation current j_{gen}. The total current density under illumination can be expressed as:

$$j(U) = j_{rec}(u) - j_{gen}(U) - j_{ph} = j_0 \cdot \left(\exp\left(\frac{qU}{nkT} \right) - 1 \right) - j_{ph} . \tag{2.8}$$

The current voltage characteristic under illumination is determined by the dark current characteristic and is shifted downwards by the value of the photocurrent $j_{ph} = j_{SC}$. This is illustrated in Fig. 2.5 where the current-voltage characteristics are calculated according to equation 2.9. A real solar cell device is not as ideal as considerations above suggest. Ohmic losses due to a non zero resistivity of the solar cell contacts as well as all wires and cables connecting the solar cell make it necessary to introduce a series resistance R_S to the equations. This is especially important for thin film solar cells that utilize transparent conductive oxide contacts that are limited because of a comparably high sheet resistance. Additionally shunts between the p- and n-contact are considered by a parallel (or shunt) resistance R_{SH}. A schematic equivalent circuit for a solar cell is shown in Fig. 2.5 (b). Beneath the current source that provides the photocurrent under illumination and the diode, a shunt and series resistance are included.

$$j(U) = j_0 \cdot \left(\exp\left(\frac{q(U - j(U)R_S)}{nkT} \right) - 1 \right) + \frac{U - j(U)R_S}{R_{SH}} - j_{ph} . \tag{2.9}$$

Up to now only radiative recombination between E_C and E_V are considered. In real solar cells also recombination via defect states and impurities in the bandgap are evident. This additional recombination path of charge carriers can be represented in the model by incorporating an additional diode. This is known as the *two diode model* [45, p. 143] and is accounted for by addition of a second diode term in Equation 2.9.
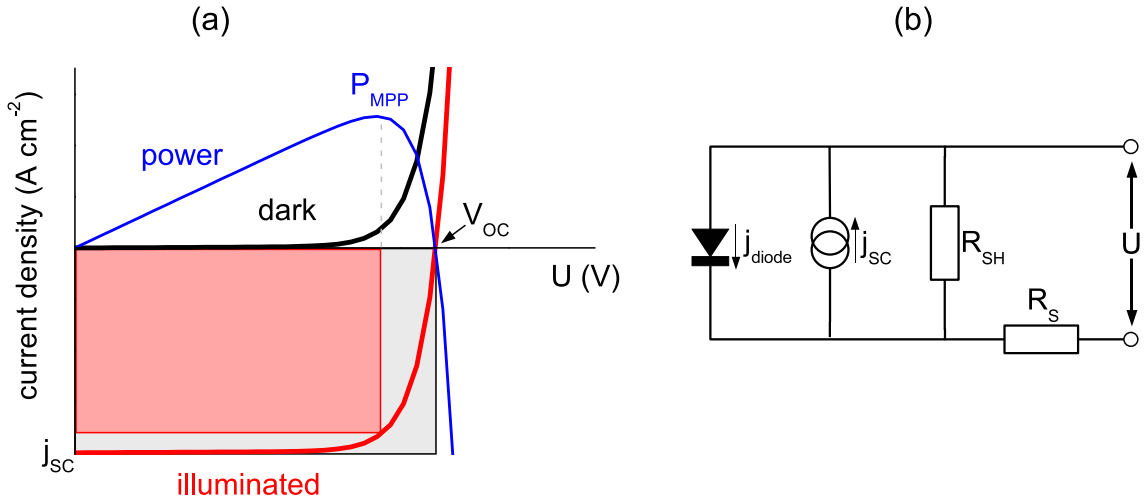
Figure 2.5.: (a) Current voltage characteristic of a solar cell under illumination and in the dark. The generated power is shown in blue, its maximum corresponds to the maximum power point P_{MPP}. (b) Equivalent circuit for a solar cell, incorporating losses due to series and shunt resistances, after [55, p. 80].

2.1.7. Solar Cell Parameters

From Fig. 2.5 (a) important quantities characterizing a solar cell can be extracted. The short circuit current density j_{SC} is measured at an applied voltage of zero. This is the current density measured at short circuited contacts of the solar cell (see Fig. 2.4 (c)).

The open circuit voltage V_{OC} is determined for $j = 0$. At this point the photocurrent is exactly balanced by the dark current. The V_{OC} is evaluated by setting equation 2.9 to zero and neglecting all losses, meaning $R_S = 0$ and $R_{SH} \to \infty$. Under the assumption that $j_{ph} = j_{SC}$ one obtains:

$$V_{OC} = \frac{nkT}{q} \ln \left(\frac{j_{SC}}{j_0} + 1 \right) \qquad (2.10)$$

The open circuit voltage increases with increasing j_{SC} and decreasing j_0. Since $j_0 \propto n_i^2$ (see Eq. 2.7) and $n_i^2 \propto \exp(-\frac{E_g}{kT})$ [46, p. 341] the open circuit voltage depends on the bandbap. The larger E_g the smaller j_0 and the larger V_{OC} [56, p. 380-381]. The decrease of j_{SC} with increasing bandgap results in a trade-off for the maximum achievable efficiency as function of E_g (already shown in Fig. 2.3).

The working point of a solar cell is the maximum power point P_{MPP}. At this point the solar cell delivers the maximum power density. P_{MPP} in turns is associated to the current density j_{MPP} and the voltage U_{MPP}. The *fill factor (FF)* can be defined with these quantities by a geometric construction. The FF is the ratio given by the (red) rectangle belonging to the maximum power point and the (gray) rectangle defined by

j_{SC} and V_{OC} [45, p. 168]:

$$FF = \frac{j_{MPP} \cdot U_{MPP}}{j_{SC} \cdot V_{OC}} \ . \tag{2.11}$$

Owing to the shape of the I-U-characteristic, the fill factor is always smaller than 1.

The overall conversion efficiency η is the amount of electrical power generated by the solar cell in relation to the incident power P_{inc}. It is the quotient of the power generated at MPP and P_{inc}:

$$\eta = \frac{P_{MPP}}{P_{inc}} = \frac{j_{MPP} \cdot U_{MPP}}{P_{inc}} = \frac{FF \cdot j_{SC} \cdot V_{OC}}{P_{inc}} \tag{2.12}$$

[45, p. 167-170] All these parameters are influenced by the series and parallel resistances of the solar cell. For an ideal cell R_S is zero while $R_{SH} \to \infty$. When R_{SH} is reduced due to conduction paths between the front and back contact or due to leakage current at the edges of the cell, the FF and V_{OC} are reduced. For an increased R_S caused by contact problems or increased resistances of the conducting layers, the FF and j_{SC} are reduced. As a consequence the conversion efficiency is reduced, when R_S and R_{SH} deviate significantly from the ideal case. [55, p. 78-80]

2.1.8. Impurity Photovoltaic Effect

In section 2.1.3 spectral loss mechanisms for solar cells have been discussed. The major losses arise, beneath the thermalization of charge carriers, from sub-bandgap photons that cannot be absorbed by the solar cell. One strategy is to use impurity levels in the forbidden gap of the semiconductor to drive transitions via a two step excitation. This *impurity photovoltaic effect (IPV)* was proposed by Wolf in 1960 [57]. The excitation via an impurity level E_{imp} is shown schematically in Fig. 2.6 (a) for the case of a level near mid-gap as well as close to E_V. Defect states near mid-gap act as efficient recombination centers [45, p. 84], competing strongly with generation of charge carriers. Theoretical predictions by Kasai et al. [58] predict a net increase of charge carrier generation for defect or impurity levels close to the band edges. Making the utilization of such levels advantageous. In addition the defects should be placed in devices at regions of low carrier concentration [59, p. 151][58]. This is the depletion region of c-Si p-n junctions or the intrinsic layer of a-Si:H p-i-n devices.

The use of defect states near mid-gap requires two photons of equal energy to generate an electron hole pair. This limits the generation rate for these kind of defects. States close to the band edge in contrast need a comparably high energy photon. The close energetic distance to the valence band however gives the opportunity to complete the transition via thermal excitation [59, p. 151-152]. The generation rate from impurity levels can be considered after Keevers et al. [60] by taking into account the optical
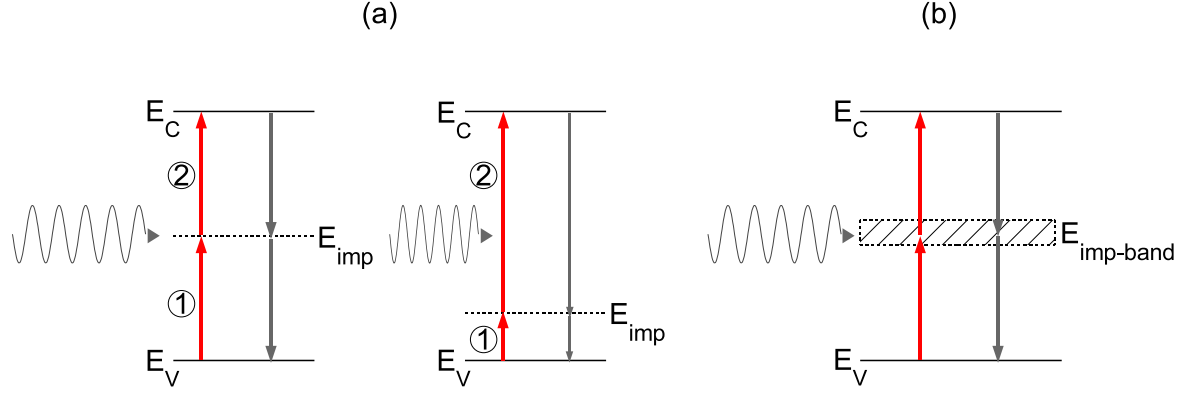
Figure 2.6.: Schematic illustration of IPV effect for impurity level E_{imp} (a) near mid-gap as well as near to E_V and (b) intermediate band solar cell. Generation and recombination paths are also indicated, the dominating recombination for mid-gap levels is reduced by using levels near to the band edges.

emission processes from the impurity level to the conduction band or the valence band to the impurity level, indicated with numbers *1* and *2* in Fig. 2.6 (a). The generation rate g_n for transitions of electrons from the impurity to the conduction band (process *2*) can be expressed as:

$$g_n = N_t \, f^e \, \sigma_n^{opt} \, \Phi_{ph}(x) \,. \tag{2.13}$$

N_t is the density of impurities, f^e is their occupation probability with electrons, σ_n^{opt} is the optical photoemission cross section for electrons from the impurity and $\Phi_{ph}(x)$ is the photon flux density at distance x from the illuminated surface. Since the solar photon flux density (AM 1.5 spectrum) as well as the optical cross section are wavelength dependent, an integration over λ is necessary:

$$g_n = N_t \, f^e \int_{\lambda(E_g)}^{\lambda(E_C - E_{imp})} \sigma_n^{opt}(\lambda) \, \Phi_{ph}(x, \lambda) d\lambda = f^e \, g_{n,max}. \tag{2.14}$$

The integration boundaries incorporate all transitions from the threshold wavelength according to the distance of the impurity to the conduction band $(E_C - E_{imp})$, up to transitions according to the bandgap energy. This simplification suggests that for photon energies above E_g transitions only occur in band to band transitions, without the incorporation of the impurity level. g_n is maximal when all impurities are occupied by electrons, i.e. when $f^e = 1$.

The process *1* in Fig. 2.6 can be handled accordingly. Here the excitation of electrons from the valence band to the impurity level or equivalent the emission of holes from the impurity to the valence band is considered. In analogy to Eq. 2.14 the generation

rate of holes g_p can be written as:

$$g_p = N_t \left(1 - f^e\right) \int_{\lambda(E_g)}^{\lambda(E_{imp}-E_V)} \sigma_p^{opt}(\lambda) \, \Phi_{ph}(x,\lambda) d\lambda = \left(1 - f^e\right) g_{p,max} \, . \qquad (2.15)$$

g_p becomes maximal when all impurities are completely empty ($f^e = 0$), i.e. when they are occupied by holes.

Both excitation steps must execute in sequence to complete the transition from the valence to the conduction band. The slower process determines the overall rate. For states near midgap the occupation of states f^e should be neither of the extremes (0 or 1) in order to provide charge carriers for both generation steps. States near one of the band edges might be of interest since one of the excitations will be executed by thermal loading and consequently only one excitation relies on a comparably weak optical transition [60].

If the density of impurities is high and the levels interact sufficiently strong, the concept of single defect levels due to atomic impurities is expanded to impurity bands. These *multi band* or *intermediate band solar cells (IBSC)* accompany a defect band in the gap of the host semiconductor (Fig. 2.6 (b)) [48, p. 95-98] [61]. For ideal operation of an ISBC the bands must be isolated from each other. The impurity band occupation by charge carriers has to be described by an individual quasi Fermi level E_{FI}. The intermediate band must be half filled to provide empty states for excitation from the valence band to impurity level and to provide electrons for excitation to the conduction band [62]. The detailed balance limit (see section 2.1.3) for the efficiency of such cells is higher than for an ordinary single junction solar cell, Luque et al. [63] calculated a limit for the efficiency of 63.1 %. This is quite close to the calculated limit for triple junction solar cells [64, 65]. If states near the band edges are involved and the second transition occurs by thermal escape to the band edge the single junction limit can not be exceeded. Because the effective bandgap is reduced going along with a reduction of the open circuit voltage [66, 67].

Improvements due to IPV effect are reported for Indium (In) impurities in c-Si [68] but with a very low outcome. For intermediate band solar cells the incorporation of InAs quantum dots in GaAs solar cells [67] a significant external quantum efficiency signal is observed for sub-bandgap photon energies.

The considerations on the IPV effect made here will be of importance in section 5.4.3.

2.2. Thin Film Amorphous Silicon Solar Cells

Silicon is the most common material in solar energy production due to its abundance as well as knowledge about its properties. The most widely used form is crystalline silicon

(c-Si) as well as polycrystalline silicon which is very similar apart from the fact that it is constituted of polycrystallites instead of a single crystal. Solar cells made of c-Si in general are build from c-Si wafers with a thickness of some hundred micrometers.

The need for material cost reduction as well as the search for new materials let to the development of thin film solar cells. Amorphous silicon (a-Si) or more specific hydrogenated amorphous silicon (a-Si:H) is one of the most frequently used forms for silicon thin film solar cells [69, p.173-176].

2.2.1. Structural and Electronic Properties of a-Si:H
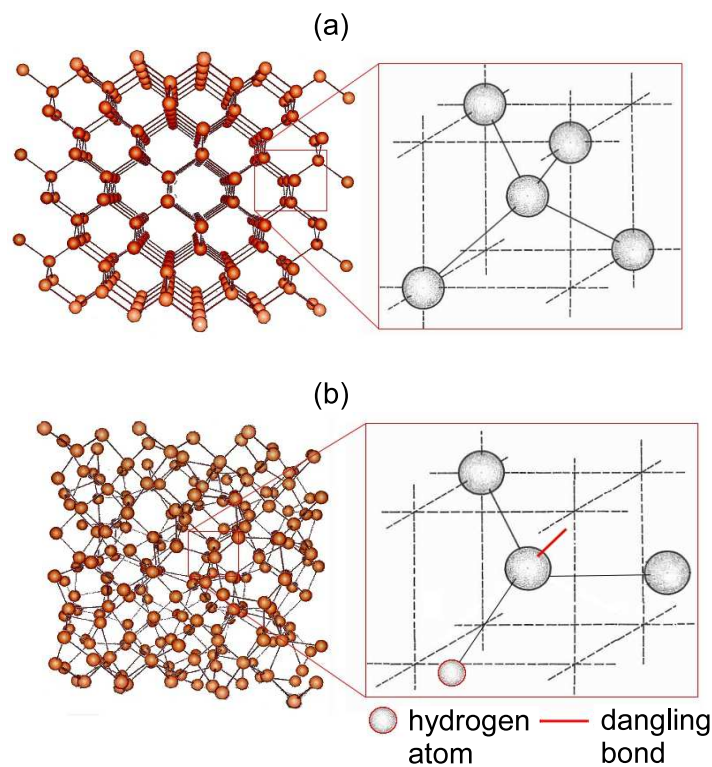
Figure 2.7.: Crystal structure of (a) c-Si and (b) a-Si:H, after [70].

Crystalline silicon (c-Si) has a diamond crystal structure with tetrahedral bonded silicon atoms (Fig. 2.7 (a)). This near range order is extended over the hole crystal forming a well defined long range order.

The crystal structure of amorphous silicon is similar to that of c-Si with respect to the near range order. The bond length of a-Si are approximately 1% larger than in c-Si (= 2.35 A) and the bonding angle of silicon atoms deviates by 10% from the tetrahedral (= 109.47 °) structure [71, p. 568]. These deviations in the near range order

are continued towards the whole crystal structure and lead to the amorphous disorder on long range scales (Fig. 2.7 (b)). The disorder and variation in bonding energies also results in weak bonds (strained Si-Si bonds) that can easily be broken. However, also open silicon bonds remain, which are called *dangling bonds* [69, p. 177-178]. High defect densities pin the Fermi level near mid-gap making a doping of the material difficult. The dangling bonds can be saturated by providing hydrogen during amorphous silicon deposition. This process called hydrogenation forms a new material: hydrogenated amorphous silicon (a-Si:H). Hydrogenation is capable of reducing the defect density caused by dangling bonds from 10^{19}cm^{-3} for a-Si to densities of 10^{16}cm^{-3} [72]. This enables doping of a-Si:H because the Fermi level is not pinned to mid-gap. However, the defect density is influenced by doping impurities [73], this was demonstrated first by Spear et al. with boron and phosphorous impurities [74].

The electronic states of c-Si are determined by the hybridization of 3s and 3p orbitals of the silicon atoms to sp^3 orbitals. The bonding and anti-bonding states of hybridized orbitals lead to the formation of valence and conduction band, respectively. At T=0 the valence band is occupied by electrons, while the conduction band is empty. The bandgap in-between has a value of 1.1 eV, which classifies c-Si as a semiconductor [46, p. 334]. c-Si has an indirect bandgap, the maximum of the valence band has a different wave vector $\mathbf{k}$ than the minimum of the conduction band. The final and initial states for transitions between these states have therefore different momentum $\hbar\mathbf{k}$. As a photon carries momentum that is much smaller than this difference, the transition is only allowed when in addition phonons are emitted or absorbed during the process [71, 75]. This leads to relatively low absorption coefficients for crystalline silicon.

For amorphous silicon where the inter atomic ordering deviates from the highly ordered c-Si structure, the band edges are not well defined. Exponential decreasing band tails arise from the valence and conduction band into the gap. This is a result of fluctuations of bonding energy caused by the variation in bonding angles and lengths as well as the missing long range order [71, 75, 76]. The width of the exponential tail for the valence band of an n-doped material has a typical value of $\Delta\text{E}_\text{V} \approx 50\,\text{meV}$, while the conduction band tail is much more narrow (25 meV) [77, p. 515-516]. The momentum conservation is relaxed in amorphous silicon, resulting in a *quasi direct* bandgap and high absorption coefficients [75].

In contrast to c-Si where no states are allowed inside the bandgap, the combination of band tails and high defect density near mid-gap in a-Si:H form a continuum of states. This makes it difficult to define a bandgap for amorphous silicon. The states inside the gap differ from the valence and conduction band states with regard to their mobility. States inside the gap are characterized by a low mobility (localized states) while states in the bands have high mobilities (delocalized states). The boundary between localized and delocalized states is denoted as *mobility edge* [71, 78]. The according energies are
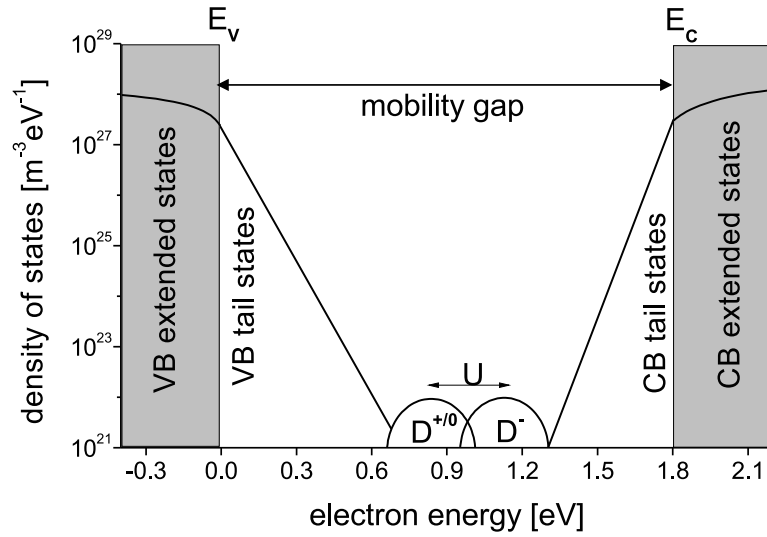
Figure 2.8.: Density of states for a-Si:H. States in the valence and conduction band have a high mobility and are separated by the mobility gap. Inside the gap localized states are evident, these are the band tails and defect states located near mid-gap, after [69, p. 180].

named E_V for the valence and E_C for the conduction band edge. The difference of E_C and E_V is the *mobility gap* E_g (Fig. 2.8). Although it is actually not a bandgap, because electronic states are allowed, it will usually be denoted as this in the following. For a-Si:H E_g has typically a value of 1.7 to 1.8 eV [79].

Dangling bonds create defect states near mid-gap and act as efficient recombination centers [78, 80]. They exist in different charge states, D^0 (neutral), D^+ (positive) and D^- (negative) [69, p. 180-181]. Since a covalent bond between two silicon atoms incorporates two electrons, each silicon atom remains with one electron after bond breaking. This results in a neutral dangling bond. By capture of a hole or an electron or release of an electron by thermal emission the neutral states are charged, resulting in D^+ and D^- states. The states are separated by an energy difference U.

Beside the inherent formation of defects due to disorder, radiation is able to break weak bonds. This light induced degradation is known as the *Staebler-Wronski effect* [81]. It results in the creation of additional dangling bonds and is able to raise the defect density by about two orders of magnitude to 10^{17}cm^{-3} [72, 80]. This process is reversible and the initial state is recovered by annealing the sample up to 200 °C [80]. By this procedure the dangling bonds are passivated and the defect density decreases in this „annealed" state towards the „initial" state before degradation [54, p. 30-32]. The creation and healing of dangling bonds are competing processes driven by irradiation and temperature. For a given temperature the formation of dangling bonds under illumination will go on until a saturation limit is reached, associated to the balance of creation and healing of defects. The degradation of defect density proceeds in a time

scale of hundreds of hours. The conversion efficiency is also affected by the increasing defect density limiting the performance of solar cells due to increased recombination.

Microcrystalline silicon (µc-Si:H)

µc-Si:H is a material that is composed of crystalline grains embedded in an amorphous matrix as shown in Fig. 2.9. The growth of the material is constituted of different
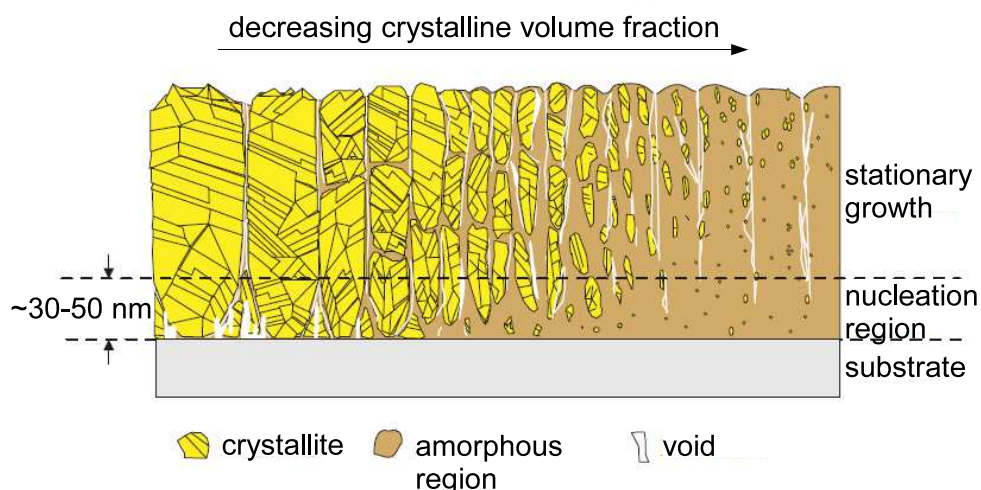
Figure 2.9.: Structure of the µc-Si:H with respect to the crystalline volume fraction, after [82, p. 60].

stages. In the beginning a nucleation of small crystallites takes place. With growing film thickness the small grains increase in size leading to a columnar growth. The crystalline volume fraction is influenced by the deposition conditions (see section 3.1.1). Films ranging from highly crystalline material to almost completely amorphous material can be prepared.

µc-Si:H is much less sensitive to the Staebler-Wronski effect and the defect density is similar or a little bit lower than in a-Si:H [83, p. 590] [79, 84, 85]. It has an indirect bandgap of 1.1 eV [86, p. 134] and is therefore capable of absorbing light up to the near infrared wavelength region at approximately 1100 nm.

2.2.2. Optical Properties of a-Si:H

The absorption coefficient α is defined from Lambert-Beer's law [87, p. 217]:

$$I(d) = I_0 \cdot e^{-\alpha x} \ , \tag{2.16}$$

while I_0 is the initial intensity and I(x) the intensity after passing a layer of width x. The penetration depth d is the distance for which $\alpha d = 1$, d is the inverse of α.

Fig. 2.10 shows the absorption coefficient and penetration depth of a-Si:H, µc-Si:H and c-Si as a function of energy. As a consequence of the quasi direct a-Si:H bandgap, light with an energy above the bandgap (1.7 to 1.8 eV) is strongly absorbed. α is stronger than for the other types of silicon. For wavelength below 500 nm even a few tens of nanometers are sufficient to absorb nearly all the incident light, as indicated from the penetration depth. This enables the use of thin films for applications in solar cells. For energies near the bandgap, α decreases. Here nearly one micrometer is needed to significantly absorb the incident photons. Such thick layers are difficult to handle due to the light induced degradation (LID) by the Staebler-Wronski effect, that is most evident for thicker layers [75]. Therefore special light management is needed to efficiently absorb the near bandgap light in thin layers (see section 2.2.3). The use of a-Si:H in combination with µc-Si:H in tandem solar cells shows a superior device stability concerning LID. Since the a-Si:H layer in tandem cells can be reduced in thickness especially when intermediate reflectors are used, the degradation of a-Si:H layers is minimized [79]. In addition µc-Si:H is advantageous for absorption of long wavelength light since it absorbs significantly up to 1100 nm.
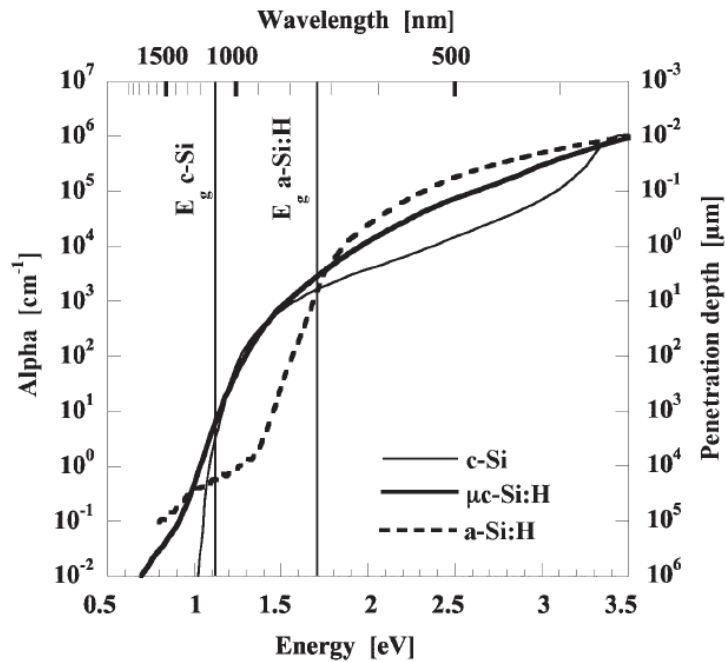
Figure 2.10.: Absorption coefficient and penetration depth of a-Si:H, µc-Si:H and c-Si versus photon energy, from [75].
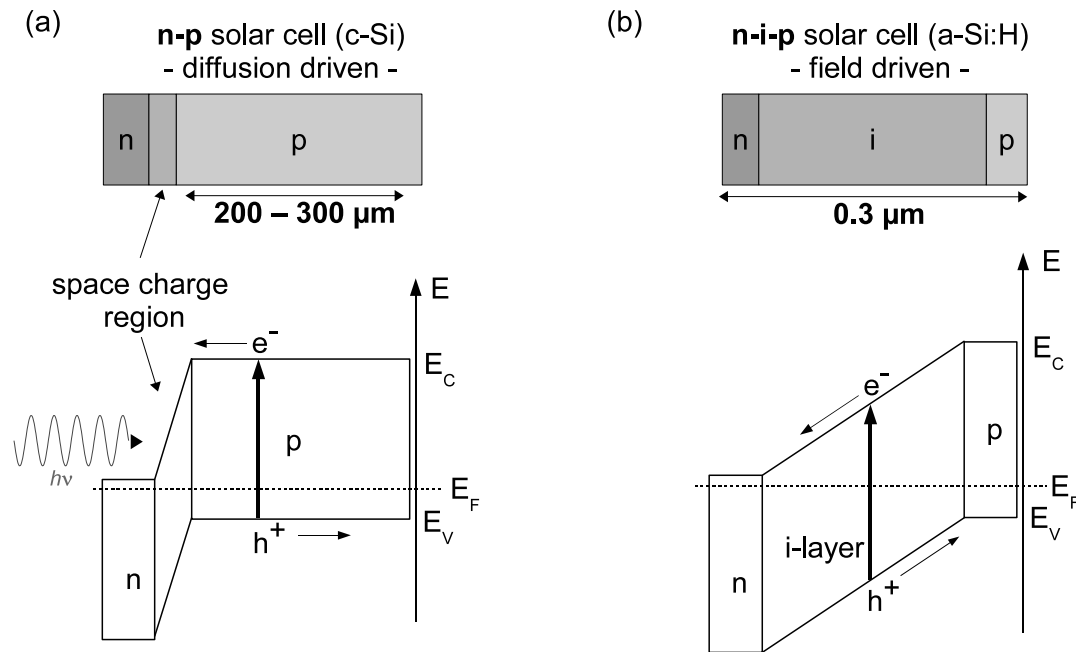
Figure 2.11.: Schematic energy diagram for diffusion and field driven devices. (a) Diffusion driven device in the n-p configuration used for c-Si solar cells. Generated electron hole pairs diffuse through the p-layer, until they reach the space charge region. (b) Field driven n-i-p device, used for amorphous silicon solar cells. Electron hole pairs generated inside the i-layer are separated by the built-in electrostatic field once they are excited.

2.2.3. a-Si:H Solar Cell Devices

For c-Si solar cells wafers with a thickness of several hundred nanometers are widely used (Fig. 2.11 (a)). On one side an n-doped region is diffused into the p-doped wafer, forming a p-n junction. Under illumination electron hole pairs are generated within the whole wafer. Because of the low defect density in c-Si, charge carriers have a long mean free path and are able to diffuse over long distances [69, p. 204]. Electrons that reach the space charge region are extracted by the field towards the n-layer. The hole diffuses to the p-contact due to the concentration gradient. The p-n junction separates the charge carriers. Due to the major role of diffusion it is also known as diffusion driven device. For thin film a-Si:H solar cells the general device design differs from the p-n design.

a-Si:H Absorber

The high defect density of doped a-Si:H prohibits the use of a p-n junction because the diffusion length of charge carriers is far too small. Doping of a-Si:H is linked to the creation of additional defect states in the bandgap. This mechanism, known as
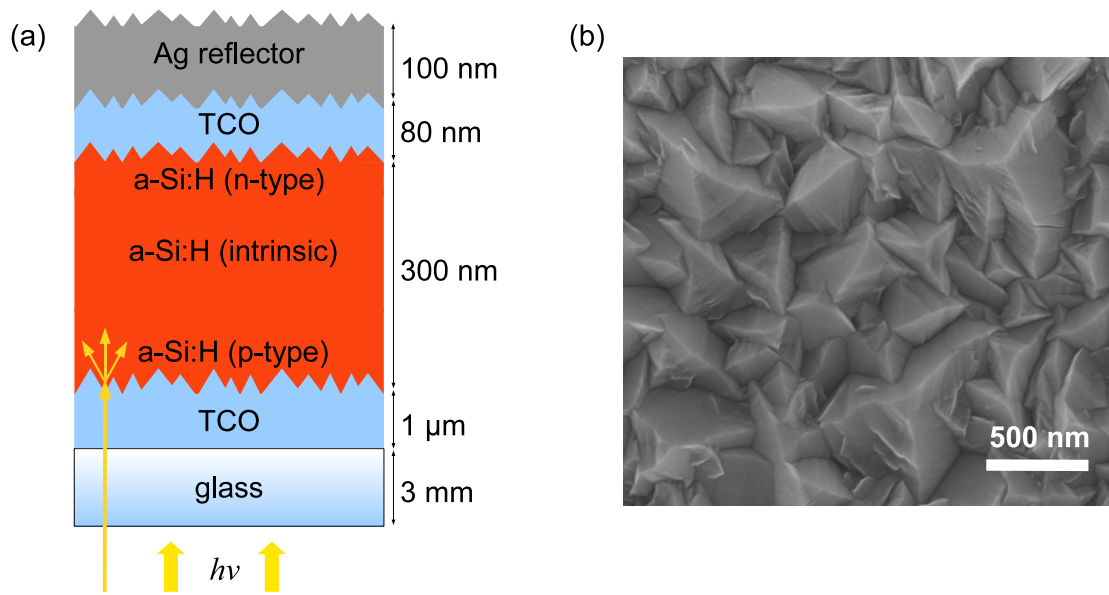
Figure 2.12.: (a) Schematic design of an a-Si:H solar cell in the p-i-n layer configuration. (b) SEM image of an LPCVD deposited ZnO front contact. The rough interface provided by the ZnO allows scattering of light at the ZnO/a-Si:H interface. In combination with the metal back reflector the light path inside the absorber is increased.

autocompensation [88], increases the defect density by two to three orders of magnitude [69, p. 196] in comparison to undoped material. In a-Si:H devices the charge carriers have to be generated in an intrinsic (undoped) region that retains a low defect density. Thus, the generation should execute in a field supported region for direct charge carrier separation. Therefore, the field driven p-i-n device design is used (Fig. 2.11 (b)). Here the intrinsic layer is placed between a p- and n-doped layer, that provide an electrostatic field across the intrinsic layer [69, p. 204-205]. Electron hole pairs that are generated inside the i-layer are separated instantaneously, avoiding their direct recombination. The light enters the cell via the p-doped layer. Since the charge carriers are subject to strong recombination in these doped regions, absorption is not intended here. Therefore the p-doped layer has to be very thin (a few nm). In addition it should have a larger bandgap than the intrinsic layer resulting in a higher transparency for the incident light. This is achieved by alloying the amorphous silicon with carbon forming a-SiC:H. Due to its higher transparency this layer is called window layer [69, p. 208]. The higher bandgap also provides a band offset at the p-i interface, that prevents the back diffusion of electrons to the p-layer [89].

The schematic cross section of an a-Si:H thin film solar cell is shown in Fig. 2.12 (a). The absorber layer of a-Si:H solar cells has typically a thickness of 200 to 300 nm. This is sufficient for absorbing nearly all photons in the visible spectral range due to the direct a-Si:H bandgap, that provides a strong absorption. On the other hand near bandgap

light, for wavelength above 650 nm, is absorbed only weakly (see Fig. 2.10). In order to provide sufficient absorption for this spectral region the light has to be coupled into the absorber as efficiently as possible and has to be kept inside until it gets absorbed. By using rough internal interfaces in combination with a highly reflective metal back contact these conditions are fulfilled. For example the rough surface morphology of *Low Pressure Chemical Vapor Deposition (LPCVD)* grown ZnO, shown in the SEM image in Fig. 2.12) (b), can be utilized for this purpose. Light that enters from the front ZnO side reaches the ZnO/a-Si:H interface. The rough morphology results in scattering of a certain portion of the incident radiation, increasing its path length inside the a-Si:H absorber. The metal back reflector in addition doubles the effective path and increases the probability for absorption.

Transparent Conductive Oxide

The effective light management in the solar cell related to the surface morphology of the TCO is already discussed above. However, the TCO has some other very important functions in the solar cell. It has to be transparent in order to transmit the incident light to the absorber without losses and it should act as electrical contact for the separated charge carriers [9]. The sheet resistance of the front TCO should be as low as possible in order not to alter the solar cell characteristics, typically values of $10\,\Omega/\text{sq}$ are acceptable [6].

SnO_2 is one of the most frequently used TCOs for thin film solar cell fabrication since the deposition techniques are well established and coated glass substrates are commercially available, even on large area substrates. SnO_2 is produced by the *Atmospheric Pressure CVD (APCVD)* method [10]. It already has an as-grown textured surface morphology that makes it suitable for light scattering purposes. The main disadvantage of SnO_2 are (i) its sensitivity to hydrogen plasmas used for a-Si:H deposition and (ii) the small feature sizes. The instability concerning H_2 leads to the formation of a metallic Sn layer that reduces its transparency. The lower transparency itself is one additional disadvantage compared to ZnO front contacts [85, 90].

The use of ZnO as front TCO is subject to different deposition techniques. ZnO films with an initially rough surface topology are prepared by *Low Pressure CVD (LPCVD)* via the oxidation of Diethylzinc $((C_2H_5)_2Zn$ also short 'DEZ') at temperatures between $150\,°C$ and $200\,°C$. A sufficient conductivity of the ZnO is achieved by using Diborane (H_6B_2) during the LPCVD process as doping gas [9] forming ZnO:B. ZnO has a Wurtzite crystal structure [46, p. 34]. Thin films show a polycrystalline growth with the c-axis in plane with the substrate. Leading to pyramidal grains emerging out of the surface and resulting in a high surface roughness suitable for scattering of light [91].

Sputter deposited ZnO films are most commonly aluminum doped ZnO films (ZnO:Al) deposited by RF- or DC-sputtering from ceramic targets [92] or by reactive magnetron sputtering from metallic Zn targets [11, 12, 93]. These films are initially flat due to the crystal orientation with the c-axis perpendicular to the substrate. For good light trapping the films have to be post treated with diluted hydrochloric acid to form craters that also act as efficient light scattering structures.

For our purposes all these types of TCO, rough SnO_2 and ZnO but especially sputtered ZnO with a flat surface topology are used. This flat devices are test structures that allow to investigate the effects of plasmonic nanostructures without additional light trapping schemes due to rough interfaces (see Chapter 5).

Back Contact

The back contact layer is either a ZnO layer that is deposited by LPCVD to a layer thickness of several hundreds of nanometers in order to achieve a high conductivity. Or as illustrated in Fig. 2.12 it consists of a double layer system of TCO and metal [94]. In the latter case usually a 80 to 100 nm thin ZnO layer is sputtered on top of the thin film layer stack followed by sputtering of a silver back reflector. The Ag layer acts as back reflector for light that passes the a-Si:H absorber. This portion of light therefore travels a second time through the absorber enhancing its absorption probability. The silver layer in addition acts as the main conductor since the conductivity of 80 nm ZnO is insufficiently low [75]. The ZnO interlayer has some important functions. First it acts as adhesion promoting layer, since the adhesion of silver on silicon is very low [95]. Further it reduces plasmonic losses at the silver reflector. The losses are assigned to coupling of light to propagating surface plasmon polariton modes at the rough interface [96] or to localized surface plasmons at protrusions of the silver surface [97] (see Section 2.4). A ZnO buffer layer with a lower refractive index (n=2) compared to silicon shifts the localized plasmon resonance to larger energies in the range of 2 eV (see section 2.4.2). Because photons of this energy regime are absorbed before they reach the back reflector plasmonic losses are not crucial for the operation of a-Si:H solar cells. In addition ZnO prevents intermixing of the metal with silicon [94] [69, p. 207]. function of the ZnO

Laser Scribing and Serial Interconnection

The advantage of thin film silicon solar cells to deposit the layers on large scale, also bears some limitations concerning the output current. A solar cell with an assumed short circuit current density of 15 mA/cm² and a cell area of 1.4 m² would produce a current of 210 A. The open circuit voltage provided by such a cell is below 1 V, since it does not depend on the illuminated area. Apart from the problem, that such high currents are not easy to handle, ohmic losses would arise. Especially due to the
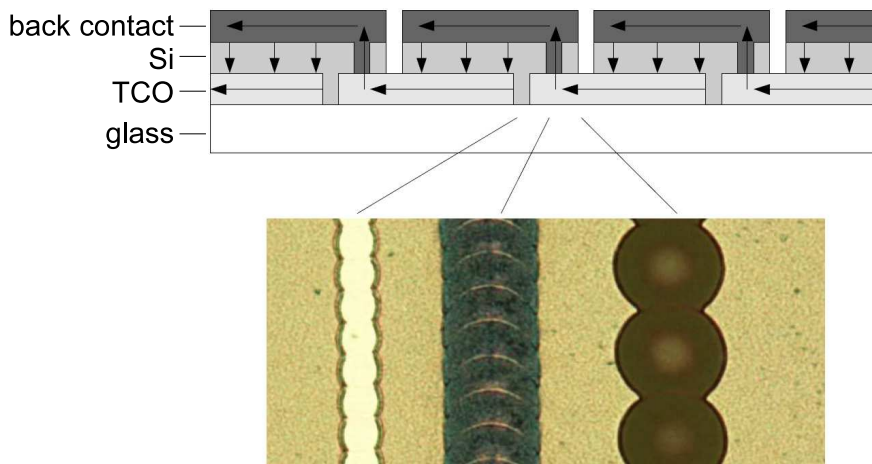
Figure 2.13.: Schematic illustration of laser scribing for a thin film silicon module, from [98]. The arrows indicate the current flow under illumination and short circuit condition.

series resistance of the front TCO, power would be consumed according to $P = RI^2$. To reduce the current of a large area module and increase the voltage, cells with a smaller area connected in series are needed. For this purpose *laser scribing* in between different deposition steps (after TCO, Si and back contact deposition) is applied. Here certain parts of the layers are selectively removed and a monolithic interconnection of individual cells is provided [99] (see Fig. 2.13). A laser line consists of ablations from adjacent laser spots that are aligned in a row and originate in individual laser pulses in the ns range. Laser scribing reduces the active cell area and therewith the conversion efficiency of the module. In this work single cells of $1\,\mathrm{cm}^2$ instead of modules are investigated. Here laser scribing is applied to prepare these separated single cells (see Fig.3.14).

2.3. Thin Film Deposition

The techniques for vacuum deposition of thin films can be classified by different characteristics [100, p. 14]. On the one hand there are *physical vapor deposition (PVD)* techniques that use evaporation of material or the impact of fast ions onto a material to dislocate atoms and deposit them on a substrate. In contrast to that, chemical deposition methods are available that use the decomposition of chemical substances to form deposits on a substrate. Here the *chemical vapor deposition (CVD)* is discussed in more detail. Depending on the type of material that should be deposited the methods have certain advantages and are chosen with respect to the desired application.

2.3.1. Chemical Vapor Deposition (CVD)

In chemical vapor deposition certain molecular compounds are transported via the gas phase to a substrate. At the surface or close to it the molecular compounds (called *precursors*) are forced to decompose into their entities. This process should execute in such a way that desired atoms or molecules are deposited on the substrate to form a solid film, while unwanted species return to the gas phase and are transported away. Depending on the conditions used or methods applied for the delivery of energy for chemical bond breaking and reaction initialization a variety of CVD methods exist. Some examples are *photo enhanced CVD (PHCVD)*, *metal organic CVD (MOCVD)* [101], *low pressure CVD (LPCVD)*, *atmospheric pressure CVD (APCVD)* and *plasma enhanced CVD (PECVD)* [100, p. 20-25].

For thin film silicon solar cell applications, especially the deposition of transparent conductive oxides used as front contacts (see section 2.2), the *low pressure CVD (LPCVD)* as well as *atmospheric pressure CVD (APCVD)* are of importance. LPCVD is used to deposit ZnO [9] while APCVD is most often used for SnO_2 deposition [10]. *Plasma enhanced CVD (PECVD)* is the most common technique for the deposition of hydrogenated amorphous silicon [83].

Plasma Enhanced Chemical Vapor Deposition (PECVD) of a-Si:H
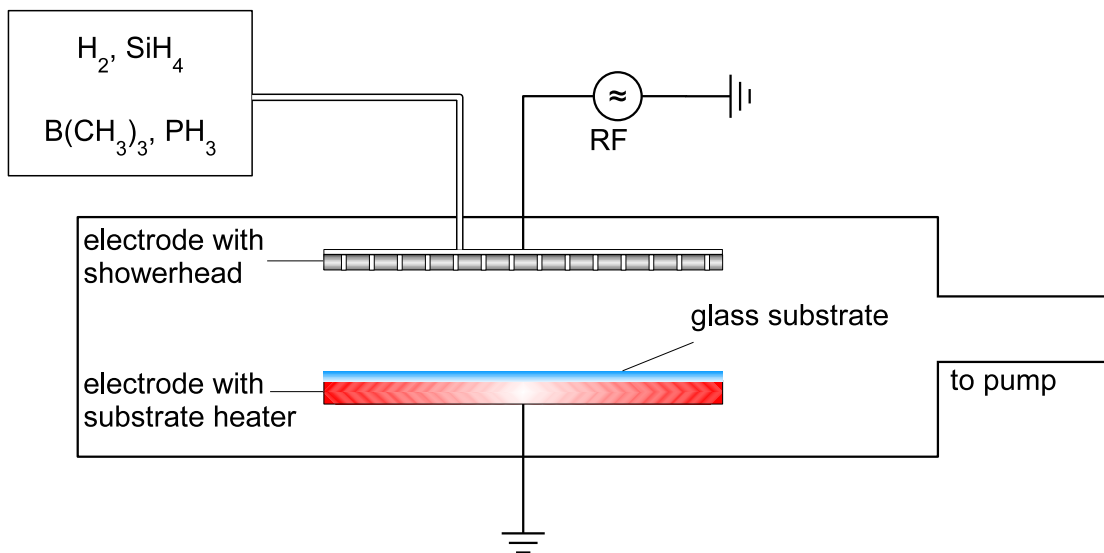
Figure 2.14.: Schematic setup of a PECVD reactor in a capacitively coupled parallel plate configuration.

In PECVD-systems a capacitively coupled plasma is used to decompose the precursor gases and deposit thin films on a substrate surface. The schematic setup of a PECVD

system is shown in Fig. 2.14. For a-Si:H deposition, the precursor gases Silane (SiH_4) and hydrogen H_2 are transported to the vacuum chamber by a gas distribution system. In the chamber a capacitor, composed of a lower and an upper electrode is used to excite a plasma in-between the electrodes. It is generated by a radio frequency (RF) excitation that is coupled to the upper electrode. The plasma provides the energy to decompose the SiH_4. Therefore less thermal energy is needed for decomposition and lower substrate temperatures can be used. Typical deposition temperatures for a-Si:H are in the $200\,°C$ to $250\,°C$ range [69, p. 198]. This produces material with a lower defect density, due to the incorporation of hydrogen in the silicon network. In thermal CVD with deposition temperatures between 400 and $500\,°C$ the diffusion and desorption is increased and less hydrogen remains for defect compensation by the hydrogenation of the surface during deposition [102, p. 18-20]. This is one major advantage of PECVD over thermal CVD. The plasma decomposition works as follows. High energetic electrons from the plasma excite the SiH_4 by inelastic collisions. The excited molecules decompose into a variety of neutral species, like: $H, H_2, Si, SiH, SiH_2, SiH_3$ [83, p. 581-582] as well as ions [103]. These created species react with the initial precursors SiH_4 and H_2 limiting their lifetimes. SiH_3 has the lowest reactivity and is the most important precursor for a-Si:H and µc-Si:H film growth. When a SiH_3 molecule adsorbs on the substrate, it diffuses over the surface until it finds a silicon binding site to form Si-Si bonds. SiH_3 can react with hydrogen that is present on the surface to form SiH_4 or by recombination with a different SiH_3 molecule to Si_2H_6. Both species desorb from the surface without contributing to the film growth [83, p. 581-584] [104].

As mentioned in section 2.2.1 the transition from a-Si:H material to µc-Si:H is controlled by the deposition conditions. The hydrogen dilution ratio R, defined as $R = \frac{[H_2]}{[SiH_4]}$ [83, p. 583], is an important quantity in this context. Here $[H_2]$ and $[SiH_4]$ are the applied gas fluxes of hydrogen and silane, respectively. µc-Si:H is formed by PECVD deposition when the hydrogen dilution ratio R is increased, i.e. when the flux of hydrogen is increased with respect to the silane flux. Atomic hydrogen must be present at the surface to form µc-Si:H. The formation of µc-Si:H is explained in literature with three different models, (i) *surface diffusion* (that is also valid for a-Si:H), (ii) *etching* and (iii) *chemical annealing model*. All three have in common that atomic hydrogen interacts with the grown film to either increase the mobility of SiH_3 on the surface, selectively etch weakly bonded silicon or promote the crystallization via the presence of a flexible silicon-hydrogen network [83, p. 584-587].

The doping of silicon layers is achieved by adding doping gases to the precursor gas mixture. P-type doping is realized with the incorporation of the trivalent Boron (B) into the silicon network. While n-type doping is realized with the incorporation of Phosphor (P), that donates an electron to the silicon. Typical doping gases are Trimethylborane

$B(CH_3)_3$ (also abbreviated TMB) for Boron doping or Phosphine (PH_3) for Phosphor doping [69, p. 194-196].

The homogeneity of thin film deposition depends on the local availability of the precursor gases forming the layers. In order to distribute the gases in a homogeneous manner, a *showerhead* configuration is used (see Fig. 2.14). For this purpose, the upper electrode is equipped with holes that are connected to the gas delivering system.

2.3.2. Physical Vapor Deposition (PVD)

The two main PVD techniques applied for thin film deposition are evaporation and sputtering, these are especially important in thin film solar cell fabrication. Both methods are also employed in this work to deposit thin silver films and silver nanoparticles.

Evaporation
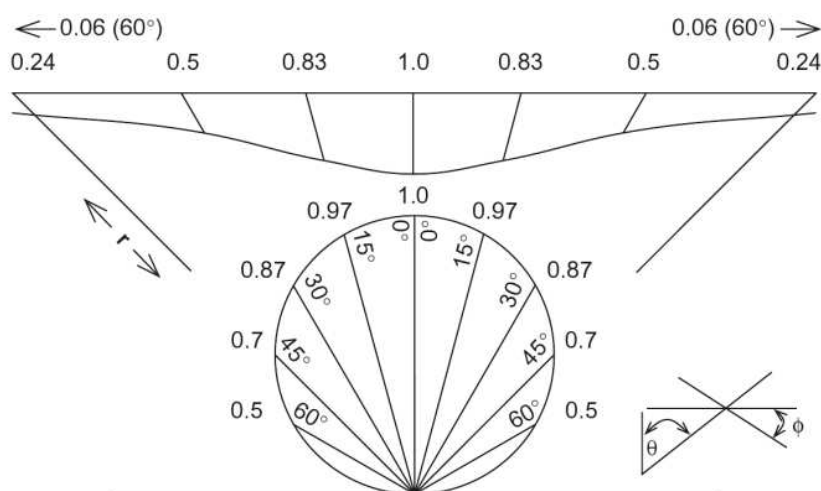
Figure 2.15.: Cosine distribution of material flux from a point source and resulting relative deposition on a planar surface which is $\propto \frac{\cos\theta\cos\phi}{r^2}$, from [105, p. 142].

Vacuum evaporation is one of the first and most simple methods for thin film deposition. Being capable of producing high quality films, this method is still an important tool in thin film deposition technology. In a high or ultrahigh vacuum chamber a metal is heated, until it either melts and evaporates or directly sublimates. The emission of atoms from an idealized point source depends on the angle with respect to the surface normal. For thermal evaporation, the atoms leaving the source (Fig. 2.15) show an angular cosine distribution [105, p. 200] [106, p. 325-326]. This means that most of the

material leaves the source in normal direction. The flux of material ejected under a certain angle θ is equal to the flux leaving in normal direction multiplied with $\cos\theta$. The amount of deposited material on a substrate in addition depends on the angle of incidence on the substrate ϕ and thus on the orientation with respect to the source. Since real deposition sources are not ideal point sources, the angular distribution is a superposition of the cosine distributions from each point [105, p. 245-346]. Different methods of evaporation techniques exist that mainly differ in the fact how the material is evaporated or how the energy is supplied. The most simple method is *thermal evaporation*, where the crucible and with it the material is heated by different methods, including *resistive heating*, *electron impact*, *inductive heating* and others. Additionally direct heating of the material by *electron beam evaporation* or *laser evaporation* can be applied [100, p. 16]. Especially metals like gold and silver are subject to evaporation due to their high vapor pressure [107][108, p. 98-99].

Sputtering

Sputtering is a process where atoms or ions with sufficient kinetic energy hit the surface of a (so called) target and dislocate atoms, molecules or clusters from it. The angular distribution of species leaving the target depends on the incidence angle of sputtering ions [109, p. 57-59] as well as on their kinetic energy. The atoms leaving the target can be adsorbed on a substrate that is mounted opposite to it. Hereby thin films are grown. Most commonly inert gas ions like Ar^+, Xe^+, Kr^+ are used as sputtering species. Beneath ion beam sputtering [100, p. 18] the most common form applied for thin film deposition is sputtering with ions from a glow discharge plasma [106, p. 320-326].

Two different modes of sputtering configurations are possible, direct current (DC) and radio frequency (RF) sputtering. In DC sputtering a high voltage is applied between two electrodes (cathode and anode) inside an evacuated chamber. A sputtering gas, for instance Ar, is applied to the chamber to an operation pressure of $10^{-3} - 10^{-1}$ mbar or 1 mbar [106, p. 344][110, p. 20]. Due to the impact of cosmic particles a very small amount of the neutral gas is ionized and free electrons are available. These electrons are accelerated in the applied electrical field towards the anode and the ion towards the cathode. On its path the accelerated electron ionizes other gas atoms. Successively a cascade of free electrons and ionized atoms is created. The ions hit the cathode with high energies. Beneath the sputtering of target atoms this results in the emission of electrons from the cathode. These secondary electrons also cause ionization. If enough gas is ionized by this process a stable plasma will build up. This plasma provides ions for sputtering of the target, that is mounted on the cathode [110, p. 19-20]. With DC excitation conductive materials can easily be sputtered. Insulating materials suffer from the accumulation of charge on their surface and hence the incident ions are deflected. For these materials RF sputtering can be applied [109, p. 98].

In the RF sputtering mode, the DC voltage is exchanged by providing a modulated voltage from a radio frequency generator to the cathode. Most commonly a frequency of 13.56 MHz is used [106, p. 328]. The main principle of plasma generation is the same as for DC excitation. The electrons are accelerated by the RF field, ionize the gas and ignite the plasma. The ions cannot follow the oscillating field quick enough to reach one of the electrodes within one half cycle of the RF field. The electrons in contrast are able to reach the electrodes. Since the RF powered cathode is capacitively coupled to the RF generation, electrons can be accumulated on it. A so called *self-bias* voltage is build-up due to this accumulation. This self-bias accelerates the ions in the plasma towards the cathode and results in sputtering of the target [110, p. 25-26][106, p. 328-329][111].

Today nearly all sputtering applications use *magnetron* sputtering configurations [106, p. 330]. In a magnetron sputter source permanent magnets placed below the cathode create a magnetic field in the target plane. Since the electrical field acts vertically to the target, electrons that are emitted from the cathode by ion impact, are forced to follow closed loops near the target surface, the so called *electron drift path*. This leads to a much more effective use of secondary electron energy in plasma excitation and a much more dense plasma near to the target [106, p. 326-331]. This plasma confinement has the disadvantage of a ring like target erosion leading to a not perfect utilization of the target material. However, due to the confinement of secondary electrons from the cathode, they are not accelerated towards the substrate. Therefore heating by high energy electrons is minimized with the use of magnetron sputtering [100, p. 18]. In magnetron sputter sources both sputtering modes (DC and RF) can be applied.

In sputtering applications also chemical reactions are utilized to prepare certain materials. This reactive sputtering uses for example oxygen gas that is applied in combination with the sputter gas argon to execute a chemical reaction of oxygen with sputtered atoms. In solar cell applications the transparent conductive oxide ZnO can be prepared by reactive oxygen sputtering of a metallic zinc target [11, 12, 93].

The energy of target atoms reaching the substrate is much higher for sputtering than in thermal evaporation. Atoms emitted by a thermal evaporation source are Maxwell-Boltzmann distributed with a mean kinetic energy of $E_{kin} = \frac{3}{2}k_BT$. Copper atoms thermally evaporated at a temperature of 1500 °C have a mean kinetic energy of 0.2 eV [105, p. 295]. The average kinetic energies of sputtered atoms are about one order of magnitude larger, they have energies of about 10 eV [106, p. 324-325]. The atoms reaching the substrate therefore have higher energy and mobility on the substrate surface than evaporated atoms.

2.3.3. Growth of Thin Films

The growth of thin films is governed by the interaction of depositing atoms with the substrate surface as well as with their neighboring species. The atoms move along the substrate surface due to their kinetic energy and collide with other species to form small clusters. The clusters desorb from the surface or collide with others to form larger clusters. This nucleation is the starting point for film growth. The density of initial nuclei depends on several parameters like energy of impacting species, along with deposition rate, surface diffusion, temperature etc. The formed clusters (called: islands) tend to reduce their surface by *coalescence*. This process is promoted by high surface mobility, due to increased temperatures for example and leads to formation of larger islands while other surface areas become exposed again [109, p. 10-13][112, p. 19-25]. A second mechanism named *Ostwald ripening* in which material is transported from smaller islands to larger ones via surface diffusion or the gas phase takes place [113, 114]. This also leads to the growth of islands.

Atoms at a solid surface obey a larger energy than bulk atoms, because they have a lower amount of bonds to other atoms. This difference gives rise to a *surface energy* γ, measured in units of J/m^2. It is defined as the amount of energy that is necessary to increase the surface area by a certain amount. Surface energy is often referred to as *surface tension* [108, p. 377-378]. The considered atoms in thin film growth are either atoms of the substrate, the already formed film or the vapor phase. This situation is depicted in Fig. 2.16 (a) where depositing atoms as well as an already formed film nucleus is indicated. The interfacial tension between the contributing phases are denoted as γ_{fv} for the tension between film and vapor, γ_{sv} between substrate and vapor as well as γ_{fs} film and substrate. According to the contact angle θ of a film on a substrate, these three quantities are connected via Young's equation [108, p. 379]:

$$\cos(\theta) = \frac{\gamma_{sv} - \gamma_{fs}}{\gamma_{fv}} \,. \tag{2.17}$$

The fact whether a smooth film ($\theta \to 0 \deg$) or islands ($\theta > 0 \deg$) are formed is determined by the three interfacial tensions. In general the thin film formation is classified into three different growth modes (Fig. 2.16): island growth (Volmer-Weber), layer by layer growth (Frank-van der Merwe) and island growth on closed layers (Stranski-Krastanov) (see Fig. 2.16 (b)). Island growth is dominating when the surface tension of the film is larger than that of the substrate. Metals have a high surface tension and therefore the deposition on top of oxides or semiconductors usually results in island formation [108, p. 378-381]. In particular the growth mode of silver on SiO_2 was found to be Volmer-Weber island growth [115]. Charton et al. [116] also observed island growth for thin Ag layers. They observed closed films above a thicknesses of 12 to 14 nm.
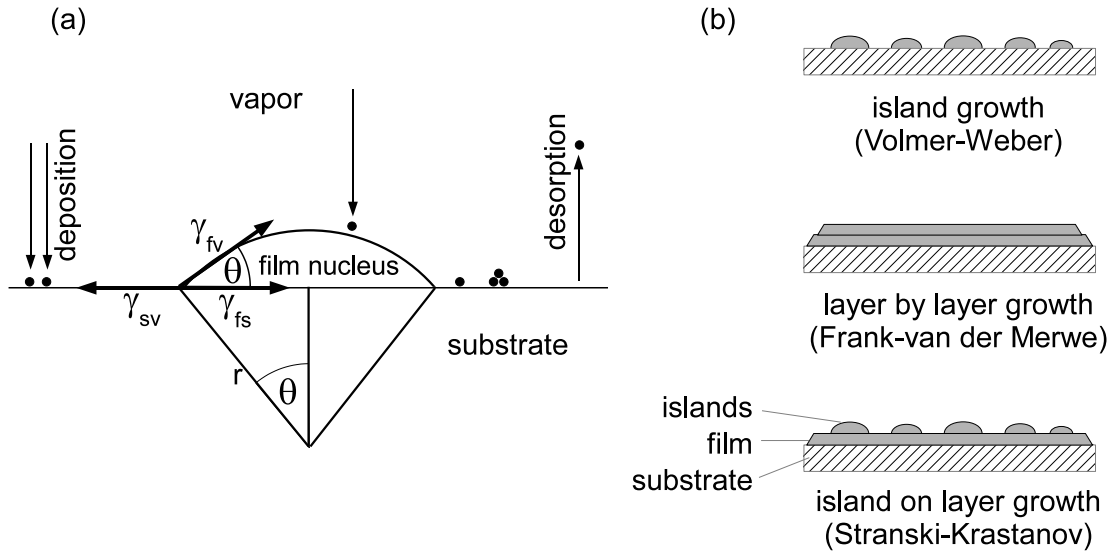
Figure 2.16.: (a) Atomistic nucleation on a substrate surface during thin film formation, after [108, p. 379]. The abbreviations are explained in the text. (b) Thin film growth modes, Volmer-Weber (island growth), Frank-van der Merwe (layer by layer) and Stranski-Krastanov type (island on layer), after [109, p. 11].

This is related to the fact, that formed islands coalesce together with growing film thickness, forming interconnected paths (*percolation*) with empty trenches in-between. During film growth these trenches are filled and closed films are produced. This process typically proceeds in the order of the first ten nanometers [108, p. 357-358]. The deposition of silver films below a thickness of $10\,\mathrm{nm}$ will therefore result most likely in 3D nanostructured films. This is in our case of advantage, since these nanostructures are desired for the excitation of localized surface plasmon modes. However the possibility to compare the behavior of closed silver films with nanoparticles will in most cases be prevented.

The deposition of closed, smooth silver films can be achieved for example by reducing the surface diffusion by the introduction of seeding layers. By this a more dense nucleation of islands takes place that results in a 3D columnar growth [115]. Apart from that also films grown in the layer by layer or island on layer growth tend to form 3D clusters, if stress due to lattice mismatch acts on the film [117].

2.4. Metal Nanoparticles and Localized Surface Plasmons

The free electrons of a metal are influenced by external electromagnetic fields and are forced to a certain motion. The collective oscillations of the metal electrons are referred to as plasmons. A Plasmon is a quasi particle because it is a many particle phenomenon, in analogy to phonons for the lattice vibrations. The electromagnetic description of plasmons and different boundary conditions result in the differentiation of three types of plasmons: bulk, surface and particle plasmons [118, p. 31]. *Surface plasmons* are shown schematically in Fig. 2.17 (a), they are also denoted as *surface plasmon polaritons (SPP)* [119].
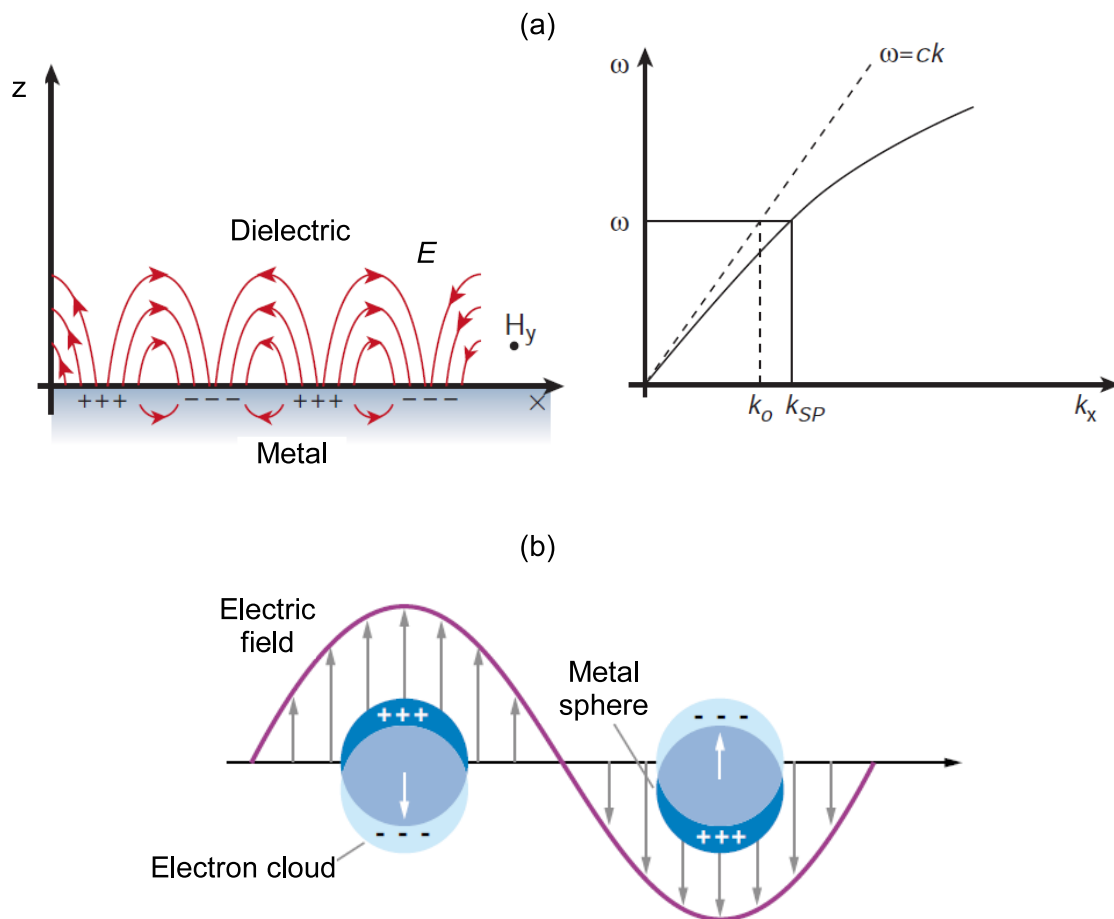
Figure 2.17.: (a) Propagating surface plasmon polariton (SPP) at a metal-dielectric interface. On the right, the according dispersion relation for an SPP mode indicates the momentum mismatch with respect to light with a linear dispersion relation, from [119]. (b) Localized surface plasmon related to collective oscillations of the metal nanoparticle electrons, from [120].

SPPs are associated to oscillations of the electron density at a metal surface that is coupled to the electromagnetic field at the metal-dielectric interface. SPPs show an evanescent character with a field component perpendicular to the interface, that decays exponentially with increasing distance [119]. SPPs are confined to the interface, along which they can propagate over distances in the order of micrometers [121, p. 127]. The excitation of SPPs at a planar metal surface is not possible with electromagnetic radiation. This is related to their dispersion relation shown on the right hand side of Fig. 2.17 (a). Here the mismatch between the SPP and light dispersion curves is illustrated. In order to excite a plasmon additional momentum must be provided. This can be achieved by special experimental configurations like prism-coupling via evanescent waves at an interface caused by total internal reflection or via grating-coupling [122]. In this grating-coupling approach the diffraction of light at the grating structures serves to match the momentum of light with that of the SPP. Randomly structured interfaces make it also possible to couple light to SPPs, for example at nano rough interfaces [123, p. 46]. This is a possible loss mechanism in solar cells due to coupling of light to SPPs at the metal back contact [96, 97] (see section 2.2).

In contrast to the propagating SPP modes at metal surfaces, plasmons in metal nanostructures are confined to these structures. Therefore these particle plasmons are called *localized surface plasmons (LSP)* [29, p. 151]. They can couple efficiently to electromagnetic radiation because the confined geometry of the nanoparticle provides a large number of possible wave vectors that fulfill momentum conservation [29, p. 153]. The excitation of an LSP is shown schematically in Fig. 2.17 (b).

2.4.1. Spherical Nanoparticles - Mie Theory

The interaction of electromagnetic fields with the special case of spherical nanoparticles can be calculated analytically by solving the Maxwell equations in spherical coordinates. The response of a metal sphere to an external electromagnetic field can be calculated in the scattering, extinction and absorption cross sections C_{sca}, C_{ext} and C_{abs} [124]:

$$C_{sca} = \frac{2\pi}{k^2} \sum_{L=1}^{\infty} (2L + 1) \left(|a_L|^2 + |b_L|^2\right) \tag{2.18}$$

$$C_{ext} = \frac{2\pi}{k^2} \sum_{L=1}^{\infty} (2L + 1) \; Re(a_L + b_L) \tag{2.19}$$

$$C_{abs} = C_{ext} - C_{sca} \, . \tag{2.20}$$

a_L and b_L are the Mie coefficients and can be written in the following way:

$$a_L = \frac{m\psi_L(mx)\psi'_L(x) - \psi_L(x)\psi'_L(mx)}{m\psi_L(mx)\xi'_L(x) - \xi_L(x)\psi'_L(mx)} \qquad (2.21)$$

$$b_L = \frac{\psi_L(mx)\psi'_L(x) - m\psi_L(x)\psi'_L(mx)}{\psi_L(mx)\xi'_L(x) - m\xi_L(x)\psi'_L(mx)} \; . \qquad (2.22)$$

Here ψ_L and ξ_L are Riccati-Bessel cylindrical functions and $\psi'_L(x)$ and $\xi'_L(x)$ their derivations with respect to x. $x = |\mathbf{k}|R$ is the size parameter with $|\mathbf{k}|$ absolute value of the wave vector and R the sphere radius. The coefficient m is $m = n/n_m$, with n the complex index of refraction for the metal particle and n_m the refractive index of the surrounding medium. For a detailed derivation of these equations see [124, p. 90-94], [125, p. 82-104] or [126, p. 26-30].

In the equations 2.18 and 2.19 a summation over all multipole orders L is conducted. L = 1 corresponds to the dipole fields, L = 2 to the quadrupole, L = 3 to the octupole [126, p. 29] and further on for higher order modes.

2.4.2. Calculations with Mie theory

In order to apply the equations 2.18-2.20 of the Mie formalism for calculations of the optical response of metal nanoparticles the program *MiePlot* [127] is used. Fig. 2.18 shows some calculated extinction spectra. In (a) silver NPs with a size of 20 nm in a medium with refractive index of n=4 are shown. A sharp dipole resonance in the range of 850 nm is observed. Towards shorter wavelengths a tiny peak appears which is the quadrupole peak. By increasing the particle size this quadrupole peak becomes more dominant as seen in (b) for 70 nm particles. Here the dipole (D), quadrupole (Q) and octupole (O) peaks are observed, while the dipole peak is shifted towards longer wavelengths. The general effect of the particle size on the dipole resonance position is shown in (c). An increasing particle size leads to a shift of the resonance towards longer wavelengths. The refractive index of the surrounding medium has a similar influence on the dipole resonance. Increasing n also shifts the resonance to longer wavelengths.

In addition to calculations on a monodisperse particle response, it is possible to calculate the response of particles with a certain size distribution. The real size distribution of particle agglomerates is evaluated from SEM measurements (see section 3.2.1). In Fig. 2.19 (a) an example histogram of a particle distribution with a mean particle diameter of 23 nm is shown. This histogram can then be applied to calculate the response of spherical particles holding this size distribution. This is done by calculating the weighed response of all contributing sizes found in the histogram [127]. The calculated response of this distribution is compared to monodisperse 23 nm NPs (b). Both are in
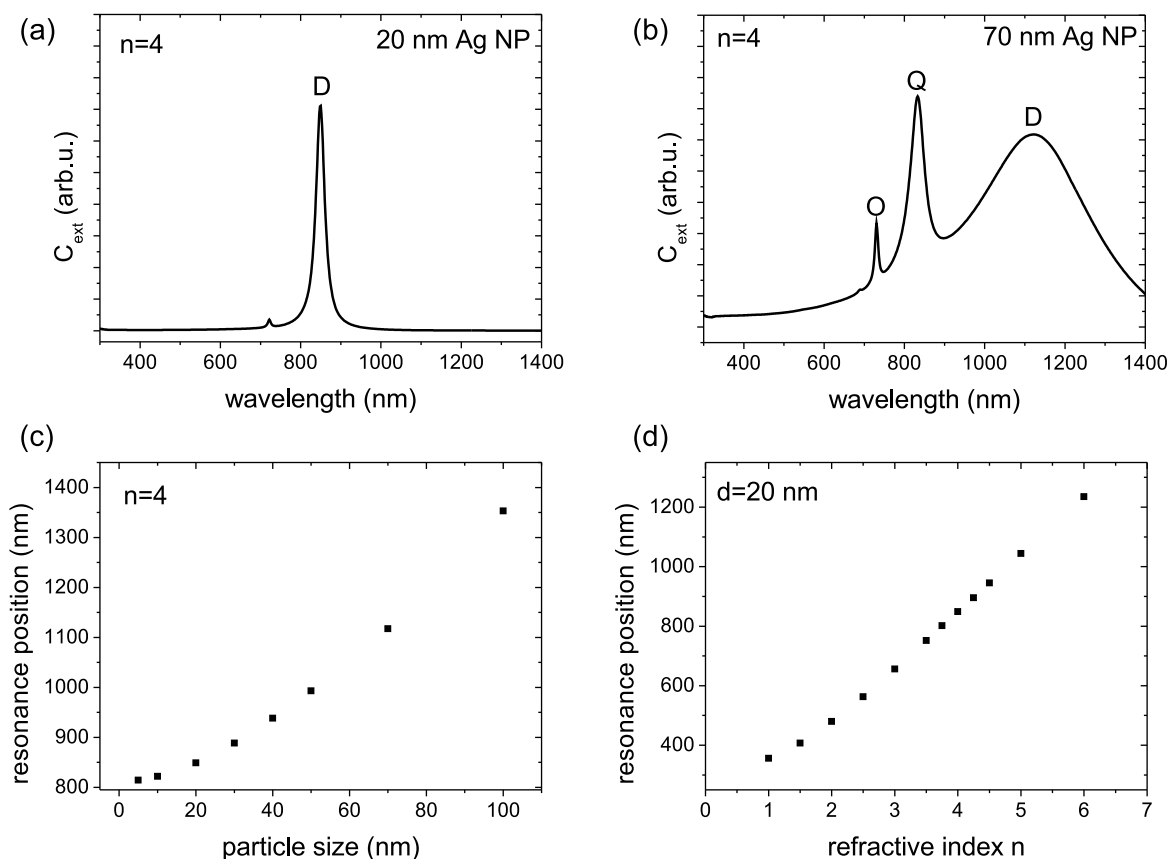
Figure 2.18.: Calculated Mie response for (a) 20 nm and (b) 70 nm diameter silver NPs in a refractive index of n = 4. In (c) the particle size and (d) refractive index influences on the dipole resonance position are drawn.

principle quite close to each other, however the distribution results in a slight shift of the maximum. In addition peak width increases and is more asymmetric towards lower energies. This is because also smaller and larger particles contribute and broaden the overall response [128].

2.4.3. Quasi-static approximation

For very small particles with radius R much smaller than the wavelength λ (R $<< \lambda$) the *quasi-static regime* can be applied. In this regime it is expected, that at each time interval the electromagnetic field does not vary spatially over the particle volume because of the small particle dimensions. The spatial field distribution can be calculated for the case of a particle in a static electric field while the time dependent oscillation of the electromagnetic wave is added to the solution [123, p. 66]. A metal particle in an electrical field E_0 obeys a certain polarizability α according to its dipole moment

(a)

(b)
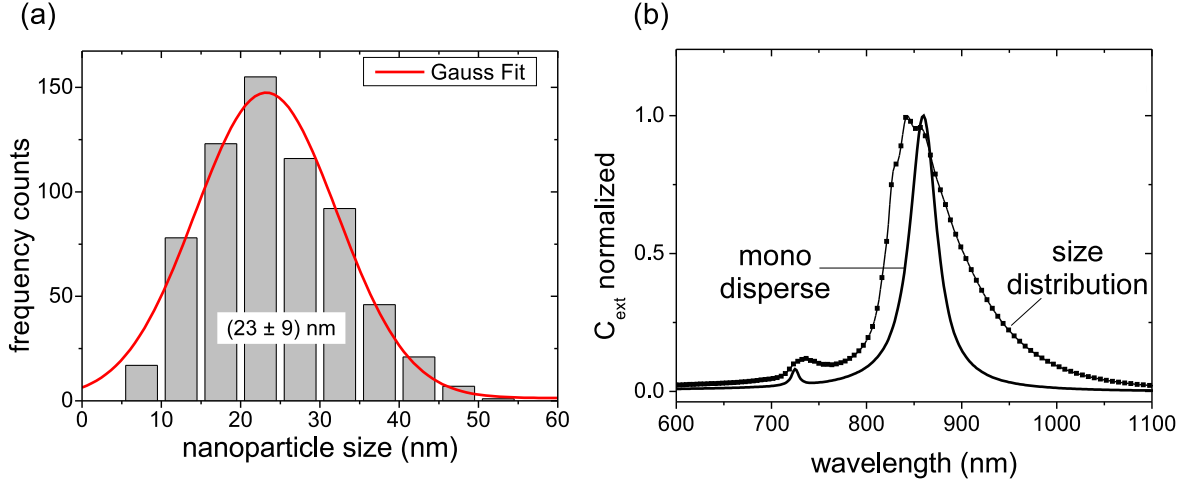
Figure 2.19.: Influence of a size distribution on the Mie response of silver particles with mean diameter of 23 nm. The particle environment is set to a refractive index of n = 4

$\mathbf{p} = \varepsilon_{\mathrm{m}} \alpha \mathbf{E}_0$:

$$\alpha = 4\pi\varepsilon_0 R^3 \frac{\varepsilon(\omega) - \varepsilon_m}{\varepsilon(\omega) + 2\varepsilon_m} \,. \tag{2.23}$$

Here the oscillating field dependence is realized by frequency dependent dielectric functions. The dielectric functions of metal $\varepsilon(\omega)$ and embedded medium ε_{m} determine the optical properties. If the absolute value of the denominator is close to zero, α becomes very large. This is characteristic for an LSP resonance. Since the dielectric function of the metal $\varepsilon(\omega) = \varepsilon_1(\omega) + i\varepsilon_2(\omega)$ is a complex quantity, the absolute value of the denominator becomes:

$$[\varepsilon_1(\omega) + 2\varepsilon_m]^2 + \varepsilon_2(\omega)^2 = 0 \,. \tag{2.24}$$

Considering the extinction cross section from Mie theory of equation 2.19, by taking only the lowest order dipole term. The Mie coefficients a_{L} and b_{L} are proportional to $(|\mathbf{k}|R)^{2L+1} = (|\mathbf{k}|R)^3$ resulting in [126, p. 30-31]:

$$C_{ext} = 9\frac{\omega}{c}\varepsilon_m^{3/2}V_0 \frac{\varepsilon_2(\omega)}{[\varepsilon_1(\omega) + 2\varepsilon_m]^2 + \varepsilon_2(\omega)^2} \,. \tag{2.25}$$

Here $|\mathbf{k}| = \omega/c$ and $V_0 = (4\pi/3)R^3$ are introduced. This gives the same resonance condition as that of the quasi-static approximation (Eq. 2.24). For the development of an LSP resonance two conditions have to be met according to this. On the one hand the imaginary part must be small ($\varepsilon_2 \approx 0$). This leads to the resonance condition $\varepsilon_1(\omega) = -2\varepsilon_{\mathrm{m}}$, which points out that the real part of the dielectric function has to be negative in order to be fulfilled. In Fig. 2.20 the dielectric function of silver is plotted
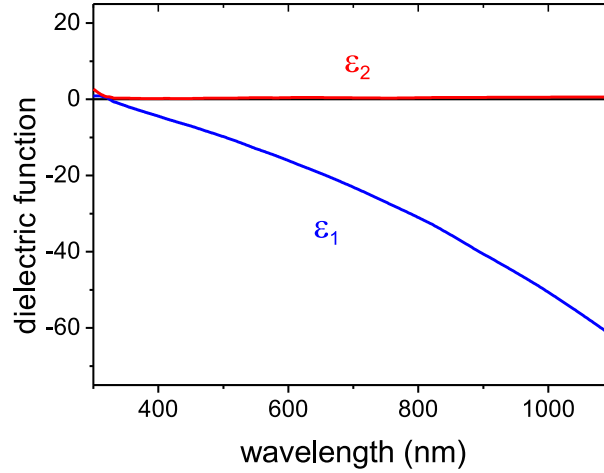
Figure 2.20.: Dielectric function of silver separated in real (ε_1) and imaginary part (ε_2).

with respect to the wavelength. Silver shows LSP resonances because the imaginary part ε_2 is very small and ε_1 is negative over a wide range. For silver nanoparticles in a silicon environment with a refractive index around n=4, $\varepsilon_{\mathrm{m}} \approx 16$ according to $n = \sqrt{\varepsilon_{\mathrm{m}}}$. The resonance will take place at $\varepsilon_1 = -2\varepsilon_{\mathrm{m}} \approx -32$, which is roughly around $800\,\mathrm{nm}$. This resonance behavior is related to the confinement of the charge carriers to the nanoparticle. At the resonance the electrons collectively oscillate in phase. The restoring force of the ions acting on the electrons enable the resonance at a specific wavelength according to the particle size and environment. This leads to a strongly enhanced resonant near field in the very close proximity of the particle [129]. This effect will be utilized for increasing the absorption of thin film silicon solar cells by incorporating Ag NPs in direct contact to the absorber layer (see chapter 5).

The ability of NPs to scatter or absorb the incident light is determined by its size. The absorption scales with R^3 while the scattering scales with R^6 [130]. Therefore large particles mainly contribute via scattering to the extinction, while small particles via absorption. In the quasi-static regime the extinction is dominated by the absorption (see Eq. 2.25) resulting in a scaling with R^3.

2.4.4. Non spherical nanoparticles

Since in reality particles are in most cases not ideal spheres, the influence of the shape on the LSP resonance is discussed in more detail. The case of spheres is generalized to ellipsoidal particles with three semi-axes a, b and c along the Cartesian coordinates x, y and z. Two special ellipsoids that are most interesting in terms of real nanoparticles are, the spheroids which have two minor or major axes with the same length (Fig. 2.21). These are the prolate shaped a > b = c and the oblate shaped a = b > c spheroids.

Considering a sphere and an ellipsoid of the same volume, the LSP resonance can be shifted to longer wavelengths according to one or two elongated major axes. Spheroids exhibit plasmon resonances according to oscillations along their minor and major axis. Spectrally separated resonances can be observed when particles of a large aspect ratio (ratio between the major and minor axis) are investigated [123, p. 72-73]. For ellipsoidal nanoparticles with parallel aligned orientations the plasmon resonance according to the respective axis can be addressed by illumination with linear polarized light [131, p. 37-39]. In this work metal films consisting of islands are used. The particles are dominantly
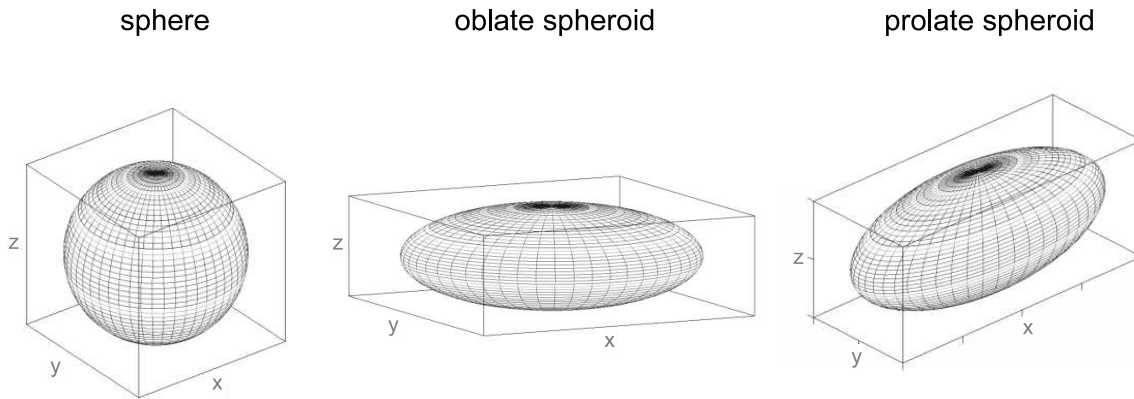
Figure 2.21.: Representation of a sphere, oblate spheroid with two major axes and prolate spheroid with two minor axes of equal length.

oblate shaped (see section 4.2) with the two major axes in the substrate plane. Because light enters generally in normal direction to the substrate, its polarization is always parallel to the major axes of the NPs. Plasmonic electron motion is therefore expected to execute in directions along the substrate plane. Because the particles are randomly oriented and show nearly circular shape only a single plasmon resonance is expected. The knowledge of the lateral particle dimensions allows the estimation of the plasmon resonance according to this and neglecting the vertical dimension.

2.4.5. Damping of LSP resonances

The electron oscillations in a metal nanoparticle correlated to the LSP resonance can be described by an harmonic oscillator that is driven by an external field [118, p. 27-28]. Since the system is not ideal, damping occurs. The oscillator amplitude dissipates with time. When the collective oscillation is separated into the motion of the individual electrons contributing to the oscillation, dephasing between the different electrons is the origin of damping. One distinguishes between radiative decay and non-radiative decay
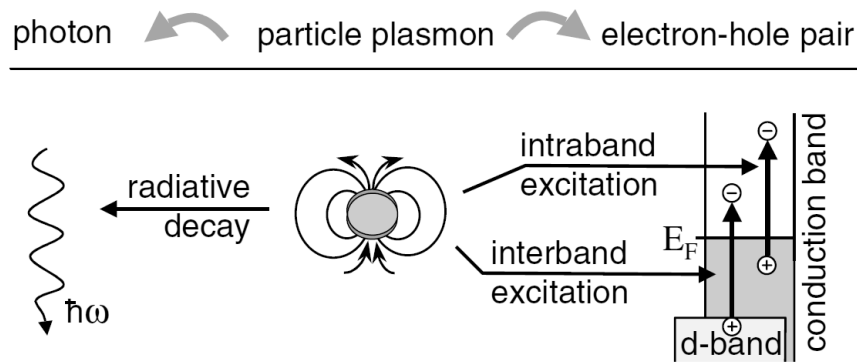
Figure 2.22.: Damping mechanisms for LSP resonances via radiative decay to photons or via nonra-
diative processes, i.e. the excitation of electrons into energetically higher states within
the metal, from [132].

(see Fig. 2.22). Radiation damping is related to the decay of a plasmonic excitation into
photons. This is more important for large particles [128]. The nonradiative damping is
caused by the excitation of electrons in the metal. Here intraband excitations between
occupied to non-occupied conduction band states or interband transitions from d-band
states into the conduction band are distinguished. The nonradiative transitions are
initiated by scattering with electrons, at phonons or material defect sites. For small
particles where the surface to volume ratio is large, also scattering at the surface is
a damping mechanism [133]. The nonradiative decay is directly linked to the dissipa-
tion of energy to heat. Damping broadens the LSP resonance linewidth especially for
increasing particle size [123, p. 74].

3. Experimental Methods

In this chapter the used preparation technology of solar cells and single layers is presented. Especially the preparation of metal nanoparticles for the use in thin film silicon solar cells as resonant absorbing nanostructures is discussed. Further the tools for characterization of nanoparticles and single layers are presented. Finally methods for the investigation of solar cell devices, especially the electrical measurements are discussed in detail.

3.1. Deposition Techniques

Thin film silicon solar cells are composed of several different materials (TCO, a-Si:H, metal reflector), that in combination build a solar cell. This section discusses the deposition and processing techniques of layers relevant for the sample preparation used here. These are in principle the silicon absorber layers as well as thin metal layers from which NPs are formed.

3.1.1. Silicon Deposition with PECVD

Hydrogenated amorphous silicon (a-Si:H) can be deposited with a variety of techniques. Beneath PVD methods including sputtering of a silicon target in the presence of H_2 [134], mainly CVD methods like *hot wire CVD* [135] and others are applied. The most common CVD technique for the deposition of high quality a-Si:H on large scales is *Plasma Enhanced CVD (PECVD)* [83]. This technique was discussed in more detail in section 2.3.1.

In this work, silicon layers are deposited with a *KAI-1200* PECVD system from Oerlikon. With this system a-Si:H and µc-Si:H layers are deposited on large area substrates with a dimension of $1100\,mm \times 1300\,mm$ ($\approx 1.4\,m^2$). As explained in more detail in section 2.3.1, the precursor gases Silane (SiH_4) and hydrogen H_2 are distributed into the vacuum chamber by a gas delivering system. In the chamber (see Fig. 2.14) the plasma that is excited between the electrodes of the capacitor provides the energy to decompose the SiH_4. Typical substrate temperatures for the deposition of a-Si:H are in the $200\,°C$ [6] to $250\,°C$ range [136]. The excitation frequency for plasma generation in the KAI 1200 is $40.68\,MHz$ [7, 137]. The higher frequency compared to standard

13.56 MHz results in lower damage of the deposited film due to reduced impact energy of ions. In addition the decomposition efficiency of SiH_4 and with it the deposition rate is increased [86, p. 135-136] [79].

The homogeneity of thin film deposition depends on the local availability of the precursor gases forming the layers. In order to distribute the gases in a homogeneous manner across the large area substrate, a *showerhead* configuration is used. For this purpose, the upper electrode is equipped with holes that are connected to the gas delivering system (Fig. 2.14).

In this work a-Si:H or µc-Si:H diodes and photovoltaic active devices composed of ultra thin intrinsic absorber layers (30 nm to 100 nm) with often only one type of doped layer are used (see Chapter 5). Herewith the influence of Ag NPs on charge carrier generation in these devices is examined. The thin layer design is applied in order to efficiently extract charge carriers from the NP region, while they are not affected by high defect densities of a doped layer.

3.1.2. Deposition of Metal Films and Nanoparticle Agglomerates

Many different approaches can be applied to prepare metal nanostructures. Chemical approaches, i.e. the formation of nanoparticles in solution [138, 139] and deposition by different techniques like spin coating [140, 141], Langmuir-Blodgett deposition [142, 143] and others are found in literature.

The deposition from the gas phase is either possible by CVD methods [144] or PVD methods. For PVD deposition techniques of nanoparticles most dominantly thermal evaporation or sputtering are applied. Quite sophisticated methods like nanosphere lithography [145, 146] can form well ordered NPs. Here Polystyrene spheres of some 100 nm diameter have to be arranged in a hexagonal closed packed structure on a surface. The gap between the adjacent spheres is then used as template for metal deposition in a regular pattern. This method is on the other hand not feasible for large area deposition.

A much more simple approach suitable for large scales is the deposition of thin metal films in the order of 10 nm and subsequent annealing. For silver films well separated NPs can be formed. The surface tension of the metal films leads to the agglomeration of NPs and a metal island film is created. This technique produces NPs with a Gaussian size distribution, whose mean particle size is influenced by the initial metal film thickness. The prepared particles have an oblate spheroid shape, i.e. their lateral size is larger than their height [147, 148]. As discussed in section 2.3.3, the deposition of metallic films like silver or gold with thicknesses below 10 nm result in island formation without subsequent annealing [113]. This makes it difficult to deposit closed layers with such thicknesses. The comparison between behavior of closed films and nanoparticle films is hence often not possible.

In this work, thermal evaporation as well as sputtering are applied to deposit thin metal films. Silver is the metal of choice because of two main reasons. Silver is used as metal back reflector in thin film solar cells, hence the deposition equipment is available in solar cell manufacturing facilities. Silver NPs in addition have an advantage over gold or copper nanoparticles due to lower losses at optical frequencies [147]. Furthermore silver is much less expensive than gold, concerning the application in industry applications silver is favored.

Thermal Evaporation

For thermal evaporation of silver the vacuum deposition system *Nano 38* from *Kurt J. Lesker* [149] is used, that is routinely applied for depositing the several hundred nanometer thick silver finger grid for contacting the front contact of single cells (see section 3.2.10). Here it is applied to deposit silver films with thicknesses below 10 nm.

The schematic setup is shown in Fig. 3.1. The evaporation source is a resistive heated tungsten boat to which silver pellets are loaded into a dimple. The effective area from which material is evaporated has a diameter of about 2 cm. The samples are clamped to a rotatable sample stage that is aligned vertically above the tungsten boat. The samples are facing down, towards the evaporation source with a distance of 24 cm. Two different sample stages are available for the loading of four or up to fourteen samples with a size of 5 cm × 5 cm, that can be deposited in parallel. In order to deposit silver films homogeneously on this quite large area, the evaporation source is placed a bit off the rotation axis of the sample stage. The cosine like distribution emitted from the source in combination with the rotation should smooth the differences between the sample positions.

The silver film thickness is monitored by a *quartz crystal microbalance* and stopped by a pneumatic shutter that blocks the evaporating material from the sample. The shutter is closed manually or automatically when the desired layer thickness is reached.

The evaporation of material is initialized by heating the tungsten boat. The silver begins to melt and evaporates from the liquid phase and condenses on the sample surface to form thin metal films. The pressure inside the vacuum vessel during deposition is kept below 10^{-5} mbar. The deposition rate can be controlled by the heating power. Typically deposition rates of $0.2 - 0.5$ Å/s are chosen while low rates of 0.02 Å/s have also been used.

To evaluate the homogeneity of deposition across the different sample positions on the rotatable sample holder, three positions (Fig. 3.1 (b)) are used to monitor the thickness variation. Because of the rotational symmetry of the sample holder these positions are sufficient for this investigation. The average thickness (shown in (c)) is calculated from five individual step profile measurements at different positions on
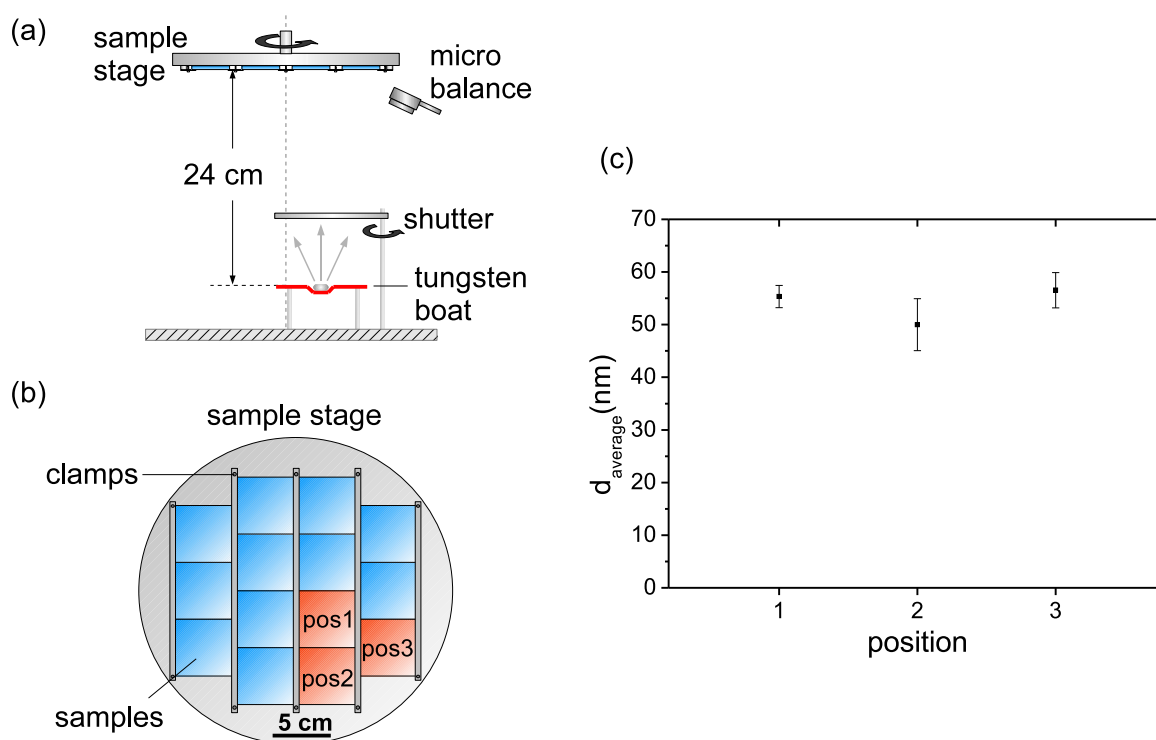
Figure 3.1.: (a) Evaporation setup, (b) rotatable sample stage with 14 samples of $5\,cm \times 5\,cm$ and (c) homogeneity of deposition for the three indicated positions.

each sample. The error bars result from the standard deviation of the individual measurements. All three samples have a thickness of about 50 to 56 nm with a standard deviation of 2 up to 5 nm. The non uniformity is therefore below 10 %. However, for the deposition of thin layers for NP formation only the inner four sample positions (equivalent to position 1) are used due to the lower deviation across this sample (about 3.7 %). This is caused by the fact, that the tungsten boat is centered below position 1. Deviations of the deposition rate due to large angles related to the cosine distribution are less important here.

Sputter Deposition

In addition to thermal evaporation, sputtering of thin silver films is investigated. Other relevant layers like the a-Si:H absorber are deposited on large area $1.4\,m^2$ substrates. One possibility is to prepare the NPs on small area $5\,cm \times 5\,cm$ substrates and use the large area deposition to prepare the other layers after or prior to Ag NP deposition. An additional approach is the deposition of Ag NPs directly on the large area substrates in order to be adaptable to solar cell manufacturing. The availability of sputter equipment in manufacturing lines of thin film solar cells makes this process highly interesting for

our applications. The sputter deposition of silver is hence executed in two different setups. A laboratory UHV sputter setup for the deposition on $5\,\text{cm} \times 5\,\text{cm}$ substrates as well as a sputter facility for large area substrates $(1.4\,\text{m}^2)$ are applied.

UHV Laboratory Sputter Setup: The laboratory sputter facility has been constructed and build in the course of this work. Details can be found in the Appendix A.2. Silver, ZnO and silicon can be sputtered on $5\,\text{cm} \times 5\,\text{cm}$ substrates from three
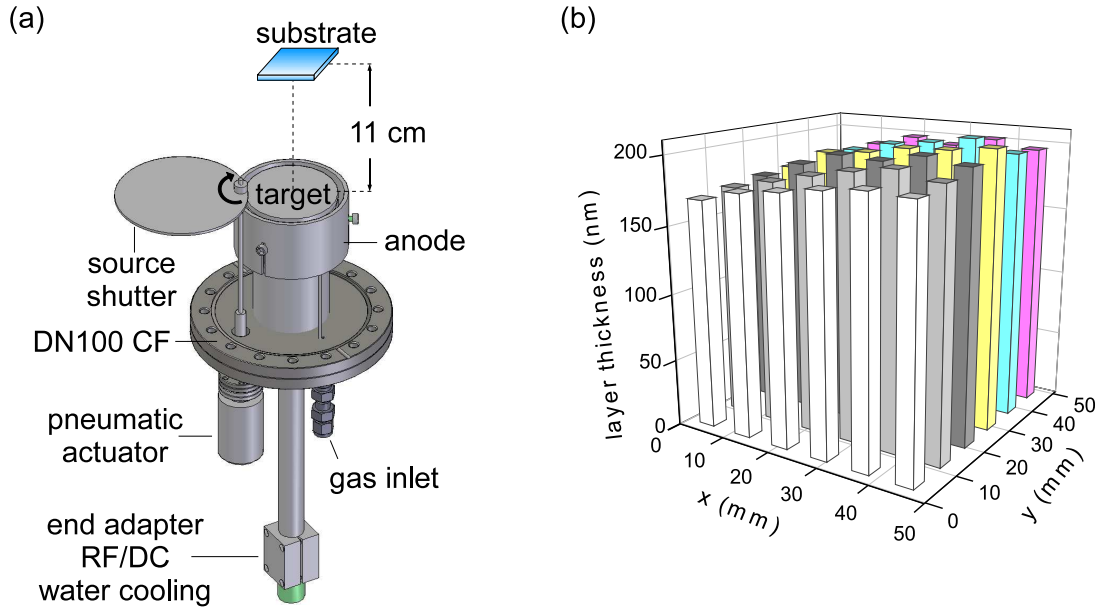
Figure 3.2.: (a) Schematic illustration of a sputter source of the UHV laboratory setup, with a target diameter of $3\,\text{inch} = 7.62\,\text{cm}$. The distance to the substrate is $11\,\text{cm}$. (b) Homogeneity of deposition for a $5\,\text{cm} \times 5\,\text{cm}$ substrate deposited at a distance of $11\,\text{cm}$, a pressure of $1\text{e}^{-2}\,\text{mbar}$, an RF power of $250\,\text{W}$ and a deposition time of $120\,\text{s}$, already presented in [150].

individual sources with the setup. The sputter sources (Fig. 3.2) operate with either DC or RF excitation. Preparation of layers in this setup is of interest due to the high flexibility in variation of process parameters.

The schematic setup of a single source is shown in Fig. 3.2. The distance of the substrate to the target can be adjusted, however if not otherwise stated, a fixed distance of 11 cm is used. For simplicity the illustration of sample manipulation including sample holder is omitted here. The circular 3 inch (7.62 cm) silver target is magnetically fixed on the cathode. The anode is electrically connected to the chamber walls as well as to ground. A pneumatic actuated shutter that is opened during deposition is closed nearly instantaneous to interrupt the deposition process. The Ar gas is injected directly in the target region.

To deduce the homogeneity of silver deposition, a relatively thick silver layer is deposited with $250\,W$ RF excitation power at a pressure of $1 \cdot 10^{-2}\,mbar$. A mean thickness of $(192 \pm 11)\,nm$ is measured, resulting in a homogeneity of $5.7\,\%$. The obtained homogeneity agrees with that given by the sputter source supplier [151].

Since no in-situ control (for example by a microbalance) is installed, the deposition rate has to be determined for fixed deposition conditions by step profiling of thick deposits. Assuming a constant deposition rate for specific conditions, the thickness is controlled simply by the deposition time. Thin silver films are deposited by using shorter deposition times and (or) adjusting the deposition rate with respect to the applied power (see Section A.2.3).

The laboratory setup is in addition equipped with a sample heating stage for in vacuum sample annealing. In an adjacent chamber, samples can be annealed before or after deposition at a background pressure, depending on the temperature between $1 \cdot 10^{-8} - 1 \cdot 10^{-7}\,mbar$. Hence, the formation of Ag NPs is executed under controlled vacuum conditions.

Large Area Inline Sputter Setup: Due to compatibility of Ag NP preparation with the deposition of other relevant layers like the a-Si:H absorber and the contact layers, one approach is to deposit NPs on the same large area substrates ($1.4\,m^2$). For this purpose a *A1500V-7 R&D* inline sputter facility from Leybold Optics is used. Basically it is applied for the deposition of the front and back contact ZnO layers (sputtered from a ceramic target with Al_2O_3 content of 1% to form aluminum doped zinc oxide ZnO:Al (AZO)) as well as silver or aluminum back reflector layers.

Silver is here deposited with DC magnetron sputtering from a cylindrical target that is mounted to a rotatable cathode tube. This cathode design allows a more effective utilization of the target material [152] due to the target rotation. In Fig. 3.3 the schematic deposition setup is illustrated. The vertical aligned substrate is moved with a constant velocity along the cylindrical target. The substrate is backed with a carrier and an in-vacuum transport system, which for clarity is not shown here. Film deposition is executed in a narrow region near to the target, promoted by static magnets that confine the plasma towards the substrate. As the substrate moves by the cathode, the film is deposited at the one end fist and subsequently towards the other end. Due to the substrate movement in this direction with a constant speed, each point on the substrate is exposed the same time interval to the coating flux. Expecting constant deposition rate the substrate should be coated homogeneously with respect to the transport direction.

To measure the homogeneity, a roughly $100\,nm$ thick silver film was deposited. The substrate was moved with a speed of $1\,m/min$ while the power was set to $7.2\,kW$ at a pressure of $1 \cdot 10^{-3}\,mbar$. The measured film thickness across the substrate is

(a)

(b)

d = (104 +/- 5) nm
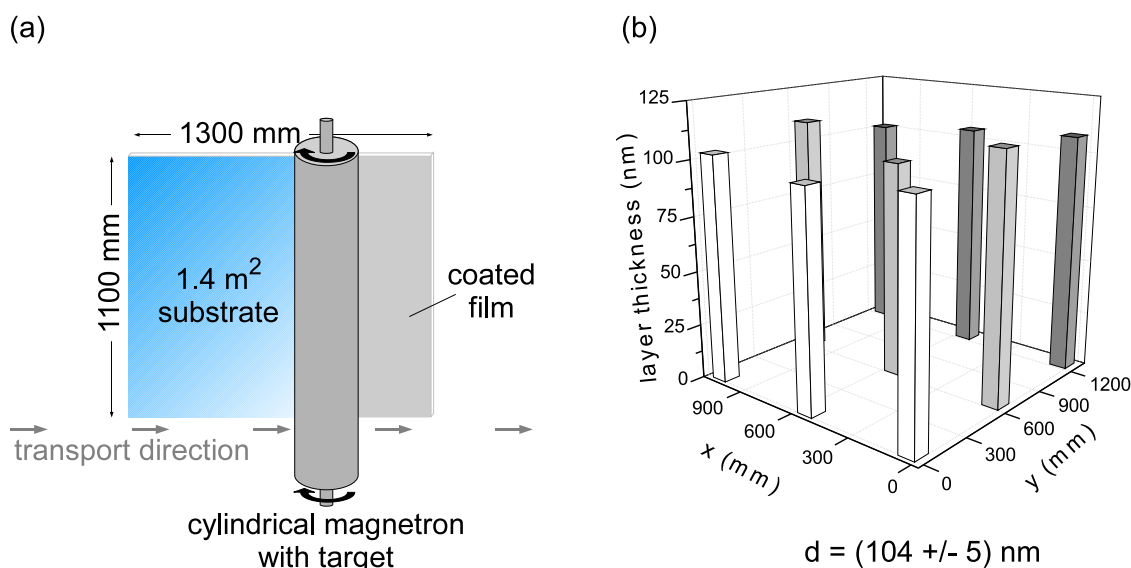
Figure 3.3.: (a) Schematic illustration of inline sputter process for large area substrates deposited by DC magnetron sputtering from a rotatable, cylindrical target. The target is spatially fixed, while the substrate is moved in a direction perpendicular to the target axis. (b) Homogeneity of deposition for 9 positions across the 1100 mm × 1300 mm substrate.

(104 ± 5) nm. This results in a relative homogeneity of 4.9% for a substrate area of $1.4\,\mathrm{m}^2$. Large area deposition is hence suitable for experiments with thin silver films at least with respect to deviations across their positions. The deposition of silver layers with thicknesses below 10 nm requires further the adaptation of process parameters. The applied power directly influences the deposition rate [108, p. 207] while the transfer speed of the substrate influences the actual deposition time. Details on that is discussed in the Appendix A.1.

Beneath thin film deposition the sputter facility allows sample annealing at a background pressure of about 10^{-6} mbar. The substrate heating is executed by radiative heating elements that are mounted at the walls of an adjacent chamber, allowing the annealing prior or after silver deposition. By this Ag NPs are formed under controlled vacuum conditions, as for the laboratory setup discussed above.

3.2. Characterization Methods

The deposited layers, nanostructures and solar cells have to be characterized. Depending on the stage of preparation various techniques are applied to monitor quality and characteristics of silicon and silver layers. Also the morphology and size of nanoparticle films as well as their response to optical excitation are investigated by different

techniques. The measurement of electrical quantities of solar cells are also discussed in this part.

3.2.1. Scanning Electron Microscopy

To investigate the metal NP films, a scanning electron microscope (SEM) *Zeiss Gemini 982 DSM* is used. The working principle of an SEM (Fig. 3.4) is as follows. An electron beam with accelerated electrons is focused on the sample surface. The backscattered or secondary electrons are collected in a detector. By scanning the electron beam over the sample surface a signal is generated in the detector for each point on the scanned area. The detector signal is used to modulate the output on a cathode-ray tube which is scanned in analogy to the sample. This creates an intensity distribution map of electrons coming from the surface. The magnification of an SEM is determined by the ratio of the scanned, constant size of the cathode-ray tube and the scanned area on the sample. The smaller the scanned area, the larger the resulting magnification on the screen [153, p. 231-232]. In principle magnifications between 25× up to 700,000× are
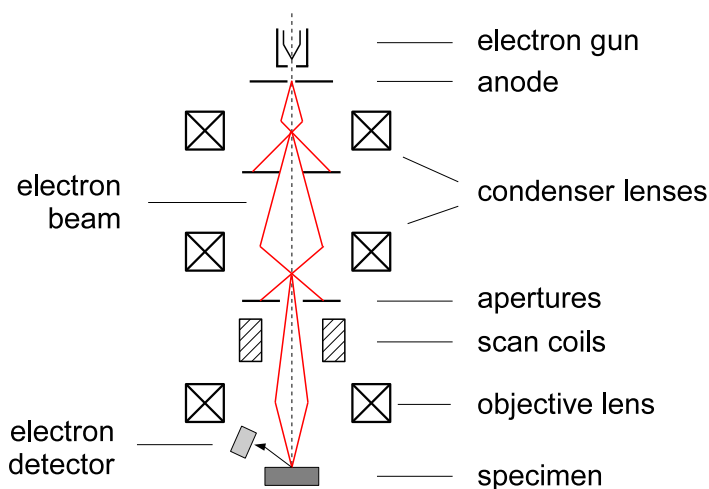
Figure 3.4.: Schematic illustration of the beam path inside a scanning electron microscope (SEM), after [154, p. 5].

possible. However, due to limitations resulting from environmental vibrations, imperfections in electron beam focusing etc. the magnification is limited to about 200,000×. The primary electron beam generates different phenomena related to the interaction with the sample atoms. Back scattered primary electrons, secondary electrons, Auger electrons and X-ray photons can be observed. Usually the low energy secondary elec-

trons resulting from inelastic scattering in the sample are used for SEM purposes. Due to their low energy the escape depth from the sample is restricted to the layers near the surface. The electrons are collected by a positive extraction voltage towards the detector. The extraction voltage results in the collection of electrons emitted in various directions from the sample surface, while the primary electron beam is strongly directed. In analogy to light microscopy, SEM images appear like the observer is in the sight of view of the primary beam while the light source seems to come from the direction of the detector position [153, p. 236].

The contrast of an object observed in an SEM image is specified by the yield of secondary electrons coming from the object. This yield depends on the inclination angle of the objects faces with respect to the incident electron beam. The larger the inclination angle the larger the electron yield, resulting in a stronger signal for these faces with respect to less inclined ones. Especially sharp asperities show a strong electron yield because the excitation volume is in this case closer to the surface and electrons can escape more easily [155, p. 146]. This contrast is known as topography contrast. Aside from this, the secondary electron signal depends on the atomic number. The larger the atomic number the more electrons contribute to inelastic scattering. This is known as material contrast.

Samples applied to SEM measurements have to be conductive to avoid charging of the surface and deflection of the electrons. The primary electron beam is accelerated by voltages in the kV regime. For measurements shown in this thesis usually an acceleration voltage of $10\,\mathrm{kV}$ is applied, while the *in-lens* detector is used to detect the secondary electrons.

The SEM is in addition equipped with an X-ray detector to measure the characteristic X-ray radiation of the sample elements. With this *Energy dispersive X-Ray analysis (EDX)* the chemical composition of the sample can be determined.[155, p. 297]

Nanoparticle Size Measurement from SEM Images

The main application of the SEM is for investigations of Ag NPs. Especially the size and size distribution of deposited NPs is measured herewith. For this purpose an SEM image of NP agglomerates is analyzed with data processing software (SPIP [156] or Gwyddion). In Fig. 3.5 an exemplary SEM image analysis of well separated particles is shown. To measure the individual sizes correctly the particles at the border of the image are excluded. For the measurement of the NP coverage they are in turn included to divide the area occupied by the particles by the total area. Since the particles are irregular shaped, the size is deduced from measuring the NP area A and calculating the diameter d of supposed lateral circular particles by $d = \sqrt{\frac{4 \cdot A}{\pi}}$. The software calculates the area of each item. This allows a statistical analysis of the NP films. The particle
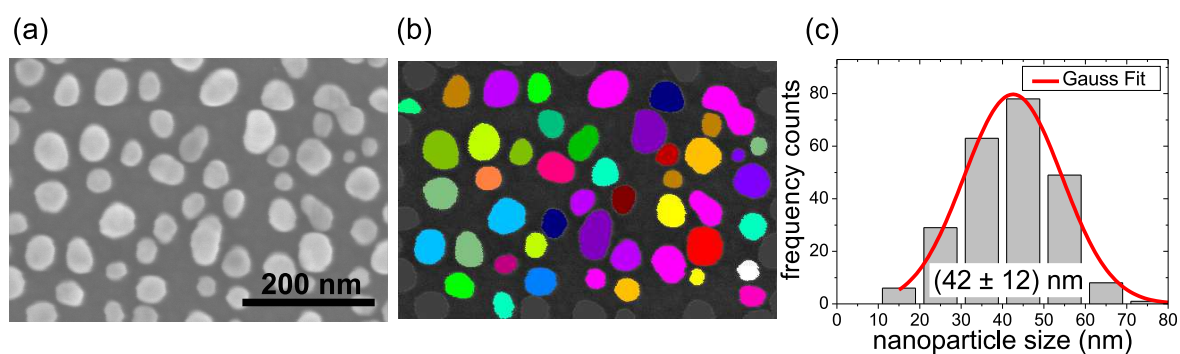
Figure 3.5.: (a)+(b) Determination of NP size by image data processing of SEM images. In (c) the size distribution histogram of this NP agglomerate is shown. The histogram is deduced from an image with larger field of view and hence larger amount of particles, due to better statistics.

size distribution is plotted in a size histogram. From this the mean particle size as well as standard deviation is extracted, supposing a Gaussian size distribution (see Fig 3.5 (c)). The determination of a particle size distribution is only reasonable, when separated NPs can be found in an image. In the case the particles are too close together and the resolution of the SEM is not sufficient to distinguish between the borders of adjacent particles the measurement uncertainty will increase. This is also true for agglomerates with very small particles, where the image processing software cannot distinguish between small particles and artifacts in the SEM image.

3.2.2. Transmission Electron Microscopy

A transmission electron microscope (TEM), in analogy to a scanning electron microscope, applies electrons to image objects (Fig. 3.6). In a TEM the electrons are detected after the transmission through a sample, demanding sufficiently thin samples to allow the transmission. This elaborates the sample preparation especially when cross sections of devices are prepared. In this work TEM is applied to observe the morphology of silver NPs inside solar cell devices. Therefore a cross sectional preparation is necessary. [1] In contrast to an SEM the electrons are not scanned over the sample surface, the sample is rather illuminated on a larger area. Electrons are emitted from a filament, directed by a Wehnelt cylinder and accelerated by an anode with a voltage of several hundred kV. The electrons then pass through apertures and are deflected by electromagnetic lenses which determine the illuminated area on the sample [157, p. 91-111]. Most of the

---

[1]The preparation and TEM measurements have been conducted by Nies Reininghaus and Dr. Wiebke Hachmann
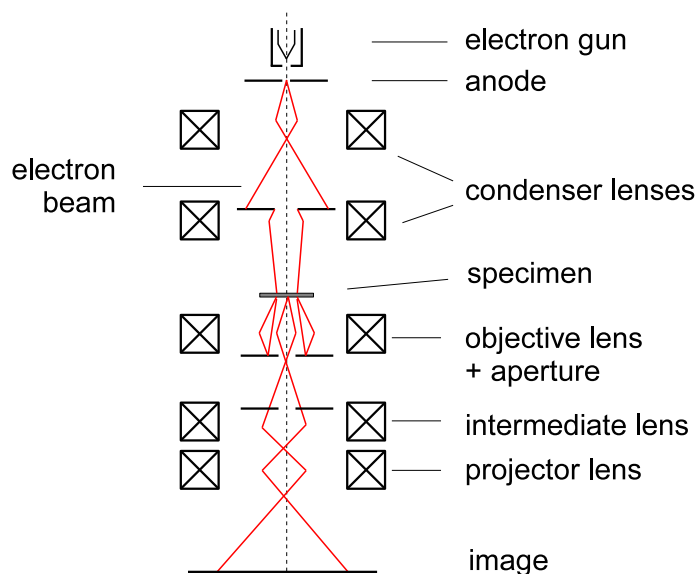
Figure 3.6.: Schematic illustration of the beam path inside a transmission electron microscope (TEM), after [154, p. 7].

electrons are transmitted by the sample without being influenced. A smaller portion of electrons is elastically or inelastically scattered.

The contrast in a TEM dominantly results from the contribution of elastically scattered electrons [157, p. 39]. Apertures allow to select the different parts of the electron beam. Scattered electrons that have trajectories far off the optical axis or those that are close to the axis because they are not scattered. Additional lenses magnify the resulting image and project it onto a CCD chip for data acquisition. The contrast is influenced by the thickness of the sample but most dominantly by the mass of evident elements. The larger the atomic weight, the stronger the electrons are scattered and the darker the elements appear in the TEM image [157, p. 41]. This should be the case for silver compared to silicon, which is investigated in Chapter 5. The used TEM is a Philips CM200 that works with an accelerating voltage of 200 kV.

3.2.3. Atomic Force Microscopy

Besides the lateral size and distribution of NP films, their vertical height is of importance. To obtain information on that *atomic force microscopy (AFM)* measurements are conducted. In an AFM the sample surface is scanned with a very fine tip, by moving the sample with the aid of a piezoelectric scanner in the x- and y-direction. The tip itself is attached to a fine cantilever that is in turn mounted to another piezoelectric

crystal (the z-piezo). A laser beam is focused on the backside of the cantilever. The re-flected light is detected by a *quadrant photodiode*. The position of the laser spot on the photodiode is determined by the differential signal between the individual quadrants of the diode. The tip is scanned in a close distance above the sample surface while it is deflected by the inter atomic forces. The cantilever deflection is measured by the differential signal of the photodiode, from this the force between the tip and the surface is calculated [158, p. 2-3]. The topography of the sample is reconstructed by adjusting the height of the tip in such a way that the force that acts on it is kept constant. This is realized by a feedback loop that utilizes the differential output of the photodiode as signal for the z-piezo. Herewith the height of the tip is adjusted. The z-piezo signal is used to reconstruct the surface topography [158, p. 20]. This procedure is used when measuring in contact mode. A different mode is the non-contact or vibrating mode. Here the cantilever is forced to vibrate at its resonance frequency while it is scanned laterally. The interaction of the tip with the surface leads to a shift of the frequency. This frequency shift is used as feedback for the z-piezo in order to obtain a topography image [158, p. 72-76]. The used AFM is a *Park Systems XE-70* that is operated in the non-contact mode.

3.2.4. Measurement of Layer Thickness

A common method for measuring the thickness of a thin film is step profiling. For this step edges in the layer of interest have to be prepared prior to measurement. Depending on the investigated material, steps are prepared by different methods. For silver layers on glass the film is removed by scratching with a knife edge, without damaging the glass surface. In the case of ZnO well defined steps are etched with diluted hydrochloric acid ($\approx 2\%$), by placing the sample vertically aligned to the liquid surface. Amorphous or microcrystalline silicon can also be etched with potassium hydroxide (KOH) after deposition. A straightforward way of forming a step in a-Si:H layers is to place lines with a permanent marker on the substrate prior to layer deposition. The overgrown silicon can then be removed by wiping the position gently with isopropanol and a soft tissue or using an ultra-sonification bath.

Step profile measurements are done using a Veeco Dektak 6M [159] stylus profiler. In such an apparatus a mechanical tip is mounted to a sensor unit that is able to detect changes of the tip height. The tip is scanned over the sample surface in one direction. Vertical deflections due to features on the surface are detected by the stylus. In terms of measuring the thickness of a thin film, step edges have to be prepared that represent the actual layer thickness. Scanning over this edge is recorded as a step like function for thickness versus scan distance. The layer thickness is averaged for multiple step profiles measured for each sample. This also allows to measure the standard deviation. For large area substrates the homogeneity of deposition is measured at 9 or 13 positions

across the sample. Due to large measurement effort in some cases only single step profiles are measured at each position. In this case an uncertainty of 3% is expected for the step height.

A different way to measure the thickness is to use optical interferometry. The thickness of single layers is determined non destructively by this method, even for large area substrates. For this purpose a NanoCalc-2000-UV/Vis-NIR spectrometer [160] is integrated in an x-y stage. This stage is able to place the measurement device across arbitrary positions on the substrate. The optical interferometry utilizes thin film interferences of deposited layers on top of the substrate (for example a-Si:H on glass) in reflection geometry. Monochromatic light between 250 and 1100 nm is directed and collected by optical fibers close to the substrate surface and directed back to a detector. The interference depends on the optical thickness of the layer, i.e. on the thickness and on the optical constants n and k. For fitting the thickness to a measured interference spectrum the device uses an integrated model for n and k. The results obtained by this method are used for the purpose of measurements of layer thickness homogeneity across a large substrate. When this method is used to deduce a reliable thickness, it is in general cross checked by step profiling.

3.2.5. Sheet Resistance Measurement

The resistance R of a thin film can be written with the specific resistance ρ in the form:

$$R = \frac{\rho \cdot l}{A} = \frac{\rho \cdot l}{d \cdot b} = R_S \cdot \frac{l}{b}, \tag{3.1}$$

while l is the length, b the width and d the thickness of the thin film. The ratio $R_S := \frac{\rho}{d}$ is referred to as the sheet resistance. R_S is measured in units of Ω, by convention it is usually given in $\Omega/\square$ (*pronounced: Ω per square*) [161] or Ω_{sq} [9] to distinguish R_S from the measured resistance R.

Measurements are conducted by the four-point-probe method, with four collinear aligned probes (Fig. 3.7), that is advantageous over two-point measurements because the contact resistance is eliminated. A measurement current I is applied via the outer probes, while the resulting potential difference U is measured between the inner probes. The potential difference can be written in the form [162]:

$$U = I \cdot R_s \cdot \frac{\ln(2)}{\pi} \cdot \frac{l}{b} \tag{3.2}$$

resulting in an expression for the sheet resistance:

$$R_s = \frac{U}{I} \cdot \frac{\pi}{\ln(2)} \cdot \frac{l}{b} = R \cdot \frac{\pi}{\ln(2)} \cdot \frac{l}{b} \tag{3.3}$$
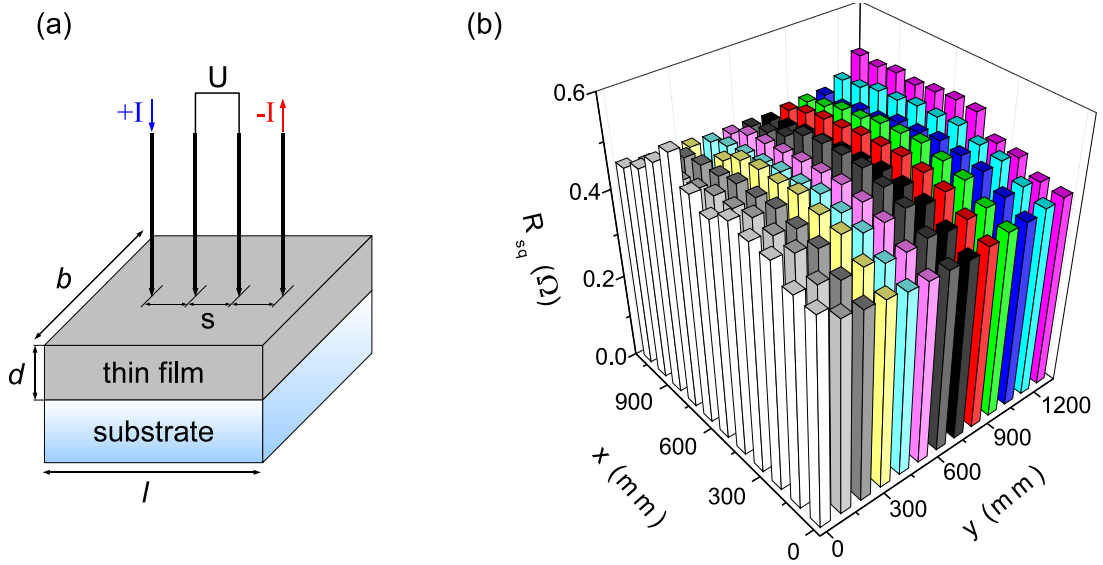
Figure 3.7.: (a) Schematic setup of a four-point-probe measurement. A current I is applied by the two outer probes, while the voltage U is measured between the inner two probes. (b) Example for a measured sheet resistance of a sputter deposited silver film on a large 1100 mm × 1300 mm glass substrate with 143 data points.

Apart from the factor l/b which is equal to 1 for quadratic samples, the sheet resistance R_S is given by the product of resistance R measured in the four-point-probe geometry and the factor $\frac{\pi}{\ln(2)}$. Equations 3.2 and 3.3 are only true if infinitely thin and laterally infinitely large films are investigated. In reality the finite size of both quantities must be accounted for by introducing correction factors f_1 and f_2 [162]. Equation 3.3 consequently changes to:

$$R_s = R \cdot \frac{\pi}{\ln(2)} \cdot f_1 \cdot f_2 \quad . \tag{3.4}$$

However, the factor f_1 for the finite width d is very close to unity in the case of an electrical isolating substrate and the assumption that the layer thickness d is negligible to the distance s of the four probes. Since the electrical measurements are carried out on electrical isolating glass substrates and the silver layer thickness is in the range between a few nm up to 100 nm, these assumptions are true. The factor f_2 for the finite lateral size depends on the ratio of l and b as well as on the ratio of l and s. For large samples ($s \ll l$) f_2 converges towards unity, for small samples f_2 differs markedly thereof. The behavior of f_2 in relation to these quantities is shown in [163].

Measurement of the sheet resistance is applied to large $1.4\,\mathrm{m}^2$ substrates with the aid of an x-y coordinate table with software controlled four-point probe measurement. Herewith data can be collected across the large substrate, utilizing the ability to monitor inhomogeneities of layer thickness and other quantities by variations in the sheet resistance.

3.2.6. Optical Spectroscopy - UV/Vis/NIR

For wavelength dependent transmission, reflection and absorption measurements of samples a *Perkin Elmer - Lambda 950 UV/VIS/NIR Spectrophotometer* is used [164]. The working principle is as follows. The radiation of a tungsten-halogen and a deuterium lamp is monochromatized by two grating monochromators in series to achieve high spectral resolution with a low stray light component. Monochromatic light between 175 and 3000 nm wavelength is provided by the spectrometer. The beam is then divided into a reference and a sample beam by a segmented chopper wheel that reflects the beam or let it pass by, each at a time. Both beams are then directed to the sample compartment (see Fig. 3.8) where an integrating sphere with a highly diffuse reflective material (*Sprectralon* ®) is used to collect the light. Two detectors, a photomultiplier for the UV/Vis range and a Peltier cooled Lead Sulfide (PbS) detector for the NIR regime are used to measure the collected light. To measure spectra over the complete range the short and long wavelength spectra are combined. At the intersection region the switching between both detectors can cause small measurement artifacts due to not optimal compliance. In measured spectra a small kink at around 860 nm is an indication of this.
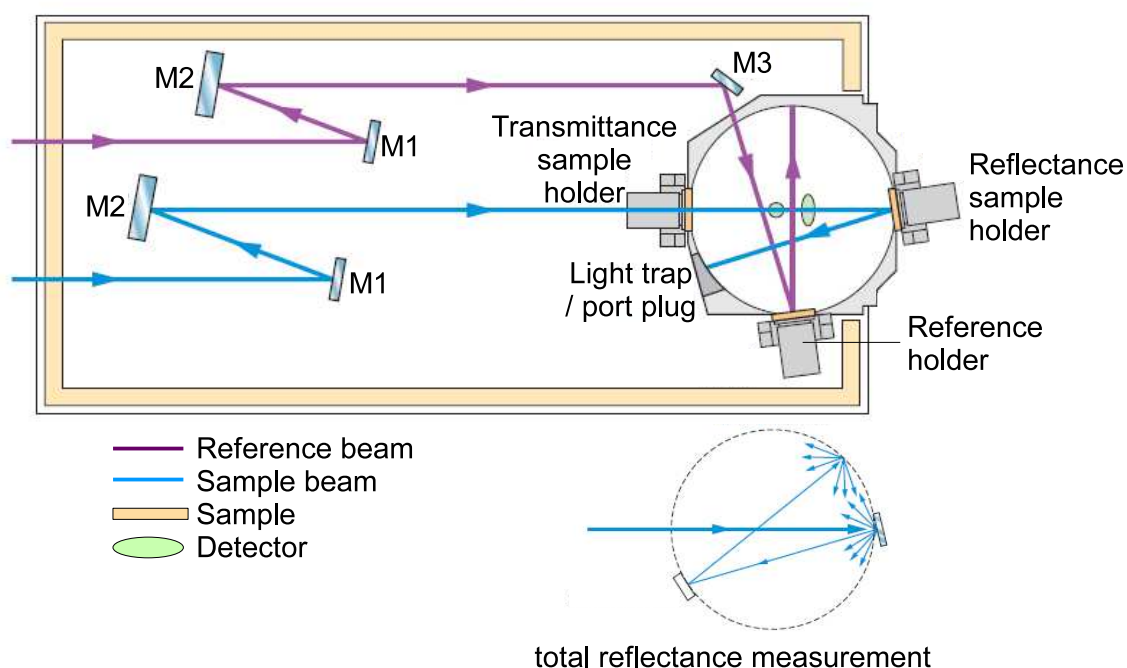
Figure 3.8.: Sample compartment of the UV/Vis spectrometer, with the integrating sphere for collection of the incident light. Samples can be mounted on the according ports for transmission and reflection measurements. The light path for total reflection measurement is shown exemplary on the bottom, from [165].

As illustrated, the samples are mounted in front of the integrating sphere for transmission or at the rear for reflectance measurements. During total transmission measurements the rear port has to be closed by a Spectralon disc. The sample beam interacts with the sample, while the reference beam enters the sphere without interaction. Due to the fact that both beams are chopped and only one of them reaches the integrating sphere at a time, the measured ratio of both signals is used to directly calculate the transmission or reflection of light at the sample. This method eliminates intensity variations of the radiation source and other long time instabilities.
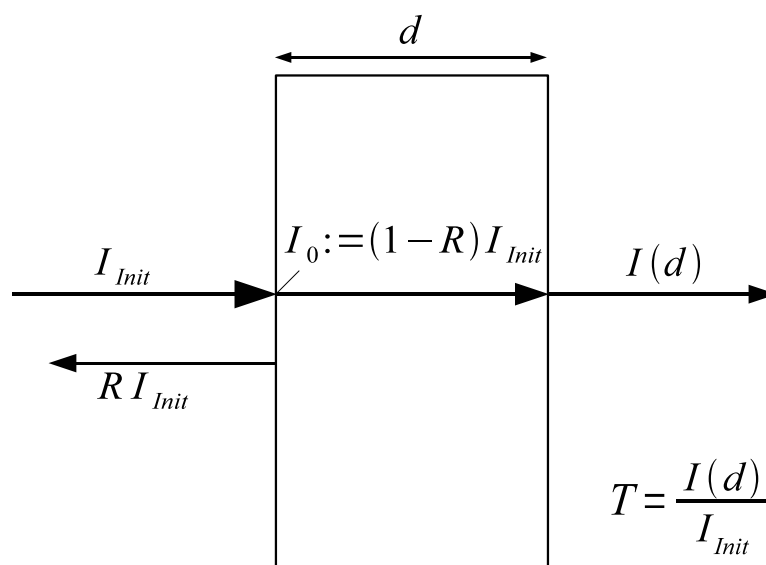
Figure 3.9.: Determination of the absorption coefficient from transmission (T) and reflection (R) measurements of a thin film with thickness d.

Bandgap Determination from UV/Vis

In addition to optical characterization of metal films as well as solar cell devices with incorporated metal films, UV/Vis measurements are utilized to calculate the optical bandgap of semiconducting layers, for example of amorphous silicon. The absorption coefficient of a material can be evaluated from measuring the transmission T and reflection R of a thin film with thickness d and using the Lambert-Beer law, as already introduced in section 2.2.2:

$$I(d) = I_0 \cdot e^{-\alpha d} \, . \tag{3.5}$$

Considering Fig. 3.9, I(d) is the intensity of light after passing the absorbing film. I_0 is in this case the Intensity entering the film, i.e. it is the initial Intensity I_{Init}, corrected

(a)

(b)
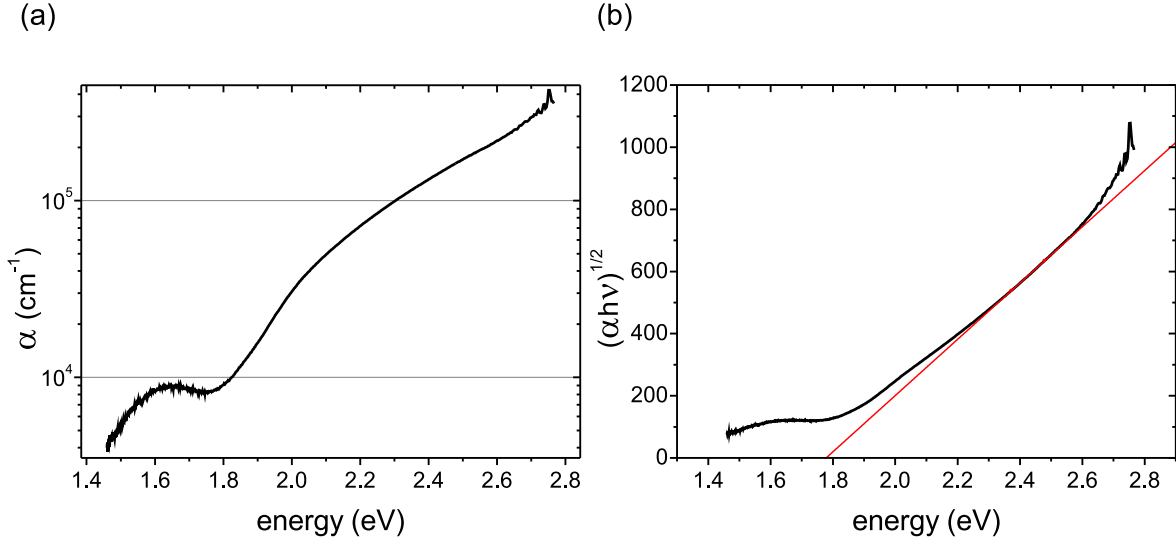
Figure 3.10.: Determination of the optical bandgap via the (a) E_{04} method by searching the energy where α has a value of 10^4 or via (b) Tauc's method by extrapolating the linear part of $\sqrt{\alpha h\nu}$ towards the abscissa.

by the reflected intensity that does not enter the film:

$$I_0 = I_{Init} - RI_{Init} = (1 - R)I_{Init} \, . \tag{3.6}$$

Introducing this into Eq. 3.5 gives:

$$I(d) = (1 - R)I_{Init} \cdot e^{-\alpha d} \;\Rightarrow\; \alpha = \frac{1}{d} \ln \left(\frac{(1 - R)I_{Init}}{I(d)} \right) , \tag{3.7}$$

the ratio $I(d)/I_{Init}$ is equal to the measured transmission T and therefore:

$$\alpha = \frac{1}{d} \ln \left(\frac{1 - R}{T} \right) \, . \tag{3.8}$$

The optical bandgap can be evaluated in different ways. For an amorphous semiconductor with a direct bandgap (like a-Si:H) the optical gap is calculated with *Tauc's method* [71, 166–168] by plotting $\sqrt{\alpha h\nu}$ versus hν and extrapolating the linear part towards the abscissa.

A different method is to estimate the optical bandgap from the measured absorption coefficient at a certain value $\alpha(E_n) = 10^n \, cm^{-1}$, with $n = 3, 3.5 \, \text{or} \, 4$ [169, 170]. A disadvantage of this procedure is the fact that it is influenced by the width of the a-Si:H band tail states [54, p. 41]. The choice of the exponent n of course influences the obtained bandgap value. $E_{3.5}$ gives similar values as E_{tauc}, however the choice is less

important when samples are compared whose bandgaps are determined with the same method.

The example in Fig. 3.10 shows the evaluation of the bandgap for an intrinsic a-Si:H layer with E_{04} and Tauc method. One has to keep in mind that the value for E_{04} is generally larger than the Tauc gap. With both methods an optical gap of around 1.8 eV is measured. Throughout this thesis Tauc's method is chosen for the bandgap determination.

The uncertainty is evaluated in the following way. The statistical deviation of the bandgap for parallel processed samples is about 0.03 eV. Since the definition of borders for the linear fit of the $\sqrt{\alpha h\nu}$ curve is done manually, an uncertainty of around 0.02 eV arises. This leads to a upper bound for the error of 0.05 eV that is applied for all evaluated bandgap values.

3.2.7. X-Ray Diffraction

The crystallographic orientation of deposited films with respect to the substrate surface is investigated with *X-ray diffraction (XRD)*. X-ray radiation delivered from an CuK$_\alpha$ x-ray tube is monochromatized by a Göbel multilayer mirror to a wavelength of 0.154 nm. The used x-ray tube from Philips is operated at a voltage of 40 kV and a current of 20 mA, while an Ortec (Model 904 - NaI-scintillation-detector with photomultiplier) is used as detector. The measurements are executed in the $\theta - 2\theta$ geometry. The x-ray beam is directed on the sample in grazing incidence. The sample is rotated by an angle θ perpendicular to this axis, while the detector is simultaneously rotated on a circle around the sample rotation center with an angle of 2θ. An incident x-ray beam with wavelength λ is constructively reflected under a certain angle θ by parallel crystal planes, if the Bragg condition is fulfilled:

$$n\,\lambda = 2\,d\,\sin\theta\,. \tag{3.9}$$

Here the integer n represents the diffraction order and d the lattice spacing [46, S.44ff]. Silver shows a face centered cubic (fcc) crystallographic growth. For this crystal the distance of the lattice planes d$_{hkl}$ is defined by [171, p. 85]:

$$d_{hkl} = \frac{a}{\sqrt{h^2 + k^2 + l^2}} \tag{3.10}$$

where hkl are the Miller indices and a is the lattice constant (a$_{Ag}$ = 0.409 nm [171, p. 72]). The diffraction angle at which constructive interference occurs can be evaluated by combining Equation 3.9 and 3.10. For the used wavelength, dominant diffraction peaks are expected at angles according to the (111) orientation at $2\theta = 38.1°$ and the (200) orientation at $2\theta = 44.3°$ [172].

3.2.8. Dark Conductivity Measurements
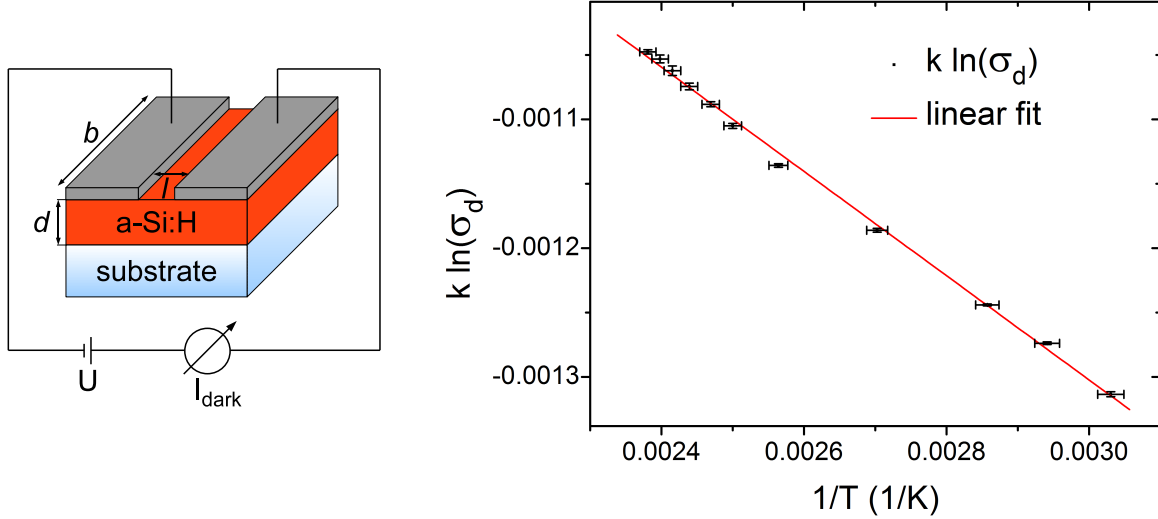
Figure 3.11.: Schematic sample geometry for measurement of dark conductivity of single a-Si:H layers on a quartz-glass substrate. The conductivity is measured between the two coplanar metal electrodes in a high vacuum cryostat. By measuring σ_d at different temperatures and plotting $k \cdot \ln \sigma_d$ versus $1/T$ the linear fit to the data gives the distance of E_F to the nearest band edge. For this example of a p-doped a-Si:H layer the fit gives a distance of $0.4\,eV$ to the valence band. See the text for discussion of measurement uncertainty.

To measure the dark conductivity σ_d of silicon samples, a-Si:H layers are deposited on quartz glass substrates with a layer thickness of approximately $250\,nm$ (Fig. 3.11). Afterwards coplanar metal electrodes are deposited on top of these layers by thermal evaporation. The resistance of a conductor with cross section A and length l can be written in the form $R = \frac{l}{\sigma_d A}$. Solving for σ_d results in:

$$\sigma_d = \frac{l}{R \cdot d \cdot b} = \frac{G \cdot l}{d \cdot b} \ , \tag{3.11}$$

where G is the conductance (reciprocal of the resistance R), l is the length of the conduction path inside the a-Si:H layer, i.e. the distance of the metal electrodes. The cross section A of the conduction path is the product of layer thickness d and width of the electrodes b. The values for $l = 5\,mm \pm 0.1\,mm$ and $b = 10\,mm \pm 1\,mm$ are fixed in the used geometry, while the layer thickness d has to be measured separately for each investigated sample.

Due to the low conductivity of a-Si:H and the resulting low currents, the measurements are performed in vacuum to exclude the influence of surface conductivity or humidity. The sample is clamped on a sample holder and placed in a high vacuum

cryostat. There the sample is heated to $150\,°C$ for more than one hour to remove surface adsorbates like water. Additionally the influence of the Staebler-Wronski effect is hereby removed [173]. The dark conductivity σ_d is measured in the coplanar contact configuration at several temperatures from $150\,°C$ downwards. The temperature is measured with a thermocouple at the sample holder. At each temperature step the sample is allowed to reach thermal equilibrium with the sample holder prior to electrical measurement. The uncertainty of temperature measurement is expected to be in the order of $2\,K$.

The current is then measured with respect to the applied voltage for several steps, typically between 0 and 10 V. The slope of the linear fit reveals the conductance $G = I/U$. The electrical conductivity σ_d is calculated by equation 3.11.

The temperature dependence of σ_d gives information about the Fermi level position of single a-Si:H layers with respect to the nearest band edge. For intrinsic or n-type a-Si:H σ_d can be written in the form [54, p. 51]:

$$\sigma_d(T) = \sigma_0 \exp\left(-\frac{(E_C - E_F)}{kT}\right) \tag{3.12}$$

or the logarithm

$$k \cdot \ln \sigma_d(T) = k \cdot \ln \sigma_0 - \frac{E_C - E_F}{T}. \tag{3.13}$$

Here E_C is the conduction band energy, k is the Boltzmann constant, T is the temperature in Kelvin and σ_0 is a conductivity coefficient. By plotting $k \cdot \ln \sigma_d$ versus 1/T and fitting the data with a linear function, the difference between conduction band and Fermi level $(E_C - E_F)$ is obtained as negative slope of the fit. For p-doped layers this method gives the distance of E_F to the valence band $(E_F - E_V)$ [54, p. 51]. For the example of a p-doped sample shown in Fig 3.11, the fit reveals a distance of around $0.4\,eV$ with respect to the valence band edge. To calculate in each case the distance of E_F to the opposite band edge, i.e. $(E_F - E_V)$ for intrinsic or $(E_C - E_F)$ for p-doped samples, one has to subtract the obtained value from the bandgap energy E_g:

$$(E_C - E_F) = E_g - (E_F - E_V). \tag{3.14}$$

The optical bandgap is calculated from UV/Vis measurements via *Tauc's method*, as described in section 3.2.6.

The conductivity measurements are performed with a *Keithley 6517B* electrometer. The accuracy of the measured current is deduced according to the electrometer specifications [174, 175]. Depending on the measurement range, the accuracy is given by a certain percentage from the measured value and the addition of a number of counts according to the displayed digits. The statistical variation of measured values is larger than the specified accuracy would allow to determine. These variations are

related to the low sample conductivity and possibly due to slight variations of the electrical contact between the contact needles and the metal electrodes. Therefore the uncertainty for the measured current is deduced by the statistical error of 5 individual measurements. This uncertainty is integrated in the uncertainty of the linear fit for the conductance G, resulting in ΔG. From that the uncertainty of the conductivity is deduced by $\Delta \sigma_d = \frac{l}{d \cdot b} \Delta G$. The errors resulting from the uncertainties of the sample geometry Δl, Δd and Δb are independent of the temperature and result only in a scaling uncertainty. They do not contribute to the determination of the slope in Fig. 3.11 and are hence not included. The error bars in Fig. 3.11 for $k \ln(\sigma_d)$ are revealed from Gaussian error propagation:

$$\Delta(k\ln(\sigma_d)) = \sqrt{\left(k\frac{\Delta\sigma_d}{\sigma_d}\right)^2} \tag{3.15}$$

and for the uncertainty of the inverse temperature 1/T to:

$$\Delta\left(\frac{1}{T}\right) = \sqrt{\left(-\frac{\Delta T}{T^2}\right)^2}, \tag{3.16}$$

by using the above stated uncertainty $\Delta T = \pm 2\,K$. From the fit for $k\ln(\sigma_d)$ versus $1/T$ the error of $(E_F - E_V)$ or $(E_C - E_F)$ is deduced. Combining this and the uncertainty of E_g, finally allows the estimation of the uncertainty of equation 3.14 with Gaussian error propagation.

3.2.9. Raman Spectroscopy

Raman spectroscopy relies on the interaction of light with matter. When light is scattered by a material two fundamental modes can occur, elastic and inelastic scattering. The most dominant one is elastic scattering (Rayleigh scattering) where the incident and final wavelengths are the same. However, a certain portion of the incident light is scattered inelastically, meaning the final differs from the incident wavelength. This inelastic scattering is also referred to as *Raman scattering*. It is a result of the interaction of radiation with the vibrational or rotational modes of molecules or phonons in the case of solids. The scattering event consists of the excitation of an electron from a ground state with a photon at the laser frequency ν_L to a virtual intermediate state. This excited state simultaneously decays to emit a scattered photon of frequency ν_S. The electron returns to a ground state, that can be in a different vibrational mode. The scattered photon will hence take up a different frequency. If $\nu_S < \nu_L$ this process is known as *Stokes shift*, if $\nu_S > \nu_L$ this is known as *Anti-Stokes shift* [176, 1-5].

In terms of Raman scattering by convention wavenumbers $\bar{\nu}$ i.e. inverse wavelengths are used: $\bar{\nu} = \frac{1}{\lambda} = \frac{\nu}{c}$. $\bar{\nu}$ is given in units of cm^{-1}, therefore a factor 10^7 has to be included to calculate the wavenumber from wavelengths in nm. For Raman spectra the *Raman shift* $\Delta\bar{\nu}$ rather than absolute wavenumbers are used. $\Delta\bar{\nu} = \bar{\nu}_{\text{Raman}} - \bar{\nu}_{\text{Laser}}$. A Raman shift of $\Delta\bar{\nu} = 0$ represents the excitation frequency of the laser [177, p. 20-21]. Because the Raman shift is calculated relative to the wavenumber of the laser, it is independent of the actual laser frequency. Different excitation frequencies can be applied, while the peaks are observed at the same position in the Raman spectra. The used Raman spectrometer is a *LabRam Aramis* spectrometer from *HORIBA Jobin*
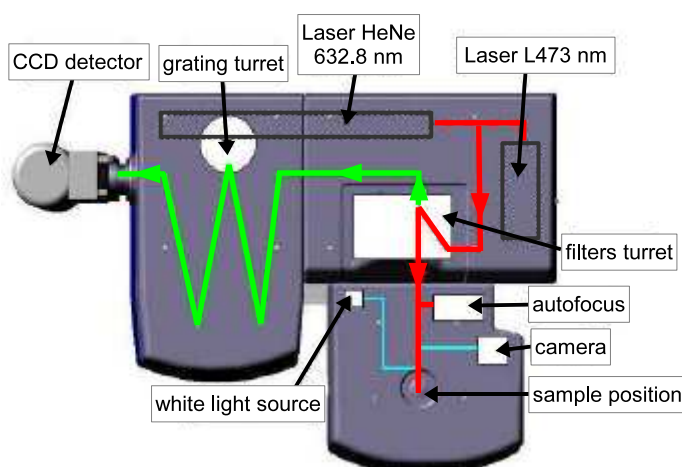
Figure 3.12.: Raman spectrometer with schematic light path. The laser light (473 nm or 633 nm) is directed on the sample after passage through a pinhole a neutral density filter for light attenuation as well as a microscope objective. The sample is placed in confocal configuration under the objective, that collects the light from the sample. The light passes a Notch filter for blocking the central laser wavelength and is then spectrally analyzed by a grating and a CCD detector, from [178].

Yvon. The schematic configuration including the optical path is illustrated in Fig. 3.12. Two different lasers can be used as excitation source, a 473 nm diode laser and a 633 nm Helium Neon laser. The laser light first passes an adjustable pinhole and a *neutral density filter*. With the filter the light intensity is adjusted. This is often necessary when adjusting the sample. However too high intensities would alter the sample properties by recrystallization etc. The light is then focused on the sample with a microscope objective. The scattered and reflected light is collected by the same objective, since the sample is mounted in a confocal configuration. The collected light passes a *Notch filter* for blocking the Rayleigh scattered light at the central laser wavelength. Finally it is spectrally analyzed by a grating and a CCD detector.

As discussed above the choice of the laser wavelength does not change the results that are obtained. Due to the different penetration depth of blue and red light into the material (a-Si:H for example), the use of both lasers gives information concerning bulk and surface properties. The collection depth d_{col} for the Raman signal is effectively the half of the penetration depth ($d_{col} = \frac{1}{2\alpha}$), because the scattered light has to leave the sample in reflection geometry [177, p. 32-34]. Compared to Fig. 5.19 (b) where the penetration depth of an a-Si:H sample is shown, blue light penetrates approximately 50 nm deep into the material. The red laser reaches several hundreds of nanometers deep. In the first case information about near surface regions are extracted, while the red laser gives information about the bulk properties of a film. The combination of both measurements contains valuable information on the growth behavior of materials with crystallinity variation. For example in µc-Si:H where the crystal growth starts from a seeding region in a column-like growth [179]. Fig. 3.13 (a) illustrates the Raman
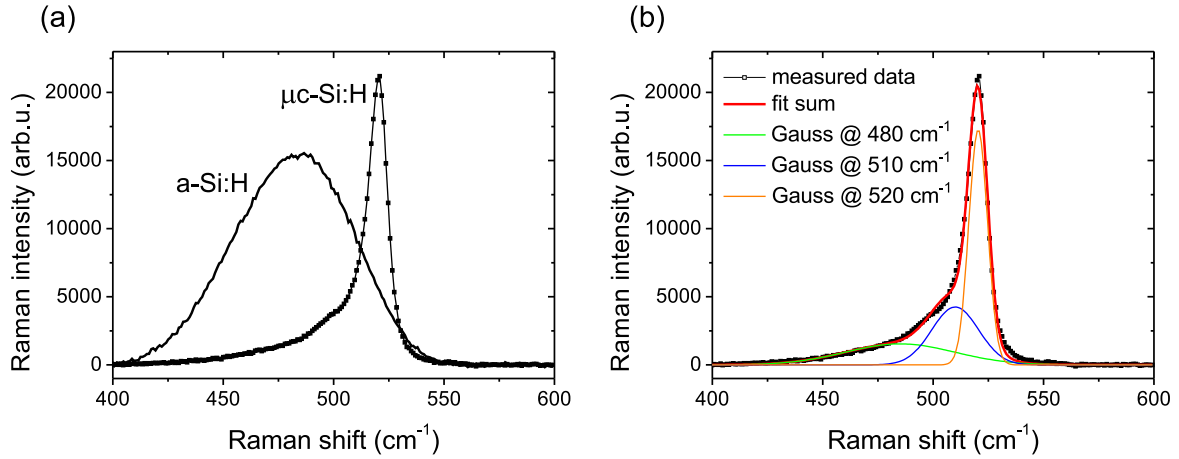
Figure 3.13.: (a) Raman spectra of amorphous and highly microcrystalline material measured with 633nm excitation wavelength. (b) Fitting of a Raman spectrum with three Gaussian peaks at I_{480} corresponding to a-Si:H, I_{510} and I_{520} corresponding to the crystalline phase.

spectra of an a-Si:H and a µc-Si:H sample. The a-Si:H sample shows a characteristic peak at $480 \, \text{cm}^{-1}$. The µc-Si:H sample exhibits a dominant peak near $520 \, \text{cm}^{-1}$ similar to crystalline silicon but also with a contribution originating from the amorphous phase near $480 \, \text{cm}^{-1}$. This is understandable because an amorphous phase is still evident in the µc-Si:H material. The detailed analysis of this spectrum is shown in (b). It is fitted by means of three individual Gaussian peaks at $480 \, \text{cm}^{-1}$ corresponding to the amorphous phase, a peak at $520 \, \text{cm}^{-1}$ related to crystalline silicon and an additional peak in between at $510 \, \text{cm}^{-1}$. The latter is correlated to a defective crystalline phase [179]. From the areas under the Gaussian peaks I_{480}, I_{510} and I_{520} a crystallinity factor

Φ_C can be extracted:

$$\Phi_C = \frac{I_{510} + I_{520}}{I_{480} + I_{510} + I_{520}} \ , \tag{3.17}$$

that gives the ratio of Raman intensities according to the crystalline phase ($I_{510} + I_{520}$) in relation to the total intensity. This crystallinity factor is not equal to the actual crystalline volume fraction in device grade material, but can be considered as a lower limit for it [180]. To estimate the real volume fraction of crystalline material a correction factor that accounts for different cross sections of Raman scattering for a-Si:H and c-Si material has to be taken into account [181]. In this work the absolute value for the determination of the crystalline fraction is not of major importance, only the trend of crystallinity for different samples is compared (see section 5.5.5). Therefore, a correction for the different sensitivity of silicon phases was not considered.

3.2.10. Solar Cell Characterization

The deposition of solar cells and relevant layers is done either on small $5\,\text{cm} \times 5\,\text{cm}$ or on large $1.4\,\text{m}^2$ substrates. In the latter case samples have to be cleaved into small samples for characterization purposes. The positions on the large substrate and cell design geometry is shown in Fig. 3.14. The positions of the 13 small ($5\,\text{cm} \times 5\,\text{cm}$) samples are chosen to be uniformly distributed over the large substrate. This allows to measure statistical or systematic variations within the depositions. On each of the $5\,\text{cm} \times 5\,\text{cm}$ samples, 8 single cells with a cell area of $1\,\text{cm}^2$ are defined by laser scribing (section 2.2.3). Here the a-Si:H and with it the back contact is removed to separate the absorber of adjacent cells. As illustrated in (c) several lines are cleaved in-between the cells. The back contact of each cell is easily accessible, while the front contact is not. In order to measure electrical characteristics of single cells the contacting to the front TCO is made by deposition of a silver finger grid on top of the inner, main laser grove. Electrical characteristics are measured with contact needles between the back contact on each cell to the common finger grid front contact.

Current Voltage Characteristic

The main principles of solar cell operation together with the most important quantities characterizing a solar cell, like $\eta, \text{FF}, \text{V}_{\text{OC}}, \text{j}_{\text{SC}}$ are discussed in section 2.1. To measure these quantities, I-V curves under *standard test conditions* have to be measured. These conditions are: a temperature of $25\,°\text{C}$, while the solar cell has to be illuminated with an AM 1.5 spectrum (section 2.1.1) and an intensity of $1000\,\text{W/m}^2 = 100\,\text{mW/cm}^2$. In the laboratory a class A solar simulator (*WACOM WXS-90S-L2 AM1.5GMM*) provides such a calibrated spectrum with the mentioned intensity. In addition the sample holder is temperature controlled to $25\,°\text{C}$. The sample faces with the layered side to the sample
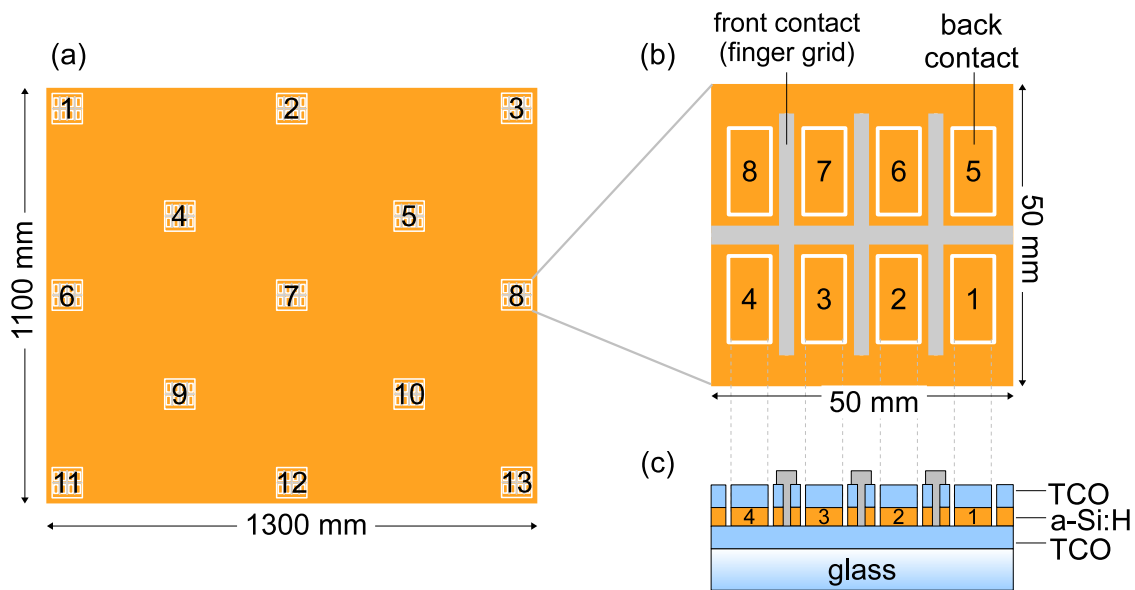
Figure 3.14.: (a) 1300 mm x 1100 mm large area substrate with 13 uniformly distributed sample positions (not true to scale). (b) 5 cm x 5 cm samples shown from the layer side. The 8 single cells with a cell area of $1\,cm^2$ are defined by laser scribing. Contacting of the front TCO is done by laser removal of the a-Si:H absorber and deposition of a silver finger grid on top of the cleared lines. (c) Cross section of cells separated by laser lines and with deposited silver finger grid for contacting the front TCO. The thickness of the layers is not true to scale

stage, to which it is attached by an underpressure. This provides good thermal contact of the sample to the stage. Metal contact needles suitably arranged for the cell layout provide electrical contact to the eight cells, whose I-V curves are measured subsequently. The light enters the cell from the glass side.

In addition dark current characteristics is measured with the same equipment. For this purpose an enclosure is used to protect the cells from parasitic light exposure.

External Quantum Efficiency

The solar cell characteristics are important quantities describing a solar cell device. However, they do not give any information about the spectral distribution of charge carrier generation and collection. For this purpose *external quantum efficiency EQE(λ)* measurements can give valuable information.

When a solar cell is irradiated by light, electron hole pairs are generated. These charge carriers are ideally transported to the contacts and are extracted to the outer electrical circuit. The EQE is a measure for the amount of collected electron hole pairs

in relation to the number of incident photons N_ν [182, p. 53-55]:

$$EQE(\lambda) = \frac{N_{e^-}(\lambda)}{N_\nu(\lambda)} = \frac{N_{e^-}(\lambda)/t}{N_\nu(\lambda)/t} = \frac{n_{e^-}(\lambda)/t}{n_\nu(\lambda)/t} .$$ (3.18)

Due to charge neutrality only electrons are considered. N_{e^-} is the number of electrons, n_{e^-} and n_ν are the electron and photon densities normalized to the solar cell area. The number of electrons generated per area $n_{e^-} = \frac{N_{e^-}}{A}$ and time can be expressed with the short circuit current density $j_{SC}(\lambda)$ as:

$$\frac{n_{e^-}(\lambda)}{t} = \frac{j_{SC}(\lambda)}{e} ,$$ (3.19)

i.e. collected charge Q per time and area divided by the elementary charge e. The number of incident photons per area and time can be written as:

$$\frac{n_\nu(\lambda)}{t} = \frac{B_{inc}(\lambda) \cdot \lambda}{hc}$$ (3.20)

where $B_{inc}(\lambda)$ is the incident power density (intensity) in $W \cdot cm^{-2}$. $B_{inc}(\lambda)$ is linked to the photon flux density $\Phi(\lambda)$ (number of photons per area and time) by dividing with the photon energy $h\nu = \frac{hc}{\lambda}$:

$$\Phi(\lambda) = B_{inc} \cdot \frac{\lambda}{hc} .$$ (3.21)

Using (3.19) and (3.20) equation (3.18) becomes:

$$EQE(\lambda) = \frac{hc}{e\lambda} \frac{j_{SC}(\lambda)}{B_{inc}(\lambda)} = \frac{hc}{e\lambda} SR(\lambda) .$$ (3.22)

Here $SR(\lambda)$ is the *spectral response* or *spectral sensitivity*:

$$SR(\lambda) = \frac{j_{SC}(\lambda)}{B_{inc}(\lambda)} ,$$ (3.23)

defined as generated photocurrent per incident power or photocurrent density per incident power density. $SR(\lambda)$ is given in units of A/W. The measurements are performed at short circuit conditions (0 V). However, also a bias voltage can be applied during measurement. The wavelength integral of the photon flux density $\Phi(\lambda)$ provided by the AM 1.5 spectrum (section 2.1.1) multiplied with $EQE(\lambda)$ (measured at 0 V) gives the short circuit current density of the solar cell:

$$j_{SC} = \int \frac{e\lambda}{hc} \cdot B_{inc}(\lambda) \cdot EQE(\lambda) \, d\lambda = e \int EQE(\lambda) \cdot \Phi(\lambda) \, d\lambda .$$ (3.24)
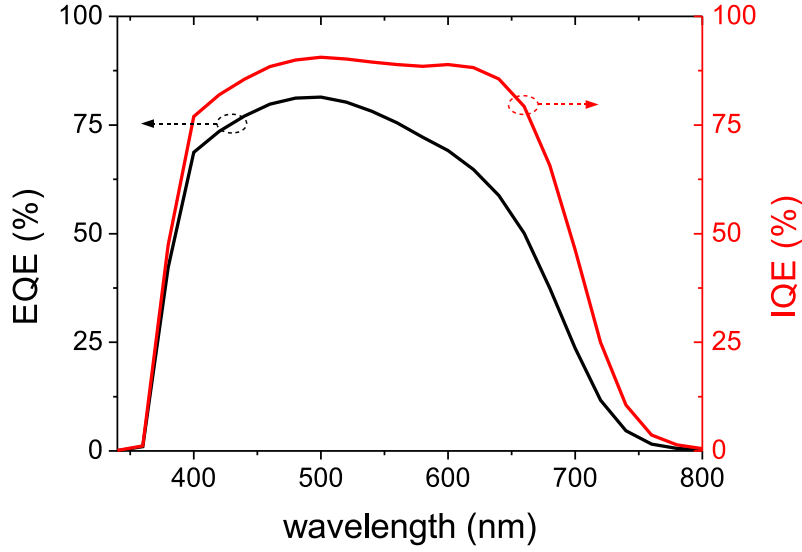
Figure 3.15.: External quantum efficiency EQE and internal quantum efficiency IQE of a standard solar cell with LPCVD ZnO front and back contact.

The measured EQE considers optical losses, reflection and transmission of photons, absorption losses in photovoltaic not active layers (p-layer, TCO) as well as collection losses. Roughly speaking it is the amount of generated charge carriers per incident photon. To measure the amount of generated charge carriers in relation to the photons that are absorbed by the solar cell all optical losses, i.e. reflection and in case of not using a reflective back contact also transmission have to be excluded [183, p. 24]. The internal quantum efficiency IQE(λ) is defined as:

$$IQE(\lambda) = \frac{EQE(\lambda)}{1 - R(\lambda) - T(\lambda)} \,. \tag{3.25}$$

It still includes absorption losses in photovoltaic not active layers. Since the denominator is smaller than unity, the IQE is larger than the EQE, as shown in Fig. 3.15 for a standard a-Si:H solar cell with an LPCVD ZnO front and back contact. The IQE would be equal to 1, when one photon generates one electron hole pair and no absorption and electrical losses are evident.

The schematic setup of the EQE system with the most important components used is shown in Fig. 3.16. A *Xenon lamp* provides a broad radiation spectrum. Two types of monochromators can be used to select monochromatic light, a *grating monochromator* or a *filter monochromator*. Usually the filter monochromator is applied, which consists of a wheel equipped with bandpass filters having a spectral width of less than 20 nm [184]. The monochromator is able to select wavelengths in the range between 300 and 1100 nm. Afterwards the light is modulated by a *chopper wheel* at a frequency
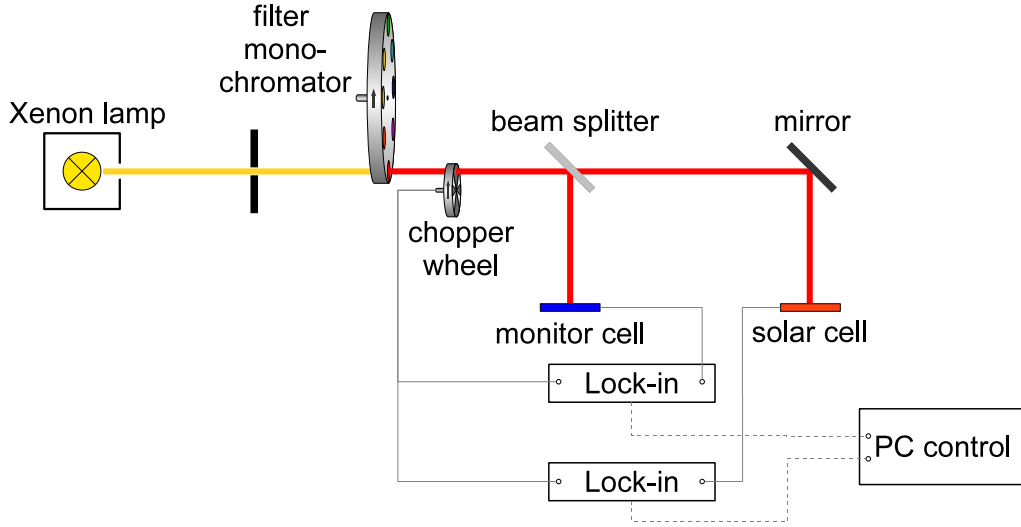
Figure 3.16.: Schematic setup of the EQE measurement system. Only the most important components are shown. The beam divergence as well as focal points etc. are omitted in this schematic setup.

in the range of 100 to 150 Hz and separated by a beam splitter into two beams. One of the monochromatic, chopped beams is directed to the solar cell under test and the other to a silicon monitor cell. Both cells are homogeneously illuminated over their cell area. The photocurrent generated in the solar cell under test and the monitor cell is measured by two individual *Lock-in-amplifiers*. These amplify the signal at the chosen chopper frequency. Therefore undesired signals e.g. resulting from ambient stray light is depressed in the current signal. Prior to measurement of the unknown solar cell under test the EQE setup or more precisely the monitor cell must be calibrated with a certified silicon solar cell with known quantum efficiency EQE_{cal}. During calibration, the ratio of current densities (current per cell area) measured for the calibrated solar cell and for the monitor cell $R_{cal} = j_{cal}(\lambda)/j_{mon}(\lambda)$ is calculated. The same is done during the measurement of the test solar cell $R_{test} = j_{test}(\lambda)/j_{mon}(\lambda)$. The EQE of the test cell is then calculated [185, p. 241-242] [186] by:

$$EQE_{test} = \frac{R_{test}}{R_{cal}} \cdot EQE_{cal} \ . \tag{3.26}$$

In order to perform the measurements at standard conditions the sample stage is temperature controlled to $25\,^{\circ}\mathrm{C}$ while the sample is attached to the stage by an underpressure.

3.3. Summary

In this chapter the PECVD deposition of thin film silicon layers, PVD preparation of thin silver films and formation of silver nanoparticles was discussed. a-Si:H deposition is the most common applied form of silicon in this work. Here ultra-thin layers with a thickness of 30 nm are deposited on large area substrates. The decomposition of Silane (SiH$_4$) with PECVD gives the opportunity to directly influence the deposited layer in electronic quality due to hydrogen incorporation that reduces the defect density of the a-Si:H material. The material can further be doped by the addition of doping gases as Trimethylborane and Phosphine during deposition. This allows to deposit electronic devices structures like p-i-n junctions (and others) necessary for solar cell applications. The material properties can further be influenced by the hydrogen content in the PECVD gas. A large content of H$_2$ leads to the formation of µc-Si:H that has different optical and electrical characteristics than a-Si:H.

The deposition of metal films is executed by two different PVD methods, thermal evaporation and sputtering. Evaporation and sputtering is possible in high vacuum laboratory setups for the deposition on small (5×5) cm^2 substrates. These setups allow a precise control of deposited film thickness by in-situ observation with a microbalance or in case of sputtering due to a known sputter rate via a precise control of deposition time. Alternatively thin silver layers are sputtered on large area substrates. Here the layer thickness is controlled by the transfer speed of the substrate that determines the deposition time as well as the used sputter power determining the deposition rate. Silver nanopaticle films are formed from the thin silver layers by annealing at moderate temperatures of $150 - 200°$. The annealing step is either executed in an oven under atmospheric pressure of inside the vacuum in the case of the laboratory and large area sputter tools.

In addition the characterization tools for layer quality and NP formation are presented. NP films are investigated by microscopy techniques like SEM, TEM and AFM to reveal information about size and distribution of the nanoparticles. Measurement of the sheet resistance is a technique feasible for the characterization of metal layers on large areas. Herewith information on the layer thickness are drawn. In particular for thin layers a discrimination between closed and not closed films is possible. The optical properties of NP films are investigated by optical spectroscopy, especially the plasmonic behavior can be studied. Structural quantities of silicon layers are accessible by Raman spectroscopy. This allows to determine the silicon phases, i.e. whether the material is amorphous or microcrystalline. Electrical measurements of the conductivity for a-Si:H layers provides information about the energetic position of the Fermi level with respect to the band edges.

Solar cell characteristics are deduced from current voltage curves under AM 1.5 spectral illumination as well as in the dark. Information about the spectral response

of solar cell devices is measured with an external quantum efficiency setup. Especially the influence of Ag NPs on the spectral generation of charge carriers is investigated with this technique.

4. Analysis of Ag NP films

The method of choice for preparing nanoparticle agglomerates is to deposit thin metal films by PVD that are subsequently annealed. This preparation is compatible to solar cell production since the deposition of metals and the ability to heat the sample to moderate temperatures of $150 - 200\,°\text{C}$ is available in deposition facilities and production lines. In wet chemical approaches where NPs are prepared in aqueous solutions have some important disadvantages compared to a PVD approach. NPs prepared from solutions could release residues of the solvent on the samples. This would be either negative for device performance or could contaminate the high vacuum facilities used for the deposition of the following layers. In addition NPs prepared in solution have to be deposited onto the substrates of interest by spin [140, 141], drop, spray coating or Langmuir-Blodgett deposition [142, 143]. These techniques are limited to relatively small lateral substrate dimensions of a few cm. The chosen PVD methods are applicable to small substrates for laboratory applications and can be scaled to large dimensions, mandatory in thin film solar cell production. Two different methods are applied for the preparation of metal films, thermal evaporation and sputtering. Before focusing on the formation of Ag NPs by annealing of thin films, the deposition characteristics of the different techniques as well as different tools (section 3.1.2) for deposition are investigated.

4.1. Initial Silver Film Formation

In section 2.3.3 the formation of thin films is discussed. There it is mentioned that silver dominantly shows island growth. This complicates the preparation of thin silver films with a dense, closed morphology. In this section thin silver films deposited by evaporation as well as sputtering are investigated.

In Fig. 4.1 thermal evaporated silver films, deposited on a-Si:H layers with a varying Ag layer thickness are shown. The films in (a)-(c) are deposited with a rate of $0.5\,\text{Å}/s$, while the thickness is increased from $3\,\text{nm}$ over $5\,\text{nm}$ to $10\,\text{nm}$. From the early stages of film formation individual islands are observed that increase in size with increasing
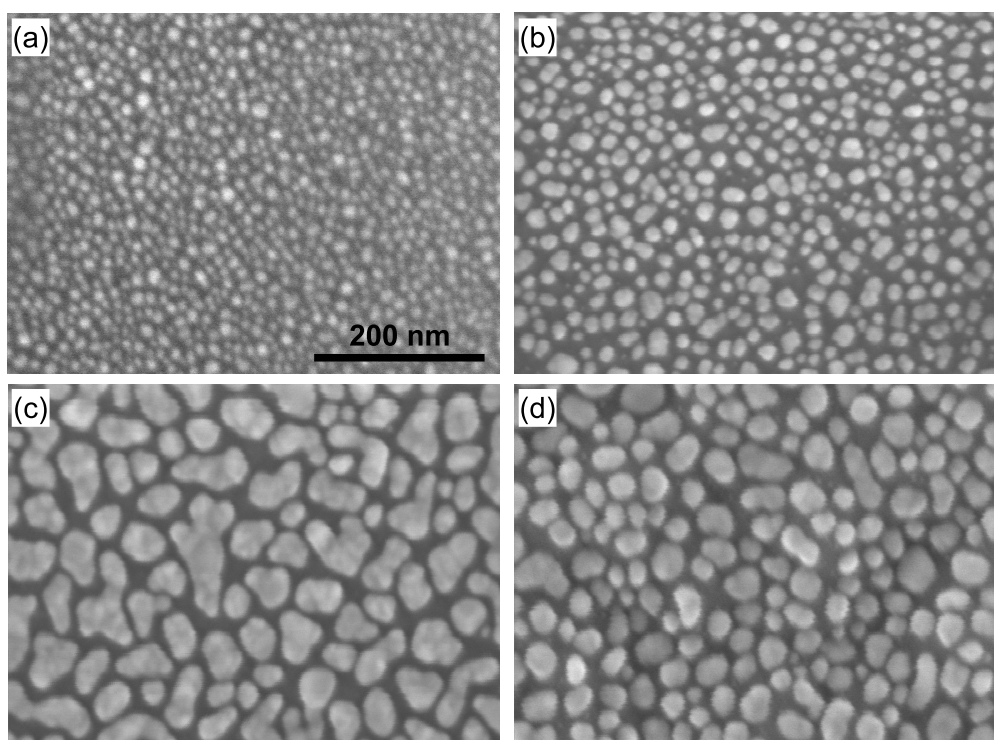
Figure 4.1.: SEM images of as deposited, thermal evaporated silver films on a-Si:H with a varying Ag mass thickness of (a) 3 nm, (b) 5 nm and (c)+(d) 10 nm. While samples (a)-(c) are deposited with a rate of 0.5 Å/s, sample (d) is deposited with a reduced rate of 0.1 Å/s.

silver mass thickness [1]. The fact that no closed films are formed could be related to the growth mode or to thermal annealing effects that lead to an agglomeration of silver nanoparticles. The silver is evaporated from a tungsten boat that is heated above the silver melting point $(962\,^\circ C)$ [187] to gain a significant deposition rate. According to that a certain amount of heat is radiated by the molten silver as well as the surrounding parts of the tungsten boat. The area from which a significant heat is radiated has a size of a few cm^2. The sample is not shielded from the thermal radiation, resulting in heating of the sample that faces the evaporation source with a distance of $\approx 24\,cm$. Thermal treatment of silver films leads to the formation of NPs as described earlier. The sample stage is not temperature controlled and because it is rotating during deposition the measurement of sample temperature with a thermo element is difficult. In order to use lower evaporation temperatures and a lower thermal load of the samples by radiation, the heating power was reduced. Along with that the deposition rate is reduced to $0.1\,Å/s$ (Fig. 4.1 (d)), as seen from comparing to Fig. 4.1 (c). Allthough the same mass thickness was used for both, the film morphology changes. The particles in (d) are even better separated and less interconnected. Hence a thermal annealing effect seems not

---

[1]mass thickness means the amount of deposited material that is equivalent to the amount necessary for a densely packed, ideal layer

to be the driving force for island formation. Rather the growth mode of Volmer-Weber type in addition to the low rates which promote a higher surface mobility [116]. This results in the observed island formation.

With thermal evaporation or at least in the investigated parameter range, the deposition of thin silver films below 10 nm leads to direct formation of Ag NP agglomerates, however they are not well separated. A subsequent annealing is favorable in terms of plasmonic applications in order to prepare separated NPs. Sputtering of silver allows for a larger variation of deposition conditions. The rate is controlled by the applied power. In addition precise control over deposition time is possible, via the shutter in the laboratory setup or via substrate speed for large area deposition. Therefore, the same thicknesses can be deposited while using different deposition rates. Fig. 4.2 shows
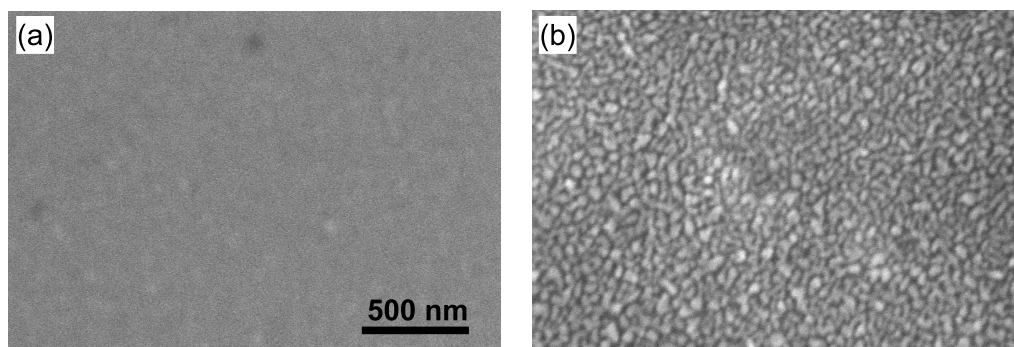
Figure 4.2.: Sputtered silver layers on glass with a thickness of 5 nm deposited with a pressure of $1 \cdot 10^{-2}$ mbar and an rf-power of (a) 150 W corresponding to a rate of R = 0.85 nm/s and (b) 50 W with a rate of R = 0.25 nm/s. For (a) a smooth and compact film is produced.

two silver layers with a thickness of 5 nm deposited in the laboratory setup. Both are sputtered at the same pressure but with different rf power and consequently with different deposition rates. Sample (a) is deposited with a rate of 0.85 nm/s, it shows a homogeneous, closed layer. Sample (b) is deposited with a lower rate of 0.25 nm/s, the film is composed of islands that are partly interconnected. Since the deposition rate is varied by means of the applied power, a higher rate also corresponds to larger energies of impinging target atoms. This increases their mobility on the surface and should promote an island formation [109, p. 10-14]. However, an opposite trend is observed, with higher energy the film becomes compact. Due to the higher rate, an impinging atom will more likely find another atom to form a new nucleus instead of hitting an existing island. Therefore nucleation is favored compared to island growth. Smaller grains are created in the initial stages and a smoother film is formed [108, p. 383-388][116]. Increasing the film thickness to 10 nm (not explicitly shown) also the low rate sample shows a closed morphology, because the islands have cumulated enough material to

interconnect to a closed film. The difference between both 5 nm thin films also be-

(a)

(b)
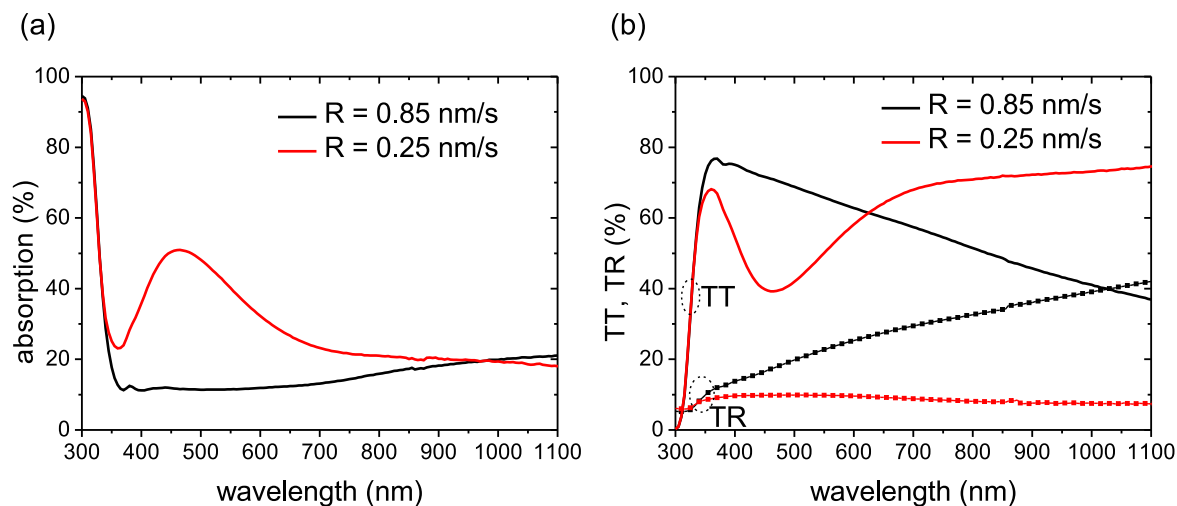
Figure 4.3.: (a) UV/Vis absorption and (b) transmission (TT) as well as reflection (TR) spectra of sputter deposited silver layers with a thickness of 5 nm deposited with different rates shown in Fig. 4.2.
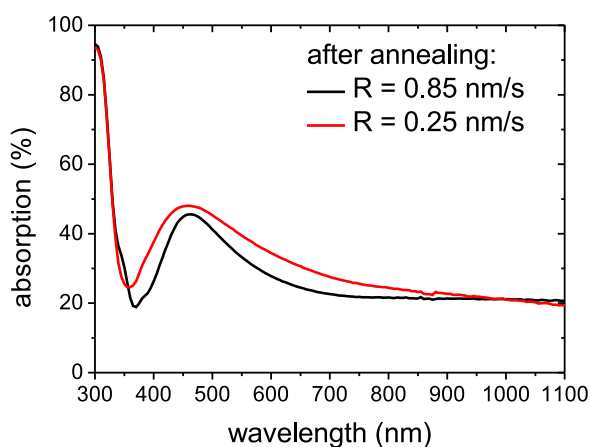
Figure 4.4.: Optical absorption of Ag layers already shown in Fig. 4.3 after annealing. The annealing leads to a similar response of both samples due to island formation.

comes obvious when comparing their optical response (Fig. 4.3). The sample deposited with the higher rate has a low absorption and a comparably high reflectivity according to a closed silver film. The absorption for the low rate sample on the other hand is increased and exhibits a peak between 450 and 500 nm. In agreement with that, the transmission shows a dip in that region, while the reflection is decreased over the complete range. This behavior originates from the isolated islands found on that sample

promoting LSP resonances. This result demonstrates that it is possible to deposit thin silver layers with different optical properties. For the application of thin silver films towards plasmonic applications in solar cells the initial stage of film formation is not of importance, since all silver layers are exposed to annealing in the PECVD reactor prior to a-Si:H deposition. This leads to formation of silver islands for both types of initial layers. The optical response of both layers after an annealing step at 150 ° for 30 min is very similar (Fig 4.4). Especially the position of the peaks related to the plasmonic excitation are very similar. However, the preparation of a closed thin film

(a)   (b)
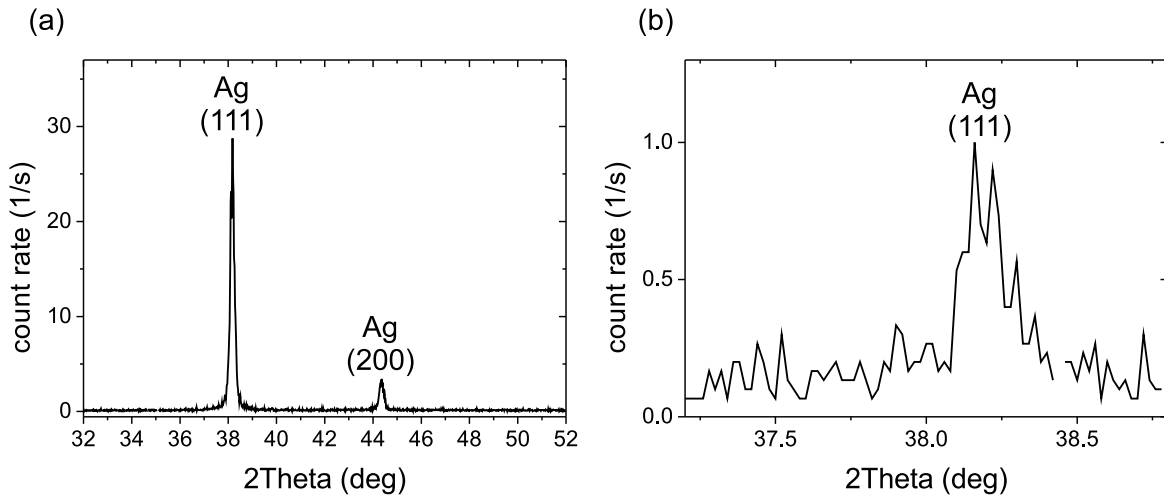
Figure 4.5.: XRD measurement of sputter deposited silver films. (a) With a thickness of about 650 nm and (b) with a thickness of 15 nm. The dominant crystallographic orientation is along the (111) direction, while minor contribution from the (200) peak arises. For the thin sample only the (111) orientation is observed due to the small signal (mind the different scales).

with respect to an initial island film gives the opportunity to investigate the optical differences between them.

Thin silver layers prepared on large area substrates are to a certain extent governed by stronger variations with respect to the large lateral dimensions. In addition the layer thickness cannot be controlled with a precision that is reached for the small area deposition in the laboratory setup. However, sputtering on large scales provides a better integration into large area deposition process of other layers in device fabrication.

The crystallographic orientation of thick silver films measured by X-ray diffraction (XRD) analysis is found to be dominantly a (111) orientation of the face-centered-cubic (fcc) lattice (see example in Fig. 4.5 (a)). A small portion of the grains are also oriented with the (200) lattice planes parallel to the substrate. This result is found for all deposition methods used and is in agreement with the literature [172]. XRD measurements deliver a good signal if the investigated layers are thick and enough

material contributes to diffraction. A statement on the growth direction in the initial stages of film formation are difficult. However the detection of a (111) peak for a film of only 15 nm thickness (Fig. 4.5 (b)) indicates that this orientation is evident from the beginning of film growth. For silver nanoparticle films formed from layers with a thickness below 10 nm the crystal orientation is difficult to observe due to the even lower amount of material and the resulting small signal.

4.2. Investigation of Annealed Ag NP Films

As shown in the previous section, the deposition of thin silver films initially forms islands, under most deposition conditions. A further annealing results in a better separation of the particles. In addition, the optical response of annealed layers does not differ significantly between initially closed films or as-grown island films.

4.2.1. Morphology of Annealed Ag NP Island Films

When the silver films are incorporated into solar cell devices they are exposed to processes where they are effectively annealed. This is in particular the case when silver layer deposition is followed by a-Si:H PECVD deposition, here annealing temperatures between 200 and 250 °C are used. Hence nanoparticles will form, even when the Ag films are not separately annealed.

To investigate the influence of annealing on the morphology, the silver films shown in Fig. 4.1 (a)-(c) are exposed to an annealing step. Here they are heated in an oven at 150 °C for 1 h. The resulting NP island films are shown in Fig. 4.6 (a)-(c). The annealing step significantly changes the appearance of the films. The particles become separated and more regular shaped. Especially for the 10 nm layer the irregular shaped particles that were close to the percolation threshold, form well separated Ag NPs. Along with the SEM images size distribution histograms are shown. Their evaluation was explained in section 3.2.1. The mean particle size x_c and distribution width are deduced by fitting the histograms with Gaussian functions. The mean particle diameter versus layer thickness is shown in Fig. 4.6 (d), for the annealed and as-grown samples from Fig. 4.1 (a)-(c). Here different observations are made. First the increase of the initial layer thickness results in an increase of the particle size as well as of the distribution width. For thin layers the annealing does not have a significant influence on the particle size, the as-grown particles are only slightly larger. For the thickest sample (10 nm), in contrast a clear difference is observed. The as-grown particles are close to the percolation threshold (Fig. 4.1 (c)) and show a broad distribution of sizes. In addition the particle shapes are irregular. Here the annealing results in the formation of round
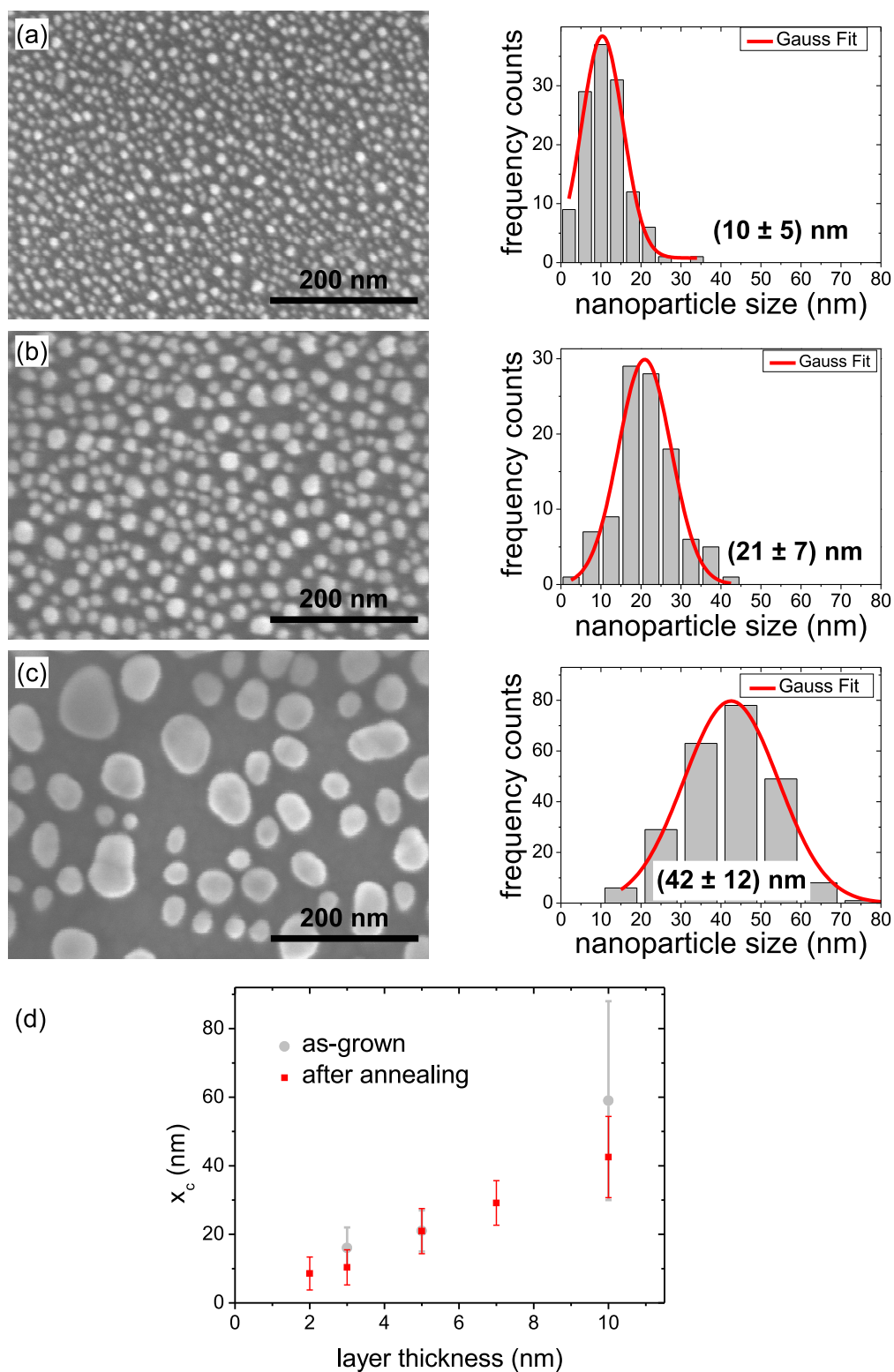
Figure 4.6.: SEM images of thermal evaporated silver films after annealing at 150 °C. The initial layer thicknesses are (a) 3 nm, (b) 5 nm and (c) 10 nm. The nanoparticle size histograms, that are shown alongside, are fitted with a Gaussian function to determine the mean particle size x_c and distribution width. In (d) the mean particle diameter x_c is plotted for as-grown and annealed samples, with respect to the layer thickness. The error bars indicate the distribution width from the Gaussian fits.

particles with a distinctly reduced size and distribution width. The islands accumulate material from their vicinity and grow in the vertical direction.
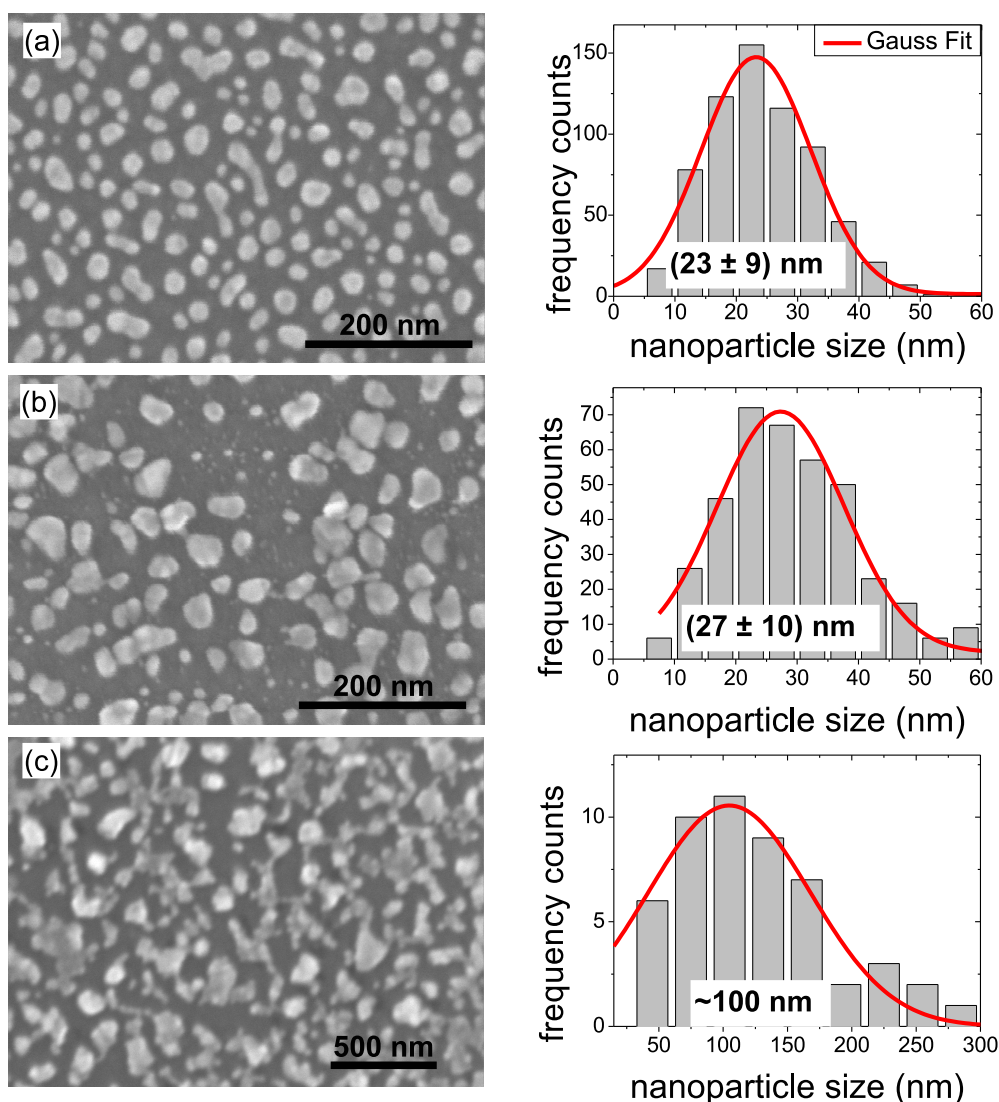
Figure 4.7.: SEM images of sputter deposited silver films after annealing at $200\,°C$ for $30\,min$. The used sputter power was (a) $0.5\,kW$ with a transfer speed of $2\,m/min$ resulting in $(23 \pm 9)\,nm$ average particle diameter, (b) $0.7\,kW$ $2\,m/min$ resulting in $(27 \pm 10)\,nm$ particles and (c) $0.7\,kW$ with $1\,m/min$ resulting in around $100\,nm$ particles. The NPs are less regular shaped than evaporated films, especially in (c).

As a result, the deposition of thin silver films and subsequent annealing allows to create NPs. Their size is adjusted by varying the deposited silver layer thickness. This is of course not true for much thicker layers. For thicknesses above $20\,nm$ a percolated network with interconnected islands is formed. Higher annealing temperatures would be necessary to form separated NPs from these films.

Silver layers sputtered on large substrate dimensions, in principle also show an increased particle size with increasing layer thickness (Fig. 4.7). However, the deposited layer thickness cannot be controlled with the same precision as for small sample dimensions. Silver layers are deposited with different applied DC powers of 0.5 and 0.7 kW resulting in layer thicknesses below and around 10 nm. By reducing the substrate transfer speed to one half, layers with twice the thickness, around 20 nm are deposited (see Appendix A.1 for details). The sputter deposited layers are in general exposed to a vacuum annealing step instead of an oven under atmospheric pressure. The nanoparticle agglomerates in Fig. 4.7 (a) and (b) exhibit a morphology that is more irregular than for evaporated films, however they are separated and have similar particle sizes. For these examples average particle diameters of 23 nm and 27 nm are measured. The tendency towards more irregular shaped particles might be related to crystalline grain formation during sputtering. In Fig. 4.7 (c) particles formed from a layer with an initial thickness of 20 nm are shown. Here a mean particle size of about 100 nm is observed. The particles are close to the percolation threshold and are hence not well separated. This in combination to the arbitrary shapes complicates the definition of a mean particle size.

The height of these nanoparticle films is determined by AFM measurements (Fig 4.8). For the sample in (a) the root mean square roughness of the island film is 9.1 nm. The according line profiles, indicated with numbers in the AFM measurement, are shown alongside. One should not be confused about the scaling of the line profiles, since the height scale is stretched with a factor of 2 with respect to the lateral distance. Therefore the features appear larger. Some individual particles have heights of 30 to 50 nm. These large particles have a lateral dimension of around 100 nm. The particles are oblate shaped instead of being spherical. Most of the features are well below 15 nm in height while their lateral dimension is again a factor 2-3 larger. The slightly thicker sample in (b) exhibits in average larger particles. This manifests in an increased root mean square roughness of 11.0 nm. Some particles reach heights of about 50 nm, while the average particles have heights of about 15-20 nm. Again the particles are laterally broader than their height. The thickest sample that is close to the percolation threshold is shown in (c). It contains large particles with lateral dimension that extent up to 200 nm. The height of the features is also increased compared to the other samples. However the maximum heights are not considerably larger. This manifests in only a slight increase of the root mean square roughness to 11.9 nm. The particle formation is obviously not completed for this sample. Higher annealing temperatures or a longer heating duration would be necessary to prepare better separated particles.
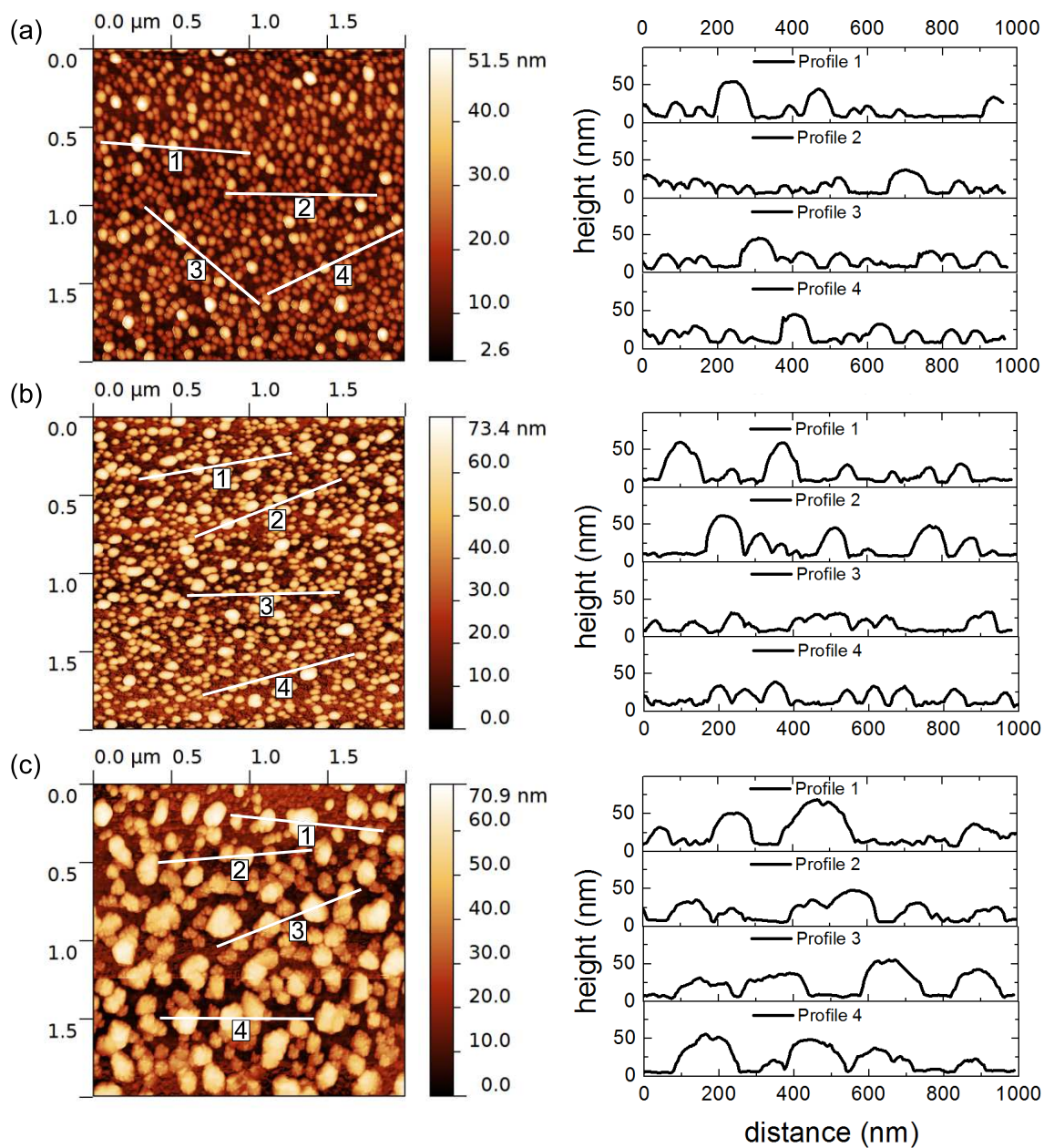
Figure 4.8.: AFM measurement of sputter deposited Ag NP film shown in the SEM measurements in Fig. 4.7. Alongside line profiles attributed to the numbered line scans in the AFM measurements are shown. (a) 0.5 kW dc power with a transfer speed of 2 m/min, (b) 0.7 kW with 2 m/min and (c) 0.7 kW with 2 m/min.

4.2.2. Optical Properties of Annealed Ag NP Island Films

To investigate the influence of the particle size on the optical response, measurements of NPs deposited on ZnO are investigated in more detail, since this is a typical configuration for solar cell deposition. Fig. 4.9 shows the optical response of Ag NP ag-
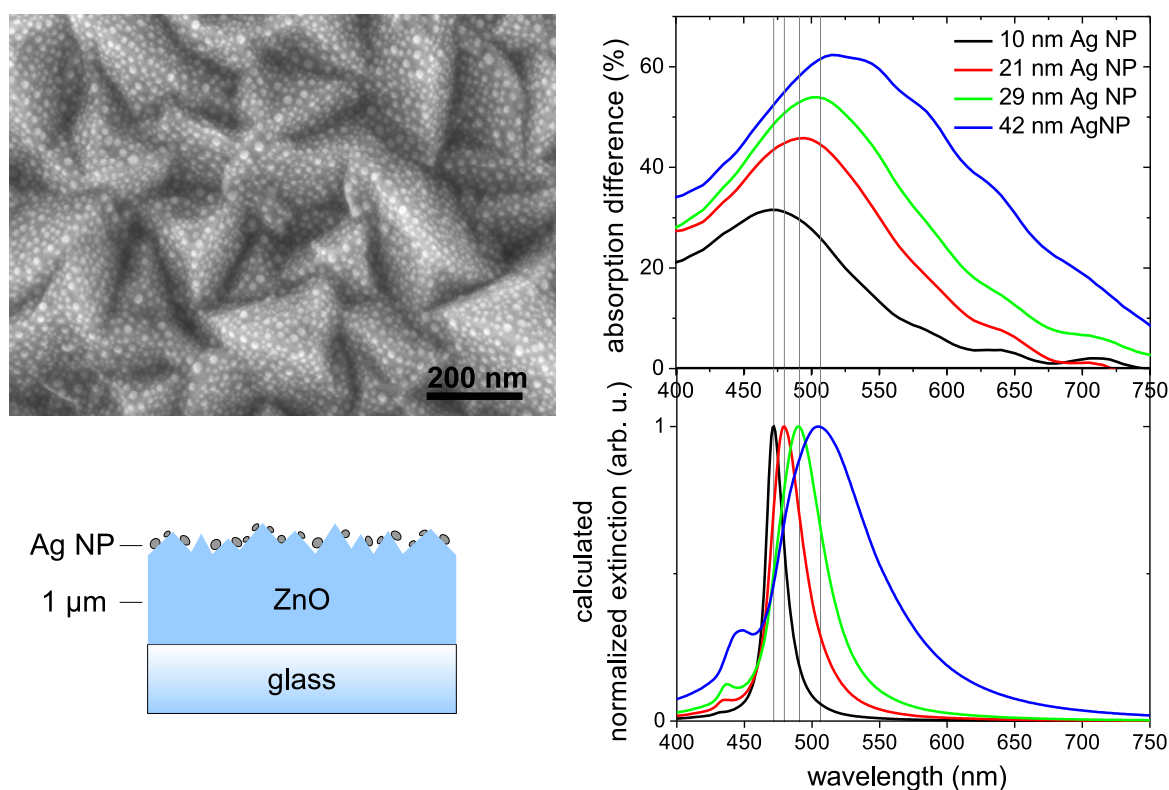
Figure 4.9.: UV/Vis measurements of Ag NPs on ZnO, the ZnO absorption is subtracted in these measurements. Different NP distributions with mean particle sizes between 10 and 42 nm are applied. In addition the calculated normalized extinction for each NP size distribution is shown below. The tendency and roughly the position of the calculated resonance fits to the observed peaks in the absorption spectra.

glomerates deposited on LPCVD ZnO substrates with a rough surface morphology. This configuration is used, since it allows to measure the optical response without thin film interferences emerging at flat surfaces. The deposited silver layer thicknesses are chosen to be 3, 5, 7 and 10 nm, equal to those used for the formation of the NP films in Fig. 4.6. The measured absorption spectra shown here are already corrected for the absorption within the underlying ZnO layer, i.e. the ZnO absorption is subtracted. Hence, only the response of the Ag NPs is illustrated here. The nanoparticle island films show a strong absorption. For all particle sizes a significant peak, according to the plasmonic resonances of the particles, is observed. An increase of the mean particle

size results in a shift of the peak towards longer wavelengths. That this is an effect of the LSP resonances is checked by calculations shown on the bottom. The normalized extinction spectra are calculated by applying the measured Ag NP size distributions to a dielectric environment of n = 2, according to ZnO. The procedure of utilizing the size distribution histograms for the calculations was explained in more detail in section 2.4.2. Since the measurement of particle size on the rough ZnO surface is not possible in an adequate manner, the distributions measured for the planar surface in Fig. 4.6 are employed. The calculated spectra overlap with the observed absorption spectra. Their maximum positions agree quite well for the small particles and deviate for larger particles. The measured absorption peaks are broader than the calculated extinction spectra. This could be related to interactions of neighboring particles [188] due to their close separation that is not taken into account in the calculations. In addition the calculations expect a size distribution of spherical particles that is indeed not the case (as discussed before). However the overall trend is well reproduced with the conducted calculations. Obviously the deviation of the particle size in the vertical dimension is of minor importance, since the polarization vertical to the direction of incident light is more important. Furthermore the peaks in the optical measurements exhibit an increased amplitude with increasing particle size. This is related to the larger volume of silver, evident for the larger particles that results in a stronger absorption [189]. For the ZnO environment the particle resonances are centered around 500 nm according to its refractive index of n $\approx$ 2.

For the application of nanoparticles to solar cells the particles have to be integrated into the silicon absorber. This results in a strong variation of the plasmon resonance as discussed earlier. Incorporating NPs in a silicon environment (n $\approx$ 4) a distinct peak is observed, as shown in Fig. 4.10. This peak is shifted to 800-850 nm. Here very thin layers of a-Si:H are applied which facilitate a strong absorption below 600 nm, while they show a weak absorption above 700 nm. Therefore the LSP resonance is explicitly revealed. Again Mie simulations for the applied Ag NP size distribution are conducted and shown below. The shape of the calculated spectrum is a bit more irregular. This is related to the larger refractive index, which makes the simulation more sensitive to contributions of different particles sizes and results in a substructure of the spectra compared to the case for lower index material. However, the maximum position is in good agreement with the measurement. The absorption peak is again significantly broader, maybe related to interactions of the nanoparticles, that are not taken into account in the calculations.
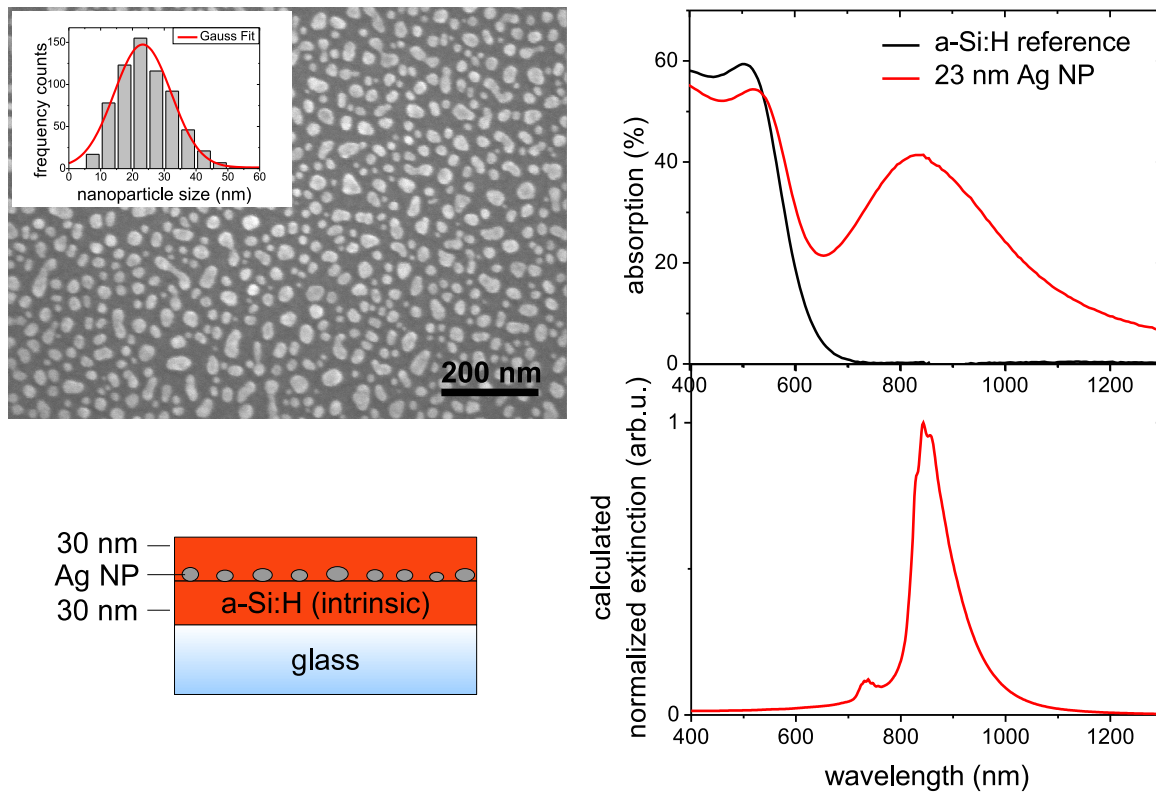
Figure 4.10.: UV/Vis measurements of Ag NPs in an a-Si:H environment. Here silver NPs of (23 ± 9) nm are incorporated in between two 30 nm thin a-Si:H layers. The calculated normalized extinction according the the particle size distribution in an environment of $n = 4$ is plotted below.

4.3. Summary

In this chapter the preparation of thin silver films and nanoparticle agglomerates, deposited by thermal evaporation and sputtering, is investigated. The findings concerning the structural and optical properties of deposited layers and silver island films can be summarized as the following:

- Thermal evaporation of layers with a thickness below 10 nm results in the formation of silver islands. This is most likely related to a Volmer-Weber growth mode of silver. A heat transfer from the evaporation source to the substrate may also contribute but is not the driving force.
- Using sputter deposition also island formation is observed. Under certain sputter conditions it is however possible to deposit dense, closed films.
- The optical response of a closed film considerably differs from island agglomerates. The island films exhibit a spectrally narrow, increased absorption, related to the

LSP resonance of the metal islands. The reflection is decreased over a broad range.

- With the setup for sputtering on large area substrates a deposition with nanometer precision is limited, compared to the small area deposition. However silver layers with a thickness below 10 nm are reproducibly deposited. The large area deposition allows for a better process integration into large area deposition of previous or following layers in device manufacturing.

- The silver films irrespective of deposition conditions and method are crystalline with a dominant orientation of the fcc (111) planes parallel to the substrate.

- Annealing of the silver films forms nanoparticles or results in a better separation of already formed islands. The particle size is dominantly influenced by the deposited silver layer thickness. With increasing layer thickness the formed NPs increase in average size. In addition the NP distribution width increases with growing particle size. AFM scans indicate that the particles are oblate shaped, their height is smaller than their lateral dimension.

- Optical measurements of annealed samples show an absorption peak, related to the LSP resonances of the particles. The position of this resonance is influenced by the size of the NPs as well as the used dielectric environment. An increase of the mean particle size red-shifts the absorption peak. By changing the NP environment from ZnO with a refractive index of n = 2 to a-Si:H with an index of n = 4, the resonance is shifted from about 500 nm to 850 nm. These effects are in agreement with Mie calculations for the used particle distributions in the according environments of ZnO and a-Si:H. Calculated spectra overlap with the measured absorption curves.

The observed optical properties of the silver NPs reveal their resonant absorption behavior due to the LSP resonances. The controlled deposition of known particle sizes in combination with the ability to control the dielectric environment of the NPs gives a tool for manipulating the spectral resonance position. In the following chapter, this is utilized to influence the absorption of a-Si:H solar cells in its low absorption regime. Especially the strong fields in the direct NP environment are of importance in this context.

5. Ag NPs in Thin Film Silicon Solar Cell Devices

The use of plasmonic structures for efficient light harvesting is utilized in several applications. For example the application of plasmonic gold nanoparticles or agglomerates to TiO_2 electrodes for photocatalytic water splitting with visible light [31]. This system is to a certain extend similar to a solar cell since it uses the absorption of light by a semiconductor, with the difference that the excited charge carriers are used to drive the catalysis of water. In the presence of the plasmonic structure on the TiO_2 electrode two main findings can be made that are typical for such systems with incorporated plasmonic structures. For wavelengths at which the absorber (TiO_2) has a strong absorption (i.e. above the bandgap) a lower photocurrent is measured at the electrode. This is related to a reduction of the amount of photons reaching the strong absorbing TiO_2 electrode. In the low absorbing region for longer wavelengths a photocurrent is measured in the presence of the plasmonic structures. The authors correlate this to the electric field enhancement in the neighborhood of strongly absorbing plasmonic structures. In this chapter the effects of resonant absorbing silver island films on the photocurrent generation in a-Si:H are investigated. For this purpose different device structures are prepared. Schottky type samples with NPs in between the front TCO and the a-Si:H absorber as well as structures with NPs embedded inside the a-Si:H layers are investigated. These structures are discussed in the following sections.

To examine the particle morphology inside a-Si:H devices, transmission electron microscopy (TEM) measurements of device cross sections are investigated. This is to check whether the bare island film morphology observed in SEM images has changed during the preparation cycle. In Fig. 5.1 images of a cross section are shown. Here a 100 nm thin a-Si:H n-layer/i-layer system is deposited on an SnO_2 front TCO with a rough surface morphology. The Ag NPs are deposited on top of the a-Si:H layers and are covered with a ZnO back contact. The NP morphology seems not to be affected by the subsequent ZnO deposition. The NPs predominantly posses an ellipsoidal shape, i.e. they are laterally broader than their height. This observation confirms the findings of the AFM measurements of section 4.2. Since the TEM cross section is not truly two dimensional, i.e. it obeys a certain thickness, several planes are observed in the TEM images. In combination with NPs at different heights due to the rough interface (some
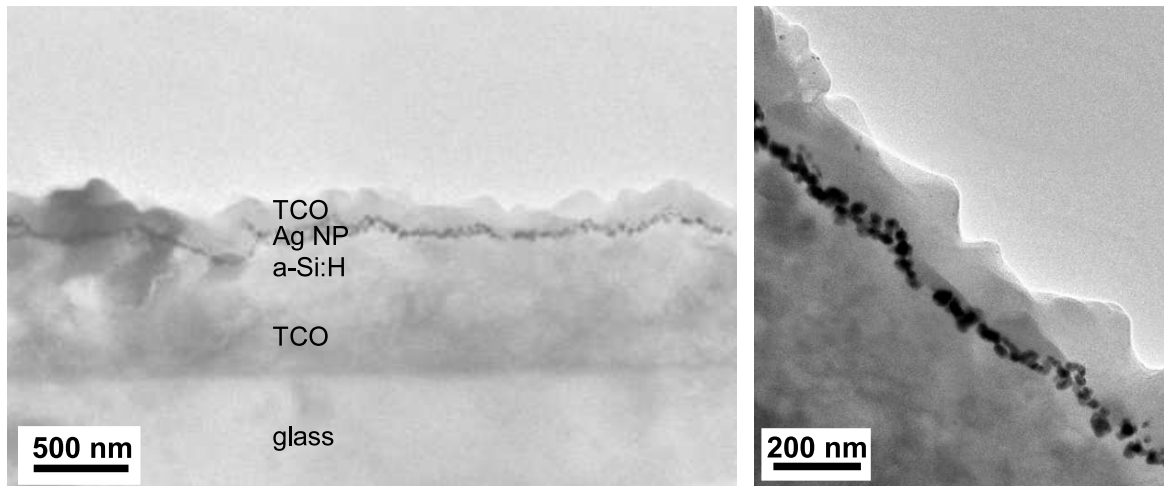
Figure 5.1.: TEM cross section of a thin film solar cell device with incorporated Ag NPs. The NPs are formed from an initial layer thickness of 10 nm, similar to Fig. 4.6 (c). The shown cross section consists of a rough SnO_2 front contact in combination with a 100 nm thin a-Si:H layer on which the NPs are deposited. The NP morphology is not affected by the introduction to the device and the deposition of the following layers. The particles are covered by a ZnO layer that has in principle a thickness of 1 µm. Due to the delicate cross sectional preparation the upper part was removed.

particles are located in the valleys and some on the ridges), the impression arises that the NPs are deposited in different layers above and behind each other. In fact they are well confined at the a-Si:H/ZnO interface. This confirms that the particles do not diffuse through the silicon layers and remain at their initial locations.

It has to be noted that the ZnO back contact or at least most of it was removed by the TEM cross section preparation. Only a 100 nm thick layer remains on top of the particles. However, the region of interest is not affected by this circumstance.

5.1. Basic Device Design

The basic design of devices used for the investigations related to the NPs is shortly presented. In general a-Si:H is used as absorber material, while µc-Si:H is applied in one special case at the end of the chapter. In contrast to standard a-Si:H solar cells that posses an absorber layer thickness of 250-300 nm, here a-Si:H layer thicknesses between 30 to 100 nm are applied. The very thin intrinsic layer thickness allows for a strong electrical field which depends according to $E = (U_D - U)/d_i$ [1] on the built-in potential U_D, the applied voltage U and inversely on the thickness d_i of the intrinsic

---

[1]This is a rough estimation, since U_D is affected by the internal field distribution. Especially when defects are incorporated by the NPs.

absorber layer [190, p. 29]. In addition the thin absorber layer allows to investigate effects according to plasmonic absorption for long wavelength light more efficiently, since such thin absorber layers only weakly absorb light above 700 nm.

The effects of plasmonic excitation on the solar cell device behavior should be investigated without the influence of additional light trapping by rough interfaces. This is the reason why in most structures smooth interfaces are applied. The interface roughness is in general determined by the front TCO. Using a flat sputtered ZnO:Al front TCO, the following interfaces are also flat. Most often the NPs are deposited in direct contact to the absorber layers in order to investigate the influence of the resonantly enhanced near fields around the nanoparticles on the photocurrent generation. Either the particles are located between the absorber and the front contact or are deposited within the absorber layer. The specific device configurations are shown in the following sections alongside their according measurements.

The back contact of all devices is composed of an 80 nm AZO layer and a 100 nm silver reflector, both deposited by sputtering. Devices with an active cell area of $1\,cm^2$ are defined by laser scribing. Cells are prepared at 13 different positions over the $1.4\,m^2$ sample (see Fig. 3.14). At each of these 13 positions 8 single cells of $1\,cm^2$ active cell area are defined.

The Ag NP formation on small samples also require the large area deposition facilities for subsequent layer deposition. This bears some problems. Especially the deposited layer thickness can vary significantly between different samples. In PECVD deposition for example, they have to be placed on a carrier substrate leading to a reduced distance of the sample surface to the upper electrode. This changes the conditions at the sample surface and alters deposition rates compared to a standard process. Especially due to the sharp edges of small samples the flux of precursor gases or the plasma conditions are changed.

5.2. Influence of Ag NPs on electrical device properties

The structures discussed in this section are samples in the TCO/AgNP/i-n (or i-p)/TCO/Ag-reflector configuration (FIG. 5.2 (a)). The absorber layers are composed of a-Si:H i-n or i-p layers with intrinsic layer thicknesses of only 30 nm with silver NPs placed at the i-layer/TCO interface. This structure is applied in order to extract the charge carriers from the NP environment as efficiently as possible due to the direct contact to the TCO. Ag NP dispersions with a mean particle diameter of 23 nm (Fig. 5.2 (b)) are applied to these devices. This particle distribution was already discussed in Fig. 4.7 and 4.8 (a).
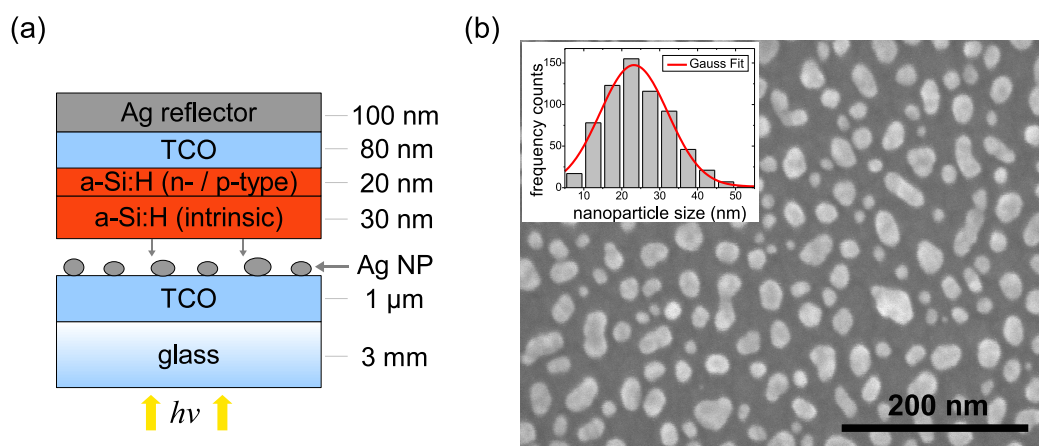
(a)

(b)

Figure 5.2.: (a) Design of a-Si:H i-n and i-p Schottky type devices. (b) SEM image and size distribution histogram of Ag NPs with (23 ± 9) nm average diameter resulting from an initial silver layer thickness of around 5 nm.

Fig. 5.3 shows the current voltage characteristic in the dark and under illumination of representative i-n and i-p devices. Due to the different polarity of the devices the ordinate and for the illuminated case also the abscissa is inverted for the i-p device. This allows for a better comparison of the curves. It has to be noted that the various cells on the large area substrate show a broad scattering of values. This is connected to different reasons, homogeneity of deposition for the different layers, shunting of cells by dust particles or variations in accuracy of laser scribing for different cells. These problems can negatively affect the device quality.

The fist remarkable observation on the dark current characteristic (Fig. 5.3 (a)+(c)) is the exponential behavior, illustrated by the linear slope in the logarithmic plots. This diode characteristic is not self-evident for these ultrathin device thicknesses in the presence of only one doped layer (n or p).

The exponential progress is affected for higher voltages by the series resistance R_S and results in a decreasing slope. Owing to the thin i-layers and the corresponding low shunt resistance, the dark current is quite large compared to standard p-i-n diodes.

The incorporation of Ag NPs to both types of devices increases the dark current for low and high voltages. For low voltages this might be related to an increase of the shunt probability caused by the NPs in the thin absorber layer system. However, for the i-n device the exponential behavior is preserved. The collection of charge carriers is therefore not strongly affected. The increased dark current, due to the NPs, in the exponential regime is an indication for an increased recombination. In contrast for the i-p device, the NPs strongly alter the diode characteristic. The devices are shunted and show an ohmic (non exponential) characteristic.
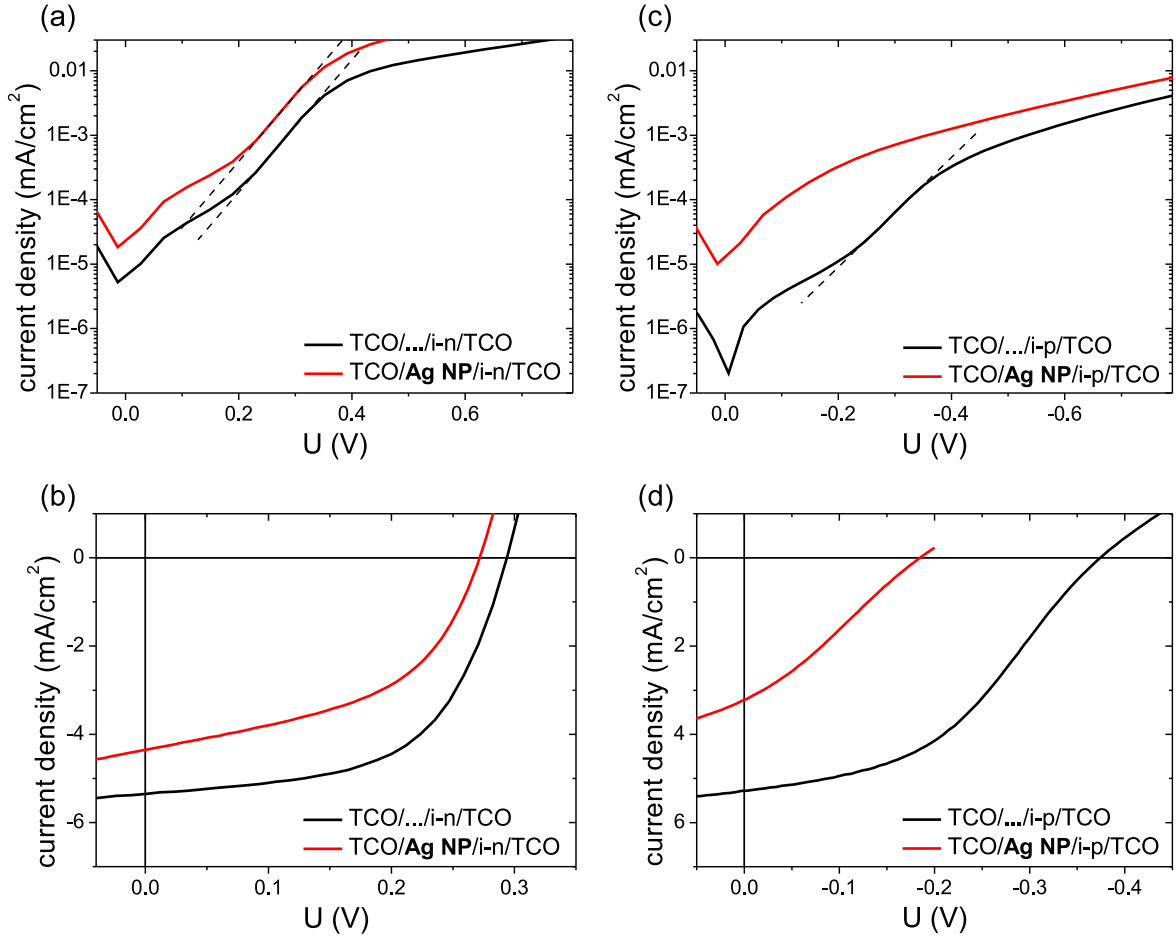
Figure 5.3.: Influence of Ag NP incorporation on I-V curves for a-Si:H i-n and i-p devices. IV curves for the i-n devices are shown (a) in the dark and (b) under illumination as well as for the i-p devices (c) in the dark and (d) under illumination.

Under illumination (Fig. 5.3 (b)+(d)) the curves for devices without NPs do not show an ideal behavior compared to standard p-i-n devices. Both types of devices have low fill factors, open circuit voltages V_{OC} and short circuit current densities j_{SC}. The i-p device in addition exhibits an S-shaped curvature indicating a high series resistance R_S and contact problems. The shown device has a series resistance of $R_S = 51.6\,\Omega cm^2$ while the mean value measured for all parallel processed samples is $27\,\Omega cm^2$. This might be related to the ZnO p-layer contact problem [191]. The low short circuit current densities around $6\,mA/cm^2$ are related to the thin absorber layer thicknesses. Hence a smaller portion of the incident photons is converted to electron hole pairs. The small V_{OC} of about $0.3\,V$ is caused by a smaller potential separation of the contact layers, because of the presence of only one doped layer. This results in a smaller splitting of the quasi Fermi levels and a smaller V_{OC} (see section 2.1.5). The smaller j_{SC} in

addition leads to a decreased V_{OC} (see equation 2.10). Due to these limitations, the overall efficiency is limited to about 1 %.

The incorporation of NPs to the i-n device alters the current voltage characteristic. All quantities FF, j_{SC} and V_{OC} are reduced. For j_{SC} this is an optical consequence of the Ag NPs itself. They are placed in front of the active layer and absorb a certain portion of the incoming light. This parasitic absorption lowers the amount of energy reaching the a-Si:H absorber leading to a reduced j_{SC}. However the ability of charge carrier collection is demonstrated with this device. In the case of i-p this is a bit more complicated since the performance is strongly affected by the NPs. Here beside the reduced j_{SC}, the FF and V_{OC} are drastically decreased due to the shunted cell. Concerning the solar cell efficiency, the incorporation of NPs does not yield a beneficial behavior. However, the optical response of the particles strongly varies with respect to the spectral region. These electrical measurements do not reveal the response with respect to spectral charge carrier generation and the influence of the nanoparticles on it. Therefore the optical and optoelectronic characteristics are investigated in the following.

5.3. Influence of Ag NPs on the Spectral Response of a-Si:H Devices

The optical absorption for the previously discussed i-n and i-p structures are shown in FIG. 5.4 (a)+(c), respectively. As pointed out in section 3.2.6, the kinks observed in all UV/Vis curves at around 860 nm are measurement artifacts caused by switching between the detectors of the UV/Vis instrument. The absorption is modulated by thin film interferences at the different layers of the device. For short wavelength only the front TCO contributes to the fringes, because the a-Si:H layers absorb strongly in this regime. Above 600 nm where the absorption decreases, the interferences are caused by the complete device and reflections at the metal back reflector. The contribution of different layers of the stack complicate a simple assignment of fringes. Slight thickness variations of contributing layers shift the fringe pattern. In order to discuss effects in a reliable manner, measurements from different sample positions are averaged. Therefore the curves are less sensitive with respect to interferences. In the measurements (FIG. 5.4 (a)+(c)) the strong absorption regime of a-Si:H is observed below 550 nm. With incorporated NPs the absorption is significantly larger in this regime. This is related to a reduced device reflection, i.e. a better in-coupling of light at the TCO/i-layer interface caused by the NPs.

Above 600 nm where the a-Si:H absorption decreases (because of the a-Si:H bandgap) the incorporation of Ag NPs leads to a broad enhanced absorption for both types of devices. The absorption is increased due to the LSP resonances to about 40 % for the

i-n and 60 % for the i-p device. However, whether the observed absorption maxima directly indicate the LSP resonance position is questionable. They are modulated by thin film interferences. To a certain extent the position of the absorption maximum will be shifted or distorted by this effect. The positions of the observed maxima are
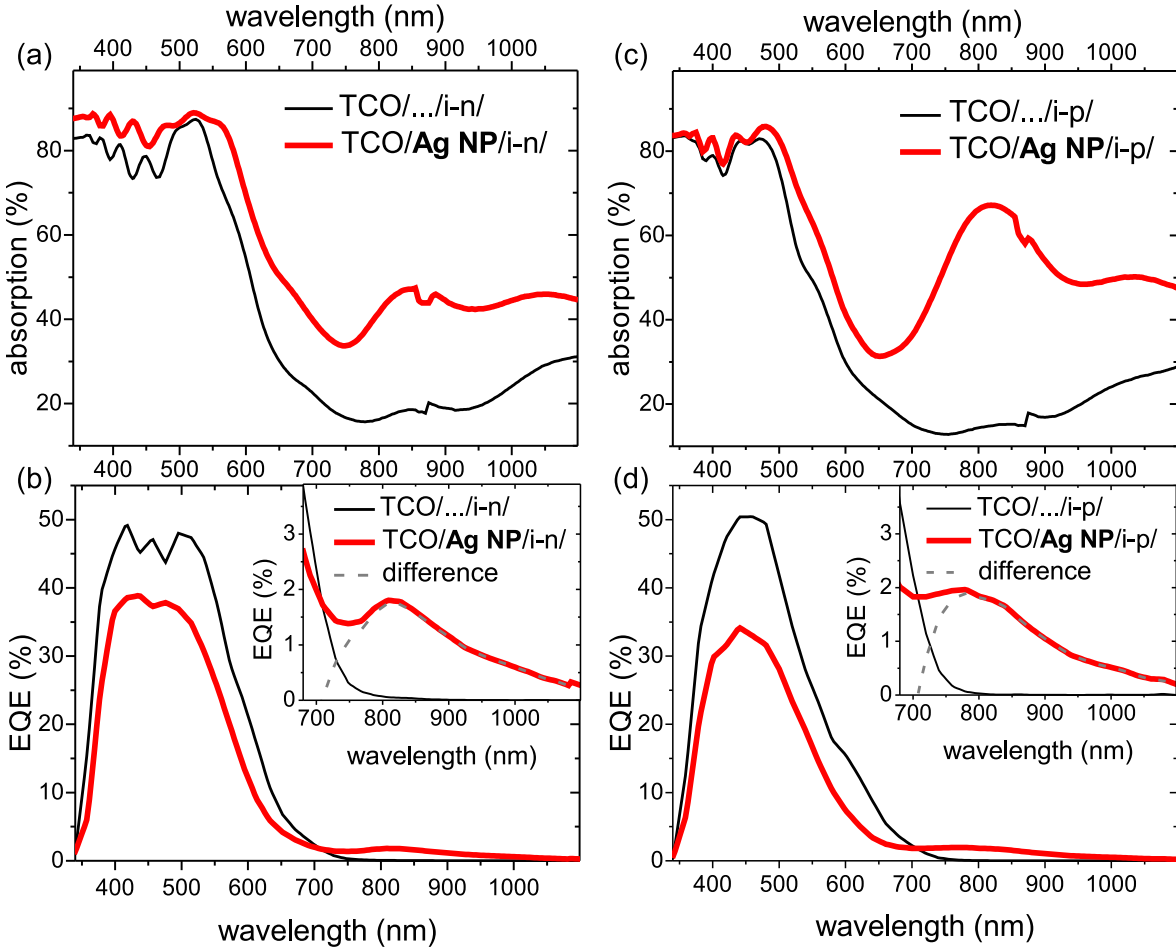
Figure 5.4.: Optical absorption and external quantum efficiency of (a)+(b) a-Si:H i-n devices (TCO/i-n/TCO/Ag reflector) as well as (c)+(d) i-p devices (TCO/i-p/TCO/Ag reflector) shown in FIG. 5.2 (a) with (thick red line) and without (thin black line) incorporated Ag NPs of 23 nm average particle diameter in between the front TCO and the a-Si:H i-layer. The insets in (b) and (d) show the EQE behavior in the NIR region with an enlarged ordinate scale.

slightly different for the different devices. The i-n device has a maximum at around 850 nm. The maximum for the i-p case is slightly blue shifted to 815 nm. The different peak amplitudes for the i-p and i-n structures might also be related to the interferences. Since the enhanced absorption is caused by the plasmon resonances, the absorption will be stronger when an interference maximum occurs close to the actual LSP resonance

position. For the used particle distribution in a silicon environment the LSP resonance is placed at about 850 nm (see Fig. 4.10). Because here the NPs are also influenced to a certain extend by the adjacent ZnO layer with a lower refractive index, the resonance might be blue shifted towards 800 nm.

The external quantum efficiency is shown in Fig. 5.4 (b)+(d). Here the amplitude of the EQE signal is limited to around 50 % due to the reduced absorber layer thickness, as already indicated by a low short circuit current density in section 5.2. In the presence of Ag NPs two main observations are made: (i) for wavelength below 700 nm the EQE signal is reduced, (ii) above 750 nm, i.e. for photon energies below the a-Si:H bandgap ($\approx 1.7\,\mathrm{eV} \cong 730\,\mathrm{nm}$) a significant EQE signal is observed. The decreased signal for energies above E_g originates in the damped plasmon oscillations of the NP electrons that lower the amount of transmitted energy to the absorber. Because a-Si:H strongly absorbs in this regime, the charge carrier generation is efficiently. If less electromagnetic radiation is transfered to the absorber the EQE signal decreases. A second reason for a decreasing EQE is the creation of electronic defects by the NPs that cause recombination of electron hole pairs. The influence of the NPs on this part of the spectrum are discussed in more detail in section 5.5.6.

For wavelength above 750 nm no EQE signal is measured for the bare a-Si:H devices, related to the bandgap. Light with a lower energy is not able to elevate electrons from the valence to the conduction band. In contrast in the presence of Ag NPs a significant EQE signal is observed, as shown in more detail in the insets in FIG. 5.4 (b) and (d). This signal is related to transitions caused by photons with sub-bandgap energies. For many samples a peak like characteristic is observed, while others show a broad increase. The shown measurements are again averaged over different sample positions to be less sensitive to interferences. Because a-Si:H does not exhibit an EQE signal in this sub-bandgap regime, the measured signal is a superposition of the a-Si:H and the NP induced contributions. By subtracting the a-Si:H reference from the total signal, the NP induced contribution remains. This is indicated by the dashed curves. For both types of devices a peak like characteristic is observed that extents up to 1100 nm and even further. The peak maximum is centered at about 790 nm (for i-p) while in accordance to the absorption measurement, the maximum is red shifted to about 815 nm for the i-n devices. The agreement to the enhanced absorption, observed in the same region, suggest a major impact of the LSP resonances on the development of the observed EQE signal. The EQE peak is shifted by changing the LSP resonance position, i.e. the average NP size. This will be discussed in more detail in section 5.5.2.

Microcrystalline silicon (µc-Si:H) is capable of absorbing light in the interesting NIR regime, where the increased photo absorption is observed. The incorporation of the silver NPs to the a-Si:H devices could in principle create a µc-Si:H phase due to metal induced recrystallization. For Ag/a-Si systems a crystallization of the amorphous phase
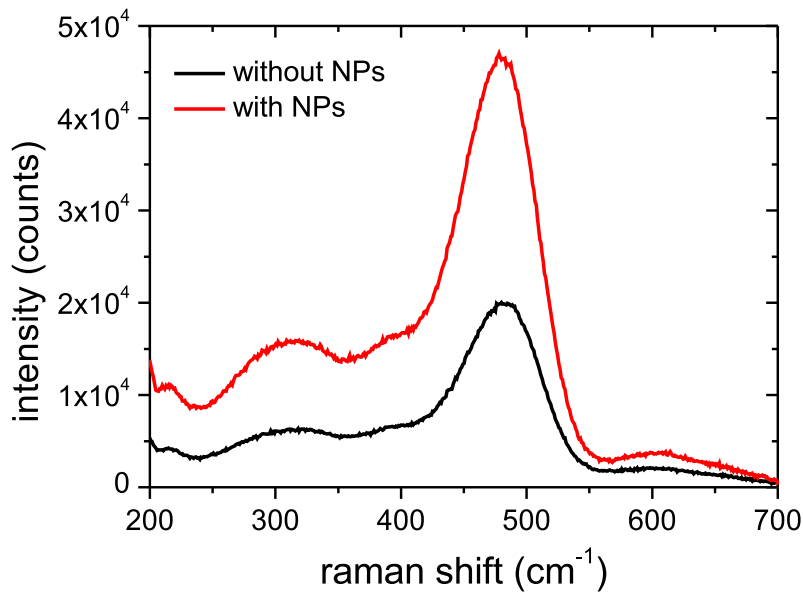
Figure 5.5.: Raman spectra of a-Si:H samples with and without embedded Ag NPs.

is observed at annealing temperatures of about $400\,^\circ$C [192]. The temperatures used here are well below this value, however it cannot be excluded at first glance. For this reason Raman spectroscopy is executed for a-Si:H layers with and without incorporated Ag NPs. Measurements are shown in Fig. 5.5. Both samples exhibit a peak at $490\,\mathrm{cm}^{-1}$ characteristic for a-Si:H. No indication for the existence of a µc-Si:H peak at $520\,\mathrm{cm}^{-1}$ is found in the presence of the NPs. However the amorphous peak amplitude is increased. This is related to the surface enhanced Raman signal due to the presence of the Ag NPs. It demonstrates, that the NIR photocurrent can not be attributed to the creation of µc-Si:H material.

5.3.1. Existing Model for the Metal NP Induced Sub-Bandgap Response

The photocurrent for energies smaller than the a-Si:H bandgap was explained by Moulin et al. [37] for a-Si:H on the basis of Westphalen et al. [33] who could observe similar effects for silver NPs in organic solar cells. Fig. 5.6 illustrates the basic explanation model for both types of configuration independently. The model is based on the fact that the TCO/AgNP/a-Si:H i-layer system forms a Schottky contact. For a device in the i-p configuration where transport is dominated by holes, an electron can be elevated from the valence band to or above the Fermi level of the contact. The hereby generated hole is transported by the built-in field to the p-layer.
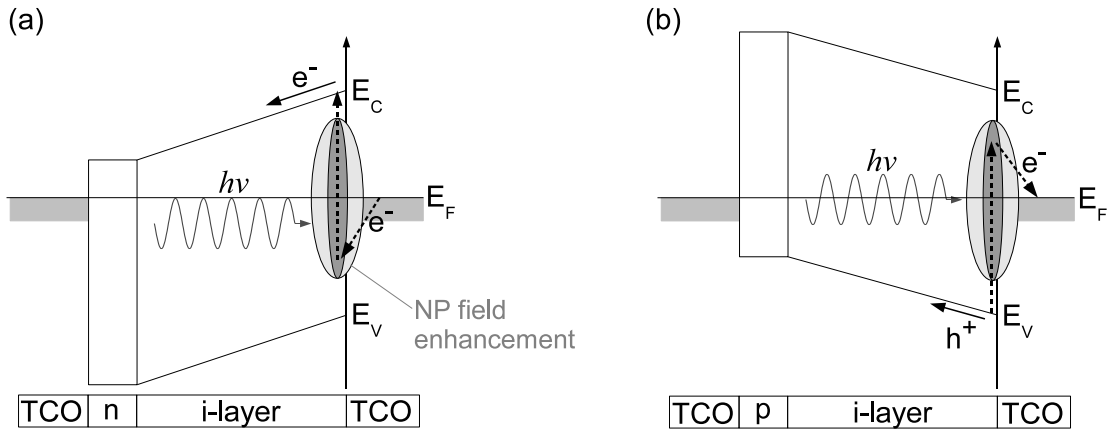
Figure 5.6.: Generation model for sub-bandbap excitation induced by LSP resonances of Ag NPs in (a) i-n and (b) i-p Schottky type structures. The excitation to or from the band edges into the Schottky contact and injection of electrons by the adjacent TCO is illustrated. On the basis of [33] and [37] and [193, p. 101].

For an i-n device, an electron is excited to the i-layer conduction band out of the defect states or by direct photoemission from the silver NP. The excited electron is driven by the built-in field to the n-layer. The direct contact to the TCO allows electron supply after the generation process. The generation process is enhanced due to the increase of the electromagnetic field in the surrounding (or inside) of the NPs caused by the LSP resonance. The authors also claim that states in the vicinity of the NPs could possibly be the origin for photo excitation to the conduction band.

Beside this explanation phonons interacting with the Ag NP/TCO interface states could be of importance [194, 195]. This interaction depends beside the NP size dispersion on the inter-particle distances.

5.4. Origin of participating inner gap states

In the previous section it was demonstrated that a significant EQE signal is measured for excitation energies smaller than the a-Si:H bandbap, when Ag NPs are incorporated in-between the intrinsic absorber and the TCO contact layer. Some kind of states must be present, that are coupled via the LSP resonances of the particles to the band edges of the a-Si:H. The question whether these states are correlated to the a-Si:H material in the form of defect states, the TCO or the interface between them is not yet answered. The nature and origin of participating states in the generation of the electrons and holes is an important issue, that will be investigated in the following. It is of special importance when dealing with nanoparticles inside the intrinsic layer of n-i-p device

structures where no direct contact to the TCO layer is available for charge compensation (section 5.4.3).

5.4.1. Ag NPs Embedded in ZnO

Applying the i-n devices used in the previous section and covering the NPs deposited on the ZnO front contact with an additional 8 nm thin ZnO layer separates them from the a-Si:H and the TCO/a-Si:H interface (Fig. 5.7 (a)). This allows to investigate the influence of NPs on the EQE (Fig. 5.7 (b)). In the visible range, especially between 500 and 700 nm the introduction of the additional ZnO layer decreases the EQE (blue curve). This could be related to the shift of the Ag NP LSP resonance inside the ZnO material compared to particles at the interface where the dielectric environment is dominated by a-Si:H. For a ZnO environment with n=2 the LSP resonance is shifted approximately to 400 nm (see section 2.4.2), enhancing the parasitic absorption. This decreases the amount of energy reaching the absorber for this wavelength regime. The NIR EQE signal for the Ag NP device (red curve) is strongly decreased by the additional ZnO layer covering the NPs (blue curve). A difference to the device without NPs (thin black curve) can not be observed even with the enlarged ordinate scale. Only by plotting the curves to a logarithmic scale a slightly higher signal is found for wavelength above 900 nm.

The optical absorption of these devices (Fig. 5.7 (c)) indicate a decreased absorption in the interesting range between 750 and 1000 nm for the addition of the intermediate TCO. However the strength of this decrease does not explain the strong losses observed in the EQE measurement, since the absorption is still enhanced compared to the reference device without NPs. Even a 8 nm thin ZnO layer covering the NPs vanishes the NIR EQE effect.

This behavior is also investigated for samples deposited in the opposite layer configuration with NPs at the back TCO prepared on $(5 \times 5)\,cm^2$ substrates (Fig. 5.8). Again a significant NIR EQE signal is observed in the presence of Ag NPs. Introducing a thin ZnO layer prior to Ag NP deposition leads to the decrease of the signal. Samples with ZnO layer thicknesses between 3 nm and 20 nm are prepared. It turns out that even the thinnest layer is sufficient to vanish the Ag NP induced effect. Increasing the layer thickness has no further influence.

The decrease of the NP induced NIR photocurrent by the introduction of a thin TCO layer was already reported by Luo et al. [38]. They attribute this either to the confinement of the electromagnetic field enhancement to the ZnO layer, resulting in the fact that no field enhancement is present in the a-Si:H or at least it is not strong enough to observe an effect. As the field enhancement is confined to the close

(a)

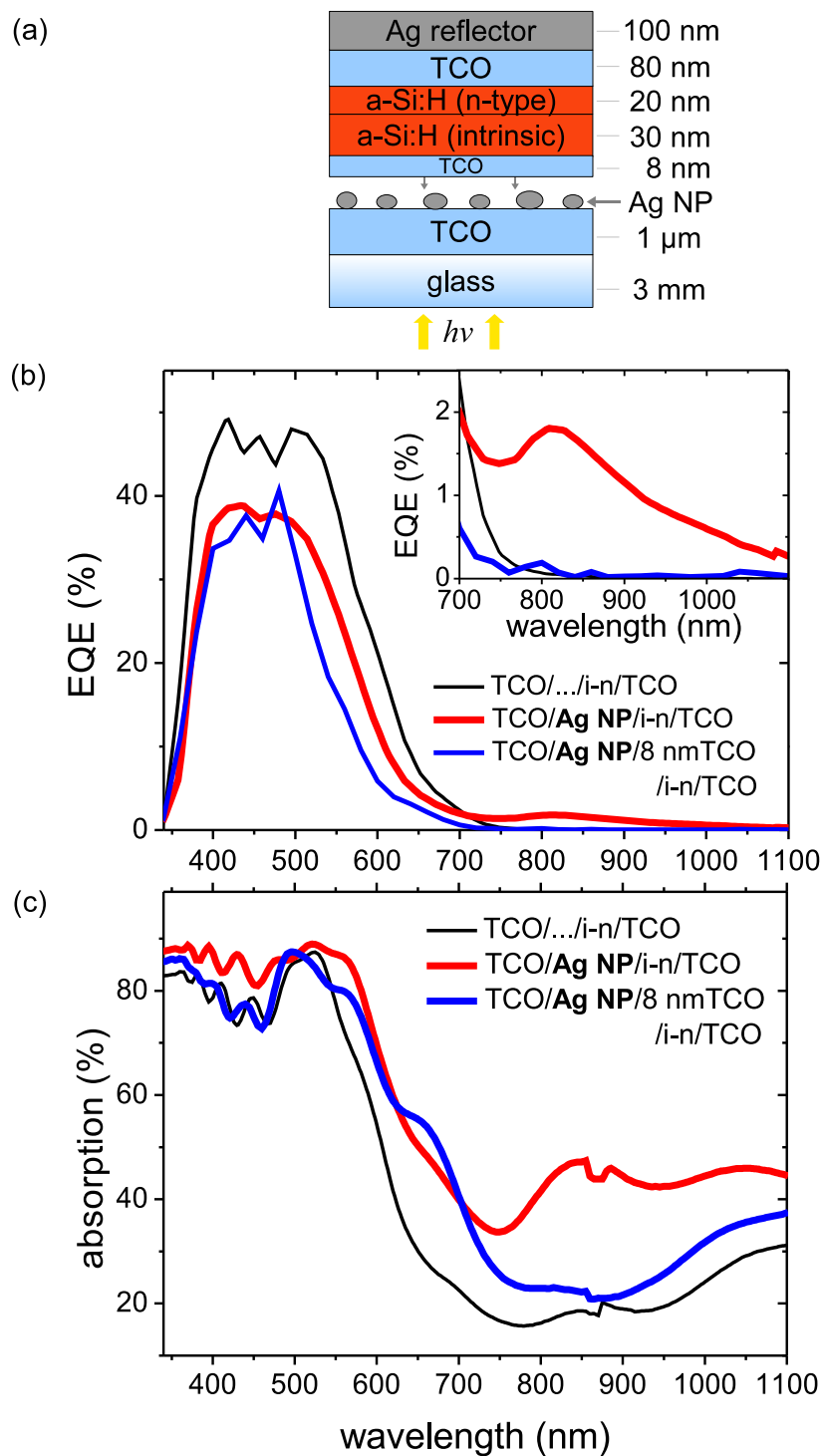|	
Ag reflector	100 nm
TCO	80 nm
a-Si:H (n-type)	20 nm
a-Si:H (intrinsic)	30 nm
TCO	8 nm
Ag NP	
TCO	1 µm
glass	3 mm

$h\nu$

(b)

(c)

Figure 5.7.: (a) Design of i-n device with Ag NPs separated by a thin AZO layer from the TCO/a-Si:H interface. (b) EQE and (c) optical absorption of devices with NPs and an additional 8 nm thin intermediate ZnO layer.
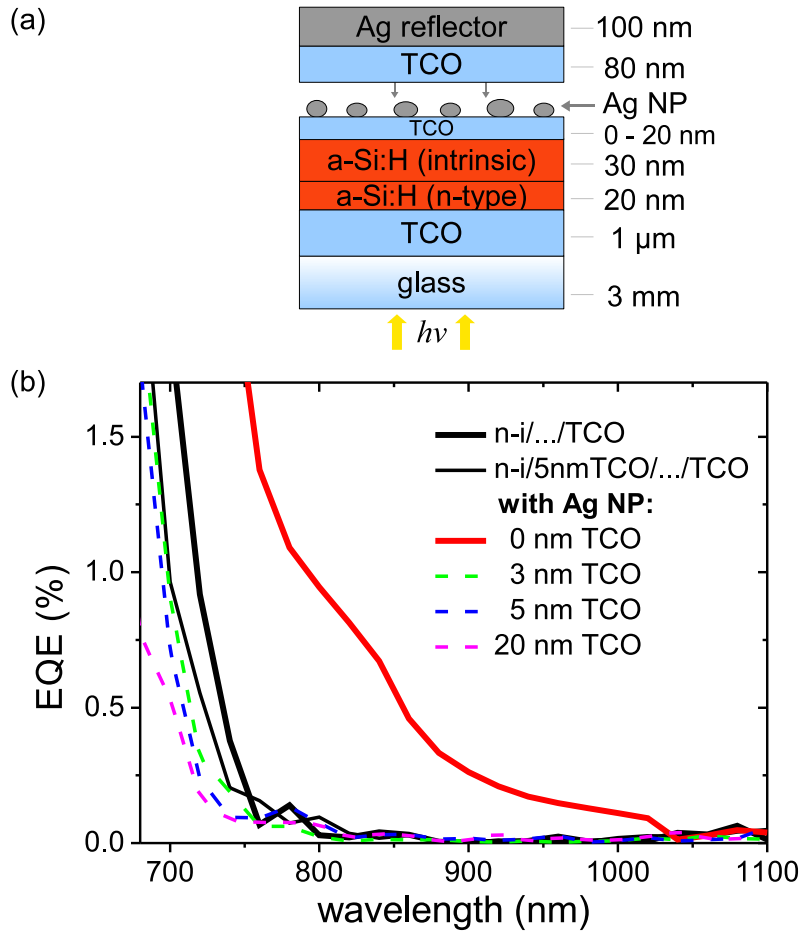
Figure 5.8.: (a) Design of n-i device with Ag NPs separated by a thin AZO layer from the TCO/a-Si:H interface. In this case the NPs, intermediate TCO and back contacts have been prepared on $(5 \times 5)\,\text{cm}^2$ substrates. (b) EQE of devices with NPs and an additional intermediate ZnO layer, illustrated only for the NIR range. The intermediate ZnO layer thickness is varied between $3\,\text{nm}$ and $20\,\text{nm}$. Even the thinnest layer completely decreases the Ag NP induced EQE signal.

vicinity of the NPs and decreases rapidly with distance [196] [28, p. 235-236], even a few nanometer separation from the absorber could be sufficient to reduce the influence on charge carrier generation. Further explanations could be the larger ZnO bandgap which requires higher excitation energies to elevate charge carriers to the conduction band or a shift of the LSP resonance towards higher energies that decreases the enhancement in the NIR. However, it can be concluded that the ZnO itself is not responsible for the NP induced NIR effect. This is supported by the observation of the effect in devices where the ZnO is replaced by an SnO_2 front contact, as demonstrated in section 5.5.3. The effect is hence independent of the TCO material and a direct contact of the NPs to the a-Si:H is necessary.

5.4.2. Ag NPs Embedded in Amorphous Silicon

While the TCO is not responsible for providing states for excitation of charge carriers, the role of the a-Si:H/TCO interface is not yet understood. For this purpose a device in the opposite n-i layer sequence (Fig. 5.9 (a)), in combination with a sputtered a-Si layer is used to separate the NPs from the TCO. The sputtering of silicon has the advantage over a PECVD deposition that Ag NP preparation and a-Si deposition is performed in the same chamber without the influence of a vacuum break.This can be of importance and will be discussed in section 5.5.4. The a-Si sputtering includes the disadvantage of a defect rich layer caused by the lack of hydrogen during the sputtering process.

The EQE measurements (Fig. 5.9 (b)) indicate that the additional a-Si layer of 20 nm thickness has nearly no influence for short wavelengths (black dashed line), in contrast to the long wavelength regime above 500 nm where the signal is decreased. Short wavelength light is absorbed in the first few nanometers of the a-Si:H absorber, due to the strong absorption coefficient. Light with wavelengths above 500 nm reaches the sputtered a-Si layer where it is partly absorbed. The hereby generated charge carriers directly recombine due to the high defect density in the sputtered a-Si layer and cannot contribute to the EQE. Compared to the reference device (without a-Si and without NPs), the additional absorption in the sputtered a-Si layer results in a decreased contribution of light, that is reflected at the metal back contact and enters the absorber layers a second time.

Incorporation of Ag NPs to devices with sputtered a-Si (orange dashed and solid line) does not alter the trend for the visible range. In contrast to the NIR range, where two main observations are made. First, a photocurrent signal is observed in the presence of NPs. Compared to the NP device without the additional a-Si layer (shown for comparison) this signal is weaker but substantially. Second, the EQE signal amplitude is only weakly affected by the thickness of the a-Si layer. By changing the thickness from ≈ 20 nm to ≈ 40 nm the signal is only slightly decreased. This tendency holds for all measured samples that are not explicitly shown.

The fact that an NIR EQE signal is measured for devices with Ag NPs separated from the a-Si:H/TCO interface also excludes states at the TCO/a-Si:H interface as origin for the sub-bandbap excitation. Involved states must be provided by the a-Si:H itself or the Ag NPs/a-Si:H system. The second finding of a signal amplitude that is only slightly dependent on the thickness of the covering a-Si layer points to the need for a modification of the model explained in Fig. 5.6. The direct injection of electrons/holes by the adjacent TCO is not conform to the observations for the discussed device structures. In the model assumption the incorporation of an additional a-Si layer in-between the TCO and the NPs is equivalent to a tunnel barrier. The increase of the barrier width would lead to an exponential decrease of the tunnel probability or
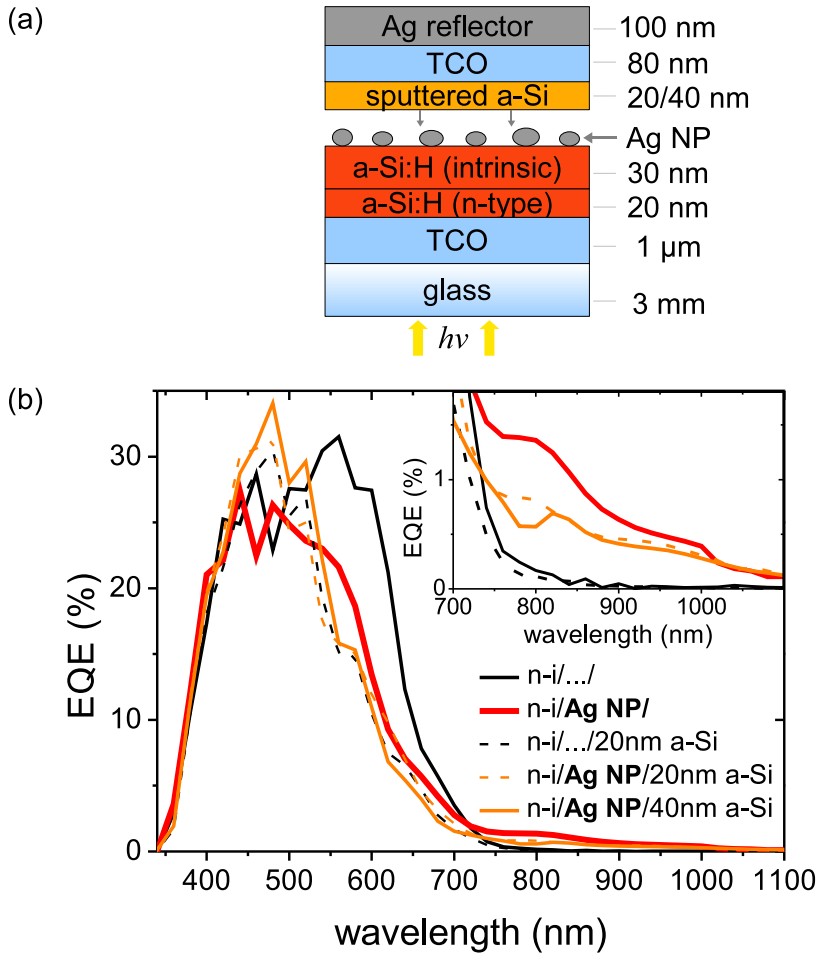
Figure 5.9.: (a) Design of n-i device with Ag NPs separated by a thin sputtered a-Si layer from the TCO/a-Si:H interface. Layer thicknesses of 20 and 40 nm are used. (b) EQE of devices with NPs and a variation of intermediate sputtered a-Si layer. The additional layer has a decreasing influence, a significant EQE signal can thus be observed.

transmitted charge carriers. A drastic decrease of the measured EQE signal would be the result. This conflict is tested by incorporating Ag NPs into the intrinsic layer of thin a-Si:H n-i-p devices (section 5.4.3). In this configuration the charge compensation can definitely not be provided by the TCO. For such a structure an electron must be transported to the n-contact in combination with a hole transported to the p-contact in order to provide charge separation.

5.4.3. Ag NPs Inside the Intrinsic Layer of a-Si:H n-i-p Devices

FIG. 5.10 (a) shows the schematic design of a-Si:H n-i-p devices with Ag NPs inside the intrinsic layer. The samples are fabricated in the TCO/n-i/AgNP/i-p/TCO/Ag-

reflector configuration by adopting the thin i-layer thicknesses of the individual i-n and i-p devices. This enables the use of a strong built-in field for the extraction of charge carriers from the NP vicinity.

The measured EQE of n-i-p devices with integrated Ag NPs is plotted in FIG. 5.10 (b). A curve for a cell without NPs is shown as reference. The signal amplitude is less than 20 % at maximum position for samples with and without NPs. This low signal, compared to i-n (and i-p) devices, is likely assigned to the interruption of a-Si:H i-layer deposition.[2] This creates defects and causes charge carrier recombination. By incorporation of Ag NPs a blue shift of the maximum EQE signal position is observed. Hence for wavelengths below 500 nm a larger signal is measured for the device with NPs. The reason for this could be a modification of the internal field distribution by deep defects [197], caused by the introduction of the metal NPs. Therefore charge carriers generated near the n-layer, i.e. by excitation with the blue part of the spectrum, are collected more efficiently. For wavelength above 550 nm the complete absorber is penetrated by light and therefore charge carriers are generated in all parts of the absorber. The device with NPs shows a lower signal because of damping losses and a lower amount of transmitted energy to the rear part of the device. Recombination at defects caused by the Ag NPs is a further reason for the decrease.

The inset in FIG. 5.10 shows the NIR range for wavelengths between 700 and 1100 nm drawn to a larger scale. Above 800 nm, once again no signal is measured for the device without NPs. In opposition, a significant EQE signal is observed between 750 nm and 1100 nm in the presence of Ag NPs. The difference signal again shows a maximum near to 800 nm and decreases towards lower energies. The magnitude is slightly lower than for the i-n and i-p devices (Fig. 5.4), however it is in the same order. This points out, that the observed effect for the n-i/AgNP/i-p system does not originate from a two photon process with a fast decaying intermediate state. Since this would result in a much weaker signal. As further assumed in section 5.4.2 states at the Schottky barrier can be excluded for these devices. Instead the effect measured for these and all other types of devices has its origin in the amorphous silicon absorber. Therefore, the model for sub-bandgap excitation has to be modified in order to explain the observed effects. This will be motivated in the following section.

5.4.4. Modified Model for the Ag NP Induced Sub-Bandgap Response

The incorporation of the Ag NPs forms internal interfaces inside the a-Si:H network (FIG. 5.11 (a)). At these interfaces real surface defects, with energetic positions within

---

[2]It has to be noted, that for the n-i/.../i-p layer system might be suspect to collection problems, already without NPs, as discussed later.

(a)

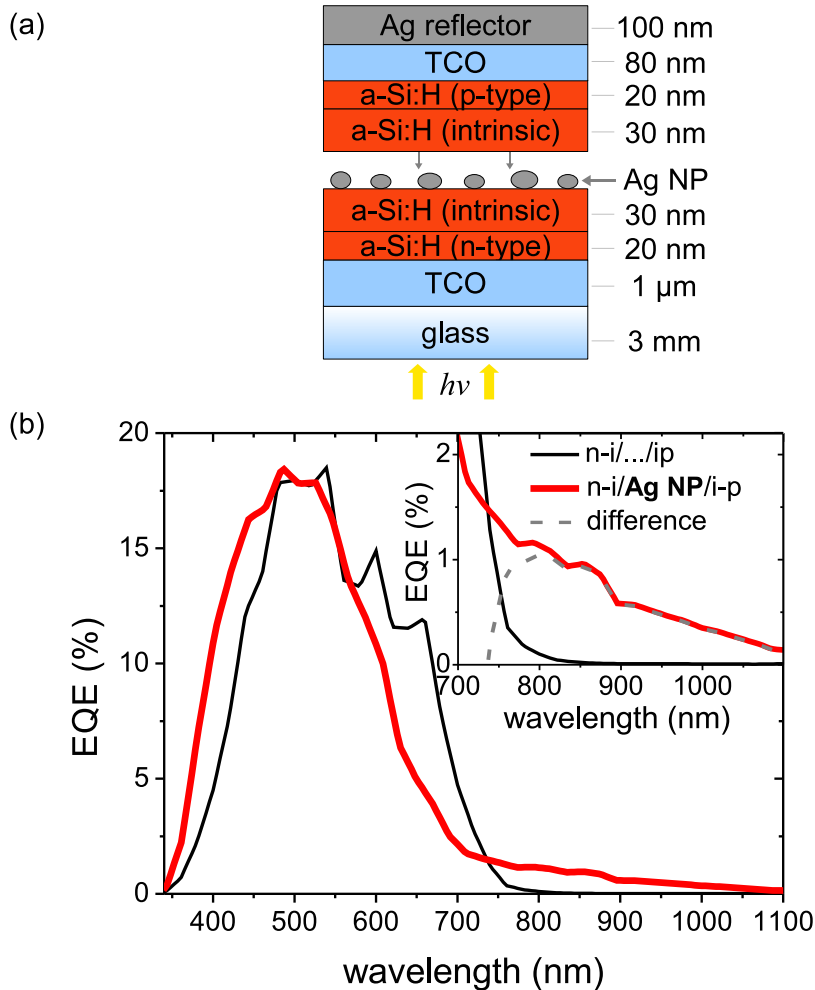|	
Ag reflector	100 nm
TCO	80 nm
a-Si:H (p-type)	20 nm
a-Si:H (intrinsic)	30 nm
Ag NP	
a-Si:H (intrinsic)	30 nm
a-Si:H (n-type)	20 nm
TCO	1 µm
glass	3 mm

hv

(b)

Figure 5.10.: (a) Device design of thin a-Si:H n-i-p devices with Ag NPs inside the intrinsic layer, in the TCO/n-i/AgNP/i-p/TCO/Ag-reflector configuration. The layer stacks are combined from the n-i and i-p devices discussed before. (b) External quantum efficiency of n-i-p devices with (thick red line) and without (thin black line) Ag NPs inside the i-layer.

the bandgap, are created [198]. In analogy to the case of crystalline silicon (c-Si), where silver atoms create impurities in the silicon network, this could also be true for a-Si:H. Silver levels inside the c-Si bandgap with a distance of around $0.3\,\text{eV}$ to the band edges are reported in literature [199]. The energetic positions derived from the EQE peaks of the i-n and i-p structures as well as those found for NPs inside the i-layer of n-i-p devices agree with these values. In addition to the existence of defects in the amorphous silicon the strength of the observed photocurrent is influenced by the LSP resonances of the NPs. The defects are located in the direct vicinity to the resonant absorbing Ag NPs and the associated strong electromagnetic fields. Since the generation rate G is proportional to the square of the electric field $G \propto |E|^2$ [31, 200], the transition rate to or from the defect states is increased by orders of magnitude. The photocurrent is therefore enhanced, when the plasmon resonance and the defect transition energy overlap.

The schematic generation mechanism is illustrated in FIG. 5.11 (b). Here a simplified energy diagram for an n-i-p device is shown. Ag NPs incorporated in the center or the intrinsic layer create defect levels (dashed parallel lines) and provide strong electromagnetic fields due to the LSP resonances (gray areas). Depending on the involved transport mechanism (electron transport for i-n or hole transport for i-p) the according defect states near the band edges, below or above E_F, are addressed. States below E_F are occupied by electrons while states above E_F are not. As in the case for the i-n layer stack, electrons from occupied states can be elevated to the conduction band by a photon with sub-bandgap energy. The electron in the conduction band will be transported to the n-contact. In the same manner as for the i-p layer stack, electrons from the valence band can be excited to empty states above E_F. The remaining holes in the valence band will be driven by the built-in field to the p-layer. Contrary to the need of a Schottky contact for the supply of charge carriers, this model includes a thermal activation step to complete the transition between the band edges. Localized defect states close to the conduction band are in thermal contact to it and have a non zero probability to be excited by thermal activation [76, 202][59, p. 151]. At room temperature the thermal activation energy is in the order of $0.2\,\text{eV}$ [202].

Similar to the thermal activation mechanism, Antolin et al. [67] propose a thermal escape of electrons from excited electrons in quantum dot states to the conduction band. In section 2.1.8 the *Impurity Photovoltaic Effect (IPV)* that utilizes defect levels in the semiconductor host material for transitions between the band edges was discussed. The n-i-p device with Ag NPs is a proof for the use of the IPV effect in a-Si:H with a significant photocurrent. It is proposed to have a positive influence on charge carrier generation when impurities are located inside the depletion or intrinsic region, with energy levels close to the band edges [59, p. 151][58]. In this context the
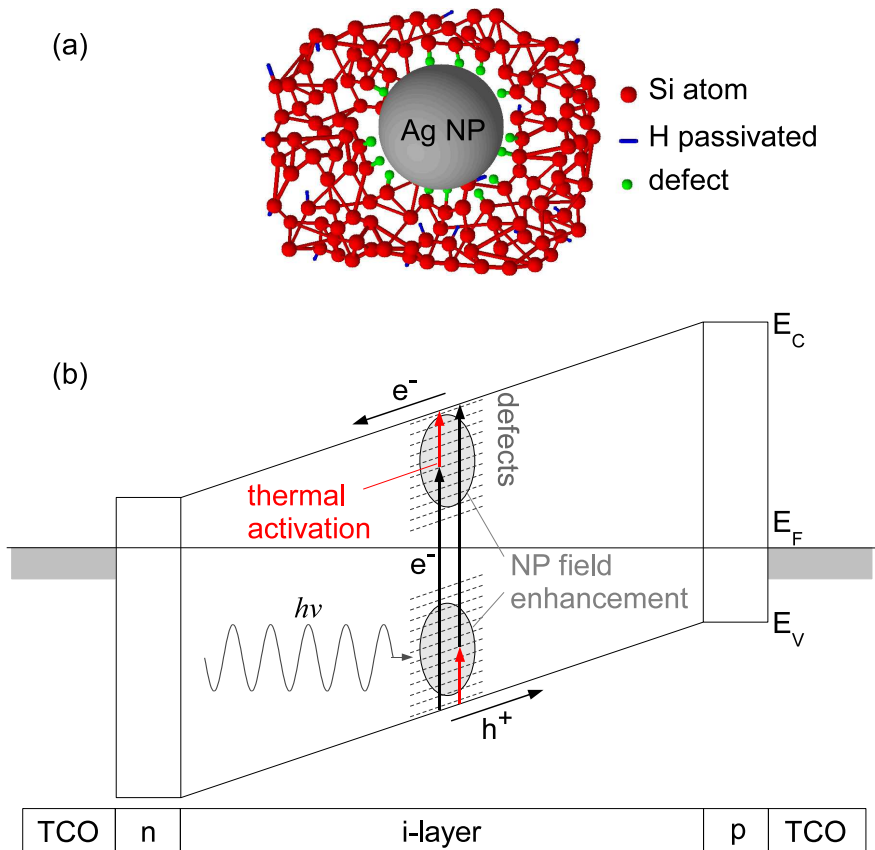
Figure 5.11.: (a) Schematic picture of an Ag NP in the a-Si:H network with created defect sites in direct vicinity of the NP (not true to scale). (b) Modified generation mechanism for sub-bandgap photons in the a-Si:H n-i-p structure. The transition of charge carriers from defect states in direct vicinity of the resonant absorbing Ag NPs is enhanced due to the strong fields. Charge compensation is realized by thermal activation to the band edges, from [201].

demonstrated approach is suitable, in combination with the strong fields at the defect locations induced by the LSP resonances.

When NPs are introduced to the intrinsic layer of standard n-i-p solar cells with an overall i-layer thickness of 250 nm, electrostatic field at the NP location is less strong. For such structures the observed EQE signal in the NIR regime is weak (not shown). It is only visible when plotting the data to a logarithmic scale. This indicates that the charge carriers cannot be efficiently extracted from the NP region. Thus recombination is a major limitation in this case.

The proposed model can be applied for all discussed situations. It incorporates in particular both cases for i-n and i-p structures and does not distinguish between them. Moreover the compensation of charged states does not depend on the position of the NPs within the device.

Energetic Position of Contributing States

The observed signals can give valuable information on the energetic position of the inner gap states with respect to the valence or conduction band edge. For all structures a dominant signal with a maximum at around 800 nm is found. The peak position represents the most dominant LSP enhanced transitions of electrons to or from inner gap states. An electron can be elevated from the valence band to these states if it is partly or completely empty. On the other hand excitation from such states to the conduction band is only possible when they are occupied by electrons. Since the Fermi level determines the occupation of states, the energetic position of states with respect to E_F could be of importance for the effect (see Section 5.5.3).

A dominant transition at a wavelength of 800 nm corresponds to a transition energy of 1.55 eV. Assuming an a-Si:H bandgap of 1.7 eV the transition corresponds to a distance of 0.15 eV of the states to the next band edge. The gap states dominantly involved in the generation processes are therefore energetically in a close distance to the band edges. The tail in the EQE signal towards 1100 nm (1.13 eV) indicates that also states deeper in the gap with distances of around 0.5 eV to the band edges contribute. These transitions occur with lower efficiency, because the energetic distance of states is not well adapted to the plasmon resonance energy. In addition the probability for thermal activated processes decreases with increasing distance to the band edge. Furthermore a decreasing density of available states, similar to a decrease of the band tail states towards the gap center could in combination reduce the outcome for lower energies.

5.5. Influencing Circumstances on Plasmon Enhanced Defect Absorption

The resonant enhanced generation of charge carriers due to the IPV effect is demonstrated for silver NPs in a-Si:H devices. Whether this generation mechanism is influenced by different device configurations or deposition conditions is investigated in the following.

5.5.1. Influence of Extracting Field

Recombination is a competing process with generation of charge carriers. The presence of defects, necessary for the IPV effect, increases the recombination rate for generated charge carriers. For an efficient extraction the position of the NPs inside the n-i-p diode could be of importance. The maximum electrical field is provided at the interface of the intrinsic layer to the n- or p-doped layers [69, p. 206]. Locating NPs in direct contact to such an interface would provide the maximum achievable field for charge carrier extraction. Since the p-i interface is one of the most delicate parts of a solar cell concerning device performance [69, p. 208] [89], the n-layer/i-layer interface is chosen for the experiments. Fig. 5.12 shows the device configuration that is similar to the previous section, apart from the omitted i-layer below the NPs. The blue response of the here shown structure is drastically decreased by the NPs (Fig. 5.12 (b)). This is likely due to reflections and the parasitic NP absorption, that screens the active layer from incident radiation. Further, the internal field distribution can be affected by the NPs resulting in a bad charge carrier extraction.

In the presence of Ag NPs a significant signal is observed in the NIR range. The magnitude is slightly larger than for the n-i/AgNP/i-p devices (Fig. 5.10). However, the strong internal fields expected at the NP location do not lead to a fundamental increase. The Schottky type devices (i-n and i-p) exhibit higher EQE signals (Fig. 5.4).

The reason for the different NIR EQE signals might be caused by different efficiencies of charge carrier extraction and/or due to optical differences. To evaluate the role of this optical contribution, the response of samples in the blue spectral region has to be considered. This gives a more reliable measure for the absorption with respect to the layer thickness than the weak signal in the low absorption regime. In table 5.1 the measured response in the blue part and the NIR part of the spectrum for the different types of samples is summarized.

Considering the blue response of samples without incorporated NPs first. The high amplitude of 40-50 % for the TCO/.../i-n system is reduced when the layer sequence is inverted (TCO/n-i/...). This is caused by absorption losses in the n-layer that do not contribute to the EQE signal. The according decrease of the NP related EQE signal
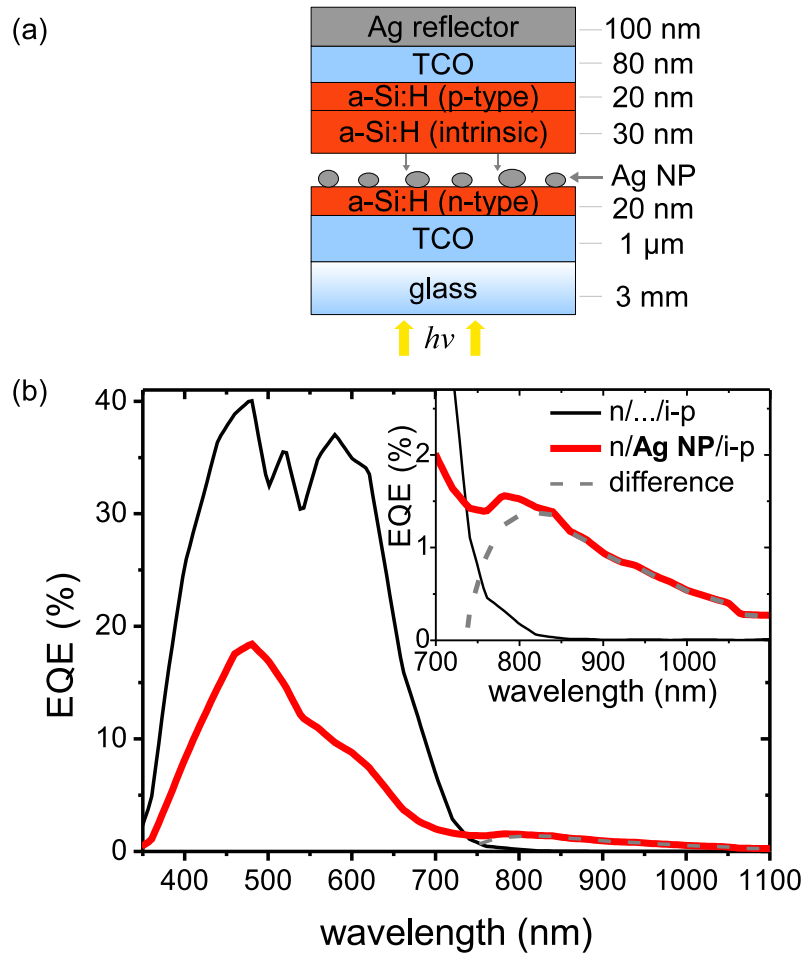
Figure 5.12.: (a) Design of a-Si:H n-i-p device with Ag NPs at the n-layer / i-layer interface to utilize the high electric field strength at this position for charge carrier extraction. (b) External quantum efficiency of n-i-p device with and without Ag NPs.

in the NIR decreases from 2% to 1.5%, which is in agreement with the optical losses caused by the n-layer.

	EQE signal amplitude (%)		
sample	blue reference	blue with NPs	NIR with NPs
TCO/NP/i-n	40-50	40	2
TCO/n-i/NP	30	20	1.5
TCO/n-i/NP/i-p	17.5	17.5	1
TCO/n/NP/i-p	30-40	17.5	1

Table 5.1.: Blue and NIR response of EQE measurements from Fig. 5.4, 5.8, 5.10 and 5.12. For this rough estimation the maximum values in the blue response and in the NIR are taken from the shown curves.

The sample in the TCO/n-i/.../i-p configuration in contrast exhibits a drastically lower blue response, although the i-layer is twice as thick as for the other samples. It should absorb significantly more photons. This points to collection losses even without NPs. This sample will therefore be excluded from the discussion here.

The blue response observed for the TCO/n/.../i-p system (in the last row) also shows a slightly decreased signal of $(30\text{-}40\%)$ compared to the i-n system $(40\text{-}50\%)$. When NPs are incorporated they should be exposed to a reduced light intensity, with respect to the case without the n-layer. In fact the NP induced signal decreases from 2% down to 1%. This is a more pronounced decline than expected from the optical point of view. Here, the transport and collection of charge carriers definately plays an important role. The EQE data for the different structures are significant. Considering the EQE enhancement in this spectral range, defined as:

$$\frac{\text{EQE}_{\text{with NPs}}}{\text{EQE}_{\text{without NPs}}}$$

reveals the strength of this effect (see Fig. 5.13). Since the reference signal is very small, strong enhancement factors are found. However, due to the low and noisy reference signal in this regime the calculated factors have to be treated with caution. For the n-i/AgNP/i-p device the EQE enhancement (plotted to a logarithmic scale) between 800 and 1100 nm obeys an enhancement of around 40. This is more than one order of magnitude. For the device with NPs placed at the n-layer/i-layer interface, enhancement factors of 50 to 100 and for the Schottky type i-p device between 200 and 550 are observed. The reason for these different enhancement factors are related to optical differences, i.e. absorption in the n-layer and differences in the charge carrier collection efficiency. Due to these enormous enhancement factors, the discussed device designs could be utilized in near infrared detector applications. While the i-p (or i-
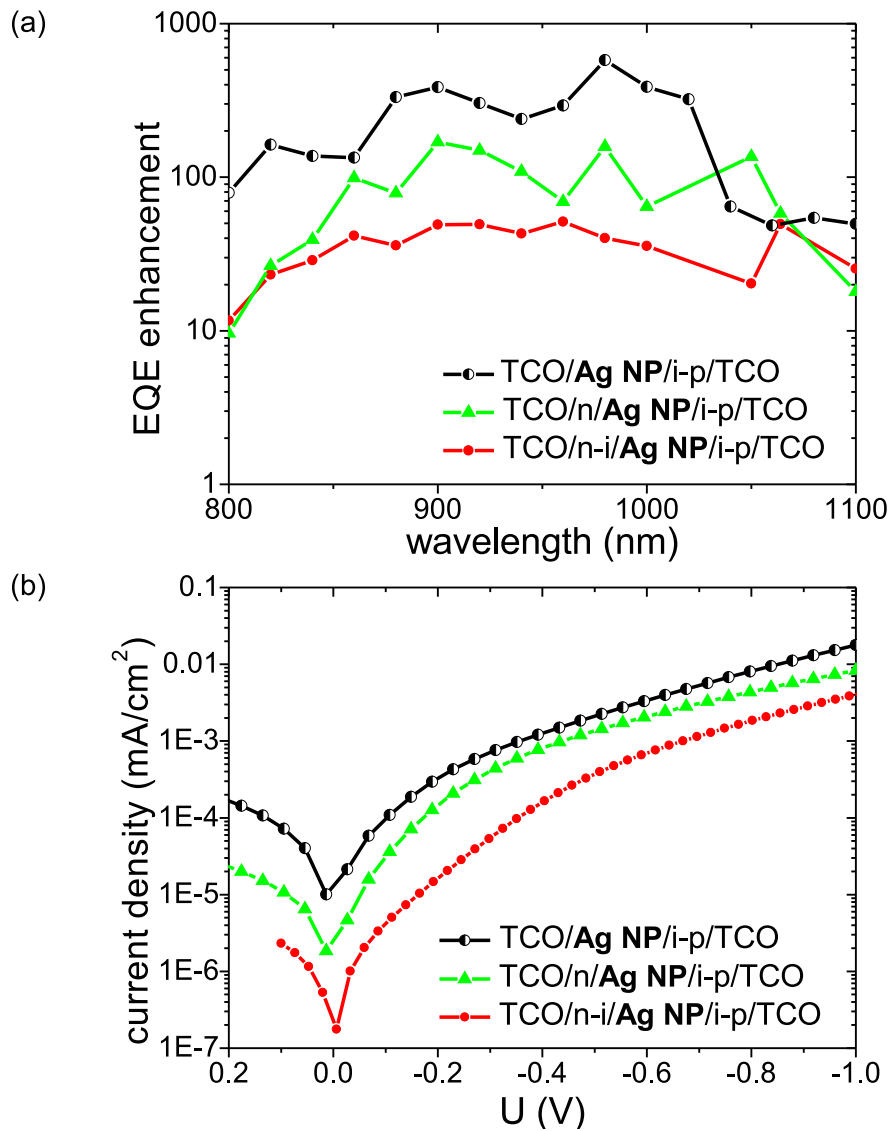
(a)

(b)

Figure 5.13.: Comparison of n-i-p device and i-n Schottky device for (a) EQE enhancement for the NIR regime and (b) current density in the dark. The EQE enhancement is calculated as quotient of EQE with NPs and EQE of reference without NPs.

n) devices have a better light harvesting efficiency, the dark current of n-i-p diodes (Fig. 5.13 (b)) is one or two orders of magnitude lower. As the i-layer thickness has an influence on this, the dark current for the thicker n-i/NP/i-p device is one order of magnitude lower than for NPs at the n-layer. The choice of the most suitable device design is a trade-off between strong enhancement, correlated to Ag NPs at very thin absorber layers and low dark current characteristics related to thicker absorber layers and/or n-i-p diode structures.

5.5.2. Influence of Particle Size on Sub-Bandgap Response

In this section the influence of the LSP resonance on the IPV induced photocurrent is investigated in more detail. The observed photocurrent is spectrally correlated to the enhanced absorption caused by the LSP resonances. According to the proposed model, the resonances provide strong fields in the NP environment. Hence the defects in direct vicinity of the NPs are exposed to these strong fields, enhancing the transition rate between the band edges and the defect levels. Here the influence of an LSP resonance energy variation on the spectral behavior is investigated. For this reason the Ag NP size distribution is altered to exploit different LSP resonance energies. Again the photosensitive a-Si:H device structures in the i-n and i-p configuration discussed in section 5.3 are applied. These experiments are conducted on large area substrates due to better process adaption. The agglomerates discussed in section 4.2 with particle sizes of (23 ± 9) nm (already used in Fig. 5.4), (27 ± 10) nm and much larger particles with a mean diameter of around 100 nm are used. The first two show well separated particles, while the third one has very irregular formed particles that are to some extend interconnected. The spectral charge carrier generation of prepared devices is illustrated in Fig. 5.14 (a)+(b). The EQE of reference devices without NPs are plotted as thin black curves. The thick, colored curves represent the measurement of samples with different particle sizes. Here similar behavior as reported before is observed. In the visible range below 700 nm, where the light absorption of a-Si:H is efficient, devices with NPs show a decreased photocurrent attributed to damped LSP oscillations. A variation of the particle size further decreases the EQE amplitude in this region. This will be discussed in more detail in section 5.5.6.

For wavelength above 750 nm, where no photocurrent is measured without NPs, a significant signal is observed for the devices with NPs. This is observed for all particle sizes. For both types of devices, an increasing particle size results in a decreasing amplitude. The differential curves that represent the NP induced contribution are indicated by the dashed curves. Here a shift of the maximum with increasing particle size is measured. This shift is more pronounced for the i-n devices where the maximum shifts from 815 nm to 880 nm. Since for the i-p device no distinct maximum is observed
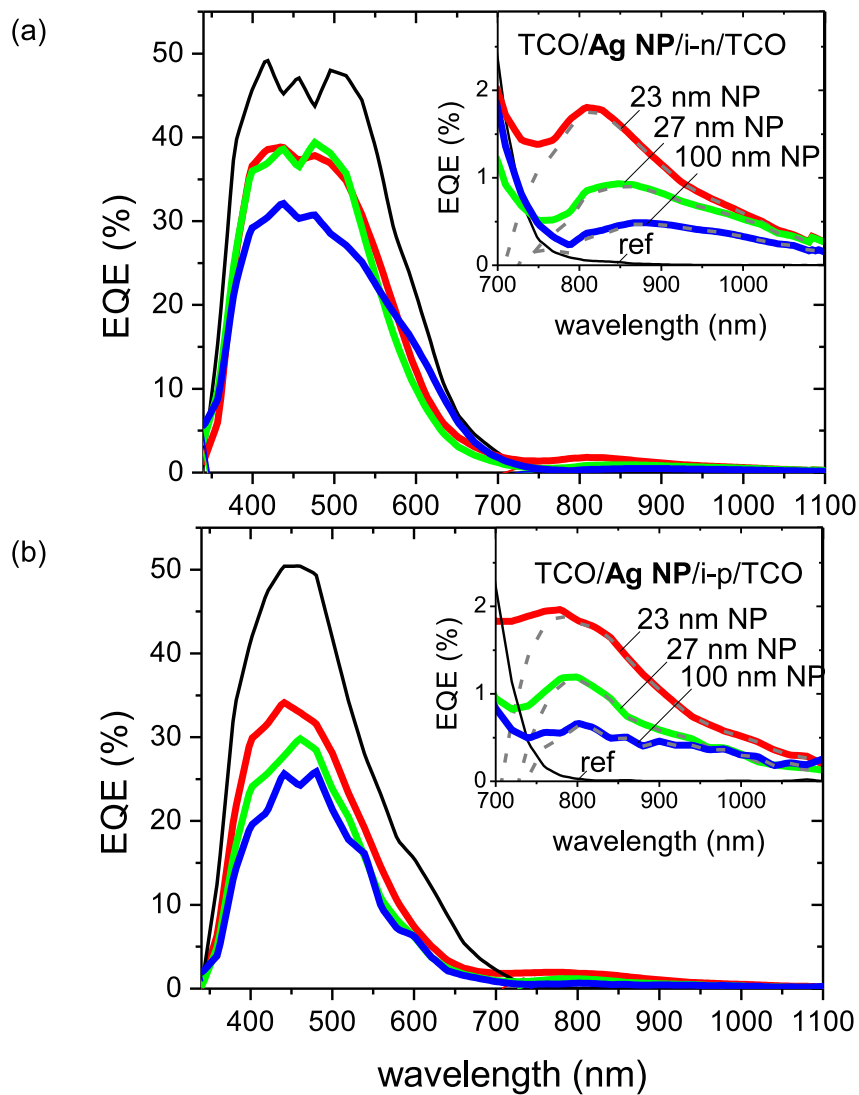
Figure 5.14.: Influence of NP size distribution on EQE enhancement in the NIR region, for (a) a-Si:H i-n and (b) i-p devices. The response of samples with different Ag NP agglomerates are shown with the thick, colored curves, 23 nm (red), 27 nm (green) and around 100 nm (blue). The thin black curves represent the reference device without NPs, while the dashed curves in the insets indicate the difference to the NP induced signals. The morphology of the used particle agglomerates are shown and discussed in Fig. 4.7 and 4.8.

for the largest particles such a statement is difficult. The optical measurement of devices (Fig. 5.15) show an increased absorption in the presence of Ag NPs. For the blue spectral region this is related to a better light in-coupling at the TCO/a-Si:H interface (as discussed previously). In the NIR regime a strongly increased absorption is observed for all particle sizes. Due to thin film interferences of the contributing layers a single LSP peak can not be distinguished. With increasing NP size the absorption increases between 900 and 1100 nm. which is likely an indication for a shift of the resonance position towards longer wavelength.

A shift of the EQE response along with a shift of the LSP resonance can be understood in the frame of the defect absorption model (Fig. 5.11). The resonant absorbing NPs accompany strong electromagnetic fields that interact with the defect states created by the presence of the Ag NPs in the silicon network. The most dominant transitions occur for levels having a distance to the band edge equal to the LSP resonance energy or close to it. The broad EQE signal between 750 and 1100 nm suggests that defect levels are distributed over the a-Si:H bandgap from shallow defects near the band edge to deep ones. Different LSP energies primarily address defect levels with different energetic positions. The defect levels are actually scanned by changing the LSP resonance energy. The above mentioned decrease of the EQE peak amplitude in the NIR accompanied by the shift can likely be related to this overall mechanism, too. Apart from the sub-bandgap excitation an additional excitation step is demanded, for instance by thermal activation. A red shift of the LSP resonance makes use of transitions with lower energy, according to defect levels deeper in the gap and hence with a larger distance to the valence band. This larger distance of levels lowers the probability for thermal loading from the valence band. As a result the efficiency of the generation process is decreased.

The decreasing EQE signal in the NIR with increasing NP size could in principle also originate in an increased radiative damping, especially for the very large particles. In addition the recombination of charge carriers could be increased due to a larger amount of silver within the device.

The observation of a less affected low energy tail with increasing particles size might be related to the fact that the deep defects are still addressed by the shifted LSP resonance. The decreasing trend is here consequently only moderate.

The difference between both types of devices concerning the initial peak position as well as their behavior with respect to a shifted LSP resonance condition is likely related to the transition mechanisms. The asymmetry of the i-n and i-p devices could result in the preference of a certain transition path. For the electron transport dominated i-n device, occupied defect states near the valence band might be preferred. For the i-p structure instead the unoccupied states near the conduction band are involved in the transitions. In case the created defects are in a certain way correlated to the a-Si:H
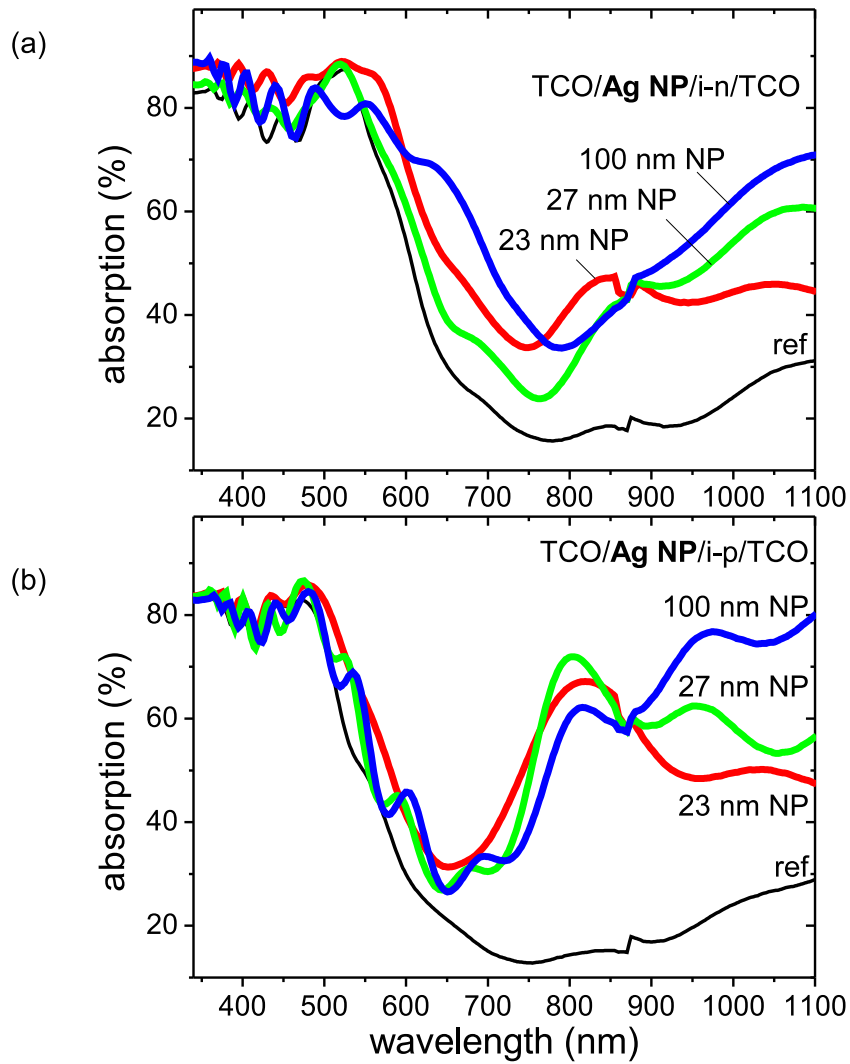
Figure 5.15.: Influence of NP size distribution on UV/Vis spectra, for (a) a-Si:H i-n and (b) i-p devices. The response of samples for the different Ag NP agglomerates are shown with the thick, colored curves, 23 nm (red), 27 nm (green) and around 100 nm (blue). The thin black curves represent the reference device without NPs.

band tails. The more narrow conduction band tail [77, p. 516-517] could explain the limited shift of the signal for the i-p devices.

5.5.3. Influence of the Fermi Level on Sub-Bandgap Response

The discussed generation and transport model for the IPV effect relies on the presence of defects in the proximity of resonant absorbing NPs. An a-Si:H i-n structure is mainly limited to electron transport due to the n-type contact. For this i-n structure the IPV effect incorporates occupied states near the valence band. The effect should be sensitive to the position of the Fermi, because the states need to be occupied. In order to investigate this, devices based on the a-Si:H i-n design used in section 5.3 are prepared. In contrast to these the doping concentration in the Ag NP environment is varied for different samples between undoped and highly p-doped. This should lead to a shift of E_F towards the valence band and defect states should become unoccupied. Fig. 5.16 (a) shows the resulting devices composed of a p-i-n layer sequence (TCO/AgNP/a-Si:H p-i-n/TCO). P-type doping by boron is realized by addition of Trimethylborane $B(CH_3)_3$ (TMB) to the PECVD gas mixture during p-layer deposition. The ratio of the TMB to Silane (SiH_4) fluxes denoted as $[TMB]/[SiH_4]$ is varied from 0 (undoped) for the reference sample to $3 \cdot 10^{-2}$ (highly p-doped). The intrinsic layer thickness of the device without the p-doped layer is approximately 30 nm. The introduced p-doped layer has a thickness of around 5 nm while the i-layer thickness is reduced to 25 nm. For all a-Si:H based devices, the total absorber layer thickness is kept constant.

In contrast to samples discussed before where an AZO (ZnO:Al) front TCO with a smooth surface topology is used, in these devices a rough Asahi SnO_2 is applied. For the experiments Ag NPs with a diameter of (23±9) nm are used. As expected, all devices with incorporated NPs exhibit an increased absorption for the near infrared range compared to the device without NPs (Fig. 5.16 (b)). A variation of the doping concentration in the NP environment does not have a significant influence on the device absorption.

The external quantum efficiency measurement (Fig. 5.16 (c)) of the i-n reference device (thin black line) exhibits a maximum EQE signal of 55 to 60%, attributed to the thin absorber layer. The introduction of Ag NPs to the i-n device (thick red curve) slightly decreases the signal in the visible range, as observed for other devices before. The application of a p-doped layer to devices with Ag NPs has nearly no influence below 500 nm, in contrast to the range between 500 and 700 nm. All p-i-n samples show a decreased signal between 500 and 700 nm, indicated by the arrow. This is discussed in more detail at the end of this section. For NIR photons above 800 nm (inset in Fig. 5.16 (c)) nearly no photocurrent response is measured for the i-n reference device. A very small signal below 0.5 % is observed up to 850 nm, assigned to the light
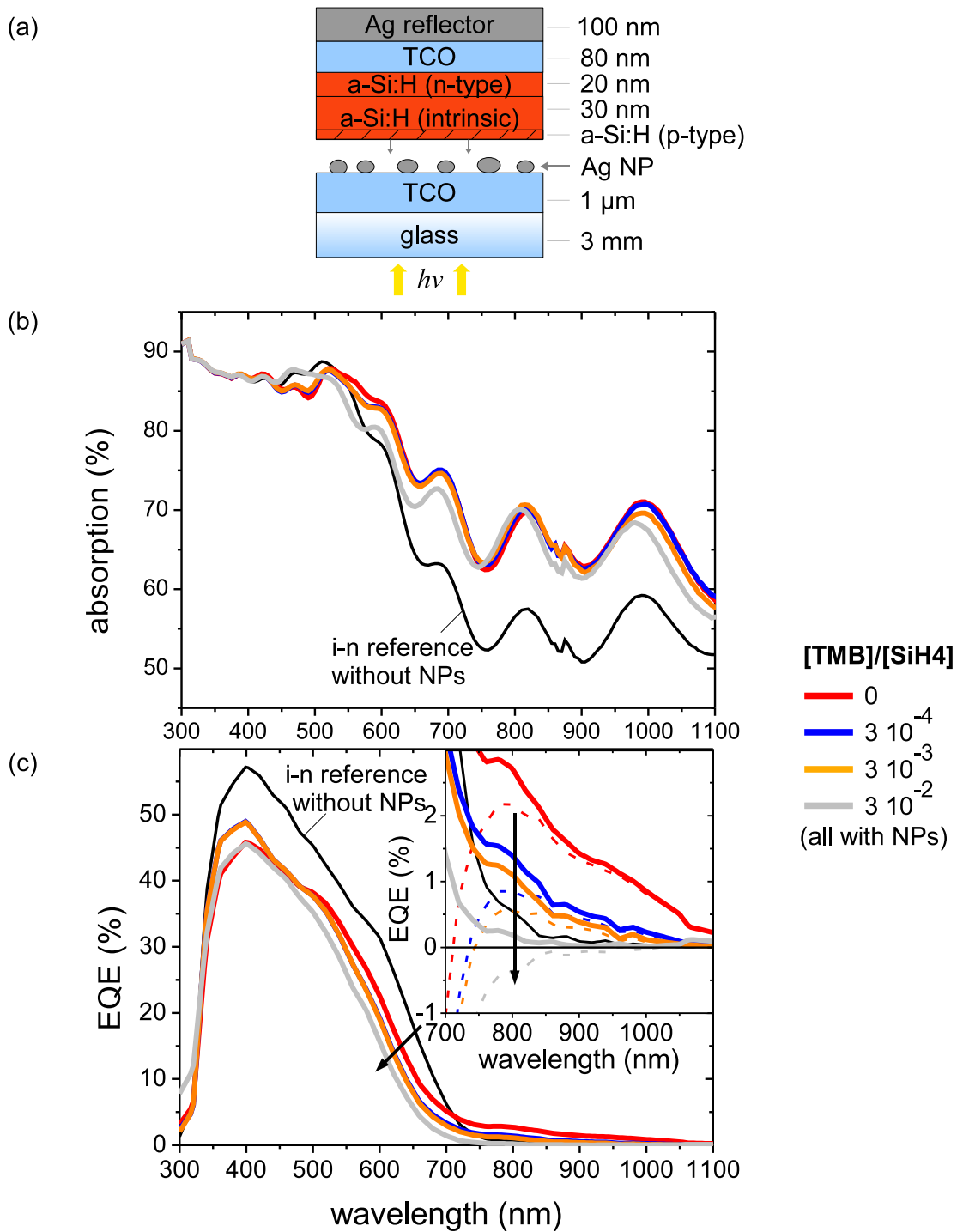
Figure 5.16.: (a) Schematic design of TCO/Ag NP/a-Si:H p-i-n/TCO structures with varying doping concentration from intrinsic to highly p-doped $(0 < [TMB]/[SiH_4] < 3 \cdot 10^{-2})$ at the front TCO/a-Si:H interface. The used front TCO is a rough Asahi SnO_2. (b) Influence of doping on device absorption and (c) on the EQE signal. The inset illustrates the EQE characteristics in the NIR range, the dashed lines indicate the difference with respect to the i-n reference without NPs.

trapping ability of the textured SnO_2 front contact. For the device with flat interfaces the threshold was at about 800 nm.

In the presence of Ag NPs two main findings are made in this regime. First, a significant EQE signal is measured in the long wavelength range as observed for the other structures before. Again, the EQE difference signal (dashed lines) show a peak at 800 nm. This is a further indication that the IPV generated signal is not related to the TCO material, as already pointed out in section 5.4.1. The effect is independently demonstrated for ZnO and SnO_2 front contacts adjacent to the NPs. The second finding made in the EQE measurements is a decreasing NIR EQE signal with increasing p-layer doping in the NP environment. The trend for samples with Ag NPs (thick curves) is indicated by the arrow in the inset of (c). The higher the p-doping concentration, the lower the NIR photocurrent. The sample with highly doped p-layer shows no (or a „negative") enhancement compared to the i-n reference device without Ag NPs. In the difference signal (dashed lines), the decreasing trend with increasing p-doping concentration is obvious. The signal reduces over the complete NIR spectral range, especially the long wavelength tail proceeds close to zero. In addition, the point at which a NP induced enhancement compared to the reference is observed, abruptly shifts to longer wavelengths once the doping is incorporated. Because the device absorption is not affected by the varying doping concentration (Fig. 5.16 (b)), optical reasons like a shift of the LSP resonance can be excluded for the decreasing signal.

The decreasing EQE signal with increased p-type doping in the NP environment could be related to a shift of the Fermi level. For this purpose the conductivity of the individual layers as a function of the doping concentration has to be known. A series of single a-Si:H layers with a layer thickness of approximately 250 nm (Fig. 5.17 (a)) and the doping gas ratios used for the p-layers of the p-i-n cell experiments are deposited on quartz-glass substrates. The Fermi level position is evaluated from dark conductivity measurements as described in Section 3.2.8. Fig. 5.17 (b) shows the distance of the valence and conduction band with respect to E_F. For better visibility of the development, E_F is set to zero in this diagram. The intrinsic a-Si:H sample has a Tauc bandgap (difference of E_C and E_V) of 1.75 eV. The p-doped layers show an increased E_g, in comparison to a-Si:H, as already observed by the larger penetration depth for p-doped layers. This is caused by carbon incorporation due to the addition of methane (CH4) to the gas flux and the presence of carbon in TMB itself [203][69, p. 208]. The bandgap of around 2.1 eV measured for low p-doping concentrations decreases with increasing TMB concentration to 1.9 eV. This is mainly related to the role of boron and H_2 incorporation [204, 205]. The energetic position of contributing IPV states (green stars) is derived from the dominant NIR signal in the EQE measurement of the i-n device with incorporated NPs. As mentioned above this is observed roughly at 800 nm,
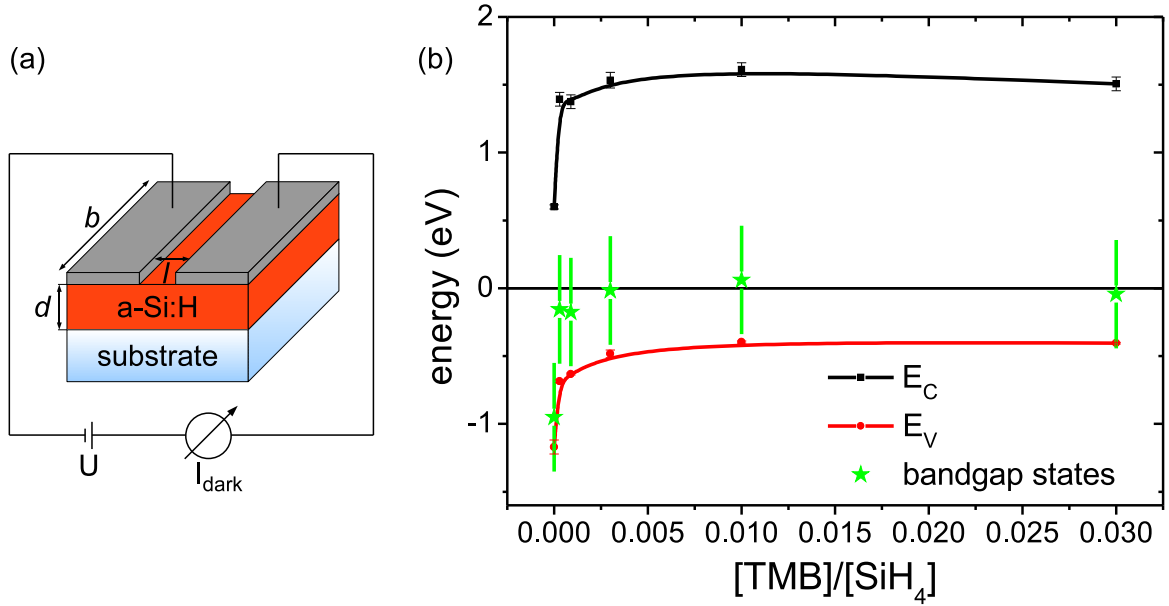
Figure 5.17.: (a) Sample geometry for measurement of dark conductivity of single a-Si:H layers with varied p-type doping. (b) Position of valence band (red dots) and conduction band (black squares) with respect to the Fermi level (set to $E_F = 0$). The measurement is carried out for single a-Si:H layers with the according doping concentrations used for the cell experiments shown in Fig. 5.16. For visual clarity, solid lines are drawn along the measured data to indicate their trend with p-type doping. The LSP induced bandgap states (green stars) with respect to the conduction band are also shown. The state energy is deduced from the energetic position of the most dominant transition ($\approx$ 800 nm $\rightarrow$ 1.55 eV) observed for the EQE measurement of the undoped sample. The error bars indicate the width of the observable NIR EQE signal especially towards the low energy side (≈ 0.4 eV).

corresponding to a photon energy of 1.55 eV. This energy is related to transitions of contributing IPV states to the conduction band, therefore they are plotted with a fixed distance of 1.55 eV to the conduction band. The error-bars represent the width of the observed NIR EQE signal of approximately 0.4 eV especially towards the low energy region (up to 1100 nm (1.1 eV)). The Fermi level moves towards the valence band and the energetic position of the defect states with increasing doping concentration. For medium and high doping concentrations E_F is already shifted to $E_F - E_V = 0.4$ eV which is in agreement with values reported in literature [205, 206]. By increasing the boron doping concentration no further significant shift of E_F towards E_V is observed. This is related to the valence band tail and the defect states in the gap. Since doping results in the creation of dangling bonds and an increase of density of states in the tails [207] due to autocompensation processes, the Fermi level can not shift further towards E_V [69, p. 194-196]. Due to the measured shift of E_F the IPV states become unoccupied. This results in a decrease of the EQE signal. The complete disappearance of the
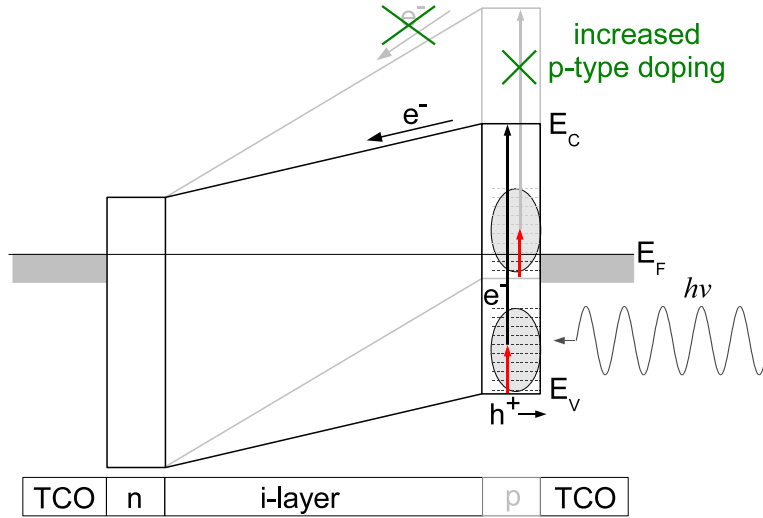
Figure 5.18.: Influence of Fermi level shift on generation of charge carriers according to the proposed generation and transport model from Fig. 5.11. An increased p-type doping results in a shift of E_F towards E_V. The IPV states that are previously occupied by electrons, become unoccupied and are not available for sub-bandgap transitions towards E_C.

NIR signal for the highest doping concentration ($[\text{TMB}]/[\text{SiH}_4] = 3 \cdot 10^{-2}$) in contrast can not be explained by this, since the shift of E_F is limited. Parts of the states still lie below E_F and have to be occupied by electrons. However, the observed EQE NIR signal is sensitive to a shift of the Fermi level towards the IPV states. This behavior is consistent with the proposed defect absorption model (illustrated for this configuration in Fig.5.18). When the contributing states become unoccupied, photons with sub-bandgap energy cannot excite electrons to the conduction band. With increasing doping concentration and shift of E_F, defect levels closer to the gap center should become unoccupied first, while those levels near to the valence band should remain occupied by electrons. In contrast to that the high energy transitions are decreased at first, indicated by the abrupt shift of the EQE difference signal even for low boron concentrations (Fig. 5.16 (c)). This seems to be related to the increased bandgap in the NP environment for boron doped samples. Therefore electrons from contributing states require higher energies to be excited to the conduction band.

It has to be pointed out, that in addition or combination other reasons could be of importance for these observations. The introduced doping increases the defect density by orders of magnitude [206, 207] and leads to increased recombination of charge carriers. In particular electrons generated inside the p-layer, i.e. for electrons originating from the sub-bandgap transitions near the NPs are affected. In contradiction to this argument, the EQE in the visible range is not affected by an increased recombination.

A further reason could be the covering of the NPs by the p-doped layer. Consequently the particles are placed outside the built-in electrostatic field of the p-i-n diode. With an increased doping concentration the transport and separation of electrons and holes, generated in the vicinity of the Ag NPs by the NIR photons, is less efficient and could reduce the measured signal.

At this point, the decreased red response observed between 500 and 700 nm due to the introduced p-doped layer, indicated by the arrow in Fig. 5.16 (c), is discussed in more detail. For this investigation, the device reflection is illustrated in Fig. 5.19 (a). The variation of the doping concentration in the p-layer has definitely an influence on the device reflection. Below 500 nm the reflection is decreased with increasing doping concentration, while above 500 nm a reverse behavior is observed, i.e. the reflection increases with increasing doping concentration. The observation below 500 nm are in agreement with the expectation. Boron doped a-Si:H has a smaller refractive index with respect to undoped material, due to the widening of the bandgap [203]. The reflection at a TCO/a-Si:H(p) interface should be reduced compared to a TCO/a-Si:H(i) interface because the difference to n_{TCO} is smaller. Above 500 nm the increased reflection with increased doping concentration is in contradiction to this assumption.

The thinner i-layer used for the p-i-n devices could be responsible. The standard i-layer thickness for the i-n device is 30 nm, while for the p-i-n devices the i-layer thickness is reduced by the thickness of the p-layer of about 5 nm. The i-layer thickness is therefore reduced to 25 nm for the p-i-n devices. Due to the higher bandgap for p-type a-Si:H (see discussions concerning the bandgap above) the absorption in the p-layer might play a minor role. Fig. 5.19 (b) illustrates the penetration depth of light exemplary for undoped and highly doped a-Si:H material in the region of interest between 450 and 700 nm. These measurements are performed on single layers, deposited with the same doping gas fluxes as the p-layers of p-i-n devices. For p-doped material (gray curve) light has a penetration depth larger than 100 nm. The 5 nm thin p-layer does not contribute significantly to the absorption. For the intrinsic material (red curve), light below 500 nm is absorbed within the first 50 nm. Taking into account that the light is reflected at the back reflector of the solar cell devices and travels a second time through the absorber, twice the i-layer thickness of $2 \times 25\,nm$ or $2 \times 30\,nm$ is sufficient to absorb the in-coupled light completely. Therefore no difference in the EQE is observed here. For this wavelength regime, only the reflection at the TCO/a-Si:H(p) layer contributes to the device reflection. Above 500 nm the thinner i-layer of the p-i-n devices (compared to the i-n device) becomes crucial. Because of the decreasing absorption coefficient the layer thickness is not sufficient to absorb the incident light completely, hence an increasing amount of light is coupled out of the device. This is observed by the increased reflection of p-i-n solar cell devices for wavelength above 500 nm. Here the decreased reflection at the TCO/a-Si:H(p) interface is overcompensated by the increased out-
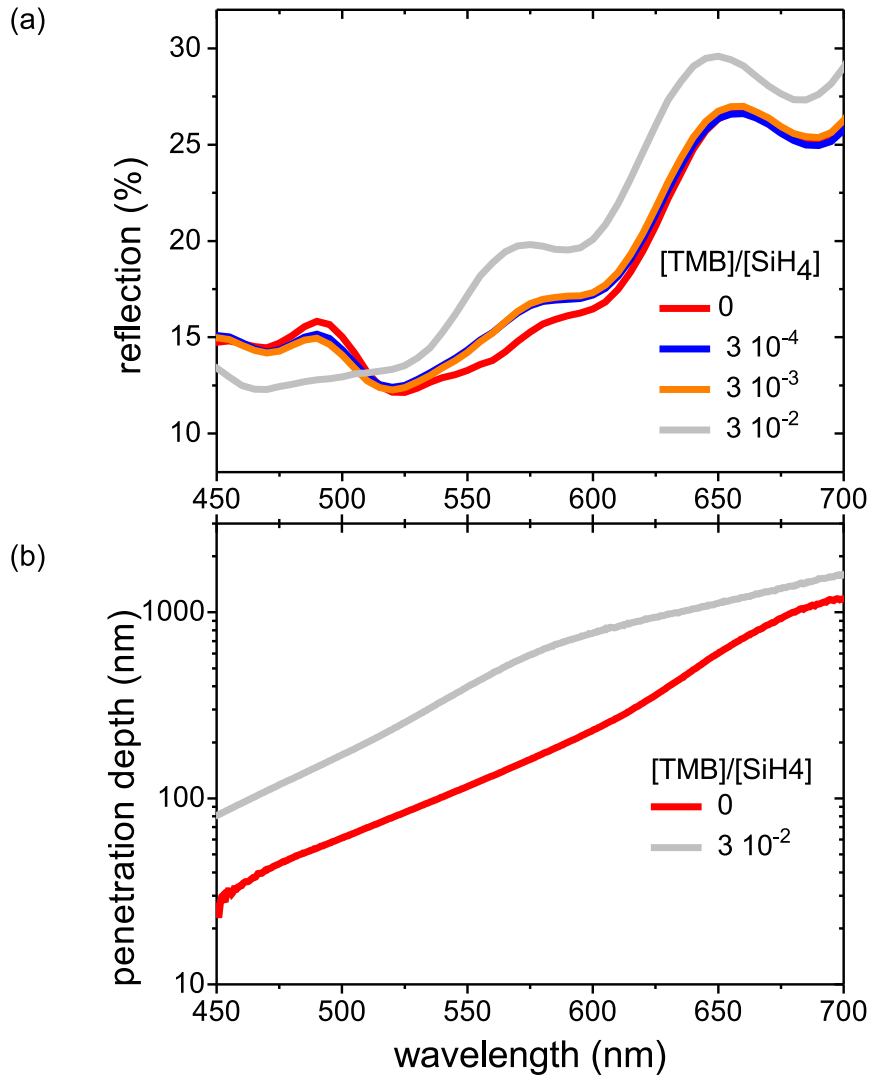
Figure 5.19.: (a) Device reflection of p-i-n samples with varying p-type doping and incorporated Ag NPs. Apart from variations, for all samples with additional p-doped layer an increased reflection is measured between 450 and 700 nm. (b) Penetration depth of light in a-Si:H for undoped and highly p-doped material, measured for single layers that are prepared with the same doping gas fluxes as p-layers applied in the p-i-n devices.

coupling of light. The thinner i-layer of the p-i-n devices therefore leads to a lower EQE signal between 500 and 700 nm.

Photon absorption in the doped layers does not significantly contribute to the EQE signal, due to the high recombination rate. The introduction of the thin p-layer might lead to absorption of light that can not be used in the generation and especially collection of electron hole pairs.

5.5.4. Influence of Oxidation and Post NP Processing - Choice of Deposition Sequence

The influence of the deposition sequence as well as a vacuum break in between certain deposition steps is investigated by applying various sample designs (Fig. 5.20 (a) and 5.21 (a)).

For structures where the NPs are deposited on an a-Si:H n-i layer stack followed by the sputtering of the AZO/Ag back contact (Fig. 5.20 (a)), the interruption of vacuum processing after silver NP deposition leads to different device behaviors. Both samples with NPs show an enhanced absorption (Fig. 5.20 (b)) in the long wavelength regime compared to the reference device. The signals are again influenced by interferences, however the absorption of the sample with vacuum break seems to be reduced above 850 nm.

In the EQE measurement (Fig. 5.20 (c)) for samples without a vacuum break (thick red line) a significant photocurrent is measured for photon energies below E_g, as previously shown. For samples with a vacuum break (thick green line) a strongly decreased signal is measured. No difference to the reference without NPs is observed in this regime. Although the optical absorption is still enhanced, no EQE enhancement is observed. The interaction of the NPs with atmosphere and especially with oxygen seems to have an adverse influence on the optical and also on the electronic properties.

Samples deposited in the inverse sequence (Fig. 5.2 (a)) TCO/Ag NPs/a-Si:H i-n/TCO behave in a different way. They are much less influenced by a break of vacuum, as demonstrated in chapter 5.3. In that configuration the particles are deposited on the front TCO and are covered afterwards by the a-Si:H absorber. Samples with NPs have to be transfered to the PECVD chamber for a-Si:H deposition, including a break of vacuum and exposure of NPs to atmosphere. However, a strong signal in the NIR is observed for samples with incorporated Ag NPs. The contact of particles with atmosphere can therefore not be the only reason for a decreasing NIR signal. An influence of the underlying substrate on the NIR response by atmosphere exposure can also be excluded, since the NIR effect is measured for NPs deposited on the TCO as well as for NPs deposited inside n-i-p devices (Section 5.4.3), i.e. on top of a-Si:H. Obviously
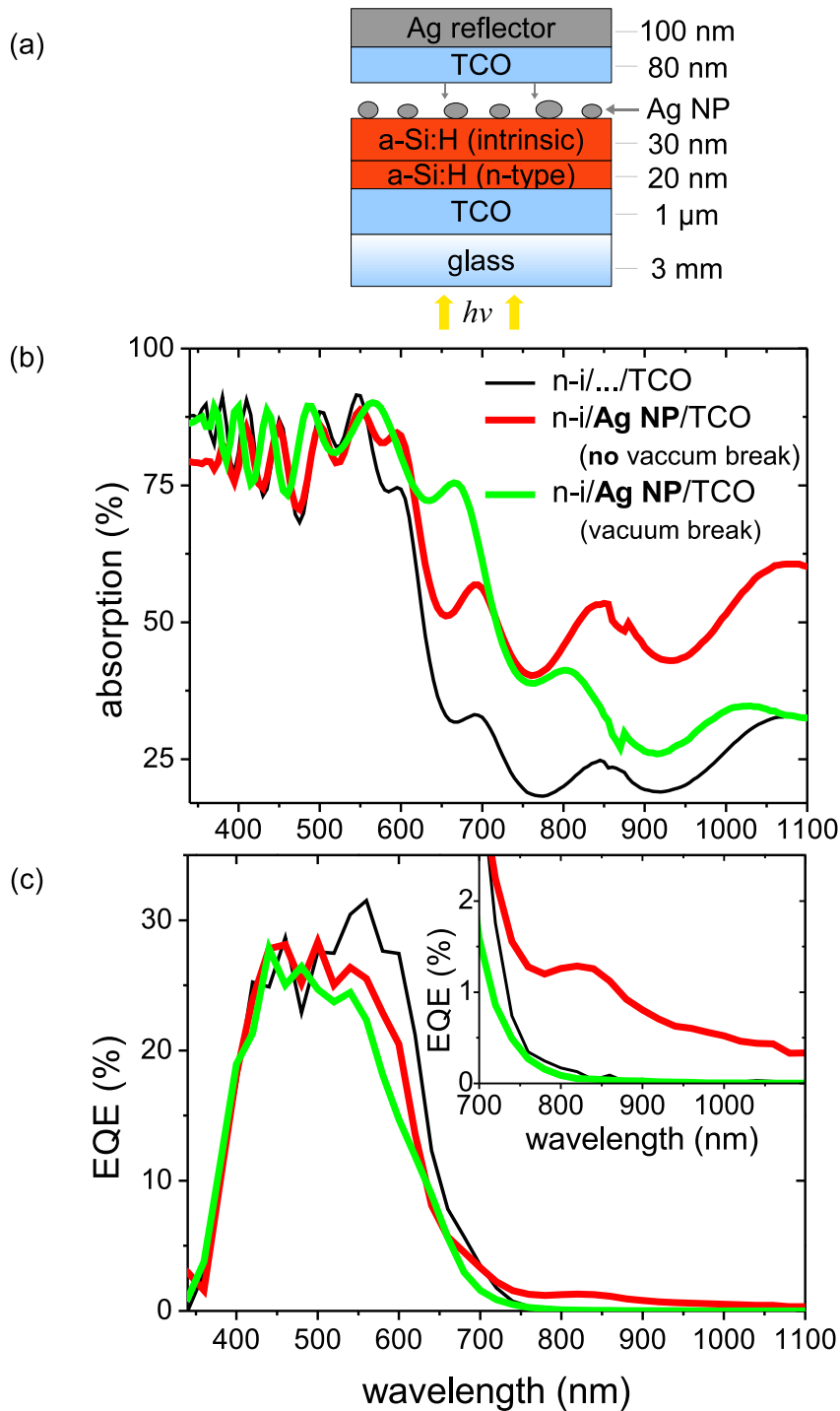
Figure 5.20.: (a) Device design for experiments on the influence of oxidation on the IPV effect in the TCO/a-Si:H n-i/Ag NP/TCO configuration. (b) Influence of Ag NP exposure to the atmosphere on optical absorption and (c) on the EQE signal.
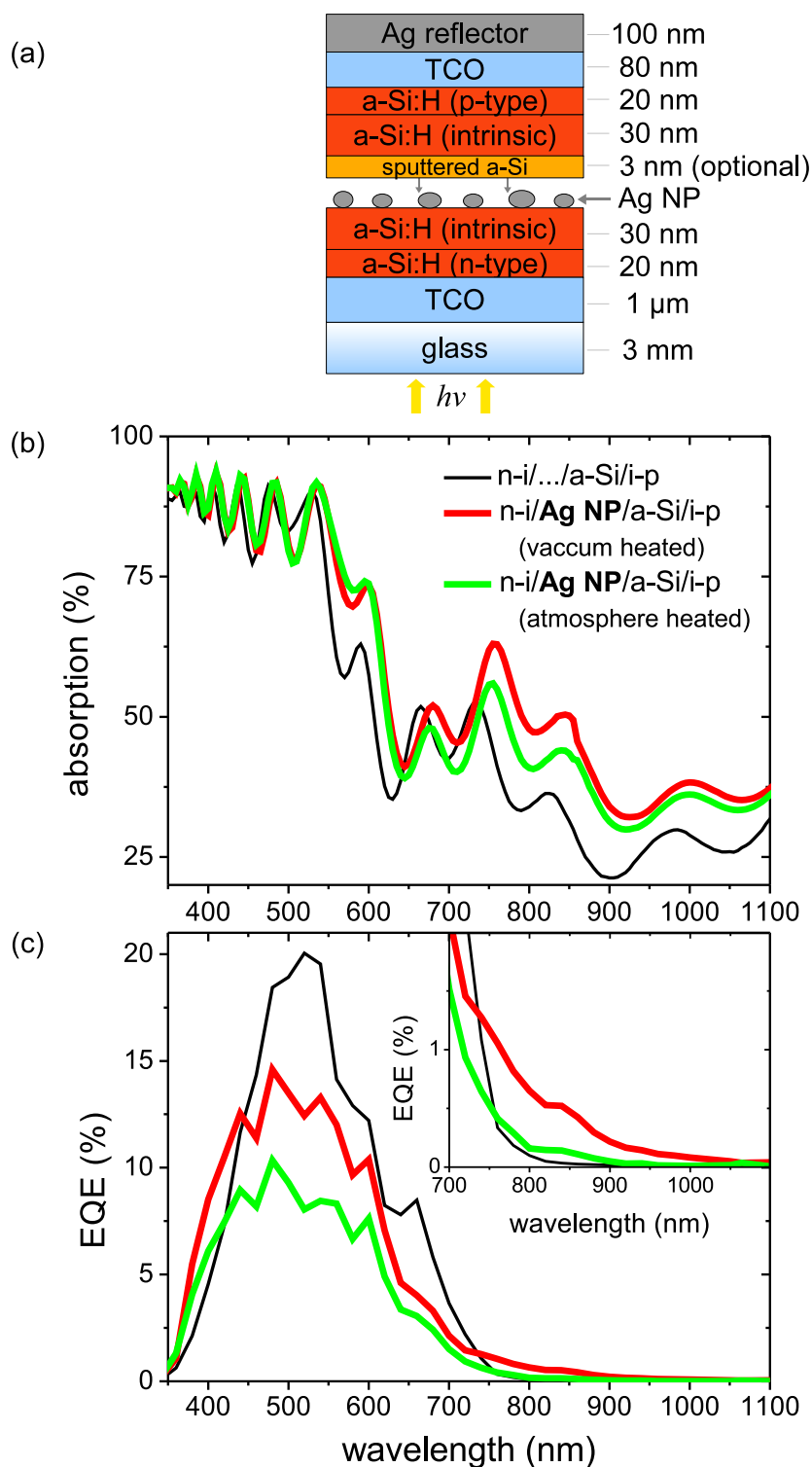
Figure 5.21.: (a) Device design for experiments on the influence of oxidation and post NP processing on the IPV effect in the TCO/a-Si:H n-i/Ag NP+sputtered a-Si/a-Si:H i-p/TCO configuration. Here the Ag NPs are covered by a 3 nm thin sputtered a-Si layer in order to exclude the influence of the following PECVD process on the Ag NPs. (b) Influence of Ag NP exposure to the atmosphere on optical absorption and (c) on the EQE signal.

the deposition step following the Ag NP fabrication seems to be of great importance, in particular when the following deposition is sputtering or a PECVD process.

In order to study the influence of atmosphere exposure as well as the following PECVD process in more detail, different samples are processed in the n-i-p configuration with Ag NPs inside the i-layer (see Fig. 5.21 (a)). For this sample geometry the NP deposition is followed by an a-Si:H PECVD deposition in a different chamber, consequently with exposure to atmosphere in between. To prevent this contact to atmosphere for certain samples an optional 3 nm thin sputtered a-Si layer on top of the Ag NPs (deposited in the same sputter chamber as the Ag NPs) is produced. a-Si sputtering is not favorable for the device quality due to the high defect density resulting from a lack of hydrogen in these layers. However this provides the possibility to prevent the direct exposure of the silver to ambient air during transfer to the PECVD chamber. In addition the particles are protected from the PECVD process itself. Consequently the influence of exposure to ambient air and the PECVD process can be investigated separately.

The measurements are shown in Fig. 5.21. For clarity reasons, measurements without the sputtered layer that are already shown in Fig. 5.10 (section 5.4.3) are omitted here. The absorption of the different samples is illustrated in Fig. 5.21 (b). In the presence of Ag NPs an increased absorption is measured for the long wavelength regime, compared to the reference device without Ag NPs. The increase is significantly smaller, than for Ag NPs without the sputtered a-Si layer shown before. Both samples with incorporated Ag NPs show a similar absorption behavior, although the vacuum heated device exhibits a slightly higher absorption.

The according EQE measurements are shown alongside in 5.21 (c). Here the influence of the introduced a-Si layer becomes obvious in a strong decrease of the EQE signal especially below 700 nm. This should be related to an increased recombination at the defect rich a-Si layer. However the sample whose NPs were heated in atmosphere show an even stronger reduction. In the sub-bandgap regime the NP samples also differ significantly. While the sample heated in the vacuum still exhibits a red response, the signal of the device annealed in atmosphere is strongly reduced. The red response is nearly not distinguishable from the reference device without NPs. Obviously the decreasing behavior in the EQE measurement is not dominantly related to optical optical reasons, since the absorption is significantly enhanced in this regime. These observations suggest that the contact to atmosphere has an influence on the NP surface or on the a-Si:H/Ag NP interface. A following PECVD process in contrast has a positive influence on the NPs and the NIR photocurrent. Since samples with Ag NPs that are exposed to PECVD exhibit a photocurrent signal in the NIR.

As demonstrated in [139], the exposure of Ag NPs to ambient air causes oxidation of the Ag surface to Ag_2O. This would create Ag/Ag_2O core shell nanoparticles. For an

increasing oxide shell thickness the LSP resonance position is shifting to lower energies, together with a decreasing strength of the LSP resonance as shown in [139, 208]. This decreased LSP resonance strength in combination with an increased distance of the Ag NP core with respect to the a-Si:H leads to a lower field strength [30, 36] at the defect sites in the a-Si:H network. The efficiency of the resonant defect absorption, responsible for the EQE signal for sub-bandgap photons, might be reduced accordingly. Similar effects are observed in [36] on the influence of the oxide thickness in $Ag/Ag_2O/TiO_2$ core/shell nanoparticles. Here an enhanced absorption of dye molecules in dye sensitized solar cells is discussed. They observe a decreasing absorption for an increased separation of the metal particle from the dye due to a thicker oxide shell.

For samples with oxidized nanoparticles that are exposed to the PECVD deposition, this situation seems to change. Ag_2O can be reduced in hydrogen (H_2) atmosphere at temperatures in the order of $200\,°C$ [209, 210]. The PECVD process is executed in this temperature regime with a lot of H_2 in the plasma (see Section 3.1.1). Therefore, an evident oxide shell might be reduced to Ag by the PECVD process. Thus the metal particles are in direct contact to the a-Si:H material and the sub-bandgap EQE signal, related to strong fields at the defect locations is recovered. In contrast the sputtering of an a-Si layer or of the TCO back contact does not change the chemical composition in the NP environment. In case the environment is oxidized before, the negative influence is conserved by the sputtered layer. It protects the oxide from the reducing PECVD process.

Obtaining experimental insight into the chemical environment of the NPs within the different devices is difficult. In our case no clear influence on the optical absorption due to oxidation is found (Fig. 5.21). EDX analysis gives information on bulk properties. Due to the small amount of silver and the large amount of oxygen within the underlying layers - ZnO, SiO_2 (glass) - it is not possible to observe oxidation states of the Ag NPs. Auger electron spectroscopy (AES) is used in literature to distinguish the oxidation state of silver or silver NPs [211, 212]. Since the particles are capped inside the silicon, depth profiles with Argon ion beam sputtering are necessary to expose the NP region and perform the surface sensitive AES analysis. Because of different sputter efficiencies for the different materials, the sputtering leads to snowplow effects and mixing of the elements. Therefore no distinct statement or proof of the Ag oxidation can be made. AES analysis on bare Ag NPs is possible but gives no information on the environment of particles inside the devices.

Nevertheless, the made observations on the influence of exposure to atmosphere and the PECVD process are valuable in terms of device manufacturing. Especially when Ag NP preparation is not followed by PECVD deposition, in-vacuum processing of following layers is of major importance.

5.5.5. Ag NPs in µc-Si:H Devices

The role of the a-Si:H absorber material for the IPV created defect absorption has been discussed above. In this section the interaction of µc-Si:H with Ag NPs is investigated with respect to the IPV effect. For this purpose Ag NPs are introduced into Schottky type samples in the TCO/µc-Si:H n-i/Ag NP/TCO configuration (Fig. 5.22 (a)). In this case the intrinsic µc-Si:H absorber has a layer thickness of around 100 nm. This thickness is sufficient to guaranty the micro-crystalline growth and is thin enough to provide a strong built-in electrostatic field for charge carrier extraction in this n-i layer system. In this section the question whether the IPV effect is exclusively coupled to the
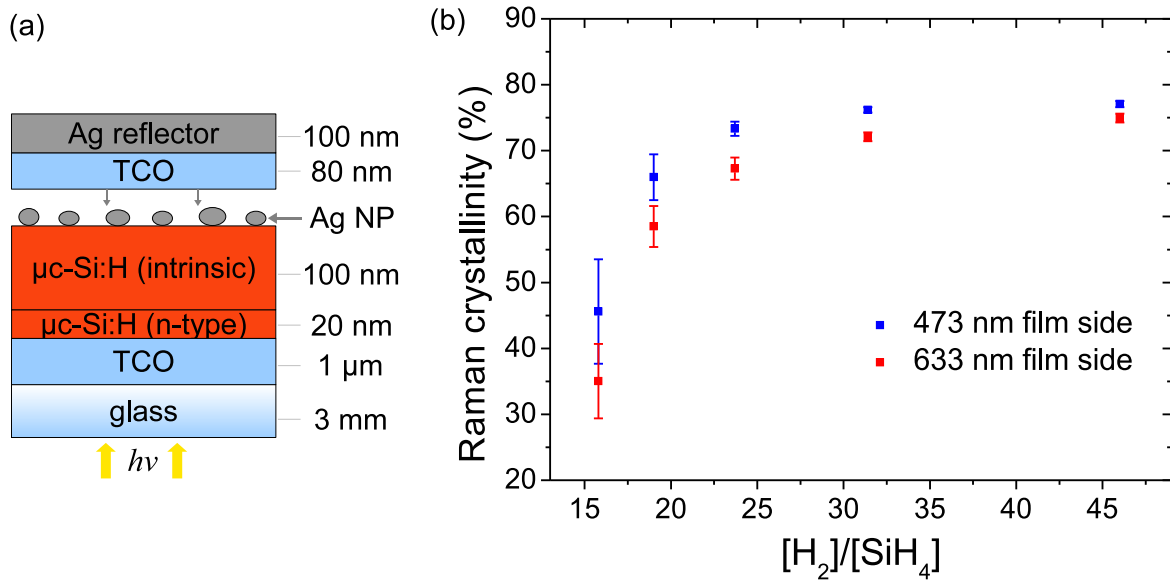
Figure 5.22.: (a) Sample design of devices used for experiments of the crystallinity influence on the NIR photocurrent. (b) Raman crystallinity versus hydrogen dilution ratio R = [H₂]/[SiH₄] in the PECVD gas flux during deposition of µc-Si:H samples. These measurements are performed on single µc-Si:H layers.

amorphous phase is investigated by using samples with different µc-Si:H crystallinities. Since µc-Si:H is composed of crystalline material in an amorphous matrix, an increase in crystallinity reduces the amorphous volume fraction.

For the cell experiments, µc-Si:H layers with an adjustable content of crystalline material and a sufficient small layer thickness had to be developed. As mentioned in section 2.3.1, the hydrogen dilution ratio $R = [H_2]/[SiH_4]$ i.e. the flux of molecular hydrogen $[H_2]$ with respect to the silane flux $[SiH_4]$ has a strong influence on the crystallinity. In the experiments, R is varied during PECVD silicon deposition, while the power as well as total gas flow are fixed. Fig. 5.22 (b) shows the Raman crystallinity factors (see section 3.2.9) versus dilution ratio $R = [H_2]/[SiH_4]$ for µc-Si:H layers deposited

on glass. With increasing dilution ratio, the crystallinity is increased and saturates for $[H_2]/[SiH_4] \geq 30$. The standard deviation of the Raman crystallinity for 19 sample positions uniformly distributed over the whole $1.4\,m^2$ substrate area is indicated by the error bars.

The decreasing width with increasing dilution ratio indicates that the homogeneity is enhanced for the most crystalline layers. In addition, these high diluted layers exhibit the best agreement of crystallinities deduced from measurements with the 473 nm and the 633 nm laser. The blue laser gives information on the top 50 nm while the red laser gives information of several hundred nm. This indicates that the crystallinity of the layers becomes more uniform in this deposition regime. To investigate the influence of the µc-Si:H material on the IPV effect, samples with different crystallinities of approximately 50-55 % and 75 % are chosen for cell experiments.
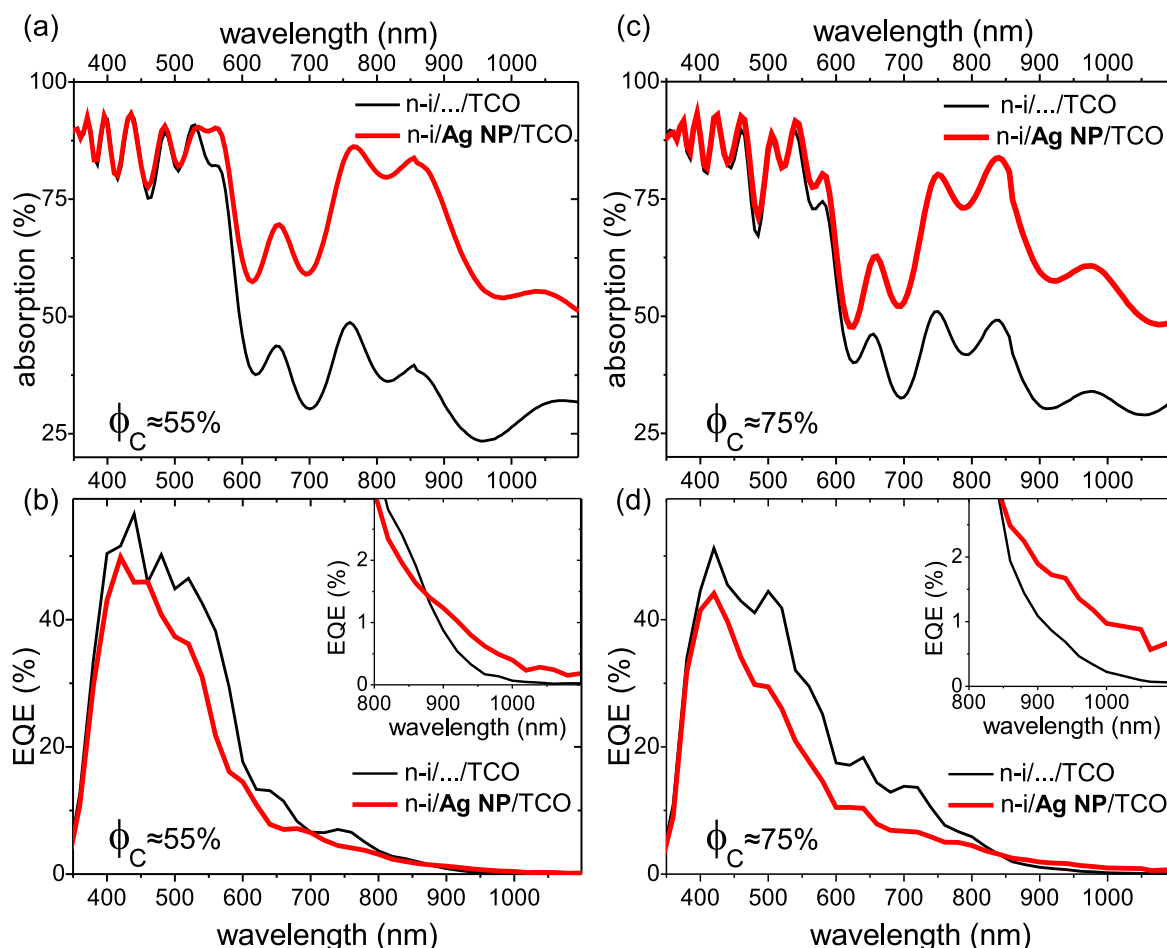

Figure 5.23.: Optical absorption and EQE of µc-Si:H samples with (a),(b) $\approx 50 - 55\,\%$ and (c),(d) 75 % Raman crystallinity.

The optical absorption, measured for the complete solar cell devices is shown in Fig. 5.23. The reference devices have a dominant absorption below 600 nm, however a significant amount of light is still absorbed up to 1100 nm. Similar to a-Si:H devices the NPs lead to a broadly enhanced absorption for NIR wavelengths, where the µc-Si:H absorption decreases.

The EQE signal (Fig. 5.23 (b)+(d)) shows a similar trend as the UV/Vis measurements. A dominant signal up to 600 nm is observed for the bare µc-Si:H samples. For larger wavelengths the EQE decreases, but in contrast to the a-Si:H samples a signal up to 1000 nm is observed. The increase of crystallinity leads to a slight redistribution of the sensitivity to different spectral regions. For the high crystalline sample the sensitivity in the visible range is reduced, while the signal in the regime above 700 nm increases and extends nearly to 1100 nm. This behavior is related to the increased microcrystalline fraction. However the layer thickness is too small in order to measure higher magnitudes. This in turn gives the opportunity to measure the influence of silver NPs on this still low absorbing regime. With incorporated Ag NPs the blue response is not strongly affected, indicating that for these wavelengths the charge carriers are generated far apart from the NP region. From 400 nm to around 900 nm the EQE is decreased. This is an indication for parasitic absorption by the NPs since the optical device absorption is enhanced in this regime. Light absorbed by the NPs cannot travel a second time through the absorber layer after reflection at the back contact. In addition recombination of charge carriers in the NP region will be involved. Above 900 nm the incorporation of NPs leads to an increase for both devices with different crystalline fraction. The NP induced signal even extends beyond 1100 nm indicated by a signal amplitude of still 1% in this region. The influence of the increasing crystallinity becomes obvious in a shift of the IPV signal towards lower energies, compared to a-Si:H samples. This is illustrated again in Fig. 5.24 where the EQE of Fig.5.23 is compared to an amorphous silicon device with the same i-layer thickness. The higher the crystallinity the stronger the response of the material to low energy photons. As in the case for a-Si:H samples a positive effect of the NPs on the photocurrent is only evident in the µc-Si:H low absorption region near the bandgap (900 nm to 1100 nm).

In conclusion, it has been shown that the IPV effect originating from the Ag NPs, is not limited to a-Si:H. Since the used µc-Si:H material has a crystallinity of 75 % a dominant coupling of the IPV effect to the remaining amorphous portion of the material can be excluded. For increasing crystallinity the sensitivity with Ag NPs is even increases and extends beyond 1100 nm. This indicates that IPV states are also present in µc-Si:H. Assuming they are broadly distributed in the bandgap, states near the bandedge are most dominantly addressed. Since the EQE measurement range is limited to 1100nm, a further judgement of the results is not possible. The variation
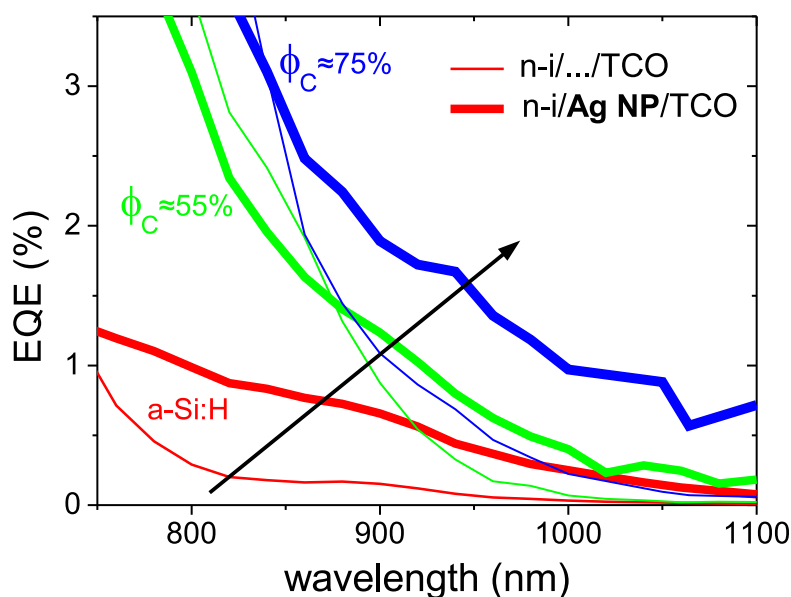
Figure 5.24.: EQE signal for wavelength above 750 nm, for a varying crystalline fraction of n-i devices with 100 nm absorber layer thickness. The Raman crystallinity is varied from amorphous silicon over $\Phi_C \approx 55\%$ up to $\Phi_C \approx 75\%$. The thin lines correspond to the reference, the thick lines to devices with incorporated NPs. The trend of the curves with an increasing Φ_C is indicated by the arrow.

of the crystalline fraction gives an additional parameter for manipulating the spectral sensitivity with respect to sensor applications and offers the opportunity to reach sensitivities above 1100 nm even for absorber layer thicknesses of only 100 nm.

5.5.6. Ag NP Induced Losses in the a-Si:H Strong Absorption Regime

Finally the optical losses caused by the Ag NPs in the visible spectral region are discussed in more detail. These losses are found for all thin film silicon devices with incorporated NPs. The device absorption in below 500 nm is close to 90 %. This indicates that nearly all light that enters the cell is absorbed, since the a-Si:H absorption is efficiently in this regime. The remaining 10 % are reflected at the glass and TCO interfaces before they interact with the absorber. For Ag NPs incorporated at the front TCO/a-Si:H interface a slight increase of absorption is measured. This is related to a reduced reflection at the TCO/a-Si:H interface (see Fig. 5.15). The NPs lead to a better light in-coupling, likely due to graded index matching effects between TCO and a-Si:H.

The general observation of a decreased EQE signal in this spectral region is hence not linked to an increased reflection. It is more likely related to absorption by the Ag NPs.

The decreasing EQE signal with increasing silver mass thickness (see Fig. 5.14) is an indication for that. The particles absorb the light which would otherwise be absorbed by the a-Si:H layers. Consequently a lower amount of electron hole pairs are generated and the EQE decreases. For samples where the NPs are positioned behind the absorber layers or at least not in front of it, behave in a different way (see for example Fig. 5.9). For the short wavelength regime the EQE signal does not reveal a significant difference between the reference and NP devices. Only above 500 nm the incorporated NPs lead to a reduction of the EQE signal. This is related to the strong a-Si:H absorption in this regime. No light is transmitted to the particle region. Above 500 nm the a-Si:H absorption coefficient becomes sufficiently small that light is transmitted to the rear side of the device. Without NPs it is reflected at the back reflector and is finally absorbed by the a-Si:H during the second pass. If NPs are present, they absorb a certain amount of the transmitted light that will not reach the absorber a second time. Hence the EQE is reduced above 500 nm.

Recombination via NP induced deep defects or surface recombination at the metal surfaces is certainly an important fact concerning the observed losses. This mechanism reduces the amount of collected electrons independent of their generation process. Charge carriers originating from band-band absorption undergo defect recombination as well as those originating from NP induced sub-bandgap excitation. Recombination and generation are competing processes. The fact that for the sub-bandbap regime the plasmonic excitation enables the generation, recombination just reduces the outcome. For the a-Si:H strong absorption regime the defect incorporation reduces the amount of collected charge carriers, without benefiting from enhanced fields in this spectral regime. The influence of recombination should be dominant for charge carriers that are generated near to the defect rich part of the device, i.e. near to the metal NPs. Due to the high recombination rate in this region, excited electron hole pairs directly recombine. If charge couples are generated apart from this region they are directly separated by the built-in field. One of the charge carriers does not have to pass the NP region and the recombination probability with an opposite carrier is lowered. Devices with NPs in the rear of the absorber should not suffer strongly from recombination for short wavelength because the blue light is absorbed within the very first part of the device and the electron hole pairs are separated before they recombine.

5.6. Summary

Ag NP agglomerates are incorporated into ultrathin photosensitive a-Si:H devices. Herewith the influence of the increased absorption caused by the LSP resonances of the metal NPs on the charge carrier generation of the a-Si:H structures is investigated. The main findings of this chapter are summarized as follows:

- The incorporation of NPs into photosensitive devices does not alter their morphology, as indicated by TEM investigations.
- The NPs have a strong influence on the spectral behavior of the developed a-Si:H structures with respect to the optical absorption as well as charge carrier generation. In the low absorption regime of a-Si:H (above 750 nm) the NPs induce a strongly increased absorption, related to their LSP resonances (see Fig. 5.4).
- The EQE measurement of different a-Si:H device configurations with incorporated Ag NPs reveals two important observations:
    1. In the a-Si:H strong absorption regime the EQE is reduced. This is related to parasitic absorption at the NPs. Hereby the absorbable amount of energy reaching the a-Si:H is reduced (discussed in section 5.5.6).
    2. The most important observation is a significant EQE signal in the presence of Ag NPs for photon energies smaller than the a-Si:H bandgap (e.g. Fig. 5.4 or Fig. 5.10).
- It is demonstrated for the first time, that the sub-bandgap signal originates in defects in the a-Si:H material that are created by the presence of the Ag NPs. The observed signal is related to the resonant enhancement of transitions due to the location of the defects in direct vicinity of the strongly absorbing NPs and according strong field enhancements. A model is proposed that in addition incorporates an alternative charge compensation and transport process. Thermal escape provides the completion of transition from the inner gap states to the nearest band edge (Fig. 5.11). The applied devices are a demonstration of the *impurity photovoltaic (IPV)* effect in a-Si:H (section 5.4.4).
- The IPV related signal is influenced by the LSP resonance energy. The IPV maximum position is shifted in agreement with a shift of the LSP resonance energy, caused by using different NP sizes (section 5.5.2).
- The position of E_F is of importance for the IPV effect, since occupied states in the bandgap are necessary for sub-bandgap transitions to occur (section 5.5.3).
- The effect is sensitive to the deposition sequence and the exposure of Ag NPs to atmosphere and the PECVD process. This behavior is probably related to oxidation and reduction of the Ag NPs (section 5.5.4).
- The IPV induced effect is also demonstrated for Ag NPs in μc-Si:H devices, it is therefore not limited to the a-Si:H phase (section 5.5.5).
- Large enhancement factors are calculated for the a-Si:H low absorption regime. Depending on the used photosensitive device structure enhancement factors between 40 and 200-500 are calculated (section 5.5.1).

The feasibility of the approach for the enhancement of solar cell performance is questionable. The losses introduced are not compensated by the advantage in the sub-bandgap regime. In addition the shown effects are observed for ultra thin photosensitive

structures. The application of NPs to devices with standard absorber layer thicknesses in the range of 200 to 300 nm only results in minor effects. Concerning a general possibility for the increase of the conversion efficiency is also questionable. As argued in [66, 67], the use of defect states close to the band edge with predominantly one optical and one thermal activated transition are not ideal for the use in the IPV effect. Such a device will not be able to overcome the limit of single junction solar cells, the voltage is reduced due to the effectively lower bandgap. Since the devices presented here suffer from other main limitations, like optical and recombination induced losses these arguments are not of importance.

Due to the enormous enhancement factors of up to 500, that are possible with these systems the effect can be of interest for near infrared detector applications. Especially the ability to control and manipulate the outcome and position of the effect might be of interest in this context. Using a comparably low µc-Si:H absorber layer thickness of only 100 nm in combination with Ag NPs results in a significant signal amplitude in the 900-1100 nm region. Without NPs a µc-Si:H layer thickness of several hundred nanometers would be necessary for a comparable signal.

6. Conclusions

The development of new concepts for PV application is an important challenge to enhance the cell efficiency. In particular an enhanced light absorption is of great interest. In this thesis the influence of metal nanostructures on solar cells and other photosensitive devices is investigated. Especially the plasmonic effects at metal nanostructures, like strong absorption and large electric field amplitudes assigned to them, are of importance. The combination of plasmonic nanostructures with amorphous silicon photovoltaics enables the enhancement of the device absorption and the application of alternative light trapping concepts.

To understand the interaction of particles with light and also the consequences of incorporated NPs on the device performance a knowledge of NP morphology is necessary. Therefore a first step was the investigation hereof. Silver film deposition is carried out by thermal evaporation as well as sputtering. Both methods are capable for preparing thin films with a controlled layer thickness. Depending on the deposition conditions initially closed films or metal islands are deposited. Subsequent annealing in all cases forms well separated NP agglomerates with a Gaussian size distribution. The mean particle size increases with increasing initial silver layer thickness. The optical response reveals the LSP resonance characteristic. The optical behavior of the particles was judged by Mie theory calculations. The observations are in good agreement with the calculations and the overall trends, as red shift with increasing particle size, can be reproduced. For a silicon environment and particles of around 20 nm diameter resonances in the range of 800 to 850 nm are observed.

The main focus of this thesis is directed on the influence of the enhanced absorption, due to the LSP resonances, on the charge carrier generation in amorphous silicon photosensitive devices. The starting point for the conducted investigations were observations of a sub-bandgap photocurrent signal in a-Si:H based devices due to the incorporation of metal NPs [37]. However, a clear identification of the phenomenon to a certain excitation path was not present and the role of the involved materials in the Ag NP environment was not yet resolved.

A deeper understanding of the processes involved in the phenomenon should be achieved. Especially the origin of states contributing to the sub-bandgap generation of charge carriers is of importance. For our investigations photosensitive devices with only one type of doped layer, i.e. i-layer/n-layer devices are used as well as more advanced systems based on n-i-p layer configurations. The variation of the particle

location within these devices enabled the investigation of the responsible mechanisms for the charge carrier generation.

For the first time it is demonstrated in this work that the sub-bandgap signal is a result of electronic states in the amorphous silicon. The defect states are exposed to the strong fields in the direct NP environment caused by the LSP resonances. Large transition rates from the defect levels to the band edges are possible. Charge carrier transport is assisted by the improved ultra thin layer design, since for standard a-Si:H layer thicknesses (200-300 nm) the built-in fields are too weak to compete with charge carrier recombination in the NP environment. A model related to this plasmon enhanced resonant defect absorption is presented, that incorporates an alternative charge compensation and transport process. Thermal escape of charge carriers from the defect levels to the nearest band edge complete the transition (Fig. 5.11). No direct contact to the TCO is necessary to provide carriers for charge compensation. The finding is a demonstration of the *impurity photovoltaic effect (IPV)* in a-Si:H.

The Fermi level position is of importance for the IPV effect, since occupied states in the bandgap are necessary for sub-bandgap transitions. The NP environment is of importance for the observation of the IPV generated photocurrent. The exposure of NPs to atmosphere has a negative influence on the observed signal. As a general advise concerning the device preparation, the in vacuum processing of Ag NPs and subsequent layers without the exposure to atmosphere should be favored.

For μc-Si:H devices a similar EQE enhancement is found in the presence of Ag NPs for near or sub-bandgap light. It is demonstrated that the IPV induced signal is not limited to the a-Si:H phase. The feasibility of the approach for the enhancement of solar cell performance is questionable. The losses introduced are not compensated by the advantages in the sub-bandgap regime. However, the effect can be of interest for near infrared detector applications. Especially due to the enormous enhancement factors that are possible with these systems. Depending on the used photosensitive device structure, enhancement factors between 40 and 200-500 are achieved.

For future investigations the influence of a mono-disperse particle distribution in the demonstrated devices could be of interest. Theoretical investigations by Akimov et al. indicate that for mono-disperse particles smaller damping losses are expected [213]. Maybe even higher enhancement factors are possible. Also the control of surface coverage would be a valuable tool. The enhancement of light trapping ability of Ag NPs for thin film solar cells depends on the coverage, as shown for example by Chen et al. [22]. The metal island film method is limited in this perspective. Here the particle coverage is specified by the amount of material as well as the annealing temperature and duration. Since the annealing for a-Si:H is limited to below 200 °C in order to keep the hydrogen in the material, this method provides no free parameters for control. Especially the question in how far the observation of the effect needs such dense

particle agglomerates, as applied in this thesis, is of interest. A lower density might accommodate lower losses, while the near field enhancement around sparsely distributed particles might be strong enough with respect to the photocurrent enhancement. Optical losses should be reduced with a lower amount of absorbing material, as it was observed for the cells with a decreasing particle size. Further investigations on this, especially by wet chemical deposition approaches, that allow a control of size, particle density etc. would be valuable. Especially the application of smaller particles should be investigated, since a decreasing EQE enhancement with increasing particle size was observed. Additionally, small particles should influence the structural properties of layers, deposited on top of them, to a lower extend than large NPs. In particular the shunting problem observed for cells with incorporated NPs should be reduced with smaller and fewer particles.

The observation of the IPV effect for µc-Si:H points to the possibility of a similar effect in c-Si devices by the incorporation of Ag NPs. Similar approaches for the combination of Ag NPs and c-Si cells have already been conducted by Catchpole et.al [16, 17, 214], with respect to light trapping (far field scattering). The near field effects related to the plasmon enhanced IPV effect might also be observable. Of course a suitable device configuration is necessary for these investigations.

A. Appendix

A.1. Development of Thin Film Sputter Deposition on Large Area Substrates
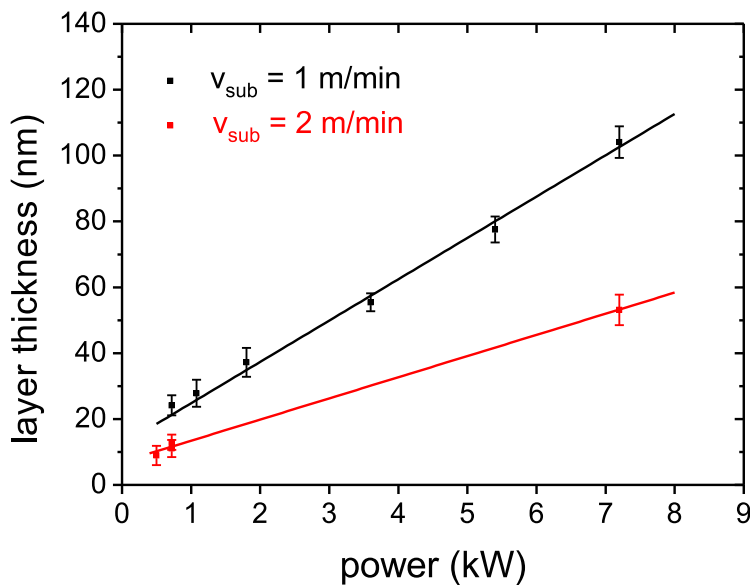
Figure A.1.: Ag layer thickness versus applied DC power for two different substrate velocities.

The inline sputter setup is designed for the deposition of thick layers in the order of several hundred nanometers. Standard ZnO layers have a thickness of approximately 1 μm. Thin layer deposition of silver in the order of 10 nm is hence a challenge. The parameter with the most dominant impact on the deposition rate is the applied dc power. For this purpose a series with different dc power values at otherwise fixed conditions was investigated. Fig. A.1 shows a variation between 0.5 and around 7 kW for two different substrate velocities, i.e. two different deposition times. Lower dc power values could not be investigated because this results in an unstable plasma excitation, due to reaching the threshold for plasma ignition. The rate is proportional to the applied power as indicated by the linear fitted increase of both data sets. The positive

offset of both curves is related to the minimum threshold power that is necessary to ignite a plasma in addition to a larger uncertainty of profilometry measurements for layer thicknesses below $20\,\text{nm}$. The deposition rate is estimated by taking into account the deposition geometry (Fig. 3.3). The target emits a material flux that coats the substrate with a certain width. Assuming an effective deposition region near to the target of approximately $s = 20\,\text{cm}$ and considering a substrate transport velocity of $v_{\text{sub}} = 1\,\text{m/min}$, for example. Then each point on the substrate moves for a time $t_{\text{trans}} = s/v_{\text{sub}} = 12\,\text{s}$ across that deposition area. Within this time the total layer thickness d is deposited. The deposition rate is then calculated by $R = d/t_{\text{trans}}$. This is a rough estimation and represents a mean deposition rate, since the angular distribution of emitted target atoms and with it a a varying rate perpendicular to the target axis is not taken into account.

Mean deposition rates of $R = (8.7 \pm 0.4)\,\text{nm/s}$ for the highest power down to $R = (1.5 \pm 0.5)\,\text{nm/s}$ for a power of $0.5\,\text{kW}$ are obtained by this estimation. This still represents a quite high rate, that is however low enough to prepare thin layers in the range of $10\,\text{nm}$ when transit times of around $6\,\text{s}$ corresponding to a velocity of $v_{\text{sub}} = 2\,\text{m/min}$ are chosen.

An adaptation of the used sputtering pressure and Ar flux was in addition investigated. Since only minor variations in the rate were obtained in the covered parameter space this approach was not further recessed. The deposition on large scales goes along with certain variations concerning thin film formation and homogeneity of initial films. In Fig. A.2 the progress of sheet resistance versus layer thickness is plotted. For film thicknesses above $50\,\text{nm}$ a low resistance is measured, that slightly increases with decreasing film thickness. Below $40\,\text{nm}$ the resistance strongly increases, while the inhomogeneity (illustrated by the error bars) accordingly increases. This is an indication for the formation of films that are not continuous. The bar plot (Fig. A.2 (b)) indicates that quite strong variations occur across the 1.4m^2 substrate. Some regions show a low resistance while others exhibit a high resistance. The SEM images belonging to these different regions illustrate very well the influence of microscopic film morphology on the resistance. In regions where a quasi closed film is found (d) the resistance is low, while in agglomerated regions (c) a high resistance is measured. The variations could be related to slight inhomogeneities in film thickness because the films are close to the percolation threshold and therefore slight differences in thickness have a strong influence on the resistance. Also local variations in substrate temperature due to the sputtering process could result in different surface mobilities and hence local agglomeration.

After annealing, such thin films posses a much more homogeneous appearance, since all over the substrate NPs are formed that exhibit similar sizes and optical response. This is exemplary illustrated in Fig. A.3 (a) by the sheet resistance for a $10\,\text{nm}$ thin
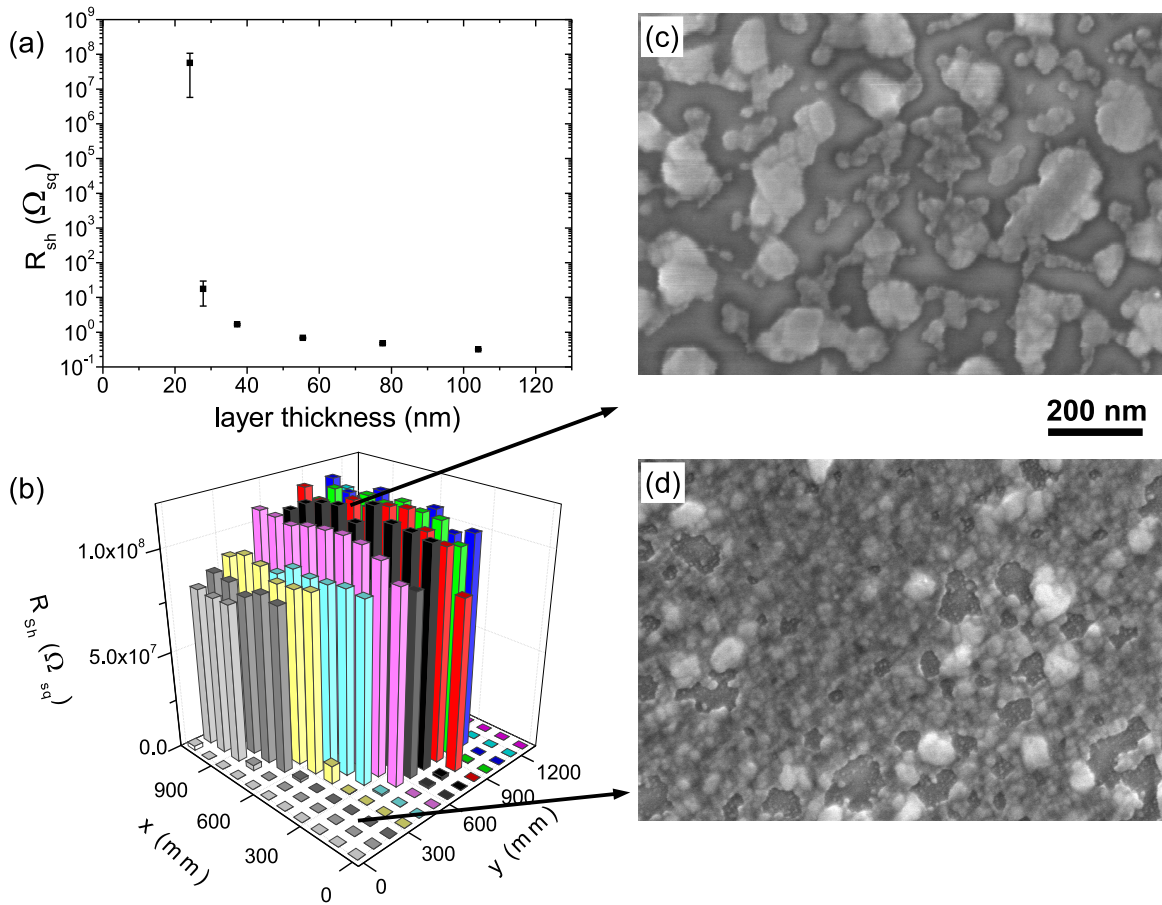
Figure A.2.: (a) Propagation of sheet resistance with layer thickness. The strong increase for small layer thicknesses indicates that the films are constituted of islands. (b) The inhomogeneous sheet resistance of a 20 nm thin Ag layer across the $1.4\,\mathrm{m}^2$ substrate. The difference between high and low sheet resistance is caused by the microstructure. Slight variations in the layer thickness result in different morphologies, that are observable in SEM images (c)+(d). In (c) an island film (related to a high sheet resistance) is observed, while in (d) a nearly closed film (low sheet resistance) is observed.

silver layer on glass after annealing. A high sheet resistance is found for all sample positions indicating the formation of NPs. For the same Ag layer thickness deposited on an ZnO:Al layer the optical response of different sample positions is shown in (b). The LSP induced absorption peak does not differ significant across the sample positions. This is an indication for a homogeneous distribution of particle sizes across the large substrate.

(a)

(b)
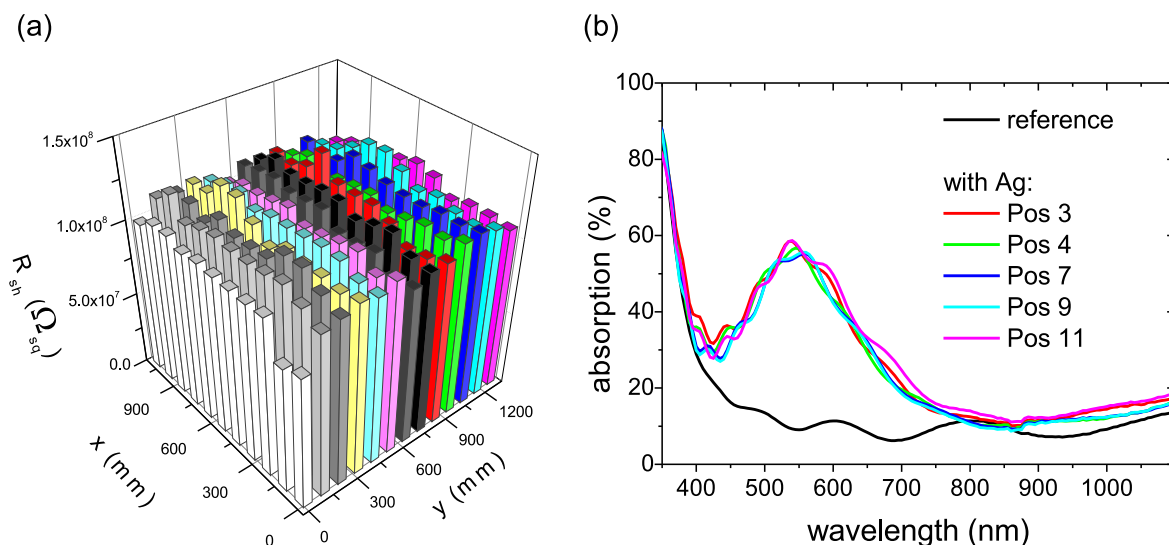
Figure A.3.: (a) Sheet resistance of 10 nm thin silver film on large area substrate after annealing on glass. The resistance is very homogeneous according to the formation of NPs at all sample positions due to annealing. (b) Optical absorption of the same silver layer thickness after annealing on a smooth ZnO:Al layer. The fringes are caused by thin film interferences. Several positions across the large substrate (according to Fig. 3.14) are indicated. Only minor variations with respect to the sample position are observed.

A.2. Development of a Laboratory UHV Multi-Chamber Sputter System

In the course of this work a facility for the deposition of thin metal films as well as silicon and ZnO on small substrates (5×5)cm^2 under UHV conditions was constructed and build up. Some special aspects of the construction and assembling have been conducted by a Bachelor's student[150]. In that thesis the setup was in general presented. Therefore, only the major setup and some special issues are discussed here.

A.2.1. Setup of the System

In Fig. A.4 the Multi-Chamber Sputter Setup is shown. It consists of different ultra high vacuum (UHV) chambers denoted as load lock, transfer and two deposition chambers (main sputter and reactive sputter chamber). The main sputter chamber contains two sputter sources as well as an evaporator for metals, while the reactive chamber contains one sputter source. These two chambers have the possibility to be separated by a gate valve in order to perform reactive sputtering in the small one without contamination of the other chamber.

Figure A.4.: UHV Multi-Chamber sputter facility with four separated UHV chambers: load lock, transfer, main sputter and reactive sputter chamber. The main components marked with numbers are: (1) magnetic transfer probes (2) Bayard-Alpert/Pirani full range pressure gauges (3) gate valves (4) sputter sources (5) x-y stage (6) turbo molecular pumps (7) butterfly valve (8) evaporator.

The vessels are separately pumped by turbo molecular pumps in combination with oil free backing pumps. The load lock is pumped by a Pfeiffer TMU 065 with a volume flow rate of 56 l/s [215] and a diaphragm backing pump. The transfer chamber is equipped with a TMU 260 (210 l/s [216]) and a diaphragm backing pump. The deposition chambers require pumping systems providing a high volume flow rate to handle large amounts of gas as well as low base pressure. The main sputter chamber has a TMU 520 (520 l/s) [217] that is backed by an Adixen ACP 28 multi-stage roots pump ($27\,\mathrm{m^3/h}$) [218]. For additional control of vacuum conditions the main chamber is equipped with a quadrupole mass spectrometer. In the reactive sputter chamber a TPU 510 (500 l/s) [219] pumps in series to a second turbo pump TMU 260 KGT that is backed with a diaphragm pump. The second turbo pump provides a good backing pressure to the TPU 510 as well as a high flow rate.

Base pressures that are reached vary between the chambers, since they obey different sizes and are pumped with different pumping equipment. The load lock chamber

reaches a pressure of $4 \cdot 10^{-8}$ mbar. In the transfer chamber, due to the comparably large dimensioned turbo pump and the heating stage a pressure of $6 \cdot 10^{-9}$ mbar is reached. The sputter chambers obey a larger surface area due to the chamber walls and the gas pipes with small diameter. This results in a base pressure of about $5 \cdot 10^{-8}$ mbar for both chambers.
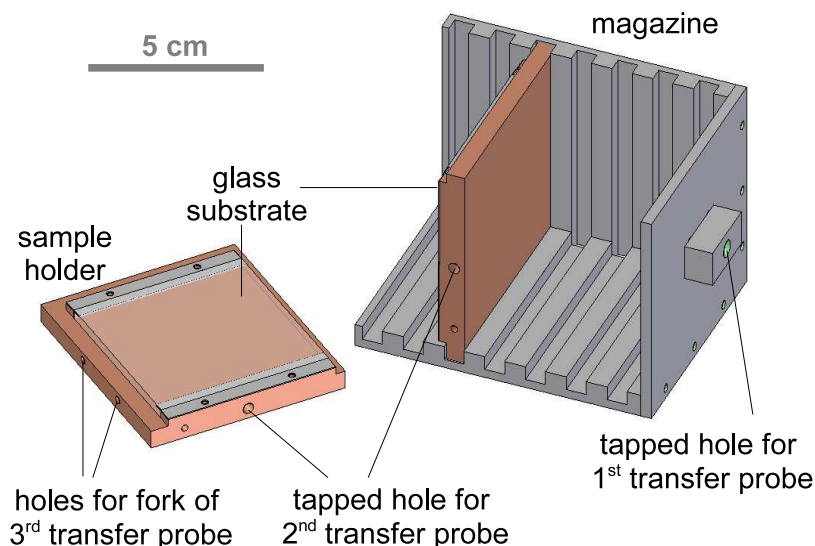

Figure A.5.: Sample magazine here shown with one copper sample holder. The magazine can support seven sample holders. Substrates of maximum $5 \times 5\,\text{cm}^2$ and a width of $3\,\text{mm}$ can be mounted to the sample holder by two copper sheets pressing the substrate onto the sample holder.

The load lock chamber is used to transfer samples into the vacuum system. For this purpose a Viton sealed view port is mounted to this chamber. The load lock is equipped with a sample magazine that is mounted to the 1$^{\text{st}}$ magnetic transfer probe. The magazine (see Fig. A.5) can be loaded with seven sample holders and are transfered in vacuum to the transfer chamber. Here a second vertically aligned transfer probe can pick up a sample holder from the magazine. This is done by a threaded bar mounted to the second probe, that fits into a taped hole in the sample holder. By rotating the transfer probe, the bar is screwed in the hole and the sample holder is rejected out of the magazine. To transfer the sample holder further to the deposition chambers the third transfer probe is used. This probe is equipped with a fork that fits into two holes of the sample holder, vertically aligned to the taped hole. Thus by introducing the fork and unscrewing the threaded bar, the sample holder is manipulated from the 2$^{\text{nd}}$ to the 3$^{\text{rd}}$ transfer probe. With this probe the sample is brought to the desired position in the main or reactive sputter chamber, shown in more detail in Fig. A.6. All three
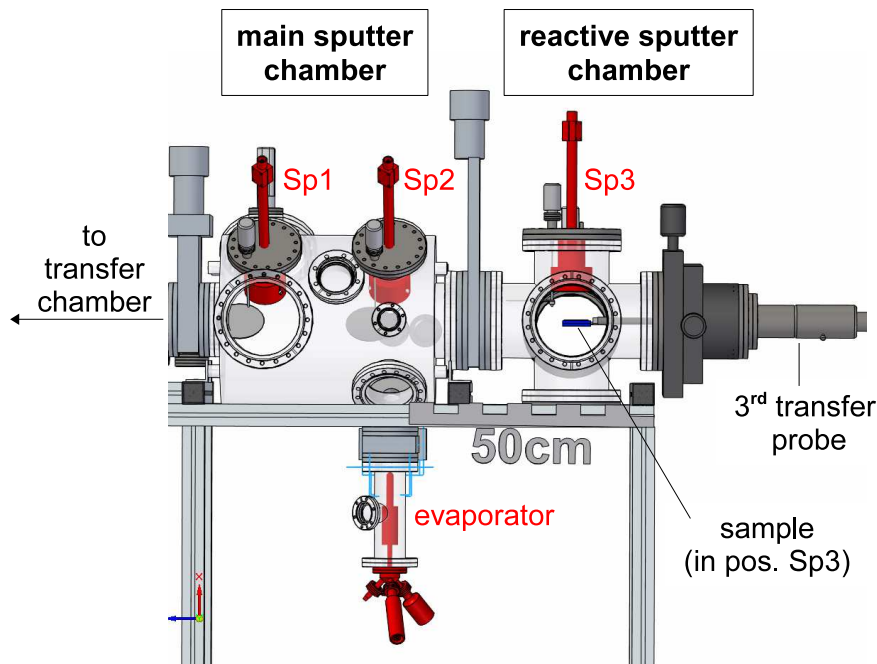
Figure A.6.: Deposition chambers with three sputter sources and the evaporator (shown in red for clarity). Vacuum vessels are made transparent for better illustration.

sputter sources are faced to the center of the chamber with a distance of 11 cm. Sputter source Sp3 is mounted vertically above the center of the chamber, while sources Sp1 and Sp2 are mounted with an angle of 45 deg with respect to the vertical. The sample surface is lying in the center of the chamber as well as coplanar to the transfer probe axis. By rotating the transfer probe, the sample surface is always faced radial towards the chamber walls. This is important because the sample has to be rotated 45 deg for vertical alignment towards Sp1 and Sp2 and providing normal incidence of target atoms on the substrate surface. The transfer probe is mounted to an x-y stage that allows the adjustment of the distance between sample and sputter sources. In the x-y stage mid position the sample surface lies in the chamber center. For depositions with SP1 and Sp2 one has to be careful in order to keep the sample centered on the sputter sources axis.

Sputter Sources

The sputter sources (Fig. A.7) used in the setup are MAK sputter sources from MeiVac Inc. with a target diameter of 3" (7.62 cm) [220]. The magnetron sputter sources consist of a magnet assembly as well as a copper cathode ring and an outer anode ring. The anode ring can be adjusted in hight. This allows to align it to targets of different thickness or to protect the target from cross contamination with other
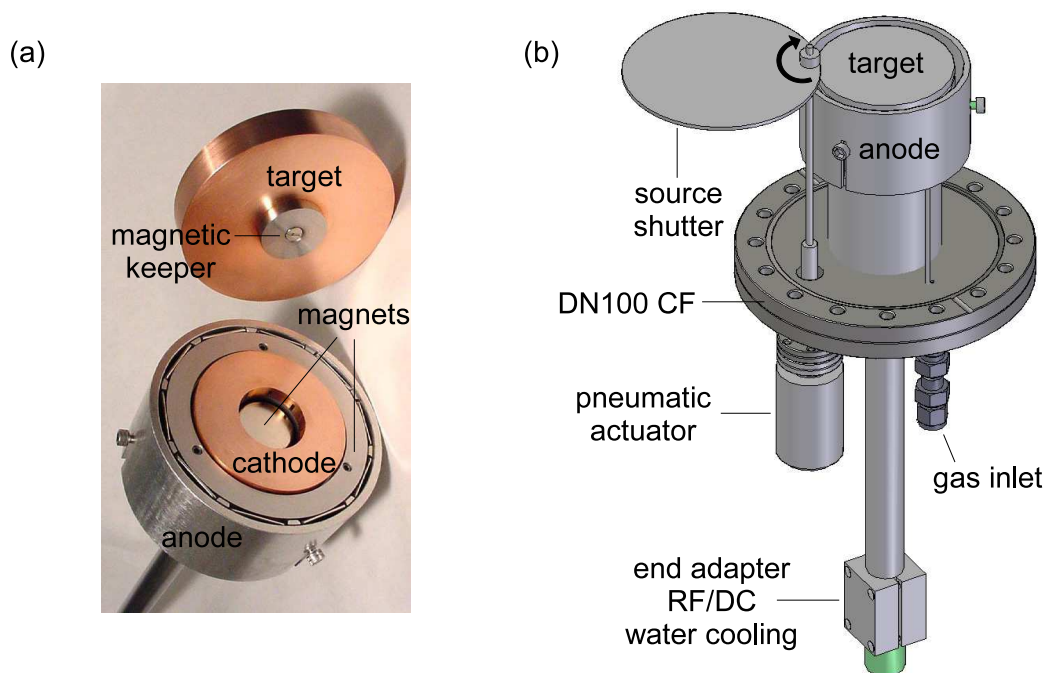
Figure A.7.: (a) Photo of MAK sputter source with demounted target, from [220]. The target has a diameter of $3\,\text{inch} = 7.62\,\text{cm}$. (b) Drawing of sputter source mounted on a DN 100 CF flange with pneumatic actuated source shutter.

materials from adjacent sputter sources. The target mounting is executed by a magnetic keeper attached at the rear of the target. It is coupled to the magnetic field provided by the source magnets. Each source is equipped with a shutter that can be rotated by a pneumatic actuator. This allows fast opening and closing of the source which is important for precise control of deposition time and resulting film thickness. The shutter additionally acts as protection from cross contamination when closed. Due to the large amount of produced heat during sputtering, the sources have to be water cooled to protect them as well as the target from overheating and thermal damage. For this purpose cooling water lines are integrated in the sources, emerging out of the end adapter. This adapter also features an HN-connector for RF or DC power supply.

Gas Management System

Gas for sputtering is injected directly to the source by a feedthrough and a metal steel pipe connected to the anode ring. A gas distribution system is responsible for the management of gas flows to the single sources (Fig. A.8. It consists of $6\,\text{mm}$ stainless steel pipes connecting the gas bottles with the sputter sources. Mass Flow Controllers (MFCs) are responsible for control of gas fluxes. Sputter sources Sp1 and Sp2 have to be fed with Argon gas for regular sputtering. The gas flow for these two sources is controlled by one mass flow controller (MFC1). Source Sp3 is optionally used for

reactive sputtering, thus it has to be supplied by Argon as well as Oxygen. For this purpose two mass flow controllers (MFC2 and MFC3) are connected to this source, providing an Ar O_2 gas mixture in an arbitrary ratio. The gas pipes can be closed at several positions by valves in order to block the flow to certain pipes or for maintenance work at the gas system without influencing other parts of the system.
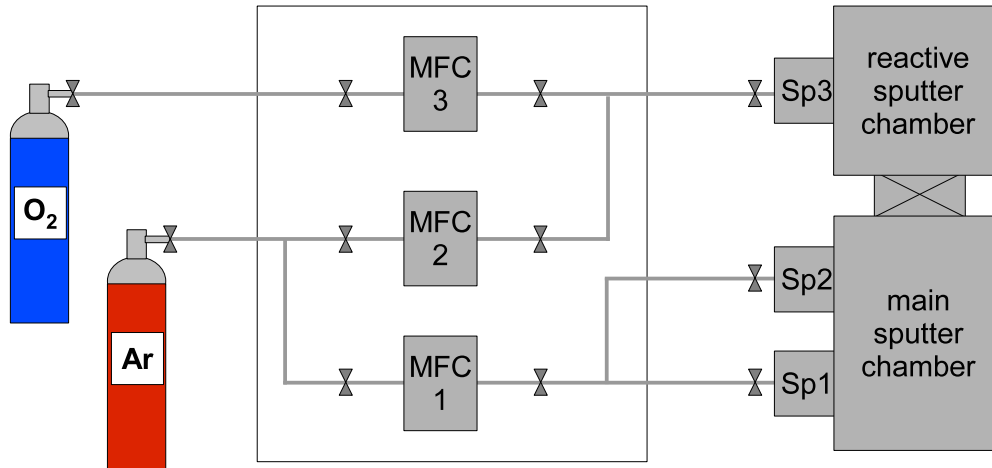

Figure A.8.: Schematic drawing of the gas distribution system. The Mass Flow Controllers Type 1179B from MKS control the gas flow of Argon and Oxygen with a maximum of 50 sccm each [221]. The system allows to distribute Argon to all three sputter sources, while Oxygen or a mixture with Argon can be injected only to sputter source 3 in the reactive chamber.

Sputter Source Power Supply

For the sputtering process a pressure in the order of $1e^{-3}$ mbar to $1e^{-2}$ mbar is used. To provide a stable pressure during sputtering the gas flow is fixed to a certain value, while the amount of pumped gas is controlled by butterfly valves. These are positioned in the tube between the turbo molecular pumps and the vacuum vessel. The PID controlled butterfly valve uses the measured pressure as feedback signal for controlling the opening profile of the tube. It is thus able to tune the pumping rate. Alternatively the position of the butterfly valve can be set in position control to a fixed value. Under certain conditions this is preferred with respect to pressure control because of better stability. The used deposition pressures are only possible with butterfly valves, without them a much higher gas flow would be necessary. Because of the limited turbo pumping speed this can not be realized.

The three sputter sources are driven by two radio frequency (RF) systems as well as one direct current (DC) power supply. The RF system consists of three main components. An RF generator (Seren R601) provides the RF power of maximum 600 W. This power is coupled to the system by high frequency cables via a matching box (Seren AT-3). This matching box is responsible for providing stable plasma conditions by matching the impedance of the vacuum vessel and the plasma to the impedance of the RF generator. This is done by inductive coils and adjustable capacitors [222, p. 5]. The matching box is controlled by a matching network (Seren MC2), this minimizes the measured reflected RF-power by adjusting the capacitor position of the AT-3. Thus the RF power coupled into the plasma is maximized and a stable plasma is provided.

For DC bias sputtering, a DC power supply (Advanced Energy MDX 500)[223] provides 500 W of power by applying a high voltage of 1000 V between the cathode and the anode. Technically this is much more simple because it does not need to be controlled over a matching network. The remote control of the MDX 500 is discussed in more detail in Section A.2.2.

Evaporator

The evaporator integrated in the setup faces to the center of the chamber and thus to the axis of sample manipulation. It has a distance of 40 cm to the sample surface plane. This evaporator has been applied in a previous setup and was used for deposition of thin metal films on small substrates ($\approx 1 \, \text{cm}^2$). The substrates used in this work have lateral sizes of $(5 \times 5) \, \text{cm}^2$. Due to the fact that the evaporator does not provide a homogeneous deposition rate over this substrate area, it is not used for sample preparation in the course of this work. The setup and operation of the evaporator is described elsewhere [224, pp. 23-28].

Sample Heating Stage

The transfer chamber is composed of two vacuum vessels, the actual transfer chamber as well as an adjacent vessel in line to the second transfer probe. This adjacent vessel is equipped with a sample heating stage (Fig. A.9) to which samples can be transfered by the second transfer probe. The heating stage consists of a rectangular copper plate with a resistive heating wire embedded at its rear side. The resistive wire is inserted in designated groves at the rear to which it fits optimally in order to guaranty a good thermal transfer to the copper block. The wire (Thermocoax SEA 15/150 [225]) has a resistance of R = 8.2 Ω. To apply a certain heating power P one has to apply a voltage U according to $P = U^2/R$. For the used power of 150 W a voltage of around 35 V is applied by a Delta Elektronika SM7020 power supply [226]. The output of the SM7020 is controlled by a Microtronic Micro 96 PID controller [227] in combination with a feedback from a thermocouple mounted to the heating plate. In this way the heating

temperature is controlled. The interior of the copper plate is equipped with channels for water, air or liquid nitrogen cooling in order to cool the sample subsequent to a heating process. The heating stage is mounted to a linear translation unit (see Fig. A.9 (a)) that allows a vertical movement of the plate (up and down). By bringing the heating plate
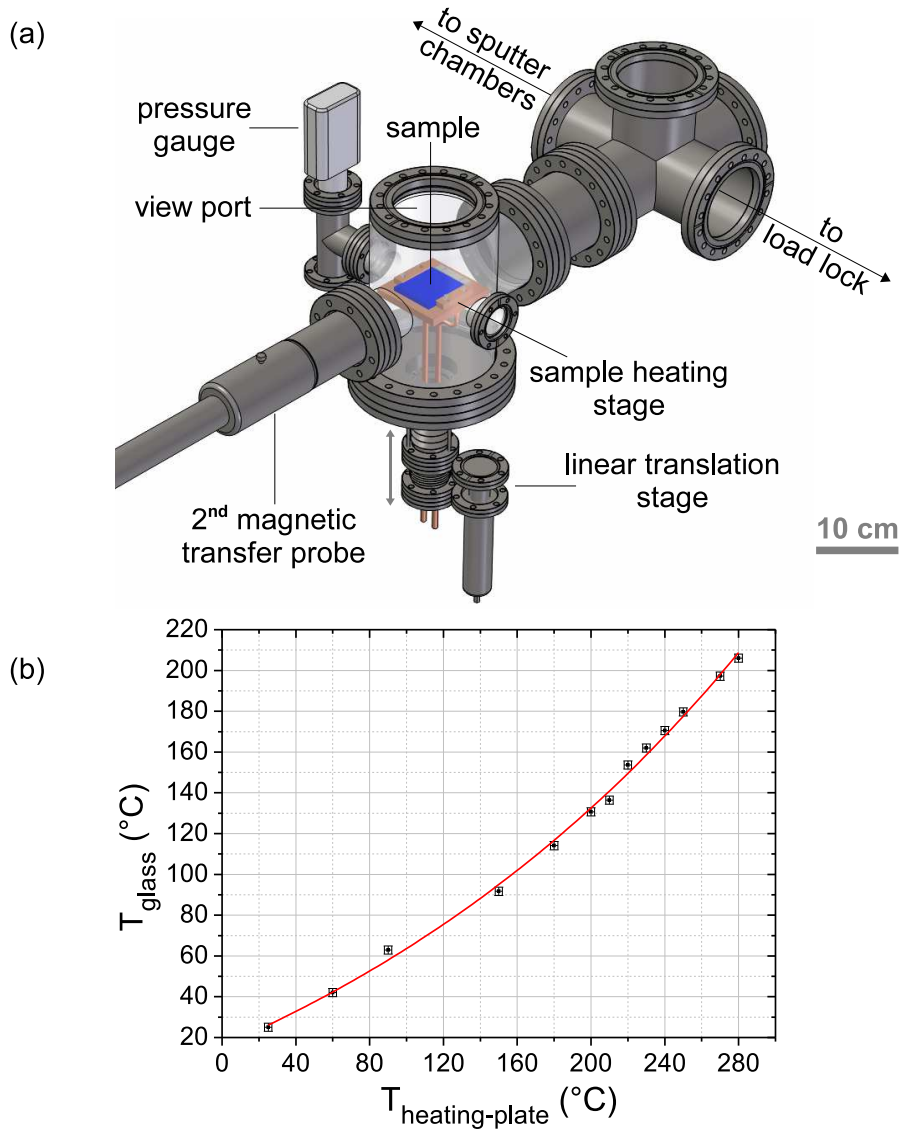

Figure A.9.: (a) Transfer chamber with integrated sample heating stage. To give an insight into the interior, the stainless steel vessel containing the heating stage is illustrated transparent. (b) Substrate temperature as function of heating plate temperature.

in the plane of the sample manipulation axis, samples can be loaded and unloaded from the transfer probe to the heating plate. The sample itself is clamped on the plate by two brackets which are depressed by four spring engaged screws. This clamping ensures a thermal contact of the sample holder to the heating plate that is as good as possible.

Since the temperature is measured at the heating plate, it does not give the actual substrate temperature. This is reduced due to a limited thermal conductivity between the heating plate and the sample holder as well as between the sample holder and the glass substrate. Direct substrate temperature measurement with a thermocouple is not possible due to sample transfer. In order to get to know the sample temperature as a function of the heating plate temperature, reference measurements are conducted. Here a second thermocouple is clamped to the glass surface allowing the simultaneous measurement of both temperatures. For the measurement (shown in Fig. A.9 (b)) the sample was allowed to reach thermal equilibrium with the heating stage for 20 min at each temperature step. The most noticeable observation is a significantly lower substrate temperature with respect to the plate. The curve is fitted quite well with an exponential curve. For using a sample temperature of around 180 °, the copper plate must be heated to 250 °.

A typical annealing process is performed as follows. For a designated sample annealing time of 30-60 min the sample is again allowed to reach thermal equilibrium for 20 min. After the 30 min additional annealing time heating is interrupted and the stage is cooled with a continuous air flow via the cooling channels. When the sample has cooled to room temperature, it is transfered to the subsequent processing step.

A.2.2. Control and Automation of Components

All relevant components of the setup are monitored and controlled via a computer. For this purpose a measurement and control program written in LabView was developed. This allows the simultaneous status read out of all components and their control. The front panel is shown in Fig. A.10 and A.11. The pressure is steadily monitored for the four individual chambers as well as the status of the eight cooling water lines for the turbo molecular pumps and the deposition sources. Via the different tabs of the front panel the status read out and manipulation of different other functions is possible. In (a) the status and position of the butterfly valves is monitored and can be adjusted. Either a fixed position is set or a specific pressure value, this forces the valves PID controller to control the pressure to the designated value. The tab in (b) allows the monitoring and control of the gas flux and its distribution to the different sputter sources. In (c) the different deposition sources are controlled and their status is monitored. Here the forward power reflected power, build up self-bias between cathode and anode are monitored. On the right hand side the layer deposition can be initialized. After the process time has elapsed, the source shutter is closed by the program and the output of the sources is turned off. The data according to that deposition run (time, gas flux, pressure, applied power, self-bias, butterfly valve position) are written to a log
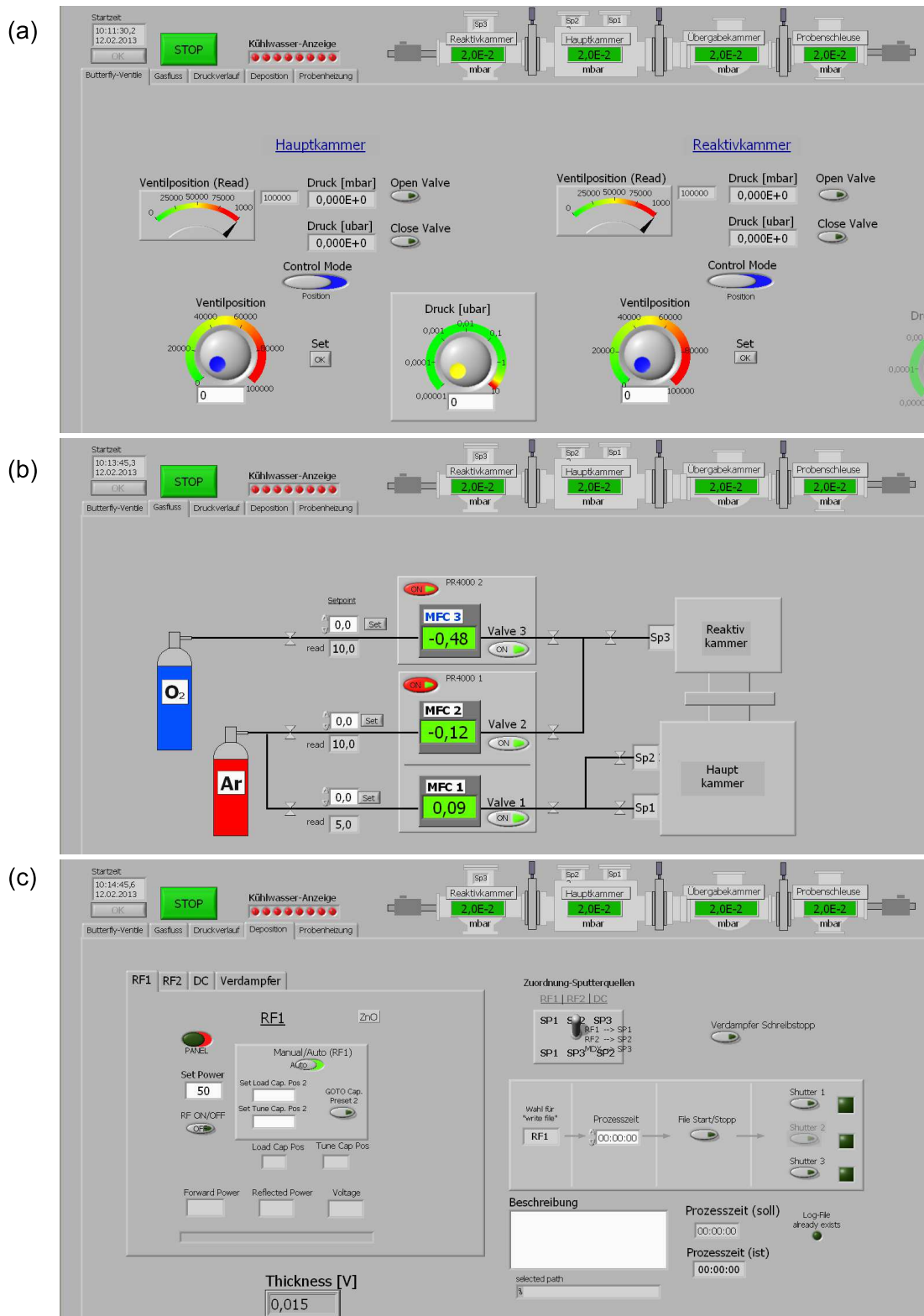
Figure A.10.: Front panel of the developed LabView program for control and monitoring of the different components of the sputter setup. (a) Control of the butterfly valves, (b) control of the MFCs for the gas distribution system and (c) control of sputter sources for thin film deposition.
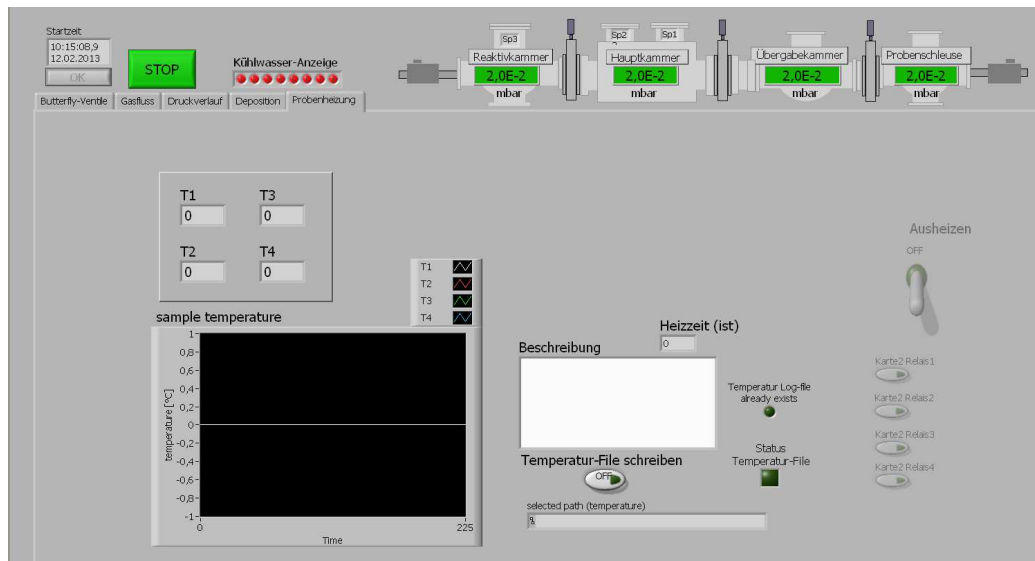
Figure A.11.: LabView front panel for control and monitoring of sample annealing.

file for process documentation. In Fig. A.11 the sample annealing is monitored, while the temperature and pressure in the annealing chamber are written to a log file. The program incorporates several interlock functions in case a certain failure occurs before or during a process. For example the cooling water of a source does not work, the operation of that specific source is not possible or will be stopped. The same happens in case when the pressure is out of the specified range for the sputter sources.

The communication to the different devices is usually provided via serial bus RS232 ports. These allow a command based control of the device functions. The remote control of the DC power supply (MDX 500) is not possible via serial bus communication. Instead the device is equipped with a 25-pin analog/digital sub-D connector [223]. The pins provide the possibility to monitor data like output current, voltage, power etc. via analog voltage signals or the status of different functions by digital signals (on/off). The control of certain functions like output set points, choice of output regulation method (current/power regulation) or switching of output power and others is possible by applying voltage signals to certain pins of the port. To control and monitor this via a remote PC, a digital analog converter / analog digital converter (DAC/ADC) is necessary. In addition a remote controllable relay card is used to switch certain pins to ground potential to turn special functions on and off (for example to turn remote control on or off). A schematic illustration of the wiring between the MDX 25pin user port, the DAC/ADC card and the relay card are shown in Fig. A.12. Additionally three interlock functions (main, vacuum and water interlock) are connected to the relay card for safety reasons. In case of too high/low process pressure or failure of the cooling
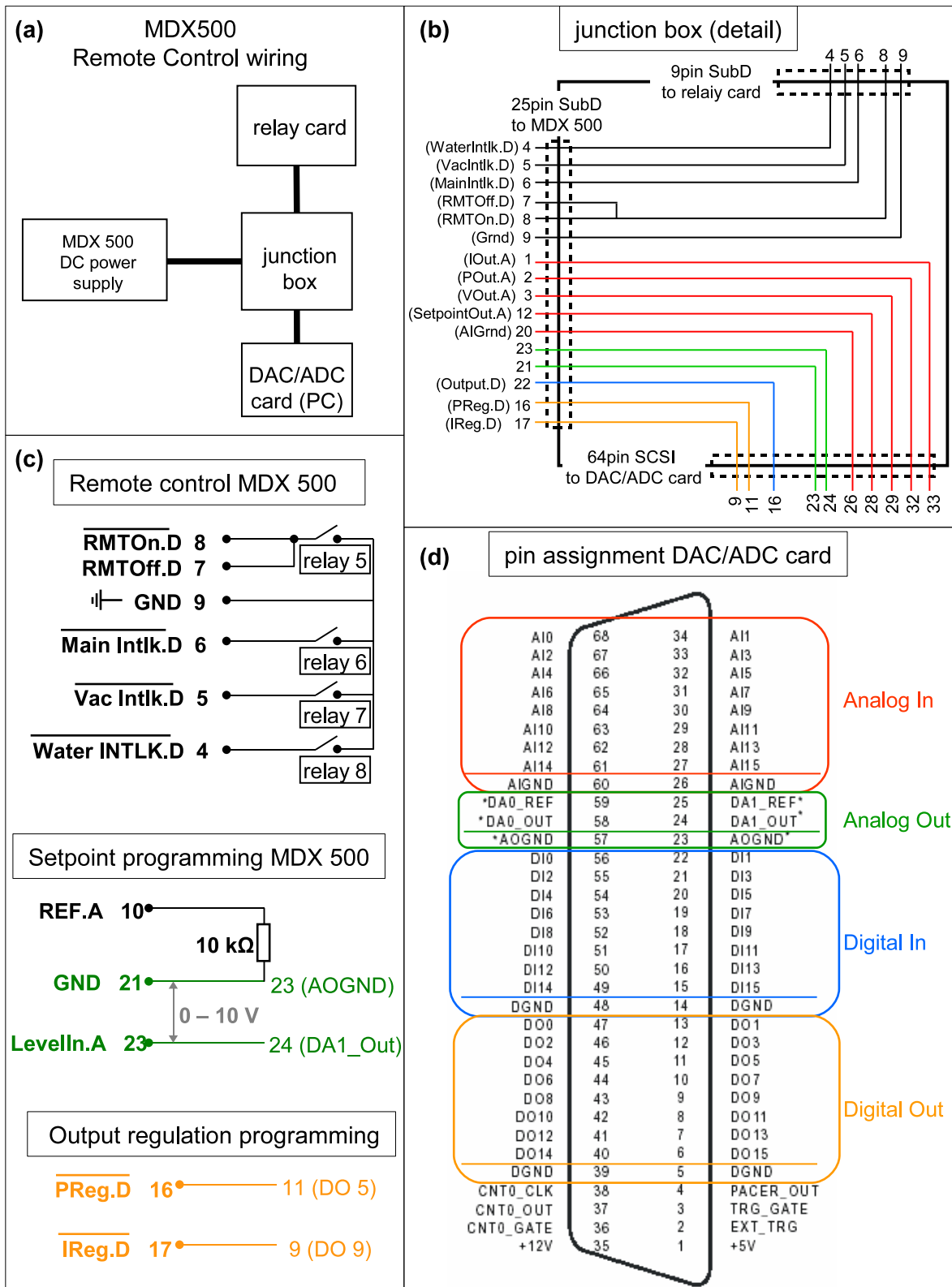
Figure A.12.: (a) Control and monitoring of MDX 500 DC power supply with a DAC/ACD card in combination with a relay card. The wiring is merged by a junction box. (b) Wiring inside the junction box connecting different ports. (c) Detailed wiring connections for different control and monitor functions of the MDX 500. (d) Pin assignment of DAC/ADC card connector.

water system, the according relay is switched by the software. In such a case the output of the MDX will switch off.

A.2.3. Characterization of Sputter Processes
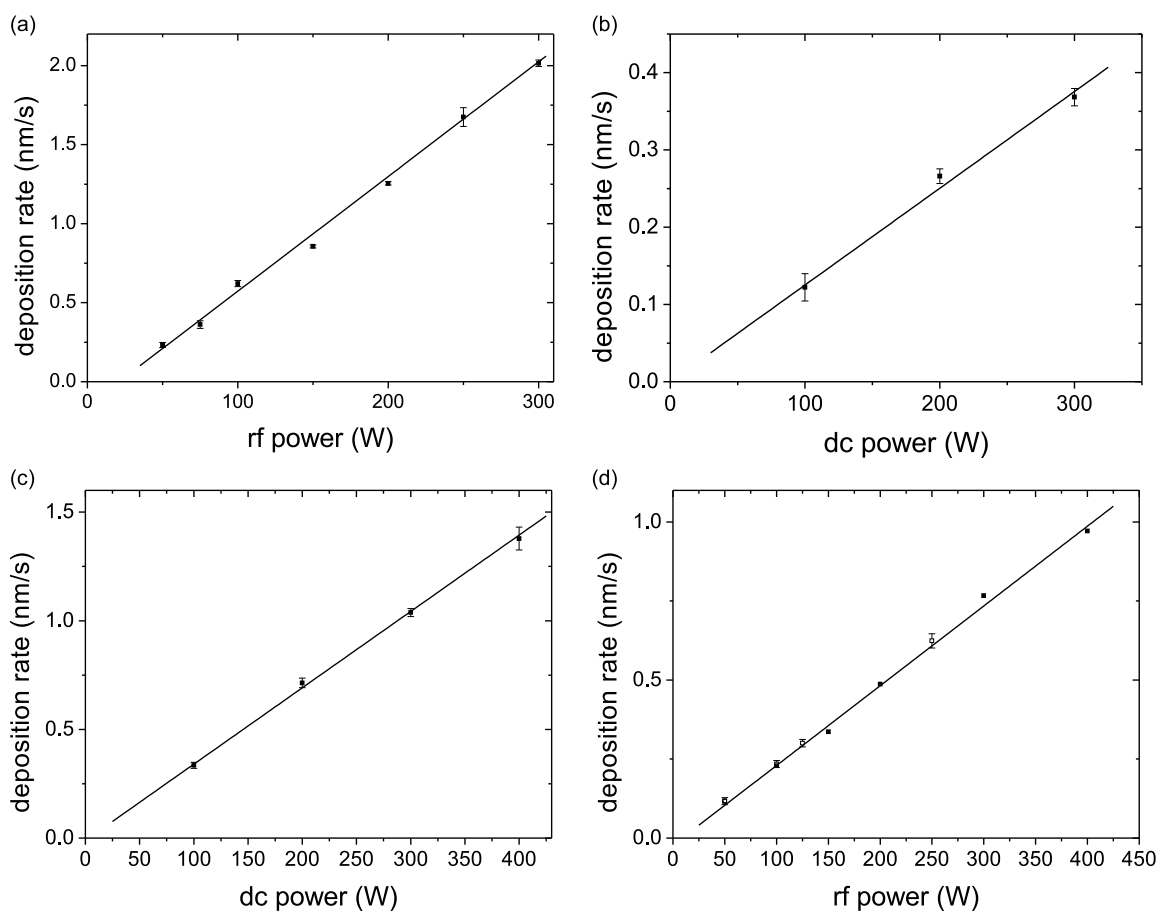
Figure A.13.: Deposition rate vs. applied power for the different targets, at a pressure of 10^{-2} mbar. (a) silver target, (b) silicon target and (c)+(d) ZnO target. The linear fits indicate the proportionality between rate and applied power.

As mentioned above the setup provides the possibility to deposit different types of material. The three sputter sources are equipped with a zinc-oxide (ZnO:Al) target (Al_2O_3 content of 1%), a silver (Ag) target and a silicon (Si) target.

The deposition rates are determined from the quotient of layer thickness measured from step profiling of prepared layers and the deposition time. The rates for the different materials are shown in Fig. A.13. The linear increase with the power points to the proportionality of both quantities. The sputter efficiency of silver is the largest under the used materials.

Bibliography

[1] M.A. Green and S. Pillai. Harnessing plasmonics for solar cells. *Nature Photonics*, 6(3):130–132, March 2012.

[2] M. Bazilian, I. Onyeji, M. Liebreich, I. MacGill, J. Chase, J. Shah, D. Gielen, D. Arent, D. Landfear, and S. Zhengrong. Re-considering the economics of photovoltaic power. Blomberg NEF: New York, USA., May 2012. retrieved from: http://about.bnef.com/2012/05/16/re-considering-the-economics-of-photovoltaic-power-a-co-authored-white-paper-on-pv-economics on 05.02.2113.

[3] C.-J. Yang. Reconsidering solar grid parity. *Energy Policy*, 38(7):3270–3273, 2010.

[4] Sunshot vision study. U.S. Department of Energy (DOE)., February 2012. retrieved from: `http://www1.eere.energy.gov/solar/sunshot/vision_study.html` on 05.02.2013.

[5] M.A. Green, K. Emery, Y. Hishikawa, W. Warta, and E.D. Dunlop. Solar cell efficiency tables (version 39). *Progress in Photovoltaics: Research and Applications*, 20(1):12–20, 2012.

[6] A.G. Aberle. Thin-film solar cells. *Thin Solid Films*, 517(17):4706–4710, 2009. 4th International Conference on Technological Advances of Thin Films and Surface Coatings.

[7] U. Kroll, J. Meier, S. Benagli, D. Borello, J. Steinhauser, E. Vallat, L. Castens, J. Orhan, Y. Djeridane, X. Multone, et al. Thin film silicon PV: From R&D to large-area production equipment. In *Photovoltaic Specialists Conference (PVSC), 2011 37th IEEE*, pages 000213–000218. IEEE, 2011.

[8] F. Yang, L. Zhang, T. Tanaka, Zheng Y., F. Schimitt, R. Wang, A. Tso, K. Reinke, N. Hammond, M. Pandit, L. Li, L. Tsuei, Z. Yuan, and B. Shieh. Uniform growth of a-Si / µc-Si tandem junction solar cells over $5.7\,m^2$ substrates. In *Photovoltaic Specialists Conference (PVSC), 2009 34th IEEE*, pages 001541–001545, june 2009.

[9] S. Faÿ, S. Dubail, U. Kroll, J. Meier, Y. Ziegler, and A.V. Shah. Light-trapping Enhancement for Thin-Film Silicon Solar Cells by Roughness Improvement of the ZnO front TCO. In *Proceedings of the 16th EUPVSEC*, page 361, Glasgow, 2000.

[10] R.G. Gordon. Criteria for choosing transparent conductors. *MRS BULLETIN*, 25:53, 2000.

[11] J. Hüpkes, B. Rech, B. Sehrbrock, O. Kluth, J. Müller, H.P. Bochem, and M. Wuttig. Development of surface-textured zinc oxide for thin film silicon solar cells by high rate reactive sputtering. In *Technical Digest of the 14th International Photovoltaic Science and Engineering Conference*, pages 379–382, 2003.

[12] V. Sittinger, F. Ruske, W. Werner, B. Szyszka, B. Rech, J. Hüpkes, G. Schöpe, and H. Stiebig. ZnO: Al films deposited by in-line reactive AC magnetron sputtering for a-Si:H thin film solar cells. *Thin Solid Films*, 496(1):16–25, 2006.

[13] M. Berginski, J. Hüpkes, M. Schulte, G. Schöpe, H. Stiebig, B. Rech, and M. Wuttig. The effect of front ZnO: Al surface texture and optical transparency on efficient light trapping in silicon thin-film solar cells. *J. Appl. Phys.*, 101:074903, 2007.

[14] T.L. Temple, G.D.K. Mahanama, H.S. Reehal, and D.M. Bagnall. Influence of localized surface plasmon excitation in silver nanoparticles on the performance of silicon solar cells. *Solar Energy Materials and Solar Cells*, 93:1978–1985, 2009.

[15] S. Pillai, K.R. Catchpole, T. Trupke, G. Zhang, J. Zhao, and M.A. Green. Enhanced emission from Si-based light-emitting diodes using surface plasmons. *Appl. Phys. Lett.*, 88:161102, 2006.

[16] S. Pillai, K.R. Catchpole, T. Trupke, and M.A. Green. Surface plasmon enhanced silicon solar cells. *J. Appl. Phys.*, 101:093105, 2007.

[17] F. J. Beck, S. Mokkapati, and K. R. Catchpole. Plasmonic light-trapping for Si solar cells using self-assembled, Ag nanoparticles. *Progress in Photovoltaics: Research and Applications*, 18:500–504, 2010.

[18] Y.A. Akimov, W.S. Koh, S.Y. Sian, and S. Ren. Nanoparticle-enhanced thin film solar cells: Metallic or dielectric nanoparticles? *Appl. Phys. Lett.*, 96:073111, 2010.

[19] H.R. Stuart and D.G. Hall. Enhanced dipole-dipole interaction between elementary radiators near a surface. *Phys. Rev. Lett.*, 80:5663–5666, 1998.

156

[20] D. Derkacs, S. H. Lim, P. Matheu, W. Mar, and E. T. Yu. Improved performance of amorphous silicon solar cells via scattering from surface plasmon polaritons in nearby metallic nanoparticles. *Appl. Phys. Lett.*, 89:093103, 2006.

[21] C.-I. Ho, D.-J. Yeh, V.-C. Su, C.-H. Yang, P.-C. Yang, M.-Y. Pu, C.-H. Kuan, I.-C. Cheng, and S.-C. Lee. Plasmonic multilayer nanoparticles enhanced photocurrent in thin film hydrogenated amorphous silicon solar cells. *J. Appl. Phys.*, 112(2):023113, 2012.

[22] X. Chen, B. Jia, J.K. Saha, B. Cai, N. Stokes, Q. Qiao, Y. Wang, Z. Shi, and M. Gu. Broadband enhancement in thin-film amorphous silicon solar cells enabled by nucleated silver nanoparticles. *Nano Lett.*, 12(5):2187–2192, 2012.

[23] H. Tan, R. Santbergen, A.H.M. Smets, and M. Zeman. Plasmonic light trapping in thin-film silicon solar cells with improved self-assembled silver nanoparticles. *Nano Lett.*, 12(8):4070–4076, 2012.

[24] V.E. Ferry, M.A. Verschuuren, H.B.T. Li, E. Verhagen, R.J. Walters, R.E.I. Schropp, H.A. Atwater, and A. Polman. Light trapping in ultrathin plasmonic solar cells. *Opt. Express*, 18(102):A237–A245, 2010.

[25] L. Zeng, Y. Yi, C. Hong, J. Liu, N. Feng, X. Duan, L.C. Kimerling, and B.A. Alamariu. Efficiency enhancement in Si solar cells by textured photonic crystal back reflector. *Appl. Phys. Lett.*, 89:111111, 2006.

[26] U.W. Paetzold, E. Moulin, D. Michaelis, W. Böttler, C. Wächter, V. Hagemann, M. Meier, R. Carius, and U. Rau. Plasmonic reflection grating back contacts for microcrystalline silicon solar cells. *Appl. Phys. Lett.*, 99:181105, 2011.

[27] H.A. Atwater and A. Polman. Plasmonics for improved photovoltaic devices. *Nat. Mater.*, 9(3):205–213, 2010.

[28] C. Wang, M. Luconi, A. Masi, and L. Fernandez. Silver nanoparticles as optical sensors. In Perez [228], chapter 12, pages 225–256. Available from: http://www.intechopen.com/books/silver-nanoparticles/silver-nanoparticles-as-optical-sensors.

[29] J. Aizpurua and R. Hillenbrand. Localized surface plasmons: Basics and applications in field-enhanced spectroscopy. In Enoch and Bonod [229], chapter 5, pages 151–176.

[30] C. Hägglund and B. Kasemo. Nanoparticle Plasmonics for 2D-Photovoltaics: Mechanisms, Optimization, and Limits. *Opt. Express*, 17(14):11944–11957, Jul 2009.

Bibliography

[31] Z. Liu, W. Hou, P. Pavaskar, M. Aykol, and S.B. Cronin. Plasmon resonant enhancement of photocatalytic water splitting under visible illumination. *Nano Lett.*, 11(3):1111–1116, 2011.

[32] O. Stenzel, A. Stendal, K. Voigtsberger, and C. von Borczyskowski. Enhancement of the photovoltaic conversion efficiency of copper phthalocyanine thin film devices by incorporation of metal clusters. *Solar Energy Materials and Solar Cells*, 37(3-4):337 – 348, 1995.

[33] M. Westphalen, U. Kreibig, J. Rostalski, H. Lüth, and D. Meissner. Metal cluster enhanced organic solar cells. *Solar energy materials and solar cells*, 61(1):97–105, 2000.

[34] C. Hägglund, M. Zäch, and B. Kasemo. Enhanced charge carrier generation in dye sensitized solar cells by nanoparticle plasmons. *Appl. Phys. Lett.*, 92(1):013113, 2008.

[35] S.D. Standridge, G.C. Schatz, and J.T. Hupp. Distance dependence of plasmon-enhanced photocurrent in dye-sensitized solar cells. *J. Am. Chem. Soc.*, 131(24):8407–8409, 2009.

[36] H. Chen, M.G. Blaber, S.D. Standridge, E.J. DeMarco, J.T. Hupp, M.A. Ratner, and G.C. Schatz. Computational modeling of plasmon-enhanced light absorption in a multicomponent dye sensitized solar cell. *The Journal of Physical Chemistry C*, 116(18):10215–10221, 2012.

[37] E. Moulin, P.Q. Luo, B. Pieters, J. Sukmanowski, J. Kirchhoff, W. Reetz, T. Müller, R. Carius, F.X. Royer, and H. Stiebig. Photoresponse enhancement in the near infrared wavelength range of ultrathin amorphous silicon photosensitive devices by integration of silver nanoparticles. *Appl. Phys. Lett.*, 95:033505, 2009.

[38] P.Q. Luo, E. Moulin, J. Sukmanowski, F.X. Royer, X.M. Dou, and H. Stiebig. Enhanced infrared response of ultra thin amorphous silicon photosensitive devices with Ag nanoparticles. *Thin Solid Films*, 517(23):6256–6259, 2009.

[39] M. Zeman. Solar cell operational principles. In *Solar Cells*, chapter 4. TU Delft, 2009. http://ocw.tudelft.nl/courses/microelectronics/solar-cells/readings/4-solar-cell-operational-principles/.

[40] NASA solar system exploration - sun: Facts and figures "Effective temperature 5777 K". Technical report, NASA, 2012. retrieved from http://solarsystem.nasa.gov/planets/profile.cfm?Object=Sun&Display=Facts on 23 December 2012.

[41] American Society for Testing and Materials (ASTM) Terrestrial Reference Spectra for Photovoltaic Performance Evaluation, ASTM International, 100 Barr Harbor Drive, PO Box C700, West Conshohocken, PA, 19428-2959 USA. *Reference Solar Spectral Irradiance: Air Mass 1.5.* retrieved from http://rredc.nrel.gov/solar/spectra/am1.5 on 18.12.2012.

[42] C.A. Gueymard, D. Myers, and K. Emery. Proposed reference irradiance spectra for solar energy systems testing. *Solar Energy*, 73(6):443 – 467, 2002.

[43] Google earth. U.S. Department of State Geographer © 2013 Google Data SIO, NOAA, U.S. Navy, NGA, GEBCO © 2009 GeoBasis-DE/BKG, April 2013.

[44] G.P. Smestad. *Optoelectronics of solar cells.* Spie Press Monograph, Pm115. SPIE–Optical Engineering Press, 2002.

[45] P. Würfel. *Physics of Solar Cells: From Basic Principles to Advanced Concepts.* Physics Textbook. Wiley-VCH, Weinheim, 2009.

[46] H. Ibach and H. Lüth. *Festkörperphysik: Einführung in die Grundlagen.* Springer-Lehrbuch. Springer, Berlin, Heidelberg, New York, 1995.

[47] O. Semonin, J.M. Luther, and M.C. Beard. Multiple exciton generation in a quantum dot solar cell. *SPIE Newsroom*, March 2012. 10.1117/2.1201203.004146.

[48] M.A. Green. *Third Generation Photovoltaics: Advanced Solar Energy Conversion.* Springer Series in Photonics. Springer, Berlin Heidelberg, 2005.

[49] T. Trupke, M.A. Green, and P. Würfel. Improving solar cell efficiencies by up-conversion of sub-band-gap light. *J. Appl. Phys.*, 92(7):4117–4122, 2002.

[50] B.S. Richards and A. Shalav. Enhancing the near-infrared spectral response of silicon optoelectronic devices via up-conversion. *Electron Devices, IEEE Transactions on*, 54(10):2679 –2684, 2007.

[51] W. Shockley and H. J. Queisser. Detailed balance limit of efficiency of p-n junction solar cells. *J. Appl. Phys.*, 32(3):510–519, 1961.

[52] W. Shockley and W. T. Read. Statistics of the recombinations of holes and electrons. *Phys. Rev.*, 87:835–842, Sep 1952.

[53] R. N. Hall. Electron-hole recombination in germanium. *Phys. Rev.*, 87:387, 1952.

[54] A.V. Shah. *Thin-Film Silicon Solar Cells.* Engineering Sciences: Micro- And Nanotechnology. EPFL Press, Lausanne, 2010.

[55] E. Lorenzo, G.L. Araújo, A. Cuevas, M. Egido, J. Minano, and R. Zilles. *Solar Electricity - Engeneering of Photovoltaic Systems.* PROGENSA, Madrid, 1994.

Bibliography

[56] G. Prakash and H.P. Garg. *Solar Energy: Fundamentals and Applications.* Tata McGraw-Hill Publishing Company, 2000.

[57] M. Wolf. Limitations and possibilities for improvement of photovoltaic solar energy converters: Part i: Considerations for earth's surface operation. *Proceedings of the IRE*, 48(7):1246–1263, 1960.

[58] H. Kasai and H. Matsumura. Study for improvement of solar cell efficiency by impurity photovoltaic effect. *Solar Energy Materials and Solar Cells*, 48:93–100, 1997.

[59] M.A. Green. *Silicon solar cells: advanced principles & practice.* Centre for Photovoltaic Devices and Systems, University of New South Wales, 1995.

[60] M.J. Keevers and M.A. Green. Efficiency improvements of silicon solar cells by the impurity photovoltaic effect. *J. Appl. Phys.*, 75(8):4022–4031, 1994.

[61] M.A. Green. Third generation photovoltaics: solar cells for 2020 and beyond. *Physica E: Low-dimensional Systems and Nanostructures*, 14:65 – 70, 2002.

[62] A. Martí, E. Antolín, C. R. Stanley, C. D. Farmer, N. López, P. Díaz, E. Cánovas, P. G. Linares, and A. Luque. Production of photocurrent due to intermediate-to-conduction-band transitions: A demonstration of a key operating principle of the intermediate-band solar cell. *Phys. Rev. Lett.*, 97:247701, Dec 2006.

[63] A. Luque and A. Martí. Increasing the efficiency of ideal solar cells by photon induced transitions at intermediate levels. *Phys. Rev. Lett.*, 78(26):5014–5017, 1997.

[64] A. Martí and G.L. Araújo. Limiting efficiencies for photovoltaic energy conversion in multigap systems. *Solar Energy Materials and Solar Cells*, 43(2):203–222, 1996.

[65] A.S. Brown and M.A. Green. Radiative coupling as a means to reduce spectral mismatch in monolithic tandem solar cell stacks theoretical considerations. In *Photovoltaic Specialists Conference, 2002. Conference Record of the Twenty-Ninth IEEE*, pages 868–871, 2002.

[66] A. Luque, A. Martí, and L. Cuadra. Thermodynamic consistency of sub-bandgap absorbing solar cell proposals. *Electron Devices, IEEE Transactions on*, 48(9):2118–2124, sep 2001.

[67] E. Antolín, A. Matí, P.G. Linares, I. Ramiro, E. Hernández, C.D. Farmer, C.R. Stanley, and A Luque. Advances in quantum dot intermediate band solar cells.

In *Photovoltaic Specialists Conference (PVSC), 2010 35th IEEE*, pages 000065–000070, 2010.

[68] M.J. Keevers and M.A. Green. Extended infrared response of silicon solar cells and the impurity photovoltaic effect. *Solar Energy Materials and Solar Cells*, 41/42(0):195–204, 1996.

[69] M. Zeman. Advanced amorphous silicon solar cell technologies. In Poortmans and Arkhipov [230], chapter 5, pages 173–236.

[70] S. Bose. Structural model of c-Si and a-Si. retrieved from: http://www.physics.brocku.ca/people/Faculty/Bose/ on 15.12.2012.

[71] Kazuo Morigaki and Chisato Ogihara. Amorphous semiconductors: Structure, optical, and electrical properties. In Kasap and Capper [231], chapter 25, pages 565–580.

[72] K. Morigaki, K. Takeda, H. Hikita, C. Ogihara, and P. Roca i Cabarrocas. The kinetics of the light-induced defect creation in hydrogenated amorphous silicon - Stretched exponential relaxation. *Journal of Non-Crystalline Solids*, 354:2131 – 2134, 2008.

[73] Y. Bar-Yam and J. D. Joannopoulos. Dangling Bond in a-Si:H. *Phys. Rev. Lett.*, 56:2203–2206, May 1986.

[74] W.E. Spear and P.G. Le Comber. Substitutional doping of amorphous silicon. *Solid State Communications*, 17(9):1193 – 1196, 1975.

[75] A.V. Shah, H. Schade, M. Vanecek, J. Meier, E. Vallat-Sauvain, N. Wyrsch, U. Kroll, C. Droz, and J. Bailat. Thin-film silicon solar cell technology. *Progress in photovoltaics: Research and applications*, 12(2-3):113–142, 2004.

[76] R.A. Street. Luminescence and recombination in hydrogenated amorphous silicon. *Advances in physics*, 30(5):593–676, 1981.

[77] X. Deng and E.A. Schiff. Amorphous silicon-based solar cells. In A. Luque and S. Hegedus, editors, *Handbook of Photovoltaic Science and Engineering*, pages 505–565. John Wiley & Sons, Ltd, 2003.

[78] M.H. Cohen, H. Fritzsche, and S.R. Ovshinsky. Simple band model for amorphous semiconducting alloys. *Phys. Rev. Lett.*, 22(20):1065–1068, May 1969.

[79] A.V. Shah, J Meier, E. Vallat-Sauvain, N. Wyrsch, U. Kroll, C. Droz, and U. Graf. Material and solar cell research in microcrystalline silicon. *Solar Energy Materials and Solar Cells*, 78:469 – 491, 2003.

Bibliography

[80] H. Fritzsche. Development in understanding and controlling the Staebler-Wronski effect in a-Si:H. *Annu. Rev. Mater. Res.*, 31(1):47–79, 2001.

[81] D.L. Staebler and C.R. Wronski. Reversible conductivity changes in discharge produced amorphous Si. *Appl. Phys. Lett.*, 31:292, 1977.

[82] L. Houben. *Plasmaabscheidung von mikrikristallinem Silizium: Merkmale der Mikrostruktur und deren Deutung im Sinne von Wachstumsvorgängen.* PhD thesis, Heinrich-Heine-Universität Düsseldorf, 1998.

[83] A. Matsuda. Amorphous and microcrystalline silicon. In Kasap and Capper [231], chapter 26, pages 581–595.

[84] J. Meier, S. Dubail, R. Platz, P. Torres, U. Kroll, J.A. Anna Selvan, N. Pellaton Vaucher, Ch. Hof, D. Fischer, H. Keppner, R. Flückiger, A. Shah, V. Shklover, and K.-D. Ufert. Towards high-efficiency thin-film silicon solar cells with the "micromorph" concept. *Solar Energy Materials and Solar Cells*, 49(1-4):35 – 44, 1997.

[85] K.L. Chopra, PD Paulson, V. Dutta, et al. Thin-film solar cells: an overview. *Progress in Photovoltaics Research and Applications*, 12(23):69–92, 2004.

[86] E. Vallat-Sauvain, A.V. Shah, and J. Bailat. Advances in microcrystalline silicon solar cell technologies. In Poortmans and Arkhipov [230], chapter 4, pages 133–172.

[87] E. Hecht. *Optik.* Oldenbourg, 2005.

[88] R.A. Street. Doping and the fermi energy in amorphous silicon. *Phys. Rev. Lett.*, 49:1187–1190, 1982.

[89] B. Rech, C. Beneking, and H. Wagner. Improvement in stabilized efficiency of a-Si:H solar cells through optimized p/i-interface layers. *Solar Energy Materials and Solar Cells*, 41-42:475–483, 1996.

[90] G. Ganguly, D.E. Carlson, S.S. Hegedus, D. Ryan, R.G. Gordon, D. Pang, and R.C. Reedy. Improved fill factors in amorphous silicon solar cells on zinc oxide by insertion of a germanium layer to block impurity incorporation. *Applied Physics Letters*, 85:479, 2004.

[91] E. Vallat-Sauvain, S. Faÿ, S. Dubail, J. Meier, J. Bailat, U. Kroll, and A.V. Shah. Improved Interface Between Front TCO and Microcrystalline Silicon pin Solar Cells. In *Mat. Res. Soc. Symp. Proc*, volume 664, 2001.

162

[92] K. Ellmer and R. Wendt. D.c. and r.f. (reactive) magnetron sputtering of ZnO:Al films from metallic and ceramic targets: a comparative study. *Surface and Coatings Technology*, 93(1):21–26, 1997.

[93] J. Hüpkes. *Untersuchung des reaktiven Sputterprozesses zur Herstellung von aluminiumdotierten Zinkoxid-Schichten für Silizium-Dünnschichtsolarzellen.* PhD thesis, RWTH Aachen, 2006.

[94] H. W. Deckman, C. R. Wronski, H. Witzke, and E. Yablonovitch. Optically enhanced amorphous silicon solar cells. *Appl. Phys. Lett.*, 42(11):968–970, 1983.

[95] W. Beyer, J. Hüpkes, and H. Stiebig. Transparent conducting oxide films for thin film silicon photovoltaics. *Thin Solid Films*, 516(2-4):147 – 154, 2007.

[96] F.-J. Haug, T. Söderström, O. Cubero, V. Terrazzoni-Daudrix, and C. Ballif. Plasmonic absorption in textured silver back reflectors of thin film solar cells. *J. Appl. Phys.*, 104:064509, 2008.

[97] U.W. Paetzold, F. Hallermann, B.E. Pieters, U. Rau, R. Carius, and G. von Plessen. Localized plasmonic losses at metal back contacts of thin-film silicon solar cells. In Ralf B. Wehrspohn; Andreas Gombert, editor, *Proc. SPIE*, volume 7725 of *Photonics for Solar Energy Systems III*, pages 772517–1 – 772517–9, 2010.

[98] S. Haas, A. Gordijn, G. Schöpe, B.E. Pieters, and H. Stiebig. Influence of the laser parameters on the patterning quality of thin-film silicon modules. In *Proc. of SPIE*, pages 66510H–66510H–10, 2007.

[99] S. Haas, G. Schöpe, Ch. Zahren, and H. Stiebig. Analysis of the laser ablation processes for thin-film silicon solar cells. *Applied Physics A*, 92:755–759, 2008.

[100] K.K. Kern, W. and Schuegraf. Deposition Technologies and Applications: Introduction and Overview. In Seshan [232], chapter 1, pages 11–44.

[101] F. Hamelmann, G. Haindl, J. Schmalhorst, A. Aschentrup, E. Majková, U. Kleineberg, U. Heinzmann, A. Klipp, P. Jutzi, A. Anopchenko, M Jergel, and S Luby. Metal oxide/silicon oxide multilayer with smooth interfaces produced by in situ controlled plasma-enhanced MOCVD. *Thin Solid Films*, 358(1-2):90–93, 2000.

[102] R.A. Street. *Hydrogenated Amorphous Silicon.* Cambridge Solid State Science Series. Cambridge University Press, 1991.

[103] J. R. Doyle, D. A. Doughty, and A. Gallagher. Silane dissociation products in deposition discharges. *Journal of Applied Physics*, 68(9):4375–4384, 1990.

Bibliography

[104] A. Matsuda, K. Nomoto, Y. Takeuchi, A. Suzuki, A. Yuuki, and J. Perrin. Temperature dependence of the sticking and loss probabilities of silyl radicals on hydrogenated amorphous silicon. *Surface Science*, 227(1-2):50–56, 1990.

[105] D.M. Mattox. *Handbook of Physical Vapor Deposition (PVD) Processing*. Elsevier Science - William Andrew Applied Science Publishers, Oxford Burlington, 2nd edition, 2010.

[106] S. Rossnagel. Sputtering and sputter deposition. In Seshan [232], chapter 8, pages 319–348.

[107] F. Geiger, C.A. Busse, and R.I. Loehrke. The vapor pressure of indium, silver, gallium, copper, tin, and gold between 0.1 and 3.0 bar. *International Journal of Thermophysics*, 8:425–436, 1987.

[108] M. Ohring. *Materials science of thin films. Deposition and structure*. Acad. Press, San Diego, 2002.

[109] K. Wasa and S. Hayakawa. *Handbook of Sputter Deposition Technology: Principles, Technology and Applicatons*. Materials Science and Process Technology Series. Noyes Publication, Westwood, NJ, 1992.

[110] S. Rossnagel. Glow discharge plasmas and sources for etching and deposition. In J.L. Vossen and W. Kern, editors, *Thin film processes. II*, Thin Film Processes, chapter 2, pages 9–78. Acad. Press, San Diego, 1991.

[111] J.W. Coburn. Plasma-assisted etching. *Plasma Chemistry and Plasma Processing*, 2, No. 1:1–41, 1982.

[112] K. Wasa, M. Kitabatake, and H. Adachi. *Thin Film Materials Technology: Sputtering of Compound Materials*. Materials Science and Process Technology Series. Electronic Materials and Process Technology. Springer - William Andrew Inc., Norwich, NY, 2004.

[113] S. Hazra, S. Pal, S. Kundu, and M.K. Sanyal. Scanning probe microscopy and X-ray studies of confined metal films. *Applied Surface Science*, 182(3-4):244–250, 2001.

[114] D.J. Semin, A. Lo, S.E. Roark, R.T. Skodje, and K.L. Rowlen. Time-dependent morphology changes in thin silver films on mica: A scaling analysis of atomic force microscopy results. *The Journal of Chemical Physics*, 105(13):5542–5551, 1996.

164

[115] L. VJ, N.P. Kobayashi, M.S. Islam, W. Wu, P. Chaturvedi, N.X. Fang, S.Y. Wang, and R.S. Williams. Ultrasmooth Silver Thin Films Deposited with a Germanium Nucleation Layer. *Nano Letters*, 9(1):178–182, 2009.

[116] C. Charton and M. Fahland. Growth of Ag films on PET deposited by magnetron sputtering. *Vacuum*, 68(1):65–73, 2002.

[117] Z. Zhang and M.G. Lagally. Atomistic processes in the early stages of thin-film growth. *Science*, 276(5311):377–383, 1997.

[118] C. Sönnichsen. *Plasmons in metal nanostructures.* PhD thesis, Ludwig-Maximilians-Universität München, 2001.

[119] William L Barnes, Alain Dereux, and Thomas W Ebbesen. Surface plasmon subwavelength optics. *Nature*, 424(6950):824–830, 2003.

[120] Katherine A Willets and Richard P Van Duyne. Localized surface plasmon resonance spectroscopy and sensing. *Annu. Rev. Phys. Chem.*, 58:267–297, 2007.

[121] J.J. Greffet. Introduction to surface plasmon theory. In Enoch and Bonod [229], chapter 4, pages 105–148.

[122] J. Homola, S.S. Yee, and G. Gauglitz. Surface plasmon resonance sensors: review. *Sensors and Actuators B: Chemical*, 54(1-2):3–15, 1999.

[123] S.A. Maier. *Plasmonics - Fundamentals and Applications.* Springer, New York, 2007.

[124] K.L. Kelly, T.R. Jensen, A.A. Lazarides, and G.C. Schatz. Modeling metal nanoparticle optical properties. In Daniel L. Feldheim, editor, *Metal nanoparticles. Synthesis, characterization, and applications*, chapter 4, pages 89–118. Dekker, New York, 2002.

[125] C.F. Bohren and D.R. Huffman. *Absorption and Scattering of Light by Small Particles.* Wiley-VCH Verlag GmbH, Weinheim, Germany, 2007.

[126] U. Kreibig and M. Vollmer. *Optical properties of metal clusters.* Springer series in materials science; 25. Springer, Berlin, 1995.

[127] P. Laven. Mie Plot v4.2 - A computer program for scattering of light from a sphere using Mie theory & the Debye series. http://philiplaven.com/mieplot.htm, 3 2010.

[128] C. Sönnichsen, T. Franzl, T. Wilk, G. Plessen, and J. Feldmann. Plasmon resonances in large noble-metal clusters. *New Journal of Physics*, 4:93, 2002.

Bibliography

[129] S.A. Maier and H.A. Atwater. Plasmonics: Localization and guiding of electromagnetic energy in metal/dielectric structures. *J. Appl. Phys.*, 98:011101, 2005.

[130] M. A. van Dijk, A. L. Tchebotareva, M. Orrit, M. Lippitz, S. Berciaud, D. Lasne, L. Cognet, and B. Lounis. Absorption and scattering microscopy of single metal nanoparticles. *Phys. Chem. Chem. Phys.*, 8:3486–3495, 2006.

[131] R. Rangel-Rojo, J.A. Reyes-Esqueda, C. Torres-Torres, A. Oliver, L. Rodriguez-Fernandez, A. Crespo-Sosa, J.C. Cheang-Wong, J. McCarthy, H.T. Bookey, and A.K. Kar. Linear and nonlinear optical properties of aligned elongated silver nanoparticles embedded in silica. In Perez [228], chapter 2, pages 35–62. Available from: http://www.intechopen.com/books/silvernanoparticles/linear-and-nonlinear-optical-properties-of-aligned-elongated-silver-nanoparticles-embedded-in-silica.

[132] C. Sönnichsen, T. Franzl, T. Wilk, G. von Plessen, J. Feldmann, O. Wilson, and P. Mulvaney. Drastic reduction of plasmon damping in gold nanorods. *Phys. Rev. Lett.*, 88:077402, 2002.

[133] H. Hövel, S. Fritz, A. Hilger, U. Kreibig, and M. Vollmer. Width of cluster plasmon resonances: Bulk dielectric functions and chemical interface damping. *Phys. Rev. B*, 48:18178–18188, Dec 1993.

[134] T. D. Moustakas, H. Paul Maruska, and R. Friedman. Properties and photovoltaic applications of microcrystalline silicon films prepared by rf reactive sputtering. *Journal of Applied Physics*, 58(2):983–986, 1985.

[135] H. Matsumura. Formation of Silicon-Based Thin Films Prepared by Catalytic Chemical Vapor Deposition (Cat-CVD) Method. *Japanese Journal of Applied Physics*, 37(Part 1, No. 6A):3175–3187, 1998.

[136] M. Zeman. Thin-film silicon solar cells. In *Solar Cells*, chapter 7. TU Delft, 2009. http://ocw.tudelft.nl/courses/microelectronics/solar-cells/readings/7-thin-film-silicon-solar-cells/.

[137] L. Feitknecht, F. Freitas, C. Bucher, J. Bailat, A.V. Shah, Ch. Ballif, J. Meier, J. Spitznagel, U. Kroll, B. Strahm, A. A. Howling, L. Sansonnens, and Ch. Hollenstein. Fast growth of microcrystalline silicon solar cells on LP-CVD ZnO in industrial KAI PECVD reactors. In *Proceedings of the 21st EPVSEC*, Dresden, Germany, 2006.

[138] D.D. Evanoff and G. Chumanov. Size-controlled synthesis of nanoparticles. 1."Silver-only" aqueous suspensions via hydrogen reduction. *J. Phys. Chem. B*, 108(37):13948–13956, 2004.

[139] Y. Yin, Z.Y. Li, Z. Zhong, B. Gates, Y. Xia, and S. Venkateswaran. Synthesis and characterization of stable aqueous dispersions of silver nanoparticles through the tollens process. *J. Mater. Chem.*, 12(3):522–527, 2002.

[140] S. Maenosono, T. Okubo, and Y. Yamaguchi. Overview of nanoparticle array formation by wet coating. *Journal of Nanoparticle Research*, 5(1):5–15, 2003.

[141] Y.K. Hong, H. Kim, G. Lee, W. Kim, J.I. Park, J. Cheon, and J.Y. Koo. Controlled two-dimensional distribution of nanoparticles by spin-coating method. *Appl. Phys. Lett.*, 80:844, 2002.

[142] K. Lee, M. Weis, D. Taguchi, E. Majková, T. Manaka, and M. Iwamoto. Effect of carrier injection process in the organic field-effect transistor by introducing metal nanoparticle monolayer. *Physics Procedia*, 14(0):239–244, 2011. 9th International Conference on Nano-Molecular Electronics.

[143] S. Chen. Langmuir- Blodgett Fabrication of Two-Dimensional Robust Cross-Linked Nanoparticle Assemblies. *Langmuir*, 17(9):2878–2884, 2001.

[144] R.C. Wang, Y.-X. Lin, M.R.S. Huang, and C.Y. Chao. Orientation-controlled growth and optical properties of diverse Ag nanoparticles on Si(100) and Si(111) wafers. *Nanotechnology*, 24(4):045601, 2013.

[145] F. Burmeister, W. Badowsky, T. Braun, S. Wieprich, J. Boneberg, and P. Leiderer. Colloid monolayer lithography-A flexible approach for nanostructuring of surfaces. *Appl. Surf. Sci.*, 144:461–466, 1999.

[146] J.C. Hulteen and R.P.V. Duyne. Nanosphere lithography: A materials general fabrication process for periodic particle array surfaces. *Journal of Vacuum Science and Technology-Section A-Vacuum Surfaces and Films*, 13(3):1553–1558, 1995.

[147] H.R. Stuart and D.G. Hall. Island size effects in nanoparticle-enhanced photodetectors. *Appl. Phys. Lett.*, 73(26):3815–3817, 1998.

[148] G. Xu, M. Tazawa, P. Jin, S. Nakao, and K. Yoshimura. Wavelength tuning of surface plasmon resonance using dielectric layers on silver island films. *Appl. Phys. Lett.*, 82:3811, 2003.

[149] Kurt J. Lesker Company Process Equipment Division, United States. *Nano 36 (38) Thin Film Deposition System*, 2013.

[150] P. Delfs. Aufbau und Inbetriebnahme einerSputteranlage mit integriertem thermischem Verdampfer. Master's thesis, University of Bielefeld, 2010.

Bibliography

[151] MDC Engineered Process Solution - Thin film deposition - MAK sputter sources. Technical report, MDC Vacuum Limited, 3 Horsted Square Bellbrook Industrial Estate Uckfield East Sussex TN22 1QG United Kingdom, 2008. retrieved from http://www.caburn.co.uk/resources/downloads/SputterForWeb.pdf on 08th Jan 2013.

[152] I. De Roeck, G. De Winter, R. De Gryse, J. Denul, A. Segers, E. Hollmann, and R. Wördenweber. The effect of composition and oxygen pressure on the superconducting properties of $NdBa_2Cu_3O_{7-x}$ thin films, deposited by rotatable magnetron sputtering. *IEEE Transactions on Applied Superconductivity*, 15(2):3070–3073, 2005.

[153] I.F. Ferguson. *Auger microprobe analysis.* Adam Hilger imprint by IOP Publishing Ltd Techno House, Redcliffe Way, Bristol BS16NX, England 335 East 45th Street, New York, NY 10017-3483, USA, 1989.

[154] L. Reimer. *Image Formation in Low-voltage Scanning Electron Microscopy.* Tutorial Text Series. SPIE Optical Engineering Press, 1993.

[155] J. Goldstein, D. Newbury, D. Joy, C. Lyman, P. Echlin, E. Lifshin, L. Sawyer, and J. Michael. *Scanning Electron Microscopy and X-ray Microanalysis.* Kluwer Academic Publishers, New York, 2003.

[156] Image Metrologie, Lyngso Alle 3A DK-2970 Horsholm Denmark. *Scanning Probe Image Prcessor (SPIP) 4.5.7 (Manual)*, 10 2007.

[157] D.B. Williams and C.B. Carter. *Transmission Electron Microscopy: A Textbook for Materials Science.* Number 1. Springer, New York, 2nd edition, 2009.

[158] P. West. *Introduction to Atomic Force Microscopy: Theory , Practice and Application.* Pacific Nanotechnology, Santa Clara, CA, 2006. http://www.paulwestphd.com/download.html.

[159] Veeco Metrology Group, Terminal Drive Plainview, NY 11803. *Dektak 6M Manual*, 2002.

[160] Mikropack GmbH, Maybachstr. 11 D-73760 Ostfildern. *Thin-Film-Measurement Spectroscopic Refelectometer NanoCalc-2000-UV/Vis/NIR*, 2008.

[161] M.L. Addonizio, R. Manoj, and I. Usatii. Optimisation of low pressure-chemical vapour deposited ZnO thin films as front electrode of thin film silicon based solar cells. *Proceedings of the 22nd European Photovoltaic Solar Energy Conference and Exhibition (Mailand)*, 22:2129–2134, 2007.

168

[162] F. M. Smits. Measurement of sheet resistivities with the four-point probe. *The Bell System Technical Journal*, 37:711–718, 1958.

[163] J. R. Senna. Finite-size corrections for 4-point probe measurements. Technical report, Instituto Nacional de Pesquisas Espaciais (INPE), Brasil, 2004.

[164] PerkinElmer Ltd, Chalfont Road Seer Green Beaconsfield BUCKS HP9 2FX United Kingdom. *LAMBDA 650/850/950 Hardware Guide*, 2004.

[165] Perkin Elmer, Inc., 940 Winter Street Waltham, MA 02451 USA. *Applications and Use of Integrating Spheres With the Lambda 650 and 850 UV/Vis and Lambda 950 UV/Vis/NIR Spectrophotometers*, 2007.

[166] J. Tauc, R. Grigorovici, and A. Vancu. Optical properties and electronic structure of amorphous germanium. *Physica Status Solidi (b)*, 15(2):627–637, 1966.

[167] D. Bruce Buchholz, Jun Liu, Tobin J. Marks, Ming Zhang, and Robert P. H. Chang. Control and Characterization of the Structural, Electrical, and Optical Properties of Amorphous Zinc-Indium-Tin Oxide Thin Films. *ACS Applied Materials & Interfaces*, 1(10):2147–2153, 2009.

[168] X. Xu, J. Yang, A. Banerjee, S. Guha, K. Vasanth, and S. Wagner. Band edge discontinuities between microcrystalline and amorphous hydrogenated silicon alloys and their effect on solar cell performance. *Appl. Phys. Lett.*, 67(16):2323–2325, 1995.

[169] J. Stuke. Review of optical and electrical properties of amorphous semiconductors. *J. Non-Cryst. Solids*, 4:1–26, 1970.

[170] M.S Abo Ghazala. Composition and electronic properties of a-SiGe:H alloys produced from ultrathin layers of a-Si:H/a-Ge:H. *Physica B: Condensed Matter*, 293(1-2):132 – 136, 2000.

[171] W.F. Smith and J. Hashemi. *Foundations of Materials Science and Engineering*. McGraw-Hill series in materials science and engineering. McGraw-Hill, 2003.

[172] N. Marechal, E. Quesnel, and Y. Pauleau. Characterization of silver films deposited by radio frequency magnetron sputtering. *Journal of Vacuum Science & Technology A: Vacuum, Surfaces, and Films*, 12(3):707–713, 1994.

[173] W. Beyer and B. Hoheisel. Photoconductivity and dark conductivity of hydrogenated amorphous silicon. *Solid State Commun.*, 47(7):573–576, 1983.

[174] Keithley Instruments, Inc., Corporate Headquarters, 28775 Aurora Road, Cleveland, Ohio 44139. *Model 6517B Electrometer - User's Manual*, 6517b-900-01 edition, June 2008.

[175] Keithley Instruments, Inc., Corporate Headquarters, 28775 Aurora Road , Cleveland, Ohio 44139. *Model 6517B Electrometer - Reference Manual*, 6517b-901-01 edition, June 2009.

[176] W.H. Weber, A. Pinczuk, and R. Merlin. *Raman Scattering in Materials Science*. Springer Series in Materials Science. Springer, Berlin Heidelberg New York, 2000.

[177] C. Droz. *Thin Film Microcrystalline Silicon Layers and Solar Cells: Microstructure and Electrical Performances*. PhD thesis, Université de Neuchâtel, Institut de Microtechnique, 2003.

[178] HORIBA Jobin Yvon - Raman Division, 231, Rue de Lille 59650 Villeneuve d'Ascq France. *LabRam Aramis User Manual*, 2007. Version 2.02.

[179] C. Droz, E. Vallat-Sauvain, J. Bailat, L. Feitknecht, J. Meier, and A.V. Shah. Relationship between Raman crystallinity and open-circuit voltage in microcrystalline silicon solar cells. *Solar Energy Materials and Solar Cells*, 81(1):61–71, 2004.

[180] L. Houben, M. Luysberg, P. Hapke, R. Carius, F. Finger, and H. Wagner. Structural properties of microcrystalline silicon in the transition from highly crystalline to amorphous growth. *Philosophical Magazine A*, 77(6):1447–1460, 1998.

[181] E. Vallat-Sauvain, C. Droz, F. Meillaud, J. Bailat, A.V. Shah, and C. Ballif. Determination of raman emission cross-section ratio in hydrogenated microcrystalline silicon. *Journal of Non-Crystalline Solids*, 352:1200 – 1203, 2006.

[182] H.G. Wagemann and H. Eschrich. *Photovoltaik: Solarstrahlung und Halbleitereigenschaften, Solarzellenkonzepte und Aufgaben*. Vieweg+ Teubner, Wiesbaden, 2nd edition, 2010.

[183] M. Hädrich. *Materialwissenschaftliche Untersuchungen an CdTe-CdS-Heterosolarzellen*. PhD thesis, Friedrich-Schiller-Universität Jena, 2009.

[184] Th. Borns Malibu GmbH & Co. KG. private communication, 2012.

[185] R. Brendel. *Thin-Film Crystalline Silicon Solar Cells: Physics and Technology*. Wiley-VCH Verlag GmbH & Co. KGaA, Weinheim, 2005.

[186] M. Pravettoni, D.J. Farrell, A.J. Chatten, R. Bose, R.P. Kenny, and Barnham K.W.J. External quantum efficiency measurements of luminescent solar concentrators: a study of the impact of backside reflector size and shape. In *Proceedings of the 24th EU PVSEC, Hamburg, Germany*, volume 24th EU PVSEC, pages 332–335. WIP Munich, 2009.

[187] T.C. Pluym, Q.H. Powell, A.S. Gurav, T.L. Ward, T.T. Kodas, L.M. Wang, and H.D. Glicksman. Solid silver particle production by spray pyrolysis. *Journal of Aerosol Science*, 24(3):383 – 392, 1993.

[188] Y.K. Mishra, S. Mohapatra, D. Kabiraj, B. Mohanta, N.P. Lalla, J.C. Pivin, and D.K. Avasthi. Synthesis and characterization of Ag nanoparticles in silica matrix by atom beam sputtering. *Scripta Materialia*, 56(7):629 – 632, 2007.

[189] C. Sönnichsen, S. Geier, N. E. Hecker, G. von Plessen, J. Feldmann, H. Ditlbacher, B. Lamprecht, J. R. Krenn, F. R. Aussenegg, V. Z-H. Chan, J. P. Spatz, and M. Möller. Spectroscopy of single metallic nanoparticles using total internal reflection microscopy. *Appl. Phys. Lett.*, 77:2949, 2000.

[190] Ch. Koch. *Niedertemperaturabscheidung von Dünnschicht-Silicium für Solarzellen auf Kunststofffolien.* PhD thesis, Universität Stuttgart, 2002.

[191] M. Kubon, E. Boehmer, M. Gastel, F. Siebke, W. Beyer, C. Beneking, and H. Wagner. Solution of the ZnO/p contact problem in a-Si:H solar cells. In *Conference Record of the Twenty Fourth. IEEE Photovoltaic Specialists Conference - 1994, First World Conference on Photovoltaic Energy Conversion*, volume 1, pages 500–503, Hawaii, 1994.

[192] T.J. Konno and R. Sinclair. Metal-mediated crystallization of amorphous silicon in silicon-silver layered systems. *Philosophical Magazine Part B*, 71(2):163–178, 1995.

[193] E. Moulin. *Thin-film silicon solar cells with integrated metal nanoparticles and metal nanostructures for enhanced light absorption.* PhD thesis, University Paul Verlaine - Metz, 2 2009.

[194] I.V. Kityk, Ebothé, K. Ozga, K.J. Plucinski, G. Chang, Kobayashi, and M. Oyama. Non-linear optical properties of the Ag nanoparticles on the ITO. *Physica E: Low-dimensional Systems and Nanostructures*, 31(1):38–42, 2006.

[195] K. Ozga, T. Kawaharamura, A.A. Umar, M. Oyama, K. Nouneh, A. Slezak, S. Fujita, M. Piasecki, A.H. Reshak, and I.V. Kityk. Second order optical effects in Au nanoparticle-deposited ZnO nanocrystallite films. *Nanotechnology*, 19(18):185709, 2008.

[196] J.Y. Lee and P. Peumans. The origin of enhanced optical absorption in solar cells with metal nanoparticles embedded in the active layer. *Opt. Express*, 18(10):10078–10087, May 2010.

[197] R.A. Street. Long-time transient conduction in a-Si:H p-i-n devices. *Philosophical Magazine Part B*, 63(6):1343–1363, 1991.

Bibliography

[198] K. Winer, I. Hirabayashi, and L. Ley. Distribution of occupied near-surface band-gap states in a-Si:H. *Phys. Rev. B*, 38:7680–7693, Oct 1988.

[199] J.W. Chen and A.G. Milnes. Energy levels in silicon. *Annual review of materials science*, 10(1):157–228, 1980.

[200] P. Spinelli, V.E. Ferry, J. van de Groep, M. van Lare, M.A. Verschuuren, R.E.I. Schropp, H.A. Atwater, and A. Polman. Plasmonic light trapping in thin-film Si solar cells. *Journal of Optics*, 14:024002, 2012.

[201] F. Lükermann, U. Heinzmann, and H. Stiebig. Plasmon enhanced resonant defect absorption in thin a-Si:H n-i-p devices. *Appl. Phys. Lett.*, 100(25):253907, 2012.

[202] R.W. Collins and W. Paul. Model for the temperature dependence of photoluminescence in a-Si:H and related materials. *Phys. Rev. B*, 25:5257–5262, Apr 1982.

[203] A. Lloret, Z.Y. Wu, M.L. Thèye, I. Zawawi, J.M. Siéfert, and B. Equer. Hydrogenated amorphous silicon p-doping with diborane, trimethylboron and trimethylgallium. *Applied Physics A: Materials Science & Processing*, 55:573–581, 1992.

[204] J. Ristein and G. Weiser. Influence of doping on the optical properties and on the covalent bonds in plasma deposited amorphous silicon. *Solar Energy Materials*, 12(3):221–232, 1985.

[205] J.D. Santos, N. González, J. Cárabe, and J.J. Gandía. Optimisation of p-type a-SiC:H for pin solar cells. *Science Jet*, 1:6, 2012.

[206] M. Stutzmann, D.K. Biegelsen, and R.A. Street. Detailed investigation of doping in hydrogenated amorphous silicon and germanium. *Phys. Rev. B*, 35:5666–5701, 1987.

[207] R.A. Street, D.K. Biegelsen, and J.C. Knights. Defect states in doped and compensated a-Si:H. *Phys. Rev. B*, 24:969–984, Jul 1981.

[208] Y.A. Akimov and W.S. Koh. Design of plasmonic nanoparticles for efficient subwavelength light trapping in thin-film solar cells. *Plasmonics*, 6:155–161, 2011.

[209] X. Zhang, Z. Qu, X. Li, M. Wen, X. Quan, D. Ma, and J. Wu. Studies of silver species for low-temperature CO oxidation on Ag/SiO$_2$ catalysts. *Sep. Purif. Technol.*, 72(3):395–400, 2010.

[210] D. Jelić, S. Mentus, J. Penavin-Skundrić, D. Bodroza, and B. Antunović. A thermogravimetric study of reduction of silver oxide under non-isothermal conditions. *Contemporary Materials*, 1:144–150, 2010.

[211] S. Bera, P. Gangopadhyay, K.G.M. Nair, B.K. Panigrahi, and S.V. Narasimhan. Electron spectroscopic analysis of silver nanoparticles in a soda-glass matrix. *J. Electron Spectrosc. Relat. Phenom.*, 152:91–95, 2006.

[212] G. I. N. Waterhouse, G. A. Bowmaker, and J. B. Metson. Interaction of a polycrystalline silver powder with ozone. *Surf. Interface Anal.*, 33(5):401–409, 2002.

[213] Y.A. Akimov and W.S. Koh. Tolerance study of nanoparticle enhancement for thin-film silicon solar cells. *Appl. Phys. Lett.*, 99:063102, 2011.

[214] K. R. Catchpole and S. Pillai. Surface plasmons for enhanced silicon light-emitting diodes and solar cells. *J. Lumin.*, 121(2):315–318, 2006.

[215] Pfeiffer Vacuum GmbH, Emmeliusstr. 33 D-35614 Germany. *Operating instructions TMH 065 / TMU 065 Turbomolecular Drag Pumps.*

[216] Pfeiffer Vacuum GmbH, Emmeliusstr. 33 D-35614 Germany. *Operating instructions TMH 260 / TMU 260 Turbomolecular Drag Pumps.*

[217] Pfeiffer Vacuum GmbH, Emmeliusstr. 33 D-35614 Germany. *Operating instructions TMH 520 / TMU 520 Turbomolecular Drag Pumps.*

[218] Alcatel Vacuum Technology France, 98, avenue de Brogny P.P. 2069 74009 Annecy Cedex. *User's Manual ACP 15 / 28 / 40 Series 2 Dry Primary Pumps*, 02 edition, June 2008.

[219] Pfeiffer Vacuum GmbH, Emmeliusstr. 33 D-35614 Germany. *Operating instructions TPH 510 / TPU 510 Turbomolecular Pump.*

[220] MeiVac Inc, 5830 Hellyer Avenue, San Jose, CA 95138, USA. *Owner's operation and maintenance manual of the MAK sputtering sources*, September 2008.

[221] MKS Instruments Deutschland GmbH, Schatzbogen 43 D-81829 München. *Benutzerhandbuch Digitale Gasflussregler Typ 1179B / 1479B / 2179B*, 04 2009.

[222] Seren Industrial Power Systems, Inc., 1717 Gallagher Drive Vineland, New Jersey, USA. *AT-3 Automatic Matching Network Operator's Manual*, September 2003.

[223] Advanced Energy Industries, Inc., 1625 Sharp Point Drive Fort Collins, CO 80525 USA. *User Manual MDX 500 Magnetron Drive*, February 2003.

[224] J. Slieh. *Präparation und Charakterisierung von Goldnanokristallen und Nanomultilayerspiegeln für Röntgenbeugungsexperimente.* PhD thesis, University of Bielefeld, 2009.

[225] Thermocoax GmbH, Brookstieg 1 D-22145 Stapelfeld Germany. *Thermocoax Heating Elements*, 2012.

Bibliography

[226] Delta Elektronika BV, Vissersdijk 4 4301 ND Zierikzee The Netherlands. *SM700-Series*, Oct 2003.

[227] Novocontrol GmbH, Obererbacher Strasse 9 D-56414 Hundsangen Germany. *Micro 96 Microtronic - Microprozessor gestützte Temperaturregelsysteme*, 6 1994.

[228] D. Pozo Perez, editor. *Silver Nanoparticles*. InTech, 2010. Available from: http://www.intechopen.com/books/silver-nanoparticles.

[229] Stefan Enoch and Nicolas Bonod, editors. *Plasmoics - From Basics to Advanced Topics*, volume 167 of *Springer Series in Optical Sciences*. Springer Berlin Heidelberg, 2012.

[230] J. Poortmans and V. Arkhipov, editors. *Thin Film Solar Cells. Fabrication, Characterization and Applications*. Wiley, Chichester, 2006.

[231] S. Kasap and P. Capper, editors. *Springer Handbook of Electronic and Photonic Materials*. Springer Science+Business Media, Inc., Boston, MA, 2007.

[232] K. Seshan, editor. *Handbook of Thin Film Deposition Processes and Techniques*. Materials science and process technology series. Noyes Publication - William Andrew Publishing, Norwich, NY, 2nd edition, 2001.

Publications related to this work

F. Lükermann, V. Mönkemöller, H. Kurz, M. Sacher, F. Hamelmann, H. Stiebig, & U. Heinzmann. 2009. Surface modification of LPCVD ZnO-Films for silicon thin film solar cells, in: Proceedings of the 24th EU PVSEC, WIP: Munich, 2299 - 2303.

F. Lükermann, U. Heinzmann, & H. Stiebig. 2012. Plasmon enhanced resonant defect absorption in thin a-Si:H n-i-p devices. Appl. Phys. Lett. 100 (25), 253907.

F. Lükermann, U. Heinzmann, & H. Stiebig. 2012. Plasmon induced NIR response of thin film a-Si:H solar cells. in: Proc. SPIE 8471, Next Generation (Nano) Photonic and Cell Technologies for Solar Energy Conversion III, 84710S-1 - 84710S-8; doi:10.1117/12.928684.

F. Lükermann, U. Heinzmann, & H. Stiebig. 2012. Photocurrent in the sub bandgap region of a-Si:H photosensitive devices induced by Ag nanoparticles, in: Proceedings of the 27th EU PVSEC, WIP: Munich, 367 - 370.

Conference contributions

F. Lükermann, V. Mönkemöller, H. Kurz, M. Sacher, F. Hamelmann, H. Stiebig, & U. Heinzmann. 2009. Surface modification of LPCVD ZNO-Films for silicon thin film solar cells, DPG Springmeeting. Dresden, Germany. (Visual presentation)

F. Lükermann, V. Mönkemöller, H. Kurz, M. Sacher, F. Hamelmann, H. Stiebig, & U. Heinzmann. 2009. Surface modification of LPCVD ZNO-Films for silicon thin film solar cells, 24th EU PVSEC. Hamburg, Germany. (Talk)

F. Lükermann, F. Hamelmann, U. Heinzmann &, H. Stiebig. 2011. Silver nanoparticles for enhanced light absorption in thin film silicon solar cells, DPG Springmeeting. Dresden, Germany. (Talk)

Conference contributions

F. Lükermann, F. Hamelmann, U. Heinzmann &, H. Stiebig. 2011. Silver nanoparticles for enhanced light absorption in thin film silicon solar cells, E-MRS Springmeeting. Nice, France. (Visual Prsentation)

F. Lükermann, U. Heinzmann &, H. Stiebig. 2012. Plasmonic enhanced NIR response of thin-film a-Si:H solar cells, DPG Spring Meeting. Berlin, Germany. (Talk)

F. Lükermann, U. Heinzmann &, H. Stiebig. 2012. Plasmon induced NIR response of thin-film a-Si:H solar cells, SPIE Optics & Photonics. San Diego, USA. (Visual Presentation)

F. Lükermann, U. Heinzmann, & H. Stiebig. 2012. Photocurrent in the sub bandgap region of a-Si:H photosensitive devices induced by Ag nanoparticles, 27th EU PVSEC. Frankfurt, Germany. (Visual Presentation)

Curriculum Vitae (Lebenslauf)

Florian Lükermann

- **born:** 20th March 1983 in Detmold (Germany)
- **nationality:** german

Education

- **01.2009 - today**
  Dissertation University of Bielefeld - Malibu GmbH & Co. KG
  Title: „Plasmon supported defect absorption in amorphous silicon thin film solar cells and devices"
- **01.2007 - 12.2008**
  Master studies at University of Bielefeld
  Master of Science, grade: 1.3
  Master-Thesis: „Untersuchung von ZnO als transparente, leitfähige Oxidschicht für Silizium-Dünnschichtsolarzellen", grade: 1.3
- **08.2006 - 12.2006**
  University of Jyväskylä (Finland), student exchange semester
- **10.2003 - 07.2006**
  Bachelor studies at University of Bielefeld
  Bachelor of Science, grade: 2.0
  Bachelor-Thesis: „Querschnittspräparation von Dünnschichtsolarzellen und Multischichtspiegeln und deren transmissionselektronenmikroskopische Untersuchung hinsichtlich Schichtaufbau und -zusammensetzung", grade: 1.0
- **1993 - 2002**
  Gymnasium of Lage (Germany), Abitur

Military service

- **2002 - 2003**
  Panzerartilleriebataillon 215, Augustdorf (Germany)

Acknowledgments (Danksagung)

180